Australian National University

Growth and Characterisation of GaN/AlGaN Nanostructures for Ultraviolet Applications

Sonachand Adhikari

January 2023

A Thesis Submitted for the Degree of Doctor of Philosophy
of the Australian National University

Department of Electronic Materials Engineering
Research School of Physics
College of Science
The Australian National University

Declaration

This thesis, to the best of my knowledge and belief, does not contain any results previously published by another person or submitted for a degree or diploma at any university except where due references are made in the text.

Sonachand Adhikari

January 2023

Acknowledgements

I would like to express my sincere gratitude to everyone for the unconditional support and help they have extended during my PhD.

First of all, I would like to thank all my supervisors, Prof. Chennupati Jagadish, Prof. Hark Hoe Tan, A/Prof. Jennifer Wong-Leung, and Dr. Mykhaylo Lysevych for their guidance, encouragement and constant support during the entire period of PhD. I am deeply grateful to my primary supervisor, Prof. Jagadish, for providing me with an opportunity to pursue PhD under his supervision. His encouragements, constant support, insightful comments, and out-of-the-box ideas have been the greatest source of motivation during my PhD.

I am extremely fortunate to have Prof. Hoe Tan in my supervisory panel. I have always enjoyed his valuable mentorship with profound knowledge of the subject and attention to detail. His continuous support and encouragement have been the source of my strength during PhD. I also would like to thank A/Prof. Jennifer Wong-Leung for the discussions on crystal structures and defects. I am also thankful to Dr. Mykhaylo Lysevych for the necessary training on MOCVD, and the discussions on epitaxial growth with MOCVD. I would also like to extend my sincere gratitude to Prof. Lan Fu for all the support.

I have been so fortunate to work along with a group full of amazing people. I would like to express my sincere thanks to all of them for their support, kindness and friendship, including Dr. Bijun Zhao, Dr. Dipankar Chugh, Dr. Inseok Yang, Dr. Rowena Yew, Dr. Parvathala Reddy Narangari, Mr. Fanlu Zhang, Dr. Vidur Raj, Mr. Ahmed Alabadla, Dr. Zahra Azimi, Dr. Naiyin Wang, Dr. Joshua Butson, Dr. Mohammad Rashidi, Ms. Nikita Gagrani, Mr. Wei-Wen Wong, Ms. Anha Bhat, Ms. Aswani Gopakumar, Mr. Joshua Soo, Mr. Bikesh Gupta, Ms. Xiaoying Huang, Dr. Siva Karuturi, Dr. Ziyuan Li, Dr. Julie Tournet, Dr. Tuomas Haggrén and Dr. Nian Jiang. This list goes on and so does the memories of time we have spent together.

This thesis would not have been possible without the experimental equipment and technical support from the ACT node of Australian National Fabrication Facility and ANU node of the Microscopy Australia. I would like to acknowledge and thank Dr. Fouad Karouta, Dr. Mark Lockrey (now at UTS, Sydney), Dr. Olivier Lee Cheong Lem, Dr. Li Li, Dr. Felipe Kremer, Dr. Kaushal Vora, Dr. Frank Brink, Mr. Chris Kafer for their expertise and technical

support in times of need. My special thank also goes to Mr. James Cotsell for providing training and access to dicing machine, without which this work would have been severely hampered.

I would like to express my sincere gratitude to Ms. Julie Arnold, Ms. Karen Nulty, Ms. Liudmila Mangos, Mrs. Sue Berkeley and Ms. Liz Micallef. They have been the best administrators I have ever come across. It is because of their continuous help that I could focus on my research without having to worry on administrative tasks.

Living and studying far away from home is not easy. I am glad to have found the families of Mr. Sukanta, Mr. Bhabindra, Mr. Karma, and Mr. Tiken. I thank my wife and daughter for their love, support and company during this journey. I would also like to thank CSIR-CEERI, Pilani, India, and my colleagues there for the unwavering support during this PhD.

Abstract

III-nitride semiconductors, comprising of AlN, GaN, InN, and their alloys are suitable materials for efficient light emitting diodes (LEDs) owing to their tunable direct bandgap from 0.7 eV in InN, 3.4 eV in GaN, to 6.2 eV in AlN. Following the successful growth of GaN on *c*-plane sapphire in the late 1990s, high-efficient GaN/InGaN blue LEDs have enabled the widespread use of white LEDs. This revolutionary change in the lighting industry has led to significant energy and cost savings owing to high efficiency and longer life of the solid-state InGaN-based LEDs. On the other hand, AlGaN-based LEDs suitable for emission in the ultraviolet (UV) wavelengths from 200 to 360 nm are yet to see the efficiency level of InGaN-based LEDs, notwithstanding their crucial requirement in replacing the mercury vapour UV lamps.

By today's standard, the external quantum efficiency of commercially available UV LEDs in the wavelength range of 200 - 360 nm is below 10%, whereas, those of InGaN-based blue LEDs have surpassed an external quantum efficiency of 80%. The key issues toward achieving highly efficient AlGaN-based UV LEDs are the high threading dislocation density (~$5x10^8$ cm^{-2}), low hole concentration as well as inefficient carrier injection, poor light extraction efficiency due to high refractive index (2.3 in GaN, and 2.15 in AlN) and transverse magnetic (TM) polarised light emission from the polar *c*-plane AlGaN quantum wells.

GaN/AlGaN nanowires have the potential to resolve most of these issues. GaN nanowires are free of threading dislocations and hence can serve as epitaxial template for subsequent growth of dislocation-free AlGaN shell around GaN nanowire sidewalls. Nanowire offers non-polar *m*-plane sidewalls and hence AlGaN quantum wells grown on GaN nanowire sidewalls are free of quantum-confined Stark effect, thus internal quantum efficiency can be increased. Further, the electric field vector of emitted light is perpendicular to the direction of propagation for emission from *m*-plane and hence, light extraction efficiency can be enhanced. Therefore, GaN/AlGaN nanowires are a potential candidate for applications in high efficiency UV LEDs. The efforts of this dissertation on the growth of GaN nanowires and subsequent growth of GaN/AlGaN nanowires towards realisation of UV emission is summarised in the following paragraphs.

First, selective area growth (SAG) of GaN nanowire on *c*-plane GaN pseudo-substrate (GaN/*c*-sapphire) is studied using metal organic chemical vapour deposition (MOCVD). Triethylgallium (TEGa) and ammonia (NH_3) are used as source of Ga and N, respectively. A mixed carrier gas of N_2/H_2 is employed for nanowire growth. A remarkable relationship has been established between the observed morphology and partial pressures of TEGa, NH_3, and H_2 for the SAG of GaN nanowires at a particular growth temperature. Based on this evidence, all of the growth parameters for SAG of GaN nanowires by MOCVD is reduced to just two parameters: (*i*) partial pressures and (*ii*) growth temperature. The optimal range of V/III ratio for SAG of GaN nanowire has been derived as 13 to 73, bases on the partial pressures of TEGa and NH_3. The present investigation also revealed that, low V/III ratio is not a sufficient criterion to determine GaN nanowire growth, but partial pressures and temperature are the key parameters that determine the GaN nanostructure morphology. Hence, this study has uncovered ways to obtain specific GaN nanostructures, more specifically, Ga-polar GaN nanowires, based on the partial pressures and growth temperature.

The selective area grown GaN nanowires developed thus far, are used as growth templates for GaN/AlGaN core-shell nanowires using MOCVD. Initial growth experiment of AlGaN shell with a mixed carrier gas of N_2/H_2 resulted in a striated surface of the AlGaN shell. A smooth surface of the AlGaN shell is a prerequisite to obtain sharp interface and avoid waviness in MQWs. Using pure N_2 as the carrier gas, AlGaN shells with smooth surface and superior optical characteristics have been obtained. This achievement is attributed to minimisation of disparity in Al and Ga adatom mobilities and reduced incorporation of unintentional impurities using pure N_2 carrier gas. AlGaN shells with gas-phase Al compositions from 15 to 60% have been grown. Elemental analysis and alloy composition determined from the emission spectra of the GaN/AlGaN core-shell nanowires indicate a lower Al incorporation in the AlGaN shell compared to the gas-phase Al composition. The reduced Al incorporation is due to the geometry of the nanowires, strain in the AlGaN layer, and gas phase parasitic reaction of trimethylaluminium and ammonia.

Finally, a systematic investigation on the growth and UV emission characteristics from $Al_xGa_{1-x}N/Al_yGa_{1-y}N$ MQWs is carried out. Microstructural and UV emission characteristics of AlGaN MQWs are studied with respect to the pitch of the nanowire arrays. It has been determined that nanowires with uniform sidewalls are obtained when the gap between the adjacent nanowires is $\geq$ 600 nm, whereas, nanowires with an inverse tapered morphology, resembling that of a trophy, is obtained for smaller gaps. Uniform emission of UV along the

length of nanowires has been achieved for nanowire array with a pitch ≥ 1.5 μm. Tunability of the UV emission wavelength has been investigated by changing the Al composition of the MQWs and UV emission in the wavelength range of 318 – 343 nm has been achieved from the nonpolar *m*-plane $Al_xGa_{1-x}N/Al_yGa_{1-y}N$ MQWs. More importantly, homogeneous emission of UV from an array of nanowires over an area of 45×45 μm^2 has been demonstrated, highlighting the possibility of scaling up for large area UV LEDs or scaling down for micro LEDs.

Overall, in this study, selective area growth of regularly arranged GaN nanowires are investigated systematically and revealed that all of the MOCVD growth parameters can be resolved to just two key parameters as partial pressures and temperature. Subsequently, using the selective area grown GaN nanowires, GaN/AlGaN core-shell nanowire growth has been investigated thoroughly. Finally, $Al_xGa_{1-x}N/Al_yGa_{1-y}N$ MQWs have been incorporated on the nanowire sidewalls and UV emission in the wavelength range of 318 to 343 nm has been demonstrated. Therefore, this work showcases the possibilities of GaN/AlGaN nanowires for UV emission. Further, the demonstration of uniform UV emission from the $Al_xGa_{1-x}N/Al_yGa_{1-y}N$ MQWs on the nonpolar *m*-plane sidewalls of regularly arranged GaN nanowires, and uniform emission of UV from an array of nanowires provide a significant step towards the future of efficient UV LEDs.

Publications

Journal Articles

1. Chugh, D., **Adhikari, S**., Wong-Leung, J., Lysevych, M., Jagadish, C. and Tan, H.H., Improving the Morphology and Crystal Quality of AlN Grown on Two-Dimensional hBN. *Crystal Growth & Design*, **2020**, 20, 1811-1819.

2. Mondal, R.K., **Adhikari, S**., Chatterjee, V. and Pal, S., Recent Advances and Challenges in AlGaN-based Ultra-violet Light Emitting Diode Technologies. *Materials Research Bulletin*, **2021**, 140, 111258.

3. **Adhikari, S**., Lysevych, M., Jagadish, C. and Tan, H.H., Selective Area Growth of GaN Nanowire: Partial Pressures and Temperature as the Key Growth Parameters. *Crystal Growth & Design*, **2022**, 22, 5345-5353.

4. **Adhikari, S**., Lem, O.L.C., Kremer, F., Vora, K., Brink, F., Lysevych, M., Tan, H.H. and Jagadish, C., Nonpolar $Al_xGa_{1-x}N/Al_yGa_{1-y}N$ Multiple Quantum Wells on GaN Nanowire for UV Emission. *Nano Research*, **2022**, 15, 7670-7680.

5. Gagrani, N., Vora, K., **Adhikari, S**., Jiang, Y., Jagadish, C. and Tan, H.H., n-SnO_x as a Transparent Electrode and Heterojunction for p-InP Nanowire Light Emitting Diodes. *Advanced Optical Materials*, **2022**, 10, 2102690.

6. **Adhikari, S**., Kremer, F., Lysevych, M., Jagadish, C. and Tan, H.H., Core-shell GaN/AlGaN Nanowires Grown by Selective Area Epitaxy. *Nanoscale Horizons*, **2023**, 8, 530-542.

Conference papers

1. **Adhikari, S**., Lysevych, M., Wong-Leung, J., Tan, H.H., Jagadish, C., Selective Area Growth of GaN Nanorods – The Role of Partial Vapour Pressures, 5th Meeting of Malaysia Nitrides Research Group (MNRG 2020), 1 – 2 December 2020.
2. **Adhikari, S.**, Lysevych, M., Wong-Leung, J., Tan, H.H., Jagadish, C., III-Nitride Nanowire Growth with MOCVD, TMOS Retreat, 3 – 4 December 2020
3. **Adhikari, S.**, Lem, O.L.C., Vora, K., Kremer, F., Lysevych, M., Tan, H.H. and Jagadish, C., UV Emission from AlGaN Multiple Quantum Wells, TMOS ECR/Student Conference 2021, 29 – 30 July 2021
4. **Adhikari, S.**, Lysevych, M., Tan, H.H. and Jagadish, C., III-Nitride Nanostructures, TMOS Conference: Meta Together, 22 – 25 November 2022

Acronyms and Symbols

ALD	Atomic layer deposition
BF	Bright field
CCD	Charged-coupled device
CCS	Close-coupled showerhead
CL	Cathodoluminescence
CVD	Chemical vapour deposition
EBL	Electron beam lithography
EDS	Energy dispersive X-ray spectroscopy
EQE	External quantum efficiency
FFT	Fast Fourier transform
FIB	Focused ion beam
HAADF	High angle annular dark field
HRTEM	High resolution transmission electron microscopy
IE	Injection efficiency
IQE	Internal quantum efficiency
LEDs	Light emitting diodes
LEE	Light extraction efficiency
MBE	Molecular beam epitaxy
MOCVD	Metal-organic chemical vapour deposition
MOVPE	Metal-organic vapour phase epitaxy
MQWs	Multiple quantum wells
NBE	Near band edge
QW	Quantum well
RF	Radio frequency
RIE	Reactive ion etching
SAED	Selected area electron diffraction
SAG	Selective area growth
sccm	Standard cubic centimetre per minute
SEM	Scanning electron microscopy

SEs	Secondary electrons
slm	Standard litre per minute
STEM	Scanning transmission electron microscopy
TEGa	Triethylgallium
TEM	Transmission electron microscopy
TMAl	Trimethylaluminium
TMGa	Trimethylgallium
TMIn	Trimethylindium
UV	Ultraviolet
VLS	Vapour-liquid-solid
WZ	Wurtzite
ZB	Zinc-blende

Contents

List of Figures

List of Tables

Chapter 1. Introduction

1.1. III-nitride semiconductors

III-nitrides semiconductors, composed of AlN, GaN, InN and their alloys have become the material of choice for efficient light emitting diodes (LEDs). The societal impact brought about by the invention of efficient GaN-based LEDs for lighting applications have led to award of the Nobel Prize in Physics 2014 to Isamu Akasaki, Hiroshi Amano, and Shuji Nakamura for their breakthrough in the research of blue LEDs [1]. Highly efficient GaN/InGaN-based LEDs have enabled the widespread use of white LEDs and have led to significant cost and energy savings.

However, the same level of efficiency is yet to be seen in AlGaN-based ultraviolet (UV) LEDs. Since the advent of III-nitride semiconductors, a lot of research has been focused on the solid-state InGaN-based LEDs for lighting application and this has led to surpassing 84% in external quantum efficiency (EQE) of blue LEDs [2], and consequently 300 lmW^{-1} luminous efficacy in white LEDs [3]. However, the EQE of state-of-the-art ultraviolet LEDs have stagnated at about 10% across the wavelength range from 200 to 350 nm.

AlGaN nanowire-based UV LEDs, on the other hand, have the potential to overcome this efficiency bottleneck of existing planar AlGaN UV LEDs. III-nitride nanowires offer crystals free of threading dislocations, nonpolar sidewalls for efficient multiple quantum wells (MQWs), and large surface-to-volume ratio for efficient UV emission.

1.2. UV light source

Due to the limited efficiency of AlGaN based UV LEDs, traditional mercury vapour UV lamps constructed of quartz tube is still predominantly used. Mercury is a toxic chemical of global concern as it is harmful to human, wildlife and the environment. In 2013, 140 countries adopted the Minamata Convention on Mercury, a global treaty aimed to protect human health and environment from the adverse effects of mercury [4]. This convention laid out a framework on phasing out manufacture, import and export of mercury-added products and mercury mining

[4]. Hence, mercury-free efficient solid-state UV LEDs are the need-of-the-hour. Further, solid-state UV LEDs have additional advantages over mercury vapour lamps as follows [5, 6]:

- Compact, robust, and portable due to lack of quartz components and filaments.
- Instant start-up without the need for warm-up time.
- High frequency on-off operation possible for just-in-time applications.
- Low voltage and power requirement.
- Variety of specific wavelengths available.

The III-nitride alloy of AlGaN is at the heart of solid-state UV LEDs due to its tuneable direct bandgap from 3.4 to 6.2 eV to cover UVA (400 – 320 nm), UVB (320 – 260 nm) and UVC (280 – 200 nm). UV light sources have been used for applications in non-line-of-sight (NLOS) communication [7-9], mass spectrometry [$10\bar{1}2$], Raman spectroscopy [13-15], DNA analysis [16], missile approach warning [17], sterilisation of water and air [6, 18], phototherapy of psoriasis, vitiligo, and atopic eczema [19-27], counterfeit detection of banknotes [28, 29], pharmaceutical assessment of drugs [30-32], curing of resins [33-36], 3D printing [37-40], plant lighting [41] and environmental monitoring [42]. The recent COVID-19 pandemic has highlighted the requirement for efficient UV LEDs in sterilisation of food and medical equipment and in water and air purification. The role of UV LEDs for applications in disinfection has been reviewed recently [6, 18]. The applications of UV LEDs based on emission wavelength and output power required are shown in Figure 1.1.

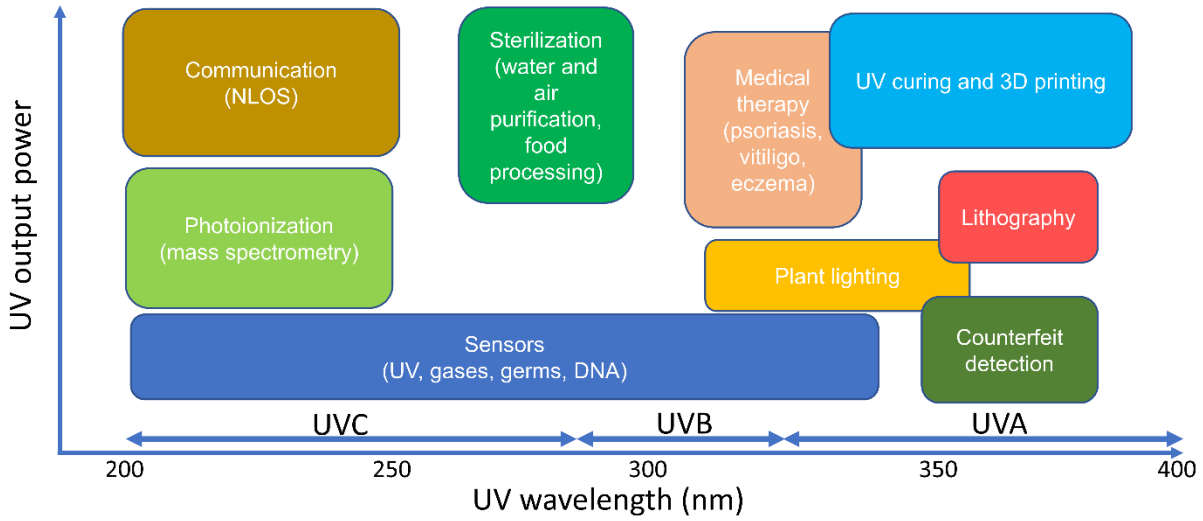

Figure 1.1 Applications of UV light.

1.3. Roadmap of UV light source market

According to the report from market analyst firm, Yole Development, the total market value of UV light sources is projected to grow at a compound annual growth rate (CAGR) of 17.8% to a market value of about $3.5 billion in 2026 as shown in Figure 1.2 [43]. The share for UV LEDs in the market has been growing steadily from a modest $100 million in 2015 to $1 billion in 2019 while conventional UV lamps have remained the mainstay during this period. However, we are about to witness a turning point in the UV light source market from 2023 onwards with solid-state UV LEDs surpassing the market share of conventional UV lamps as can be seen from the roadmap (Figure 1.2). A market share of $2.66 billion out of a total of $3.5 billion is projected to be due to UV LEDs in 2026.

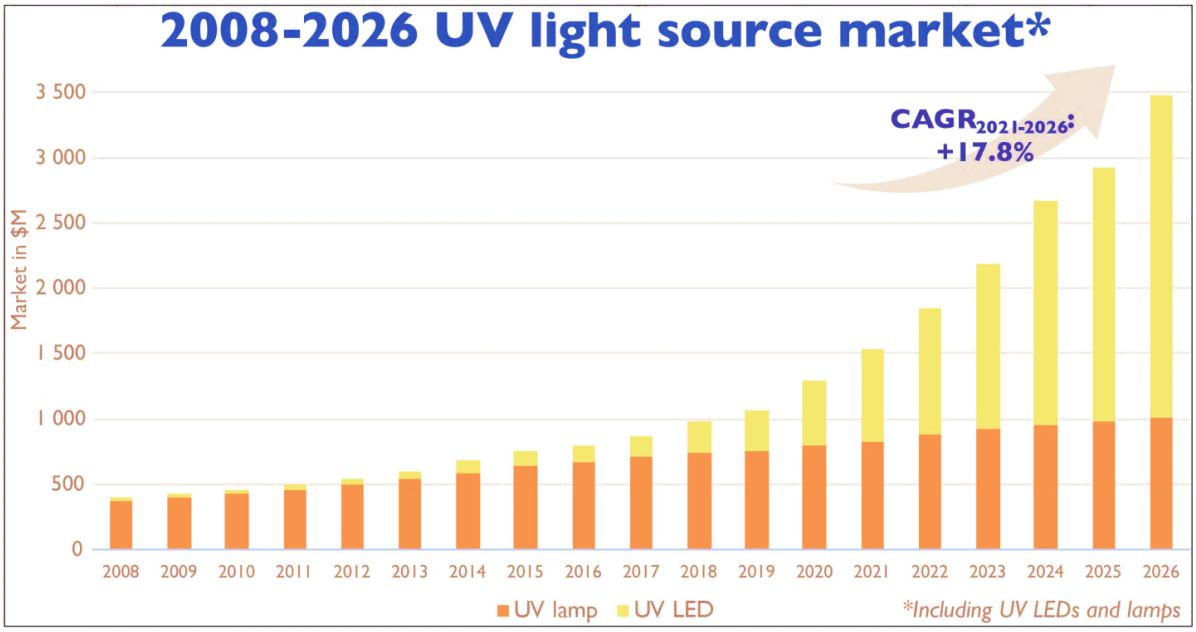

Figure 1.2 UV light source market trend from 2008 to 2026 according to Yole Development's report in Nov 2021 [43].

1.4. Performance parameters of UV LEDs

Important performance metrics of UV LEDs, which needs to be understood and addressed in order to achieve high efficiency are, internal quantum efficiency (IQE), external quantum efficiency (EQE), light extraction efficiency (LEE), wall-plug efficiency (WPE) and voltage efficiency (VE).

IQE is the ratio of number of photons generated to the number of electron-hole pairs injected in an LED. It is closely related to material quality in III-nitride epitaxial material and is numerically expressed as:

$$\text{IQE} = \frac{\text{Number of photons generated inside the LED}}{\text{Number of carriers injected}}$$

In the planar AlGaN UV LEDs, most of the generated photons are unable to escape from the LED due to total internal reflection, photon absorption within the material and in the p-type GaN contact layer. The fraction of photons escaped per photons generated inside the LED is called LEE and is expressed as:

$$\text{LEE} = \frac{\text{Number of photons emitted}}{\text{Number of photons generated inside the LED}}$$

Therefore, the useful emitted light per injected electron-hole pair is given by EQE as:

$$\text{EQE} = \frac{\text{Number of photons emitted}}{\text{Number of carriers injected}} = \text{IQE} \times \text{LEE}$$

For practical purposes, UV LEDs are electrically driven at a certain voltage (V) and current (I). The optical power output (P_{out}) with respect to the electrical power input (P_{in}) is called the wall-plug efficiency (WPE) and is given by:

$$\text{WPE} = \frac{P_{out}}{P_{in}} = \frac{P_{out}}{I \times V}$$

The electrically driven nature of UV LEDs also introduces an efficiency term called voltage efficiency (VE) defined as:

$$\text{VE} = \frac{\text{Photon energy}}{\text{Device voltage} \times \text{e}} = \frac{hc/\lambda}{eV}$$

where, h is the Planck's constant, c is the speed of light, λ is the emission wavelength, and e is the elementary charge. VE essentially provides the ratio of bandgap energy (photon energy of emitted light) to the electrical driving voltage required to operate the UV LED. A higher VE signifies optimum device performance, whereas a lower VE is indicative of highly resistive material that requires higher voltage to operate the LED.

1.5. State-of-the-art UV LEDs on planar substrates

Based on the performance parameters discussed above, the different efficiency parameters of state-of-the-art UV LEDs are summarised as follows:

IQE: The highest reported IQE of AlGaN UV LED is 91% [44]. It has been achieved by using a 4° misoriented sapphire substrate for AlGaN growth. Report also exists for IQE of 80% [45], however, IQE remains at about 60% or lower for most of the AlGaN UV LEDs [46, 47].

LEE: The highest reported LEE so far is 33%, which was achieved by KOH roughening of the N-polar AlN surface after SiC substrate removal [48]. This value is followed by an LEE of 30% [46], and 24% [49]. However, most of the UV LEDs have an LEE of 10% or below [6].

EQE: The highest reported EQE for AlGaN UV LED in the wavelength range of 200 – 360 nm is 20.3%, reported in 2017 [49], followed by an EQE of 15.7% recently reported in 2021 [50]. Apart from such few reports, EQE for most of the UV LEDs remain below 10% to this day [51, 52], as shown in Figure 1.3(a).

WPE: The highest reported WPE of UV LED is 21.6% [53]. It has been achieved by employing a multiplicative photoelectric optic converter composed of p-i-n GaN layers which acts as a hole multiplier to enhance injection of holes in the MQW. This value is followed by 15.3% WPE [50], whereas, WPE for the majority of UV LED is still below 10% [51], as shown in Figure 1.3(b).

VE: The forward voltage of UV LED as low as 5 V has been achieved, compared to the high operating voltage (> 100 V) required in mercury vapour lamps [6]. Such low operating voltage of UV LEDs, close to the value of bandgap energy has led to VE of about 80% in a large number of UV LEDs.

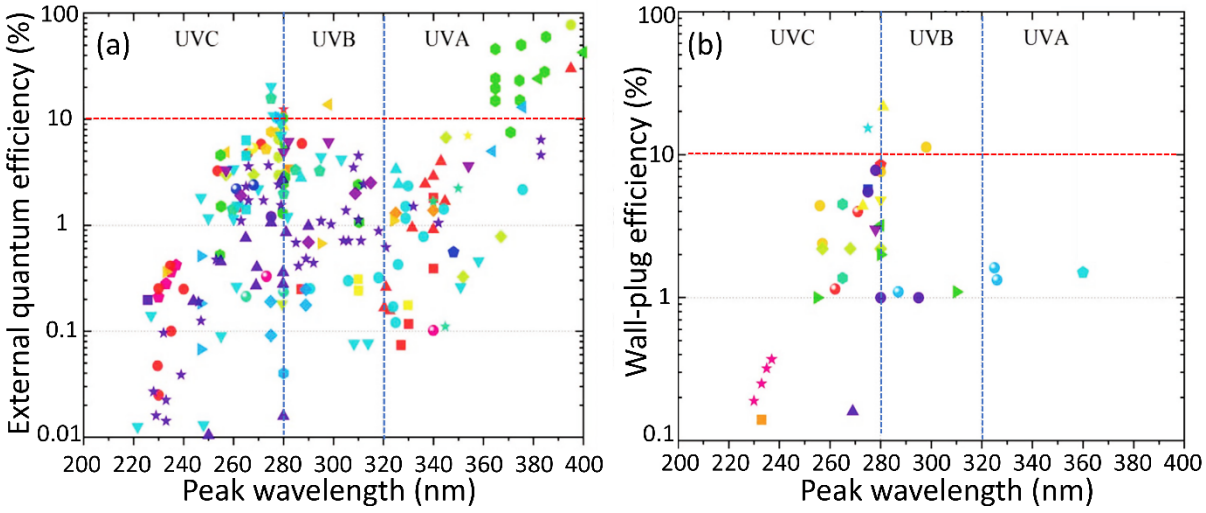

Figure 1.3 (a) External quantum efficiency (EQE), and (b) wall-plug efficiency (WPE) of UV LEDs [51].

1.6. Nonpolar and semipolar planes for UV LEDs.

Despite the large number of research groups and manufacturers working on improving the performance of AlGaN UV LEDs, the overall efficiency is still ≤ 10% as discussed above and shown in Figure 1.3.

All of the AlGaN UV LEDs discussed so far and the majority of research are on polar (0001) *c*-plane. One potential approach to improve the performance of UV LEDs is by adopting nonpolar or semipolar planes. III-nitrides crystallise in a wurtzite structure and the lack of inversion symmetry in wurtzite structure along the c-axis results in an inherent electrostatic field due to spontaneous and piezoelectric polarisations in this direction. The (0001) *c*-plane is therefore called the polar plane due to the presence of strong spontaneous and piezoelectric polarisations, whereas, $(11\bar{2}0)$ *a*-plane, and $(10\bar{1}0)$ *m*-plane are called nonpolar planes due to the absence of spontaneous and piezoelectric polarisations in these planes, while any other plane with orientation between polar and nonpolar planes are called semipolar planes.

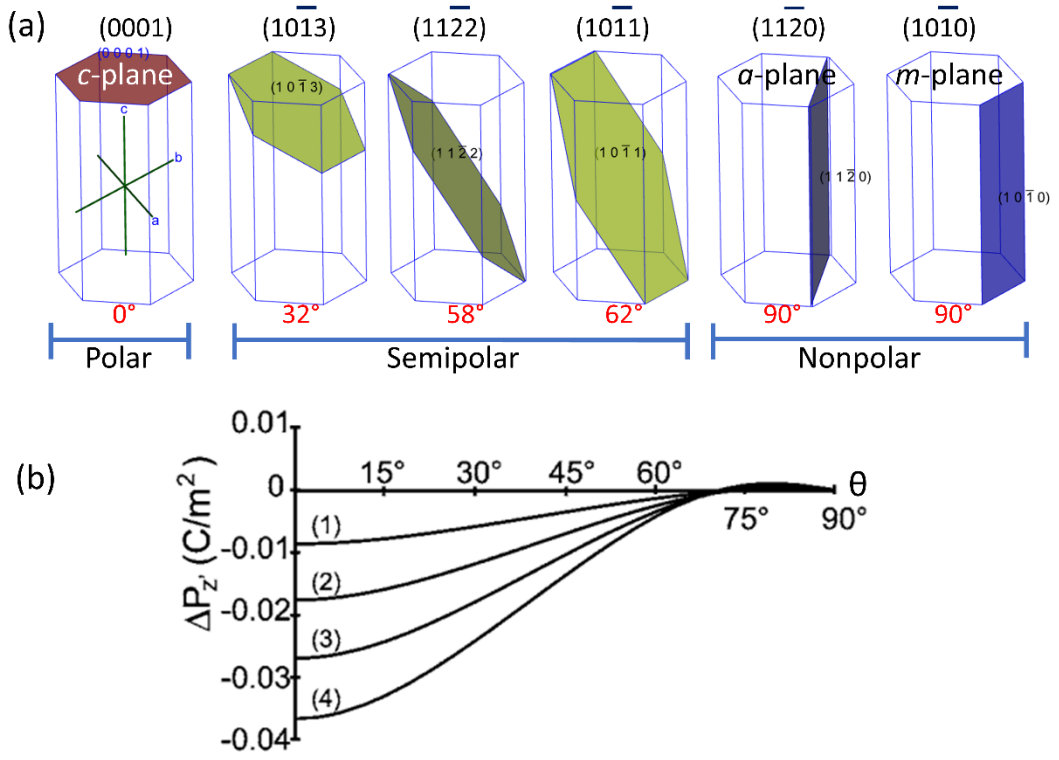

Figure 1.4 (a) Polar, semipolar, and nonpolar planes of wurtzite III-nitrides with their orientation angles. (b) Total polarisation of $Al_xGa_{1-x}N$ layer strained on GaN as a function of orientation angle of planes with respect to polar *c*-plane for AlN mole fractions x = 0.1 (1), 0.2 (2), 0.3 (3), and 0.4 (4). 0° refers to *c*-plane while 90° refers to *a*-, and *m*-planes [55].

Nonpolar and semipolar planes provide the advantage of reduced built-in electric field, leading to faster recombination resulting in higher efficiency [54]. Schematic illustration of polar (0001) *c*-plane, nonpolar $(11\bar{2}0)$ *a*-, and $(10\bar{1}0)$ *m*-planes, and some low-index semipolar planes of wurtzite III-nitride are shown in Figure 1.4(a).

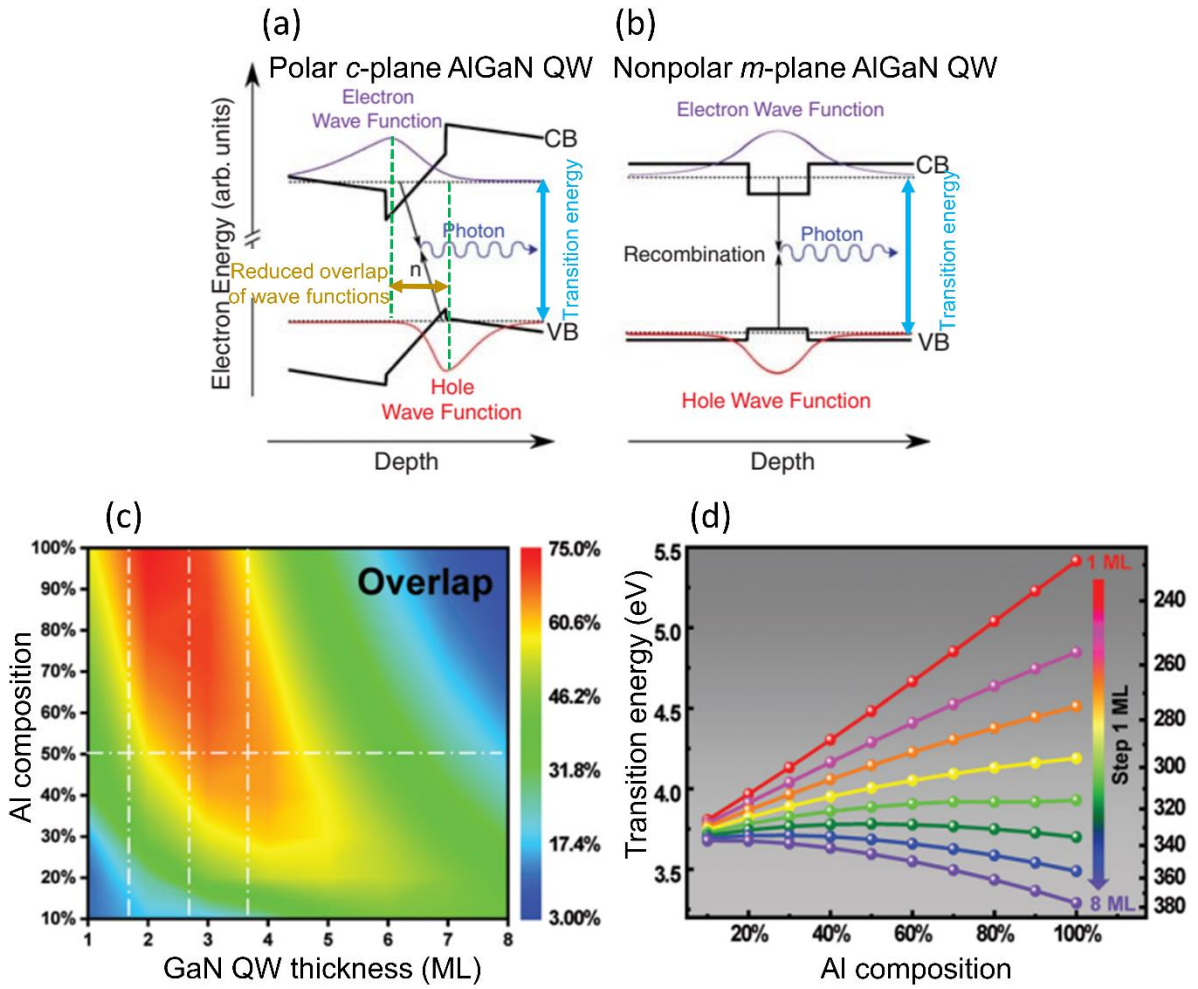

Figure 1.5 Conduction band (CB) and valence band (VB) profiles of QWs in (a) polar, and (b) nonpolar planes, adapted from [56]. (c) Overlap of electron-hole wavefunction in polar *c*-plane GaN/AlGaN MQWs as a function of GaN QW width. (d) Emission energy of GaN QW for various QW widths as a function of barrier Al content [57].

Heteroepitaxially grown AlGaN layer on GaN experiences different magnitudes of spontaneous and piezoelectric polarisations depending on the orientation angle and strain due to lattice mismatch. For calculation of the built-in electric field, the polar *c*-plane is generally considered as reference and assigned $\theta = 0°$, the nonpolar planes are therefore at $\theta = 90°$ with respect to the *c*-plane, and semipolar planes are at orientation angles $0° < \theta < 90°$. Figure 1.4(b) shows the sum of spontaneous and piezoelectric polarisations for AlGaN layer strained on GaN as a function of orientation angle for different Al compositions [55]. Semipolar planes show a reduced net polarisation compared to polar c-plane with a crossover at about 70° for all alloy compositions. The net polarisation is always zero for nonpolar orientations ($\theta = 90°$) irrespective of Al composition, whereas, it increases with Al composition in c-plane ($\theta = 0°$).

The built-in electrostatic field in polar *c*-plane results in tilting of the band structure of a quantum well (QW) is shown in Figure 1.5(a), whereas, band structure with a flat profile is maintained in nonpolar QW as shown in Figure 1.5(b) [56]. The tilted band structure of QWs in polar *c*-plane reduces the optical transition probability due to the decreased overlap integral of electron-hole wavefunctions as shown in Figure 1.5(c) [57]. Consequently, the IQE is reduced and the emission wavelength is redshifted with increasing QW width as shown in Figure 1.5(d). This phenomenon is called the quantum-confined Stark effect (QCSE). Note that the overlap of electron and hole wavefunctions deteriorates severely beyond QW width of 4 monolayers (MLs, 1 ML of GaN equals to 2.6 Å), as evident from Figure 1.5(c), and consequently redshifts the emission wavelength as can be seen from Figure 1.5(d).

The detrimental effect of built-in electrostatic field in AlGaN UV LED structures grown on polar orientation can be eliminated or reduced by growing MQWs on nonpolar and semipolar orientations [58, 59]. Thereby, the internal quantum efficiency of AlGaN UV LEDs can be increased by using nonpolar planes. Calculations have shown a strong droop in IQE of polar *c*-plane MQWs due to the internal polarisation field, whereas the MQWs on nonpolar *m*-plane showed a weaker droop [60], as shown in Figure 1.6(a) and (b).

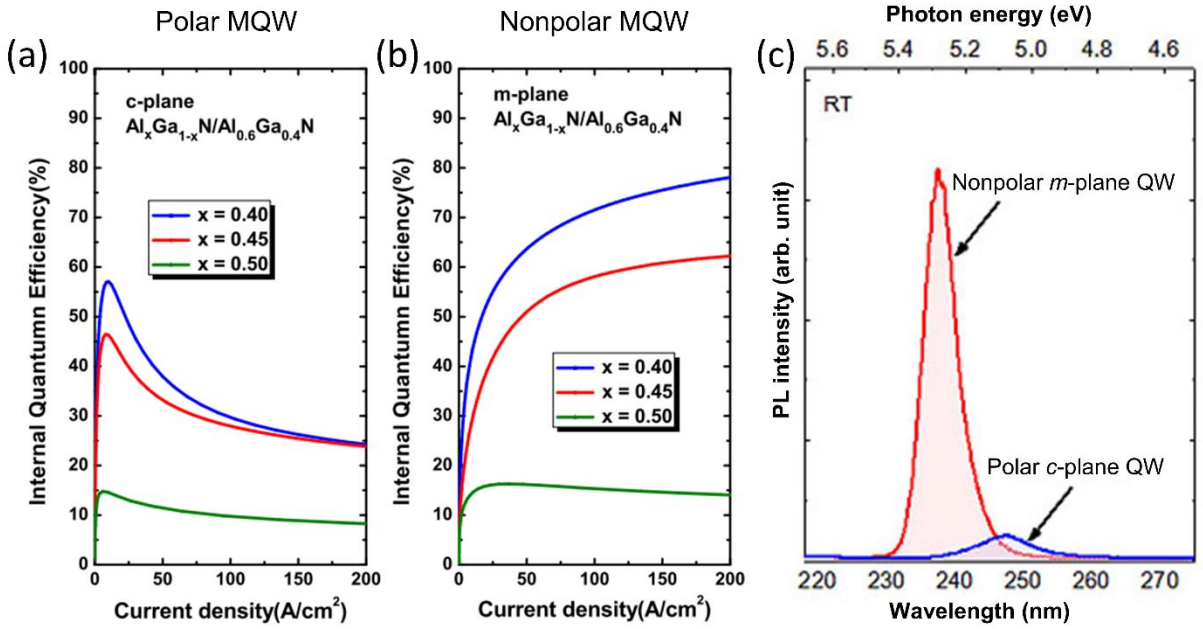

Figure 1.6 Internal quantum efficiency of (a) polar *c*-plane MQWs, and (b) nonpolar *m*-plane MQWs [60]. (c) Room temperature photoluminescence spectra from polar and nonpolar AlGaN QW [61, 62].

UV emission from nonpolar *m*-plane GaN/AlGaN MQWs at a wavelength of 356 nm (3.48 eV), free of built-in electrostatic field, was demonstrated for the first time by Waltereit *et al.* in 2000 [54]. Since then, higher photoluminescence (PL) intensity compared to the *c*-plane and QCSE-free emissions have been reported for nonpolar *a*-plane $(11\bar{2}0)$ GaN/$Al_{0.15}Ga_{0.85}N$ MQWs [63], as well as *m*-plane $Al_xGa_{1-x}N/Al_yGa_{1-y}N$ MQWs [61, 62]. Figure 1.6(c) shows the enhanced PL intensity from nonpolar *m*-plane MQWs compared to the polar *c*-plane MQWs. The absence of QCSE in nonpolar planes resulting in emission at shorter wavelength have also been observed consistently.

1.7. III-nitride nanowires for UV emission

In spite of the advantages of MQWs on nonpolar planes for UV emission, growth of nonpolar and semipolar oriented planes on sapphire substrate has not reached the maturity of *c*-plane GaN. Therefore, growth of AlGaN with nonpolar orientations are characterised by high threading dislocation density and basal plane stacking faults (BSFs) [64, 65]. The superior performance observed from nonpolar or semipolar orientations have been achieved on bulk substrates with very low threading dislocations and BSFs [62]. Material growth issues and defect reduction for nonpolar and semipolar orientations on sapphire substrate is an ongoing issue [66].

GaN/AlGaN nanowire offers the combined advantage of reduced threading dislocation density, QCSE-free emission from nonpolar sidewalls, and better light extraction efficiency to achieve high performance UV LEDs. Furthermore, costly and limited size of nonpolar bulk substrates are no longer an issue as III-nitride nanowires can be achieved using planar *c*-plane GaN on sapphire as well as Si substrate [65].

First, the issue of high threading dislocation density in planar AlGaN films and its detrimental impact on the IQE can be eliminated or significantly reduced by using nanowires. Selective area grown GaN nanowires are free of threading dislocations [67-70]. Second, GaN/AlGaN nanowires can provide an increased surface area of emission through a core-shell structure compared to the planar structure. Third, the nonpolar *m*-plane sidewalls of GaN/AlGaN nanowires can eliminate the deleterious effect of QCSE, and additionally, improve the light extraction efficiency. In *c*-plane AlGaN, the emitted light is extracted in [0001] *c*-direction, and in this orientation the electric field vector, *E*, of the emitted light is parallel to *c*-axis ($E \parallel c$) and results in transverse magnetic (TM) polarised light with low intensity for AlGaN with Al composition higher than 25% [71]. In contrast, nonpolar *m*-plane sidewalls of AlGaN

nanostructure offers efficient extraction of the $E \parallel c$ (or $E \perp m$-axis) light as shown in Figure 1.7.

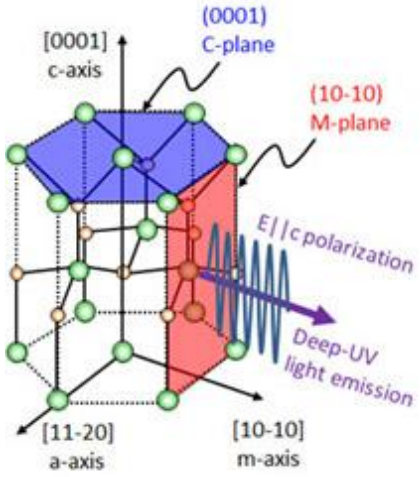

Figure 1.7 Schematic of efficient $E \parallel c$ polarised light emission from nonpolar m-plane sidewall. Adapted from [61].

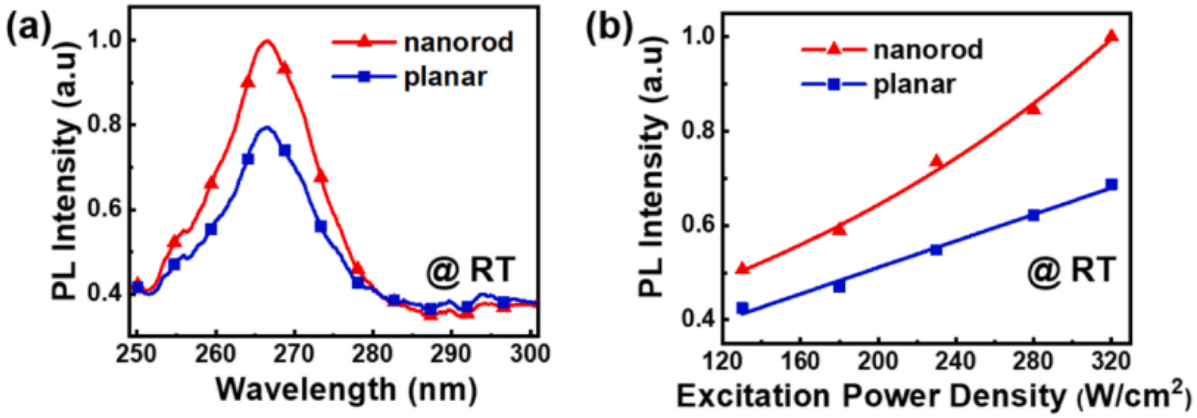

Figure1.8 (a) Room-temperature photoluminescence spectra of the nanowire array and planar samples. (b) Excitation power dependent photoluminescence intensity of the nanowire array and planar samples [72].

Furthermore, the major hurdle of low LEE from planar substrate can be alleviated by using regularly arranged nanowires. Selective area growth of GaN/AlGaN nanowires offers control over the dimensions and positions of the nanowires, and therefore, serves as a suitable template for heteroepitaxial growth of GaN/AlGaN nanowire for UV LEDs. Top-down fabricated nanowire arrays have demonstrated a higher PL intensity at room temperature (Figure 1.8(a)) as well as in the excitation power dependent PL (Figure 1.8(b)) compared to the planar structure [72]. Yet, the research and realisation of AlGaN nanowire arrays grown in a bottom-up fashion

using MOCVD still is in its infancy despite the potential of AlGaN nanowire arrays to enhance the performance of UV LEDs.

Owing to the huge potential of GaN/AlGaN nanowires in enhancing the performance of UV LEDs, two major LED manufacturers, CrayoNano AS of Trondheim, Norway, and SemiLEDs Corporation of Hsinchu, Taiwan, have recently signed an agreement to jointly develop nanowire-based next-generation UV LEDs [73]. Another company, NS Nanotech Inc. based in Ann Arbor, Michigan, USA, is aiming to deliver III-nitride nanowire-based LEDs for UV disinfection and large format as well as for augmented and virtual reality display applications [74]. These unprecedented moves by companies to focus their attention on III-nitride nanowire-based UV LED products are a testament to the advantages of III-nitride nanowires over the existing planar epitaxial layer in the UV LED market.

1.8. Thesis aim and scope

This thesis aims to provide an in-depth knowledge on the three closely-knit aspects of III-nitride nanowire growth leading up to the UV emission from AlGaN MQWs. First, selective area growth of Ga-polar GaN nanowire using MOCVD is addressed in detail. Second, growth of GaN/AlGaN core-shell nanowire heterostructure is studied using the selective area grown GaN nanowire as templates for subsequent growth of AlGaN shell. Consequently, using the combined knowledge of GaN and GaN/AlGaN core-shell nanowire growths, $Al_xGa_{1-x}N/Al_yGa_{1-y}N$ MQWs have been grown on the nonpolar *m*-plane sidewall and UV emission in the wavelength range of 318 – 343 nm has been demonstrated.

1.9. Thesis outline

This introductory chapter is followed by Chapter 2 that provides an overview on the properties and polarity of III-nitrides. A brief review on selective area growth (SAG) of GaN and AlGaN nanostructures, efficiency limitations on UV emission from planar structure and how nanostructures can aid in overcoming the efficiency bottlenecks of planar structure is also discussed in Chapter 2. Chapter 3 provides information on the experimental procedures and the theoretical background of the experimental techniques used for substrate preparation, nanowire growth, and characterisation of the nanowires.

In Chapter 4, a systematic investigation on the growth of GaN nanowires and the relevant findings are presented. GaN nanowire growths have been conducted in different conditions by varying the flow rates of triethylgallium, ammonia and total flow rate of the gas. The effect of

carrier gas composition, reactor pressure and growth temperature on the morphology of GaN nanowire has also been studied. Detailed morphological characterisation of GaN nanostructures obtained from various growths have led to the significant finding that, all of the growth parameters for SAG of GaN nanowires can be resolved into just two parameters *viz*. (*i*) partial pressures and (*ii*) growth temperature.

In Chapter 5, growth of GaN/AlGaN core-shell nanowires with various Al compositions is presented. The effect of carrier gas on the surface morphology of AlGaN shell has been studied for mixed H_2/N_2 and pure N_2 carrier gases. Al incorporation in solid phase with respect to gas phase Al composition has been investigated using energy dispersive x-ray spectroscopy (EDS) and cathodoluminescence (CL) measurements. Additionally, AlGaN shells of various Al compositions have also been studied using transmission electron microscopy (TEM) for structural defects.

In Chapter 6, growth of $Al_xGa_{1-x}N/Al_yGa_{1-y}N$ multiple quantum wells (MQWs) and the relevant characterisations are presented. AlGaN MQWs are grown on nonpolar *m*-plane sidewalls of GaN nanowire using MOCVD. The morphology of AlGaN nanowire array consisting of MQWs on the sidewalls is studied for structural uniformity with respect to the pitch of the nanowire array. TEM and CL studies have been carried out on AlGaN MQWs for analysis of structural and optical characteristics. By tuning the Al composition of AlGaN quantum well, UV emission in the wavelength range of 318 to 343 nm has been achieved.

Finally, Chapter 7 summarises the conclusions from this thesis and some suggestions for future work are outlined.

References

1. "The Nobel Prize in Physics 2014." [Accessed on: 9/10/2022]; Available from: https://www.nobelprize.org/prizes/physics/2014/summary/.
2. Narukawa, Y., Ichikawa, M., Sanga, D., Sano, M. and Mukai, T., "White light emitting diodes with super-high luminous efficacy." *Journal of Physics D: Applied Physics*, **2010**, 43, 354002.
3. "Cree First to Break 300 Lumens-Per-Watt Barrier." 2014 [Accessed on: 9/10/2022; Available from: http://www.cree.com/News-and-Events/Cree-News/Press-Releases/2014/March/300LPW-LED-barrier.
4. "Minamata Convention on Mercury." [Accessed on: 20/10/2022]; Available from: https://www.mercuryconvention.org/en/about.
5. Würtele, M.A., Kolbe, T., Lipsz, M., Külberg, A., Weyers, M., et al., "Application of GaN-based ultraviolet-C light emitting diodes – UV LEDs – for water disinfection." *Water Research*, **2011**, 45, 1481-1489.
6. Zollner, C.J., DenBaars, S.P., Speck, J.S. and Nakamura, S., "Germicidal ultraviolet LEDs: a review of applications and semiconductor technologies." *Semiconductor Science and Technology*, **2021**, 36, 123001.
7. Yuan, R. and Ma, J., "Review of ultraviolet non-line-of-sight communication." *China Communications*, **2016**, 13, 63-75.
8. Drost, R.J. and Sadler, B.M., "Survey of ultraviolet non-line-of-sight communications." *Semiconductor Science and Technology*, **2014**, 29, 084006.
9. Xu, Z. and Sadler, B.M., "Ultraviolet Communications: Potential and State-Of-The-Art." *IEEE Communications Magazine*, **2008**, 46, 67-73.
10. Brodbelt, J.S., Morrison, L.J. and Santos, I., "Ultraviolet Photodissociation Mass Spectrometry for Analysis of Biological Molecules." *Chemical Reviews*, **2020**, 120, 3328-3380.
11. Zhang, H., Li, N., Wang, Y., Zhao, D., He, J., et al., "Real-time monitoring of the degradation of Cu (II)-EDTA in H2O2/UV using illumination-assisted droplet spray ionization mass spectrometry." *Chemosphere*, **2017**, 184, 932-938.

12. Stinson, C.A., Zhang, W. and Xia, Y., "UV Lamp as a Facile Ozone Source for Structural Analysis of Unsaturated Lipids Via Electrospray Ionization-Mass Spectrometry." *Journal of the American Society for Mass Spectrometry*, **2018**, 29, 481-489.

13. Kuramochi, H., Fujisawa, T., Takeuchi, S. and Tahara, T., "Broadband stimulated Raman spectroscopy in the deep ultraviolet region." *Chemical Physics Letters*, **2017**, 683, 543-546.

14. Guo, Q., Sun, K., Feng, Z., Li, G., Guo, M., et al., "A Thorough Investigation of the Active Titanium Species in TS-1 Zeolite by In Situ UV Resonance Raman Spectroscopy." *Chemistry – A European Journal*, **2012**, 18, 13854-13860.

15. Jin, S., Feng, Z., Fan, F. and Li, C., "UV Raman Spectroscopic Characterization of Catalysts and Catalytic Active Sites." *Catalysis Letters*, **2015**, 145, 468-481.

16. Stützer, A., Welp, L.M., Raabe, M., Sachsenberg, T., Kappert, C., et al., "Analysis of protein-DNA interactions in chromatin by UV induced cross-linking and mass spectrometry." *Nature Communications*, **2020**, 11, 5250.

17. Rehm, R., Driad, R., Kirste, L., Leone, S., Passow, T., et al., "Toward AlGaN Focal Plane Arrays for Solar-Blind Ultraviolet Detection." *physica status solidi (a)*, **2020**, 217, 1900769.

18. Raeiszadeh, M. and Adeli, B., "A Critical Review on Ultraviolet Disinfection Systems against COVID-19 Outbreak: Applicability, Validation, and Safety Considerations." *ACS Photonics*, **2020**, 7, 2941-2951.

19. Zhang, P. and Wu, M.X., "A clinical review of phototherapy for psoriasis." *Lasers in Medical Science*, **2018**, 33, 173-180.

20. Wong, T., Hsu, L. and Liao, W., "Phototherapy in Psoriasis: A Review of Mechanisms of Action." *Journal of Cutaneous Medicine and Surgery*, **2013**, 17, 6-12.

21. Hönigsmann, H., "Phototherapy for psoriasis." *Clinical and Experimental Dermatology*, **2001**, 26, 343-350.

22. Bae, J.M., Jung, H.M., Hong, B.Y., Lee, J.H., Choi, W.J., et al., "Phototherapy for Vitiligo: A Systematic Review and Meta-analysis." *JAMA Dermatology*, **2017**, 153, 666-674.

23. Hamzavi, I.H., Lim, H.W. and Syed, Z.U., "Ultraviolet-based therapy for vitiligo: What's new?" *Indian J Dermatol Venereol Leprol*, **2012**, 78, 42-48.

24. Pacifico, A. and Leone, G., "Photo(chemo)therapy for vitiligo." *Photodermatology, Photoimmunology & Photomedicine*, **2011**, 27, 261-277.

25. Böhm, M., Schunter, J.A., Fritz, K., Salavastru, C., Dargatz, S., et al., "S1 Guideline: Diagnosis and therapy of vitiligo." *JDDG: Journal der Deutschen Dermatologischen Gesellschaft*, **2022**, 20, 365-378.

26. Musters, A.H., Mashayekhi, S., Harvey, J., Axon, E., Lax, S.J., et al., "Phototherapy for atopic eczema." *Cochrane Database of Systematic Reviews*, **2021**. Issue 10. Art. No.: CD013870

27. Branisteanu, D.E., Dirzu, D.S., Toader, M.P., Branisteanu, D.C., Nicolescu, A.C., et al., "Phototherapy in dermatological maladies (Review)." *Exp Ther Med*, 2022, 23, 259.

28. Lee, J.W., Hong, H.G., Kim, K.W. and Park, K.R., "A Survey on Banknote Recognition Methods by Various Sensors." *Sensors*, 2017, 17, 313.

29. Huang, K., Deng, J., Leong, H.S., Yap, S.L.K., Yang, R.B., et al., "Ultraviolet Metasurfaces of ≈ 80% Efficiency with Antiferromagnetic Resonances for Optical Vectorial Anti-Counterfeiting." *Laser & Photonics Reviews*, **2019**, 13, 1800289.

30. Pavelicova, K., Rypar, T., Markova, K., Mravec, F., Adam, V., et al., "UV-responsive fluorescent behavior of pharmaceuticals assessed by UV-induced fingerprint spectroscopy (UV-IFS)." *International Journal of Pharmaceutics*, **2022**, 122289.

31. Singh, S., Prasad, B., Savaliya, A.A., Shah, R.P., Gohil, V.M., et al., "Strategies for characterizing sildenafil, vardenafil, tadalafil and their analogues in herbal dietary supplements, and detecting counterfeit products containing these drugs." *TRAC Trends in Analytical Chemistry*, **2009**, 28, 13-28.

32. He, J., Yang, Y., Li, Y., He, Z., Chen, Y., et al., "Multiple anti-counterfeiting guarantees from simple spiropyran derivatives with solid photochromism and mechanochromism." *Cell Reports Physical Science*, **2021**, 2, 100643.

33. Sangermano, M., Razza, N. and Crivello, J.V., "Cationic UV-Curing: Technology and Applications." *Macromolecular Materials and Engineering*, **2014**, 299, 775-793.

34. Hong, B.T., Shin, K.S. and Kim, D.S., "Ultraviolet-curing behavior of an epoxy acrylate resin system." *Journal of Applied Polymer Science*, **2005**, 98, 1180-1185.

35. Shukla, V., Bajpai, M., Singh, D.K., Singh, M. and Shukla, R., "Review of basic chemistry of UV-curing technology." *Pigment & Resin Technology*, **2004**, 33, 272-279.

36. Vitale, A., Trusiano, G. and Bongiovanni, R., "UV-Curing of Adhesives: A Critical Review", in *Progress in Adhesion and Adhesives*. **2018**. p. 101-154.

37. Geisler, E., Lecompère, M. and Soppera, O., "3D printing of optical materials by processes based on photopolymerization: materials, technologies, and recent advances." *Photonics Research*, **2022**, 10, 1344-1360.

38. Jiang, F. and Drummer, D., "Analysis of UV Curing Strategy on Reaction Heat Control and Part Accuracy for Additive Manufacturing." *Polymers*, **2022**, 14, 759.

39. Zheng, J., Cai, Y., Zhang, X., Wan, J. and Fan, H., "Eugenol-Based Siloxane Acrylates for Ultraviolet-Curable Coatings and 3D Printing." *ACS Applied Polymer Materials*, **2022**, 4, 929-938.

40. Ning, L., Chen, J., Sun, J., Liu, Y., Yi, D., et al., "Preparation and Properties of 3D Printing Light-Curable Resin Modified with Hyperbranched Polysiloxane." *ACS Omega*, **2021**, 6, 23683-23690.

41. Loconsole, D. and Santamaria, P., "UV Lighting in Horticulture: A Sustainable Tool for Improving Production Quality and Food Safety." *Horticulturae*, **2021**, 7, 9.

42. Constant, D., Gonzalez, C., Touraud, E., Guigues, N. and Thomas, O., "UV Spectrophotometry: Environmental Monitoring Solutions", in *Rapid Chemical and Biological Techniques for Water Monitoring*. **2009**. p. 91-106.

43. "UV LED market to grow to $2.466bn in 2026, driven by impact of COVID-19." 2021 [Accessed on: 9/10/2022; Available from: https://markets.businessinsider.com/news/stocks/uv-led-market-to-grow-to-$2-466bn-in-2026--driven-by-impact-of-covid-19-10796232.

44. Sun, H., Mitra, S., Subedi, R.C., Zhang, Y., Guo, W., et al., "Unambiguously Enhanced Ultraviolet Luminescence of AlGaN Wavy Quantum Well Structures Grown on Large Misoriented Sapphire Substrate." *Advanced Functional Materials*, **2019**, 29, 1905445.

45. Hirayama, H., Fujikawa, S., Noguchi, N., Norimatsu, J., Takano, T., et al., "222–282 nm AlGaN and InAlGaN-based deep-UV LEDs fabricated on high-quality AlN on sapphire." *physica status solidi (a)*, **2009**, 206, 1176-1182.

46. Shatalov, M., Sun, W., Lunev, A., Hu, X., Dobrinsky, A., et al., "AlGaN Deep-Ultraviolet Light-Emitting Diodes with External Quantum Efficiency above 10%." *Applied Physics Express*, **2012**, 5, 082101.

47. Mondal, R.K., Adhikari, S., Chatterjee, V. and Pal, S., "Recent advances and challenges in AlGaN-based ultra-violet light emitting diode technologies." *Materials Research Bulletin*, **2021**, 140, 111258.

48. SaifAddin, B.K., Almogbel, A.S., Zollner, C.J., Wu, F., Bonef, B., et al., "AlGaN Deep-Ultraviolet Light-Emitting Diodes Grown on SiC Substrates." *ACS Photonics*, **2020**, 7, 554-561.

49. Takano, T., Mino, T., Sakai, J., Noguchi, N., Tsubaki, K., et al., "Deep-ultraviolet light-emitting diodes with external quantum efficiency higher than 20% at 275 nm achieved by improving light-extraction efficiency." *Applied Physics Express*, **2017**, 10, 031002.

50. Matsukura, Y., Inazu, T., Pernot, C., Shibata, N., Kushimoto, M., et al., "Improving light output power of AlGaN-based deep-ultraviolet light-emitting diodes by optimizing the optical thickness of p-layers." *Applied Physics Express*, **2021**, 14, 084004.

51. Liang, S. and Sun, W., "Recent Advances in Packaging Technologies of AlGaN-Based Deep Ultraviolet Light-Emitting Diodes." *Advanced Materials Technologies*, **2022**, 7, 2101502.

52. Kneissl, M., Seong, T.-Y., Han, J. and Amano, H., "The emergence and prospects of deep-ultraviolet light-emitting diode technologies." *Nature Photonics*, **2019**, 13, 233-244.

53. Wang, S., Long, H., Zhang, Y., Chen, Q., Dai, J., et al., "Monolithic integration of deep ultraviolet LED with a multiplicative photoelectric converter." *Nano Energy*, **2019**, 66, 104181.

54. Waltereit, P., Brandt, O., Trampert, A., Grahn, H.T., Menniger, J., et al., "Nitride semiconductors free of electrostatic fields for efficient white light-emitting diodes." *Nature*, **2000**, 406, 865-868.

55. Romanov, A.E., Baker, T.J., Nakamura, S. and Speck, J.S., "Strain-induced polarization in wurtzite III-nitride semipolar layers." *Journal of Applied Physics*, **2006**, 100, 023522.

56. Speck, J.S. and Chichibu, S.F., "Nonpolar and Semipolar Group III Nitride-Based Materials." *MRS Bulletin*, **2009**, 34, 304-312.

57. Wang, Y., Rong, X., Ivanov, S., Jmerik, V., Chen, Z., et al., "Deep Ultraviolet Light Source from Ultrathin GaN/AlN MQW Structures with Output Power Over 2 Watt." *Advanced Optical Materials*, **2019**, 7, 1801763.

58. Jo, M., Oshima, I., Matsumoto, T., Maeda, N., Kamata, N., et al., "Structural and electrical properties of semipolar $(11\bar{2}2)$ AlGaN grown on m-plane $(1\bar{1}00)$ sapphire substrates." *physica status solidi (c)*, **2017**, 14, 1600248.

59. Ichikawa, S., Iwata, Y., Funato, M., Nagata, S. and Kawakami, Y., "High quality semipolar (1-102) AlGaN/AlN quantum wells with remarkably enhanced optical transition probabilities." *Applied Physics Letters*, **2014**, 104, 252102.

60. Wang, C.-P. and Wu, Y.-R., "Study of optical anisotropy in nonpolar and semipolar AlGaN quantum well deep ultraviolet light emission diode." *Journal of Applied Physics*, **2012**, 112, 033104.

61. Banal, R., Taniyashu, Y. and Yamamoto, H. "Enhanced Deep-UV Light Emission from Nonpolar M-plane AlGaN Quantum Wells." [Accessed on: 20/10/2022]; Available from: http://www.brl.ntt.co.jp/E/activities/file/report13/report03E.html.

62. Banal, R.G., Taniyasu, Y. and Yamamoto, H., "Deep-ultraviolet light emission properties of nonpolar M-plane AlGaN quantum wells." *Applied Physics Letters*, **2014**, 105, 053104.

63. Ng, H.M., "Molecular-beam epitaxy of GaN/$Al_xGa_{1-x}N$ multiple quantum wells on R-plane (10$\bar{1}$2) sapphire substrates." *Applied Physics Letters*, **2002**, 80, 4369-4371.

64. Li, H., Zhang, H., Song, J., Li, P., Nakamura, S., et al., "Toward heteroepitaxially grown semipolar GaN laser diodes under electrically injected continuous-wave mode: From materials to lasers." *Applied Physics Reviews*, **2020**, 7, 041318.

65. Monavarian, M., Rashidi, A. and Feezell, D., "A Decade of Nonpolar and Semipolar III-Nitrides: A Review of Successes and Challenges." *physica status solidi (a)*, **2019**, 216, 1800628.

66. Farrell, R.M., Young, E.C., Wu, F., DenBaars, S.P. and Speck, J.S., "Materials and growth issues for high-performance nonpolar and semipolar light-emitting devices." *Semiconductor Science and Technology*, **2012**, 27, 024001.

67. Hersee, S.D., Rishinaramangalam, A.K., Fairchild, M.N., Zhang, L. and Varangis, P., "Threading defect elimination in GaN nanowires." *Journal of Materials Research*, **2011**, 26, 2293-2298.

68. Sundaram, S., Gmili, Y.E., Puybaret, R., Li, X., Bonanno, P.L., et al., "Nanoselective area growth and characterization of dislocation-free InGaN nanopyramids on AlN buffered Si (111) templates." *Applied Physics Letters*, **2015**, 107, 113105.

69. Katsumi, K. and Shunsuke, I., "Selective-area growth of GaN nanocolumns on Si (111) substrates for application to nanocolumn emitters with systematic analysis of dislocation filtering effect of nanocolumns." *Nanotechnology*, **2015**, 26, 225602.

70. Coulon, P.-M., Alloing, B., Brändli, V., Vennéguès, P., Leroux, M., et al., "Dislocation filtering and polarity in the selective area growth of GaN nanowires by continuous-flow metal organic vapor phase epitaxy." *Applied Physics Express*, **2016**, 9, 015502.

71. Nam, K.B., Li, J., Nakarmi, M.L., Lin, J.Y. and Jiang, H.X., "Unique optical properties of AlGaN alloys and related ultraviolet emitters." *Applied Physics Letters*, **2004**, 84, 5264-5266.

72. Fan, A., Zhuang, Z., Zhang, X., Li, C., Jiang, H., et al., "Optical properties of quasi-ordered $11\bar{2}2$ AlGaN multi-quantum-well nanorod arrays." *Journal of Alloys and Compounds*, **2021**, 885, 161166.

73. "CrayoNano and SemiLEDs to co-develop nanowire UV-C LED chips." 11 Feb 2022 [Accessed on: 10 Oct 2022]; Available from: https://www.semiconductor-today.com/news_items/2022/feb/crayonano2-110222.shtml.

74. "A Personal Purifier, Far-UVC Emitters, and NanoLEDs." [Accessed on: 10 Oct 2022]; Available from: https://www.nsnanotech.com/products.

Chapter 2. Literature Review

2.1. Introduction

This chapter provides details on the properties of III-nitrides, a review on the growth and properties of planar GaN and AlGaN from the perspective of improving crystal quality by reducing the threading dislocation density in polar *c*-plane and basal plane stacking faults (BSFs) in nonpolar planes. A review on the growth of GaN nanowires, and current status on the growth of AlGaN nanowires using metal organic chemical vapour deposition (MOCVD) is also addressed. Finally, the advantages and challenges of GaN/AlGaN nanowire are presented.

Juza and Hahn reported the synthesis of GaN by reacting hot gallium with ammonia in 1938[1], and two decades later, Grimmeiss and Koelmans reported photoluminescence from GaN in 1959 [2]. Significant advancement in the growth of single-crystalline GaN was reported by Maruska and Tietjen using hydride vapour phase epitaxy (HVPE) in 1969 [3]. They carried out the growth of GaN on 2 cm^2 *c*-plane [0001] sapphire substrate, and through room temperature optical absorption measurement, GaN was confirmed to have a direct bandgap of 3.39 eV. Due to lack of native substrate, growth of single crystalline device-quality GaN layer was plagued for decades until late 1980s to early 1990s, when AlN buffer layer [4], and GaN buffer layer [5] was introduced and achieved GaN with mirror-finish giving rise to the birth of a new semiconductor material system known as “III-nitrides”.

2.2. Properties of GaN and AlN

III-nitrides exhibit unique physical and chemical properties with respect to other semiconductors [6]. They display high hardness, good thermal conductivity and good resistance to radiation and chemicals. These properties make III-nitride a robust semiconductor candidate for several applications. This section aims to highlight the crystal structure and fundamental properties of III-nitride semiconductors.

2.2.1. Basic properties of GaN and AlN

As we will be dealing with GaN and AlGaN nanostructures, we focus our attention to the basic properties of GaN and AlN binaries. Lattice parameters and optical properties are listed in Table 2.1. Physical and mechanical properties of GaN and AlN are listed in Table 2.2, Table 2.3 lists the deformation potentials, and thermal properties are listed in Table 2.4.

Table 2.1 Lattice parameter and optical properties of GaN and AlN [7].

Parameter	**GaN**	**AlN**
Lattice parameters		
Lattice constant *c* (Å)	5.189	4.982
Lattice constant *a* (Å)	3.190	3.112
Optical and electrical properties		
Bandgap energy E_g (eV)	3.42	6.2
Breakdown field (V cm^{-1})	$3\text{-}5\times10^6$	$1.2 – 1.8\times10^6$
Electron affinity (eV)	4.1	1.45
Refractive index *n*	2.3	2.15
Dielectric constant	$E\|\|c$ = 10.4, $E\perp c$ = 9.5	$E\|\|c$ = 9.32, $E\perp c$ = 7.76
Effective mass of electron	$0.2m_0$	$0.25 – 0.39m_0$
Effective mass of heavy hole	$1.4m_0$	$3.53m_0$

Table 2.2 Physical and mechanical properties of GaN and AlN [7].

Parameter	**GaN**	**AlN**
Molecular mass (g mol^{-1})	83.7267	40.9882
Molar volume (cm^3 mol^{-1})	13.61	12.47
Density (g cm^{-3})	6.15	3.28
Density of atoms (cm^{-3})	8.9×10^{22}	9.58×10^{22}
Bulk modulus *B* (GPa)	204	210
Young's modulus *E* (GPa)	150	308
Poisson's ratio ν	0.198 – 0.37	0.18 – 0.21
Yield strength (GPa)	0.1 at 1000 K	0.3 at 1000 K
C_{11} (GPa)	367	396
C_{12} (GPa)	135	137
C_{13} (GPa)	103	108

C_{33} (GPa)	405	373
C_{44} (GPa)	95	116

Table 2.3 Deformation potentials of GaN and AlN [8].

Parameter	GaN	AlN
a_{cz} - D_1 (eV)	-6.07	-4.36
a_{ct} - D_2 (eV)	-8.88	-12.35
D_3 (eV)	5.38	9.17
D_4 (eV)	-2.69	-3.72
D_5 (eV)	-2.56	-2.93
D_6 (eV)	-3.88	-4.58

Table 2.4 Thermal properties of GaN and AlN [7].

Parameter	GaN	AlN
Melting point (°C) [6]	2518	3214
Thermal conductivity κ (W cm^{-1} K^{-1})	2.3 at 300 K	2.85-3.2
Thermal expansion	$\Delta a/a = 5.59\times10^{-6}$, $\Delta c/c = 3.17\times10^{-6}$	$\Delta a/a = 4.2\times10^{-6}$, $\Delta c/c = 5.3\times10^{-6}$
Specific heat C_p (J mol^{-1} K^{-1})	$38.1+8.96\times10^{-3}T$	$45.94+3.347\times10^{-3}T-14.98\times10^{5}T^{-2}$
Heat capacity (J mol^{-1} K^{-1})	35.4	
Heat of formation (kcal mol^{-1})	-26.4	-64

2.2.2. Crystal structure

III-nitrides exists as wurtzite (WZ) structure with the space group $P6_3mc$, due to WZ being the most thermodynamically stable phase [9]. III-nitrides can also exist in zincblende (ZB) structure with the space group $F\bar{4}3m$ and under high pressure exceeding 12 GPa, they can also undergo a phase transformation to NaCl (rock-salt) structure with the space group $Fm\bar{3}m$. The metastable ZB structure can be stabilised by topological compatibility through epitaxial growth

on {011} planes of cubic crystals such as Si, SiC, MgO, and GaAs, however, epitaxial growths cannot produce III-nitrides in rock salt structure [10].

In our discussion throughout the thesis, all of the nanostructures are in WZ phase. The WZ structure is composed of two interpenetrating hexagonal sublattices, where one sublattice is displaced by 3/8 units in fractional coordinates from the other sublattice along the [0001] *c*-axis. One hexagonal sublattice is composed only of metal (Al, Ga, or In), while, the other is composed only of N. Each atom in the WZ structure is surrounded by four atoms of the other type forming a tetrahedron as shown in Figure 2.1. In Figure 2.1, only the tetrahedron of III atoms surrounded by N is illustrated, and it should be noted that N atoms are also similarly surrounded by four III atoms. The wurtzite crystal structure of III-nitrides shown as Figure 2.1 is generated using the three-dimensional visualisation software VESTA [11].

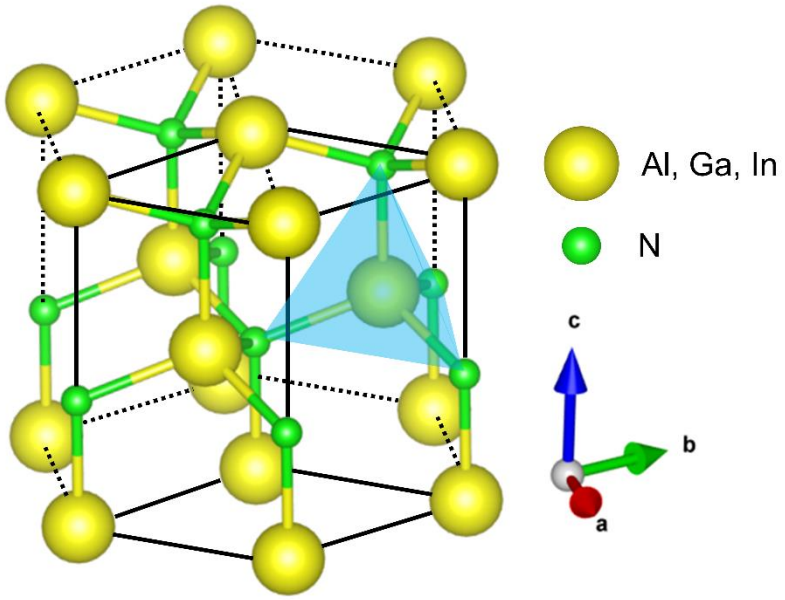

Figure 2.1 Schematic diagram of III-nitride wurtzite crystal structure.

2.2.3. Polarity in GaN

In the commonly occurring WZ phase of III-nitrides, this structure lacks an inversion symmetry along the *c*-axis and gives rise to inherent spontaneous polarisation along the [0001] direction. Polarity in GaN is defined with reference to the bonding of Ga-N along the *c*-axis, such that the vector pointing from Ga to N is adopted as positive direction of the *c*-axis. If *c* points upwards from the substrate it is Ga-polar or [0001], whereas, if *c* points downward towards the substrate then, it is N-polar or $[000\bar{1}]$ [12] and are shown in Figure 2.2(a) and (b), respectively. Some text refers to Ga- or N-polarity as Ga- or N-face, it should be noted that Ga-polar or N-polar does not mean the surface is terminated by Ga or N. A Ga-polar GaN may be

terminated by N atoms but it will always be Ga-polar unless the crystal is flipped [13]. In existence, both Ga- and N-polar surfaces are always stabilised by Ga [14].

Hellman [15], as well as, Sumiya and Fuke have reviewed the polarity in GaN [16]. Polarity of GaN layer grown on sapphire substrate can be managed during the initial phases of growth by high temperature annealing in H_2 [17-19], nitridation of the sapphire substrate [16, 20], choice of GaN or AlN as buffer layer material [21], low-temperature GaN buffer layer thickness [21, 22], and GaN buffer layer annealing condition [21, 23]. A roadmap and a flowchart on polarity management for planar GaN growth on *c*-plane sapphire using MOCVD is provided in [24] and [25], respectively. A flowchart of the polarity management in GaN growth on *c*-plane sapphire substrate is shown as Figure 2.2(c). Process similar to polarity management in GaN may also be adopted in the case of planar *c*-plane AlN growth. AlN grown on *c*-plane sapphire and Si-face SiC shows Al-polar, whereas, growth on nitridated sapphire substrate results in N-polarity [26].

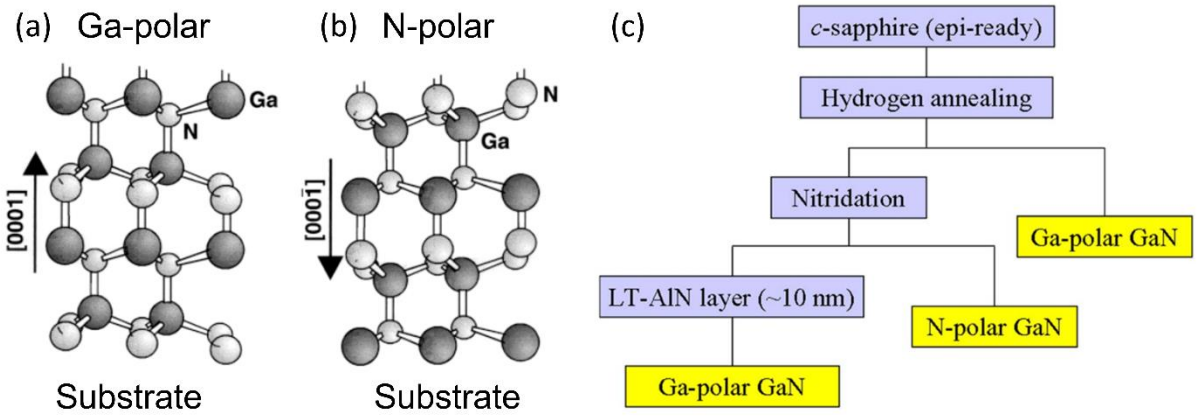

Figure 2.2 Schematics of (a) Ga-polar GaN, (b) N-polar wurtzite GaN (adapted from [13]), and (c) polarity of GaN with different growth conditions [25].

2.2.4. Polarity in GaN nanowires

Polarity in GaN has a strong influence on the surface morphology of thin-films as well as nanowire morphology. Since the earliest days of polarity determination in GaN, polarity and the observed surface morphology on planar layers have been related to as: (*i*) flat samples are unipolar with Ga-polarity, (*ii*) hexagonal pyramids are of mixed polarity where a Ga-polar core is surrounded by an N-polar matrix [12], and (*iii*) hexagonal prisms with flat tops are of N-polarity [27]. The latter two conditions are important for GaN nanostructures. In general, Ga-polar GaN nanowire typically exhibits a pyramidal top, whereas, pure N-polar GaN nanowire has a flat top.

Either pyramidal or flat top, depending on Ga- or N-polarity, respectively, determines the ease with which GaN nanowires can be grown as well as semipolar or axial heterostructures can be incorporated in nanowires. GaN also exhibits different growth rates on [0001] +*c* and $[000\bar{1}]$ -*c* directions. GaN growth is faster on +*c* as compared to -*c* direction [28, 29]. In the presence of slow growing $\{10\bar{1}1\}$ inclined semipolar facets during the Ga-polar GaN nanostructure growth, faster growth rate of (0001) plane leads to extinction of (0001) plane and the nanocrystal is terminated by $\{10\bar{1}1\}$ inclined facets resulting in pyramidal structures. N-polar GaN nanowires, on the other hand, are relatively easier to grow due to the presence of flat $(000\bar{1})$ surface on top of nanowires and initial success on catalyst-free self-assembled growth of GaN nanowires using MOCVD were achieved with N-polarity [30]. Early experiments on the selective area growth (SAG) of Ga-polar GaN resulted in only pyramidal structures defined by six $\{10\bar{1}1\}$ inclined facets without vertical sidewalls [31-34]. Therefore, polarity plays a key role in the growth of GaN nanowire and the resulting morphology [35].

2.3. Review on the growth of GaN nanowires using MOCVD

Based on the crystal polarity discussed above, polarity management in the GaN nanowire growth, as well as the advantages and shortcomings of GaN nanowires with each polarity will be discussed in this section.

2.3.1. Selective area growth of N-polar GaN

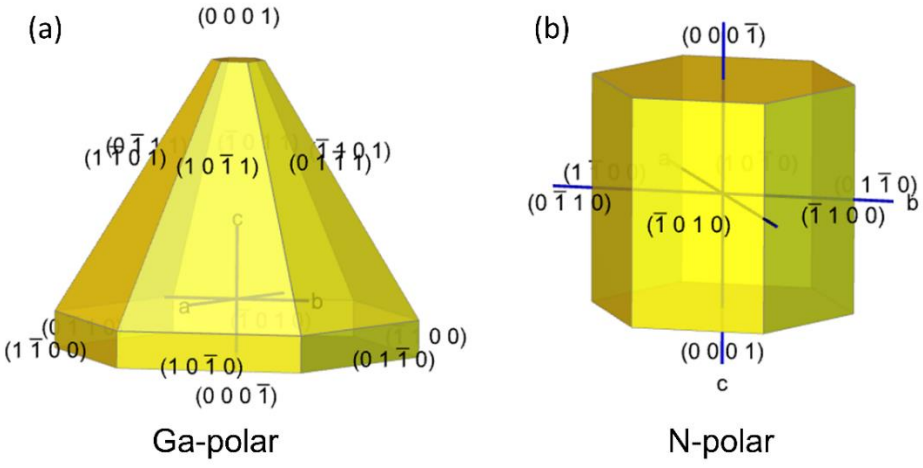

Figure 2.3 Schematic illustrations of selective area grown GaN nanostructure. (a) Ga-polar GaN, and (b) N-polar GaN.

In the SAG of GaN nanowires with MOCVD, the polarity of GaN nanowires can be managed by using different substrates. N-polar GaN nanowires are obtained on nitridated

sapphire substrates or N-polar planar GaN substrates, whereas, Ga-polar GaN nanowires are obtained on planar Ga-polar GaN substrates [35]. As mentioned earlier, SAG of Ga-polar GaN nanostructures often results in pyramidal GaN defined by six $\{10\bar{1}1\}$ inclined semipolar planes, whereas, N-polar GaN nanowires are relatively easier to grow as nanowires and are composed of vertical sidewalls of $\{10\bar{1}0\}$ *m*-planes and top $(000\bar{1})$ -*c*-plane as shown schematically in Figure 2.3(a) and (b), respectively.

SAG of N-polar GaN nanorods grown on nitridated sapphire was reported by Bergbauer *et al.* in 2010 [36]. They reported that a minimum H_2/N_2 ratio in the carrier gas is necessary to obtain nanorod with vertical sidewalls. Pyramidal nanostructures were obtained in pure N_2 carrier gas, whereas, nanorods were obtained in mixed carrier gas of H_2/N_2 with a ratio of 1/2 for the N-polar GaN. Further, the nanorod diameters were found to decrease with increasing hydrogen content in the carrier gas but remained constant after the H_2/N_2 ratio exceeded unity. Similarly, Li *et al.* also reported that the growth of N-polar GaN microrods with vertical sidewalls can be obtained either on nitridated sapphire or bulk N-polar GaN substrates using a mixed H_2/N_2 carrier gas, however, SAG on GaN on GaN/sapphire substrate under the same condition resulted in pyramidal GaN structures [35]. Apart from SAG, pyramidal Ga-polar GaN nanostructures have also been reported for self-assembled growth on *c*-plane GaN substrates [37].

The formation of pyramidal structures in the SAG of N-polar GaN while using pure N_2 carrier gas has been resolved by using a mixed H_2/N_2 carrier gas [36], whereas, Ga-polar GaN still preserves the pyramidal morphology even in the presence of H_2 in the carrier gas has led to the conclusion that it is due to the differences in surface termination of the inclined $\{10\bar{1}1\}$ *r*-plane semipolar surfaces and the etching characteristics of hydrogen [35]. The surface of semipolar $\{10\bar{1}1\}$ *r*-planes in Ga-polar GaN are largely terminated by nitrogen atoms as shown in Figure 2.4 (a), and hydrogen present in the MOCVD reactor during growth can easily passivate these $\{10\bar{1}1\}$ inclined surfaces by formation of N-H bonds, leading to the formation of pyramids. On the other hand, the corresponding $\{10\bar{1}\bar{1}\}$ *r*-planes in the N-polar GaN nanowire are terminated by Ga, rather than N, as shown in Figure 2.4 (b). The Ga-terminated $\{10\bar{1}\bar{1}\}$ *r*-planes in the case of N-polar GaN are easily etched by hydrogen to form vertical $\{10\bar{1}0\}$ *m*-plane sidewalls as shown in Figure 2.4 (c), thus leading to formation of GaN nanowires with vertical sidewalls in the case of N-polar GaN. Therefore, the relative ease in N-polar GaN nano/microrod growth with a vertical sidewall is attributed to the etching of $\{10\bar{1}\bar{1}\}$ inclined semipolar facets due to addition of H_2 in the carrier gas [36, 38].

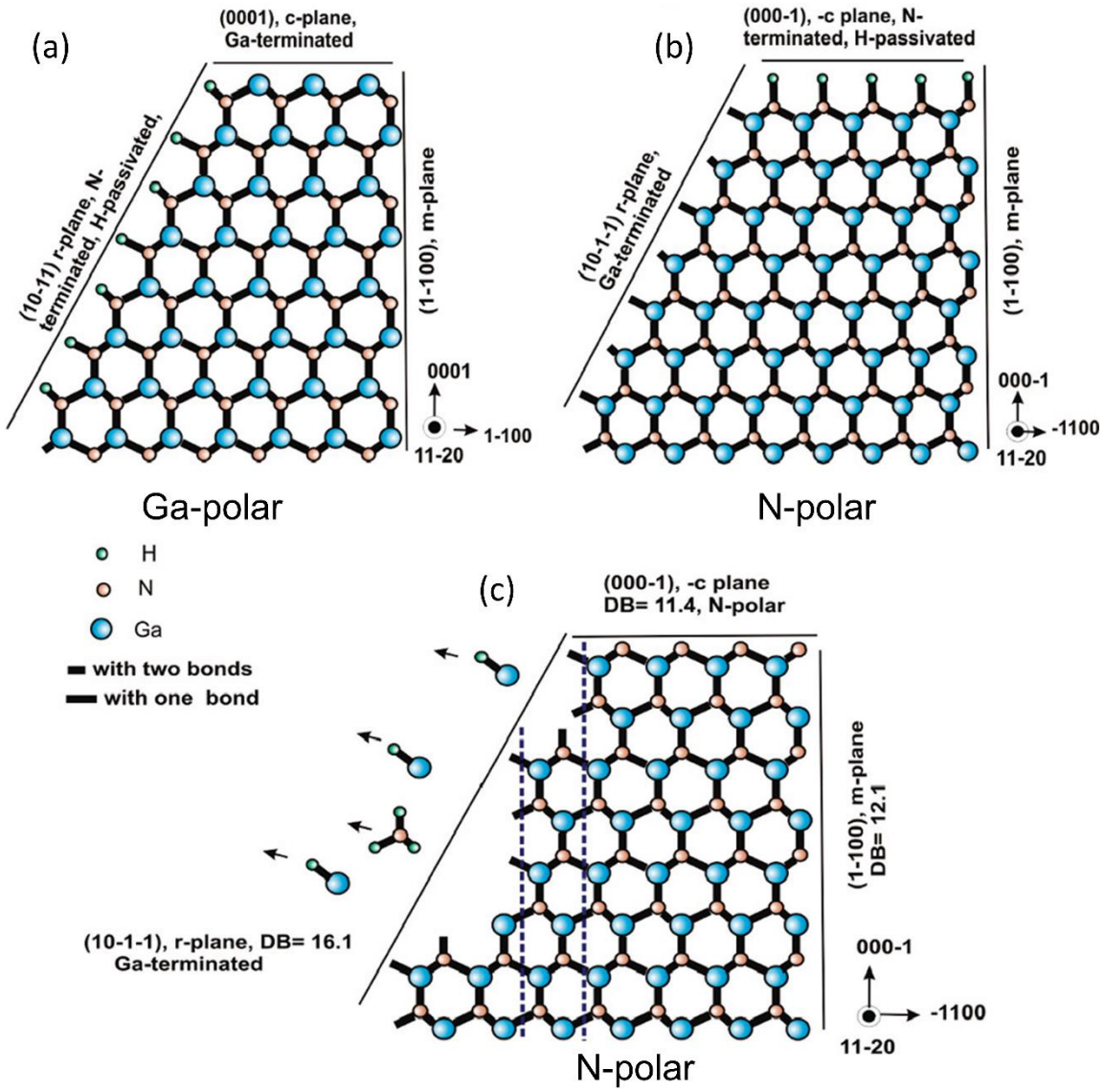

Figure 2.4 Ball and stick model of GaN (a) Ga-polar (b) N-polar. (c) Etching of $\{10\bar{1}\bar{1}\}$ plane in the case of N-polar GaN by H_2 [35].

2.3.2. Advantages and disadvantages of N-polar GaN nanowires

N-polar GaN nanowires are easier to grow than Ga-polar nanowires, they can be grown on sapphire substrates and can potentially provide a flat top surface suitable for vertical (axial) MQW structure. However, almost all of the N-polar GaN nanostructures obtained by SAG are of mixed polarity and show pyramidal facets (due to Ga-polar) surrounding the top flat surface [36, 37, 39]. The N-polar core with a flat top surface grows from the exposed regions of sapphire substrate, while Ga-polar shell with pyramidal facets surrounding the N-polar core grow from the periphery of SiN_x [37], or SiO_x mask [35, 39]. The interface between N-polar core and Ga-polar shell is an inversion domain boundary which runs along the length of nanowire.

Furthermore, as the growth of N-polar GaN nanowires are generally carried out on sapphire substrates, a high density of threading dislocations is present near the bottom of nanowires [36]. Consequently, threading dislocations running throughout the entire length has been reported in selective area grown N-polar GaN nanowires and microrods [36, 40]. The main concept of nanowire growth is to avoid defects, however, the presence of inversion domain boundaries and threading dislocations in N-polar GaN nanowires is counter-intuitive for the approach through nanowires for efficient devices. Thus, Ga-polar nanowires may be more suitable for applications involving GaN nanowires, and in the next section, a review on SAG of Ga-polar GaN nanowires is presented.

2.3.3. Selective area growth of Ga-polar GaN

Early efforts in the SAG of Ga-polar GaN resulted in merely pyramidal structures [31-34]. It was not until the report from Hersee *et al.* in 2006 that Ga-polar GaN nanowires were successfully grown using a pulsed growth scheme by MOCVD [41]. Almost a decade and a half later, the breakthrough in SAG of Ga-polar GaN nanowire using continuous flow mode was reported by Choi *et al.* in 2012 [42]. Since then, the SAG of Ga-polar GaN using MOCVD has been classified into two categories

(i) Pulsed growth, and
(ii) Continuous growth.

In the pulsed growth scheme, either group III precursor, or group V precursor, or both are injected intermittently at different times. Although, most of the present day MOCVDs have different injection lines for group III and V sources to provide a spatial separation to avoid (or minimise) gas phase parasitic reactions, pulsed growth further provides a temporal separation between the group III and V precursors and aids in increasing adatom mobility. In molecular beam epitaxy (MBE), another popular epitaxial growth tool commonly used for GaN nanowire growth, the continuous growth mode resembles that of the pulsed growth or migration-enhanced epitaxy in MOCVD [43]. In MBE, group III and V precursors approach the nanowire sidewalls from different sides and they are also separated in time as a result of the substrate rotation and the vertical configuration of nanowires [44].

2.3.3.1. Pulsed growth

Much of the interest in SAG of Ga-polar GaN nanowires has been triggered after the seminal work of Hersee *et al.* in 2006 [41]. In their SAG of GaN nanowires, continuous growth,

akin to that of two-dimensional layer growth was employed for a brief period of time until the openings were filled, after which the growth was switched to pulsed growth mode. It was realised that prolonging the continuous growth resulted in lateral growth, consequently, resulting in the loss of the nanowire geometry, hence, pulsed growth became necessary for SAG of GaN nanowires. The GaN nanowires were defined by a top (0001) central region surrounded by inclined $\{10\bar{1}2\}$ semipolar facets and vertical $\{10\bar{1}0\}$ nonpolar sidewalls.

2.3.3.2. Mechanism of pulsed growth

In 2012, Lin *et al.* from the University of Southern California carried out several pulsed growth experiments for GaN nanowires to analyse the effect of various parameters [45]. They concluded that the growth of GaN nanowire is driven by the differences in Ga adatom kinetics in terms of its adsorption, desorption, and diffusion behaviour on various crystallographic planes. They identified the major contributions in achieving nanowire morphology are the higher sticking coefficient and the longer residual time of Ga adatoms on the top (0001) plane. Further, the necessity for intermittent supply of Ga and NH_3 has been described as follows:

- Interruption of Ga is necessary for selective desorption from *m*-plane and to promote Ga adatom diffusion to the top *c*-plane, hence, minimising the lateral growth of *m*-plane and shaping the nanowire morphology, and
- Interruption of NH_3 is necessary to flush out hydrogen that passivates the $\{10\bar{1}1\}$ inclined semipolar planes to avoid the growth terminating with a pyramidal morphology.

They found the interruption times of 2 sec for Ga and 4 sec for N as the optimal condition to modulate the Ga adatom kinetics and hence achieved good GaN nanowire growth. Increasing growth temperature was also found to promote vertical-to-lateral growth ratio. Similar evolution in the nanowire morphology with pulse duration and temperature have also been reported by Jung *et al.* in 2014 [46]. They also reported that the nanowire morphology is transformed to a thin film in the case of longer Ga injection duration. This is similar to the first report on SAG of GaN nanowire by Hersee *et al.*, who highlighted the need for pulsed growth to avoid formation of film [41]. Another key observation from the aforementioned pulsed growth experiments is that if the N interruption time is reduced to zero [45], or in other words, if the N exposure time is increased too much [46], the growth resembles that of continuous mode and produces pyramidal nanostructures instead of nanowires.

In the pulsed growth mode, several combinations of injection and interruption cycles are possible and this leads to added complexity for optimisation of GaN nanowire growth. In an

effort to normalise the injection and interruption duration, Jung *et al.* defined a parameter called the Pulsed-Mode Growth Ratio (PMGR) as follows [46]:

$$\text{PMGR} = \frac{\text{N injection time / Ga injection time}}{\text{N interruption time / Ga interruption time}}$$

They emphasised that the condition to obtain nanowire growth is 1 < PMGR < 4, with a PMGR value of 3 concluded to be the optimal for growth of GaN nanowires [47].

In another effort to reduce the growth parameters for pulsed growth mode, Lin *et al.* [48] devised a growth mode in which only NH_3 was pulsed while a continuous flow of TMGa was maintained. Under this simplified pulsed growth mode, they were able to achieve an optimal nanorod growth regime with a medium range of NH_3 flow (25 sccm*)* combined with a medium interruption duration (2 sec).

Although the V/III ratio cannot be exactly defined in a pulsed growth scheme as it would mean *infinite* during the Ga interruption i.e. when only NH_3 is flowing, and *zero* during the NH_3 interruption, it may well be assumed that the effective V/III is lowered compared to that of continuous growth with the same fluxes of V and III due to the temporal separation (or small overlap) between NH_3 and group III precursor supplies. Nonetheless, pulsed mode growth is inefficient in precursor utilisation, has slower growth rate, and requires a larger set of parameter optimisation. Therefore, continuous growth mode is advantageous for SAG of GaN nanowires.

2.3.3.3. Continuous growth

Early experiments on the selective area growth (SAG) of Ga-polar GaN carried out using micron-sized hole apertures during the late 1990s resulted in pyramidal structure defined by six $\{10\bar{1}1\}$ inclined facets and seldom with a small (0001) top flat plane [31-34]. Choi *et al.* reported the successful SAG of GaN nanowire through continuous flow mode in MOCVD for the first time in 2012 [42]. Ga-polar GaN nanowires with diameters of 56 ± 6 nm, the smallest reported till date using MOCVD, has been achieved using a $0.4H_2$:$0.6N_2$ mixed carrier gas, a growth temperature of 990 °C, and a V/III ratio of 127 (with 8.1 µmol/min of Ga and 23 sccm of NH_3). They have pointed out a requirement of higher NH_3 flow as the aperture size reduces and vice-versa.

Choi *et al.* studied the influence of NH_3 flow rate and temperature on the morphology of GaN nanowires for continuous flow growth and the SEM images of nanowires are shown in Figure 2.5 [42]. They have classified the GaN nanowire growth into three regions. In region I

with very low NH_3 flow rate, nanowire growth is unable to sustain due to the lack of precursor. Region II is the nanowire growth window with sufficient supply of NH_3. In region III, enhanced lateral growth of $\{10\bar{1}0\}$ *m*-plane and the presence of inclined facets $\{10\bar{1}1\}$ and $\{10\bar{1}2\}$ became dominant at the nanowire top with increased NH_3 flow rates. They concluded that the key to achieve Ga-polar GaN nanowire under a continuous flow is *low V/III ratio* combined with *low fluxes of Ga and NH_3*, under which the anisotropy in growth rates of (0001) and $\{10\bar{1}0\}$ reaches a maximum and favours vertical growth.

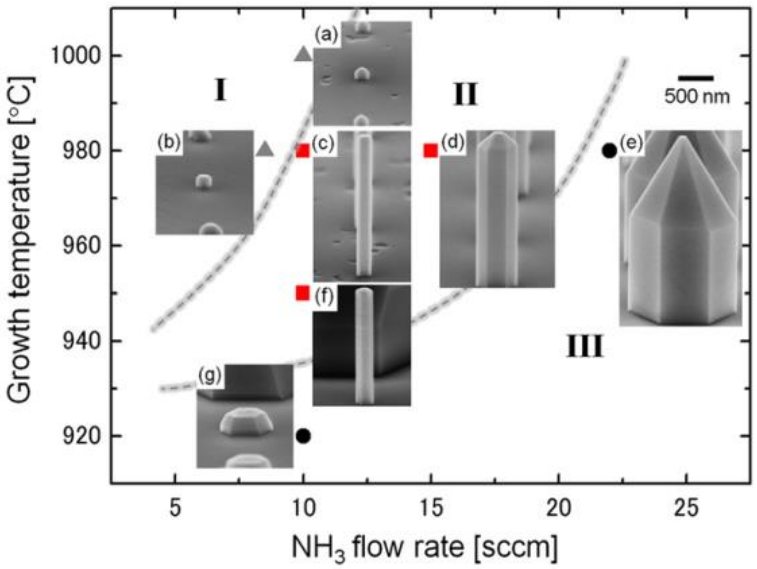

Figure 2.5 Morphology Ga-polar GaN nanowires grown by continuous flow method in MOCVD with respect to NH_3 flow rate and growth temperature [42].

In addition to V/III ratio and low precursor fluxes, carrier gas also plays an important role in the SAG of GaN nanowire growth. The necessity for H_2 in the carrier gas to etch the semipolar $\{10\bar{1}1\}$ *r*-plane has been highlighted by Li *et al.* and discussed earlier [35]. Choi *et al.* [42] and Coulon *et al.* [49] obtained Ga-polar GaN nanowires using mixed carrier gases of $0.4H_2$:$0.6N_2$, and $0.4H_2$:$1N_2$, respectively. Wang *et al.* used pure H_2 as carrier gas and suggested that the three essential conditions for achieving Ga-polar GaN nanowire are: (*i*) a carrier gas of H_2, (*ii*) an appropriately low V/III ratio, and (*iii*) moderate silane flow [50]. They determined an optimal V/III ratio of 33 with H_2 as the carrier gas, however, if the carrier gas was replaced by pure N_2 under this condition, the growth resulted in pyramidal morphology. However, Lin *et al*. reported of Ga-polar GaN nanowire growth using pure N_2 carrier gas [48]. Thus, the role of carrier gas remains elusive in the growth of Ga-polar GaN nanowires. A detailed investigation on the growth of GaN nanowires, including the effect of carrier gas, reactor

pressure, growth temperature, and partial pressures of Ga and N precursors are presented in Chapter 4.

2.3.3.4. Advantages and disadvantages of Ga-polar GaN nanowires

Selective area grown Ga-polar GaN nanowires studied by TEM have revealed that they are free of twins, stacking faults and threading dislocations [48], compared to the presence of threading dislocations in selective area grown N-polar GaN nanowires and microrods due to lattice mismatch with the sapphire substrate [36, 40]. The elimination of threading dislocations in Ga-polar GaN nanowires is attributed to two mechanisms: *(i)* bending of the dislocation towards sidewall to reduce the dislocation line energy by shortening its length, and *(ii)* the dislocation filtering effect provided by nano-apertures of SAG [51, 52].

Further, the growth of Ga-polar GaN nanowires on GaN pseudo-substrates is advantageous for realisation of electrically injected nanowire devices, compared to the N-polar GaN nanowire typically grown on electrically insulating sapphire substrate.

However, the top pyramidal facets of Ga-polar GaN nanowire may be considered as a shortcoming for incorporation of axial (vertical) heterostructures, compared to the flat top surface on N-polar GaN nanowires.

2.4. Selective area growth of AlGaN nanostructures by MOCVD

Very few reports exist on the SAG of AlGaN nanostructures using MOCVD, unlike the relatively widespread report of GaN nanowires reviewed in the preceding section. Early experiments on SAG of AlGaN nanostructures using MOCVD were carried out on stripe geometry with SiO_2 mask. Study on the growth mechanism revealed that AlGaN growth ends either in a triangular stripe with $\{10\bar{1}1\}$ sidewalls or trapezoidal stripe composed of a (0001) flat top and inclined sidewalls of $\{10\bar{1}0\}$ *r*-planes [34, 53, 54]. Based on the SAG of GaN and AlGaN in stripe geometries, Kato *et al.* concluded that Al has a smaller diffusion length compared to that of Ga [54]. Further, the Al composition showed a gradual decrease from top to bottom in the micro-stripes and attributed the reduction of Al content near the base of stripes to the dilution effect of Ga adatom with longer surface diffusion length on the mask [54].

Recent efforts in the SAG of AlGaN on circular apertures reported observation of pyramidal or truncated pyramidal structures, but not nanowires [55-57]. SAG of AlGaN with higher Al fraction is another challenging issue as it led to reduction in height of AlGaN pyramids, whereas, the thickness of unwanted AlGaN deposition on the mask increased [55,

56]. Increasing the Al composition from 11% to 33% in the gas phase led to a decrease in vertical growth rate from 22 to 5 nm/min, and further increasing the Al content to 66% produced no appreciable growth of nanostructure as shown in Figure 2.6 [56].

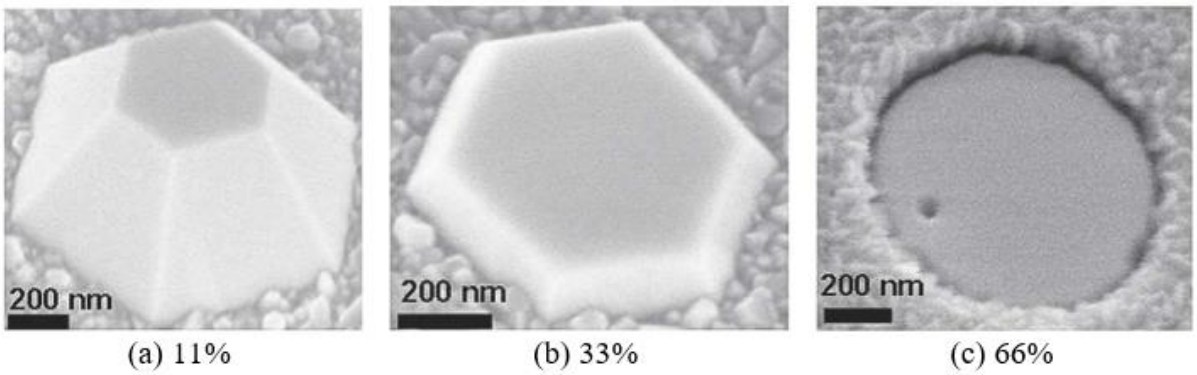

Figure 2.6 SAG of AlGaN nanostructures on GaN with SiO_2 mask for Al compositions of (a) 11%, (b) 33%, (c) 66% [56].

The role of underlying substrate and hence different strains in the SAG of AlGaN was investigated by Jindal *et al.* using AlN/sapphire, $Al_{0.5}Ga_{0.5}N$/sapphire, and GaN/sapphire substrates [57]. They concluded that higher interfacial compressive strain promoted three-dimensional growth during SAG of AlGaN, thereby showing higher Al incorporation and higher growth rate of AlGaN grown on AlN/sapphire substrate compared to that on GaN/sapphire substrate. However, Boughaleb *et al.* reported that irrespective of GaN or AlN substrate, AlGaN nanopyramids evolved in the same way and hence an AlN substrate is not necessary for growth of AlGaN nanopyramids [55].

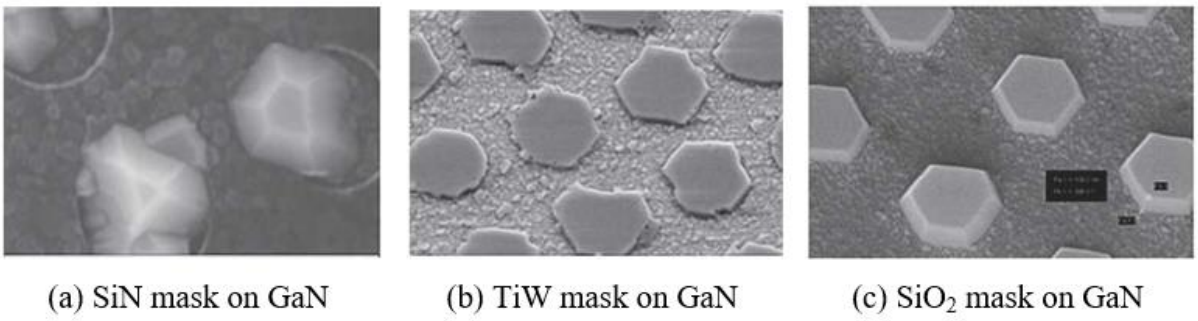

Figure 2.7 SAG of AlGaN nanostructures on GaN substrates using different mask materials: (a) SiN, (b) TiW, (c) SiO_2 [56].

The role of different mask materials *viz.* SiO_2, SiN, and TiW was evaluated for SAG of AlGaN nanostructures by Jindal *et al*. [56]. They concluded that, except for the SiO_2, all the other mask materials resulted in formation of high density of polycrystalline material and poor-

quality nanostructures due to lower diffusion length as shown in Figure 2.7. Parasitic growth of AlGaN polycrystals on the mask are a common observation during the SAG of AlGaN due to the high sticking coefficient of Al adatom on the mask [34, 53, 58, 59].

Jie *et al.* carried out heteroepitaxial growth of AlGaN on GaN micro-pyramids via SAG [60]. The GaN micro-pyramids achieved by SAG have smooth facets as shown in Figure 2.8 (a), whereas, heteroepitaxial growth of AlGaN on GaN micro-pyramids exhibited wrinkled surface near the base as shown in Figure 2.8 (b). The authors suggested the reason for such wrinkling is due to the blocking of adatom diffusion by parasitically-grown AlGaN polycrystals on the mask.

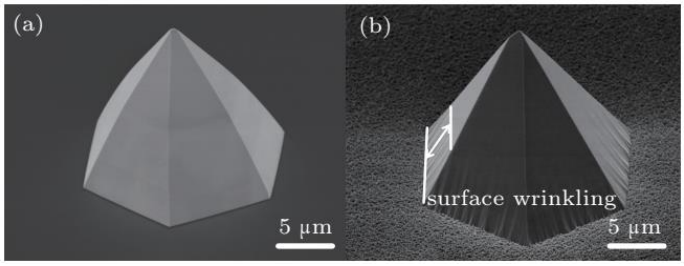

Figure 2.8 SEM image of (a) GaN and (b) wrinkled surface for AlGaN on GaN micro-pyramid [60].

In summary, selective area growth of AlGaN nanostructures in MOCVD has proven to be challenging due to the very small diffusion length of Al adatom. The AlGaN nanostructures are either pyramids or truncated pyramids and nanowire growth has not been achieved via SAG. Thus, for practical purposes, AlGaN nanowires can be achieved in the form of GaN/AlGaN core-shell nanowires. A detailed investigation on the growth and properties of core-shell GaN/AlGaN nanowires is presented in Chapter 5.

2.5. Role of AlGaN nanowires for UV emission

The overall external quantum efficiency (EQE) of electrically driven UV LEDs depends on injection efficiency (IE) of carriers, internal quantum efficiency (IQE), and light extraction efficiency (LEE) [61]. The various factors affecting IE, IQE, and LEE are listed in Figure 2.9(a) and shown schematically with respect to a UV LED device structure in Figure 2.9(b). In this section, we discuss the existing hurdles in IE, IQE and EQE of the planar UV LEDs and highlight how AlGaN nanowires can be helpful in overcoming those issues.

2.5.1 Injection efficiency

The low EQE of deep UV planar LEDs has been attributed to poor IE and radiative recombination efficiency by Guttmann *et al.* [62]. Poor IE in AlGaN based UV LEDs results from highly resistive nature of p-type AlGaN. The realisation of conductive *p*-type AlGaN is difficult due to the three reasons of *(i)* high activation energy of acceptors, *(ii)* self-compensation by nitrogen vacancies, and *(iii)* limited solubility of the dopant atoms. The activation energy of acceptors increases from 200 meV in GaN to 510-630 meV in AlN [63, 64], resulting in very low free hole concentration of 10^{10} cm^{-3} [64]. Self-compensation due to nitrogen vacancies also increases with Al content due to considerably lower formation energy of nitrogen vacancies in AlN compared to GaN [65]. Therefore, a minimum concentration of Mg dopant is required to offset the impurities and self-compensation, however, structural defects and inversion domain boundary formation deteriorates electrical transport beyond a maximum dopant limit [66]. Thus, p-type doping remains a challenging and ongoing issue in planar UV LEDs.

AlN nanowire LEDs with a turn-on voltage of only 6 V has been reported by Zhao *et al*. compared to the relatively higher turn-on voltages of 20 - 40 V in planar AlGaN LEDs [67]. The significantly low turn-on voltage that corresponds to the material bandgap has been attributed to efficient doping of Mg in nanowires compared to planar layer. Room temperature PL measurement of the Mg doped AlN nanowires showed acceptor level optical transition with an activation energy of 610 meV. However, electrical measurement indicated a significantly lower activation energy of 23 meV in the temperature range of 300 – 450 K. Such low activation energy resulting in a free hole concentration of $\sim 6\times10^{16}$ cm^{-3} has been attributed to hopping conduction in Mg impurity band owing to enhanced dopant incorporation in the nearly defect-free AlN nanowires [68, 69].

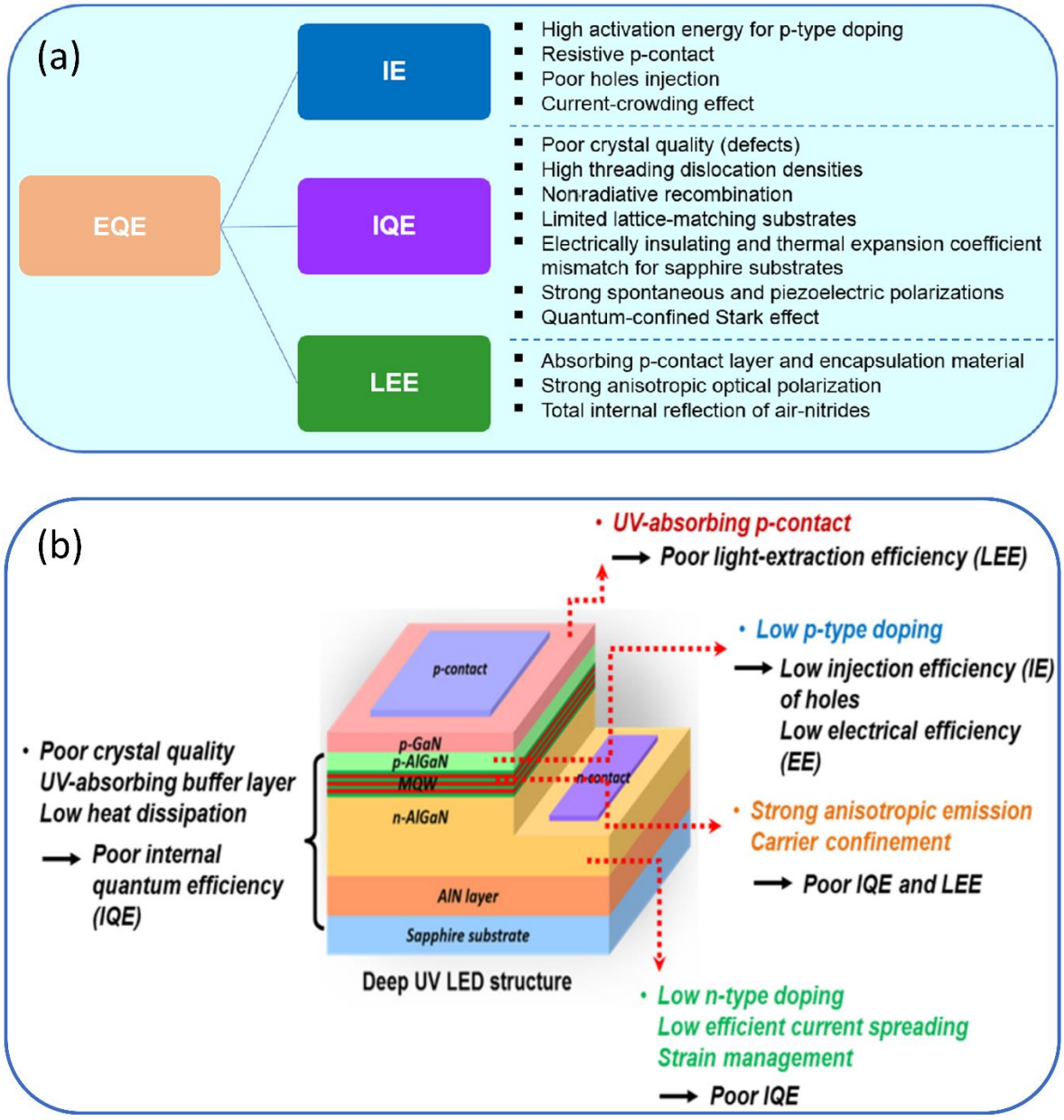

Figure 2.9 (a) Summary of the limiting factors (IE, IQE, and LEE) in UV LEDs [61], and (b) schematic illustration of these limiting factors with respect to a UV LED device structure [70].

2.5.2 Internal quantum efficiency

Ban *et al.* measured IQE of planar AlGaN MQW LEDS by excitation dependent PL measurement for almost the entire composition range of AlGaN covering a wavelength range of 230 – 350 nm [71]. They concluded that IQE strongly depends on dislocation density irrespective of AlGaN composition (emission wavelength). An IQE of 64% was achieved for a dislocation density of $2x10^8$ cm^{-2}, which drastically reduced to a mere 4% as the dislocation density increased to $6x10^9$ cm^{-2} as shown in Figure 2.10 (a). Further investigation through a

theoretical model of nonradiative recombination at dislocations revealed that the nonradiative recombination coefficient increased with dislocation density as shown in Figure 2.10 (b).

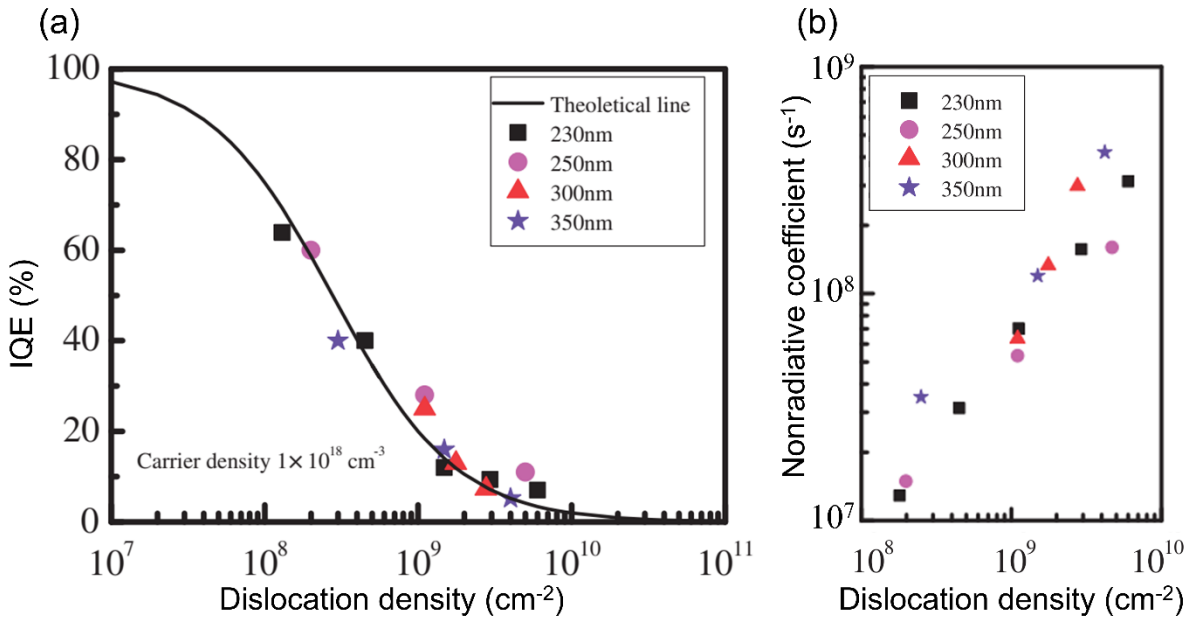

Figure 2.10 (a) IQE as a function of dislocation density measured under weak excitation, (b) Nonradiative recombination coefficient as a function of dislocation density [71].

Therefore, several efforts have been put in place to reduce the dislocation density and improve the IQE from planar *c*-plane AlGaN layer. However, the dislocation density of AlGaN layer grown using various methods have not been able to achieve a dislocation density below 1x 10^8 cm^{-2}, except in the case of bulk GaN and AlN substrates [72], as shown in Figure 2.11. Consequently, IQE of the majority of AlGaN UV LEDs is about 60% or below [73].

Further, the IQE of planar *c*-plane UV LEDs is also reduced due to spontaneous and piezoelectric polarisation field induced QCSE. This specific issue can be remedied by using nonpolar and semipolar oriented quantum well devices. A major issue in nonpolar and semipolar planes has been the high density of basal plane stacking faults (BSFs) of the order of 10^5 to 10^6 cm^{-1} [74]. Research from several groups spanning over 20 years have finally succeeded in achieving semipolar GaN free of BSFs for $(20\bar{2}1)$ plane only [75]. A chronological order of development in BSF reduction for nonpolar and semipolar GaN is shown as Figure 2.12. However, it should be noted that $(10\bar{1}0)$ and $(11\bar{2}0)$ nonpolar GaN orientations (shaded grey ellipse and top of blue circle in Figure 2.12), and consequently AlGaN heteroepitaxy on nonpolar planes still suffer from low crystal quality and contain high BSFs of the order of 10^5 to 10^6 cm^{-1} [76].

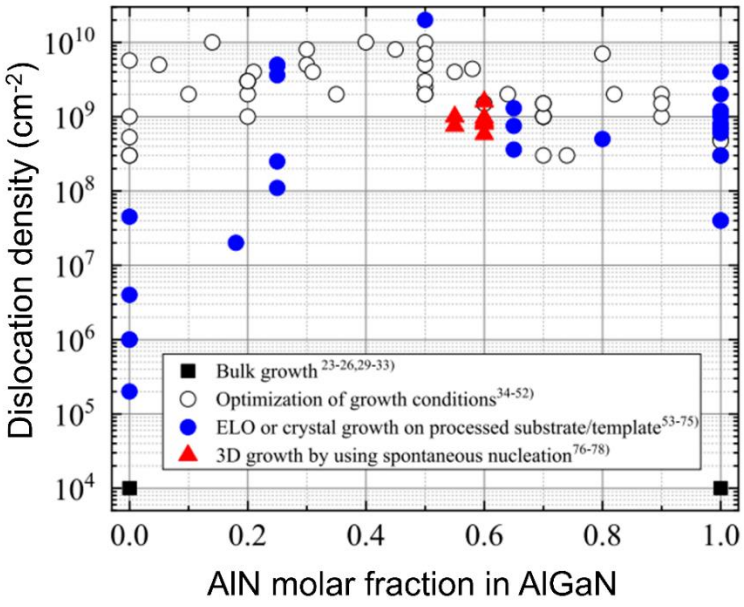

Figure 2.11 Dislocation density of AlGaN for various AlN molar fractions [72].

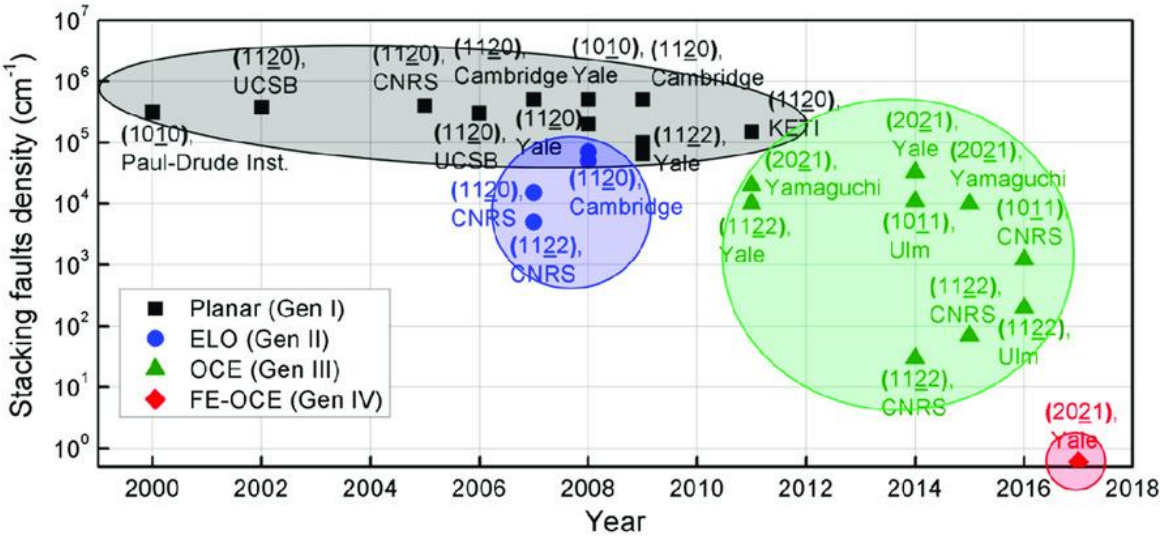

Figure 2.12 BSF density of nonpolar and semipolar GaN grown on foreign substrates ($LiAlO_2$, Si, SiC, and sapphire) by various methods [75].

In terms of planar nonpolar UV LEDs, Zhao *et al.* have demonstrated a commendable IQE of 39% on nonpolar $(11\bar{2}0)$ *a*-plane AlGaN MQW with an emission wavelength of 280 nm [77, 78]. They have identified the detrimental effect of BSFs in nonpolar AlGaN is due to the change from radiative to nonradiative recombination of excitons as a result of electron delocalisation at higher temperature, hence, resulting in low IQE for planar nonpolar AlGaN MQW.

Ga-polar GaN nanowires obtained from SAG are free of twins, stacking faults and threading dislocations and provide a large nonpolar surface [48]. Therefore, such nanowires are potential templates for subsequent growth of GaN/AlGaN heterostructures to realise high IQE by eliminating dislocations and BSFs, and additionally eliminating the deleterious effect of QCSE. Kim *et al.* reported an IQE of 73% for *m*-plane AlGaN MQW regrown on AlN nanorods compared to the 59% IQE for MQW on planar AlN as shown by the improved photoluminescence results in Figure 2.13 [79]. The improvement in IQE has been attributed to the reduced defect density and strain relief offered by the nanostructures.

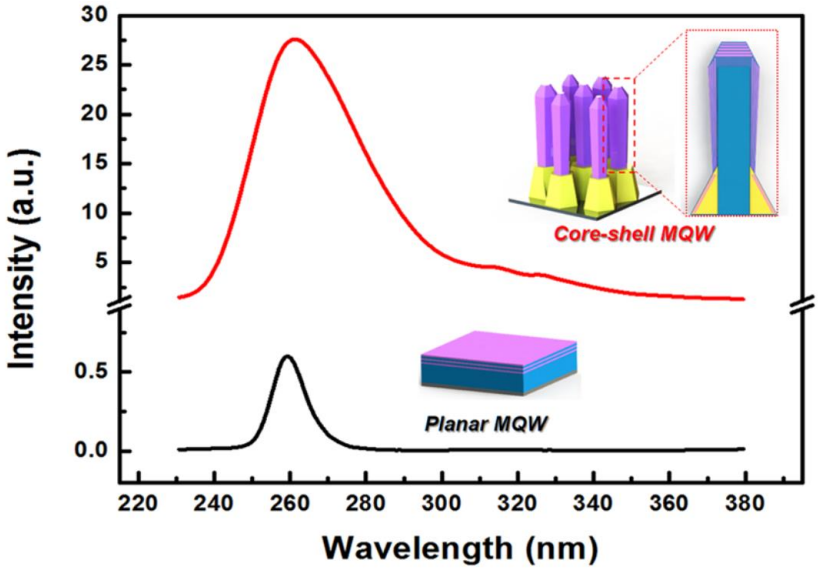

Figure 2.13 Photoluminescence spectra of AlGaN/AlN MQW from core-shell nanorods and planar structure [79].

2.5.3 External quantum efficiency

EQE is the most useful metric as it takes into account of IQE and LEE to provide the overall efficiency. The performance metrics for state-of-the-art commercial UV LEDs are: IQE of 60% and LEE $\leq$ 10% [80], therefore, yielding EQE = IQE $\times$ LEE $\leq$ 6%. Benchmarking of commercial UV LEDs carried out by the U.S. Department of Energy, Office of Energy Efficiency & Renewable Energy in November 2021 concluded that the efficiency of UV LEDs emitting in the wavelength range of 275 – 310 nm is 2 – 5% [81]. The poor LEE of $\leq$ 10% has remained one of the major bottlenecks in enhancement of EQE for UV LEDs.

The factors that affect LEE in planar AlGaN UV LEDs are *(i)* absorption in p-GaN contact layer, *(ii)* predominantly transverse magnetic (TM) polarised light emission from higher Al composition AlGaN, and *(iii)* total internal reflection. Due to lack of a metal with suitable work

function for electrical contact and high resistivity of p-AlGaN, a thin p-GaN layer is generally used for contact in planar AlGaN UV LEDs. However, such p-GaN layer absorbs UV light and reduce the LEE to below 10% even for a p-GaN thickness of only 25 nm [82]. AlGaN UV LEDs predominantly emit TM polarised light due to cross-over from heavy hole (HH) to crystal-field split-off hole (CH) band in the valence band of AlGaN. The estimated critical Al composition where TM polarised emission occur varies from 0.07 to 0.81 [83-86]. The TM polarised UV light is confined in the *c*-plane and tend to escape from the sidewalls and consequently results in poor light extraction efficiency from *c*-plane surface. Further, the high refractive index of AlN limits the light escape cone in planar UV LEDs to $\leq 26°$ and results in 5% LEE [80].

Top down fabricated nanowire UV LEDs have demonstrated superior light output and EQE compared to the planar counterpart as shown in Figure 2.14 (a). Ordered nanowire array UV LEDs demonstrated LEE of 12% in transverse electric (TE) and 9% in transverse magnetic (TM) modes [87]. These LEEs are enhanced by a factor of 1.6 and 35 in TE and TM polarised modes, respectively, compared to planar UV LEDs. The improved LEE, combined with improved IQE of nanowires resulted in an EQE of ~6% compared to ~3% EQE from the planar UV LEDs as shown in Figure 2.14 (a). Figure 2.14 (b) shows state-of-the-art EQE of UV LEDs including the conventional chips (≥ 500 μm), newer generation micro-LEDs (1 – 100 μm), as well as the nanorod-based UV LEDs discussed above. It is evident that nanorod-based UV LEDs emitting at 274 nm exhibiting an EQE of ~6% is on par or superior to most of planar UV LEDs.

In summary, nanowire-based UV LEDs are an effective approach towards realisation of efficient UV LEDs. The distinct advantage of nanowire architecture compared to planar device is that it collectively addresses the key issues of *(i)* low IQE due to dislocations and QCSE, and *(ii)* low LEE due to predominantly TM polarised light emission and total internal reflection, unlike addressing individual issues separately in planar LED. Therefore, AlGaN nanowire holds the key to future of highly efficient UV LEDs.

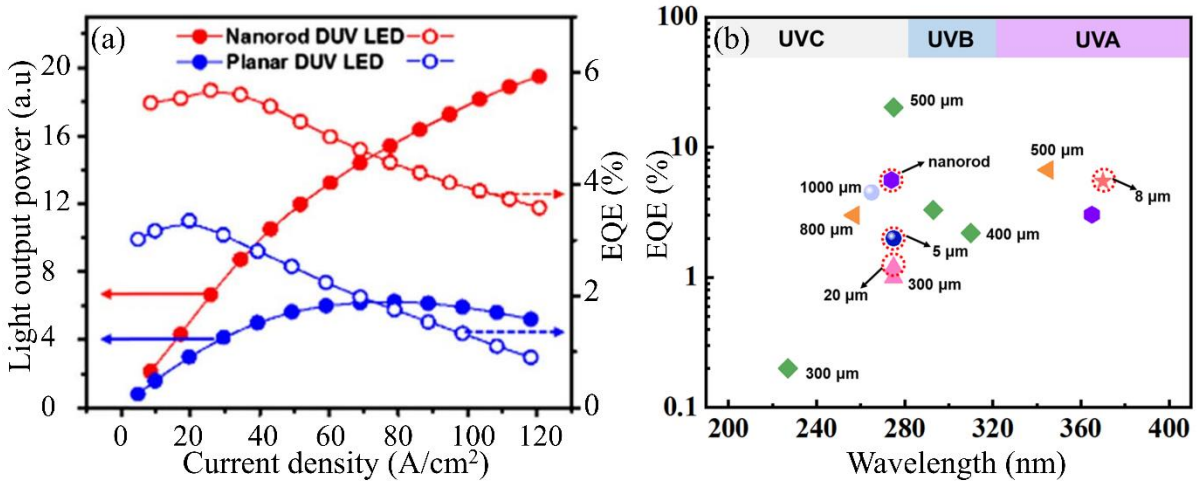

Figure 2.14 (a) Light output power and EQE of planar and nanorod UV LEDs emitting at 274 nm [87], (b) EQE of UV LEDs including nanorod and micro-LEDs. The chip-size of planar devices are indicated [88].

2.6. Challenges for nanowire-based UV LEDs

Finally, we discuss here some of the major challenges and possible resolutions for nanowire-based UV LEDs

2.6.1. Homogeneity

Uniformity of the nanowire dimensions, density and arrangement of nanowires, and compositional homogeneity in ternary materials are important for reliable and efficient UV emission from nanowires. Selective area growth of nanowires by defining suitable nano-apertures, periodicity, and regular arrangement in triangular, square, or rectangular pattern is expected to aid in achieving uniform nanowire arrays.

2.6.2. Contact fabrication

Ultimately, electrically injected nanowire devices will be required for practical applications. Hence, fabrication of optimal metal contacts to nanowire devices is another challenge. In the case of single nanowire, contact fabrication is carried out through pattern definition using electron beam lithography and subsequent metal deposition followed by resist lift-off. Contact fabrication in nanowire array device generally involves planarisation step in which the gaps between the nanowires are filled with a suitable dielectric material like BCB, PMMA, PDMS and spin-on-glass followed by contact metal deposition.

However, the metal contacts on nanowires pose a problem for absorption loss. Therefore, a proper consideration is required for contact fabrication in the nanowire devices. Graphene is becoming a potential contact material due to high transparency and conductivity. The developed methodology for transfer of large area graphene (45 mm × 45 mm) [89], and successful utilisation of graphene electrodes on p-type AlGaN [90] as well as on AlGaN nanowires [91] will potentially hasten the achievement of AlGaN nanowire devices.

2.6.3. Heat dissipation

Electrically injected devices generate heat and heat affects the performance of semiconductor devices. Thermal conductivity of GaN nanowires is found to be rather small, 13 – 19 $Wm^{-1}K^{-1}$ at 300K for diameter in the range of 97 – 181 nm [92, 93]. GaN thin-films, on the other hand, have an order of magnitude higher thermal conductivity [94]. Such low thermal conductivity could prove to be detrimental for nanowire device operation without proper heat sinking.

2.6.4. Large scale production

Scaling up of nanowire device production will be necessary to meet the demands and economy. In this aspect, with proven evidence, growth of III-nitride nanostructures with MOCVD will be suitable for large-scale production. What remains to be solved is the time taken for the patterning of nano-holes using electron beam lithography. Newer fabrication techniques like nano-imprint-lithography (NIL) could potentially resolve this issue and provide much faster throughput in terms of patterning of the substrates.

References

1. Juza, R. and Hahn, H., "Über die Kristallstrukturen von Cu_3N, GaN und InN Metallamide und Metallnitride." *Zeitschrift fur Anorganische und Allgemeine Chemie*, **1938**, 239, 282-287.

2. Grimmeiss, H.G. and Koelmans, H., "Über die Kantenemission und andere Emissionen des GaN." *Zeitschrift für Naturforschung A*, **1959**, 14, 264-271.

3. Maruska, H.P. and Tietjen, J.J., "The Preparation and Properties of Vapor-Deposited Single-Crystal-line GaN." *Applied Physics Letters*, **1969**, 15, 327-329.

4. Amano, H., Sawaki, N., Akasaki, I. and Toyoda, Y., "Metalorganic vapor phase epitaxial growth of a high quality GaN film using an AlN buffer layer." *Applied Physics Letters*, **1986**, 48, 353-355.

5. Nakamura, S., "GaN Growth Using GaN Buffer Layer." *Japanese Journal of Applied Physics*, **1991**, 30, L1705-L1707.

6. Moustakas, T.D. and Paiella, R., "Optoelectronic device physics and technology of nitride semiconductors from the UV to the terahertz." *Reports on Progress in Physics*, **2017**, 80, 106501.

7. Morkoç, H., "Handbook of Nitride Semiconductors and Devices Vol. 1: Material Properties, Physics and Growth". **2008**, Wiley-VCH Verlag GmbH & Co. KGaA: Weinheim.

8. Yan, Q., Rinke, P., Janotti, A., Scheffler, M. and Van de Walle, C.G., "Effects of strain on the band structure of group-III nitrides." *Physical Review B*, **2014**, 90, 125118.

9. Yeh, C.-Y., Lu, Z.W., Froyen, S. and Zunger, A., "Zinc-blende--wurtzite polytypism in semiconductors." *Physical Review B*, **1992**, 46, 10086-10097.

10. Morkoç, H., "General Properties of Nitrides", in *Handbook of Nitride Semiconductors and Devices*, H. Morkoç, Editor. **2008**. p. 1-129.

11. Momma, K. and Izumi, F., "VESTA: a three-dimensional visualization system for electronic and structural analysis." *Journal of Applied Crystallography*, **2008**, 41, 653-658.

12. Daudin, B., Rouvière, J.L. and Arlery, M., "Polarity determination of GaN films by ion channeling and convergent beam electron diffraction." *Applied Physics Letters*, **1996**, 69, 2480-2482.

13. Ambacher, O., "Growth and applications of Group III-nitrides." *Journal of Physics D: Applied Physics*, **1998**, 31, 2653.

14. Zywietz, T., Neugebauer, J. and Scheffler, M., "Adatom diffusion at GaN (0001) and (000$\bar{1}$) surfaces." *Applied Physics Letters*, **1998**, 73, 487-489.

15. Hellman, E.S., "The Polarity of GaN: a Critical Review." *MRS Internet Journal of Nitride Semiconductor Research*, **1998**, 3, e11.

16. Sumiya, M. and Fuke, S., "Review of polarity determination and control of GaN." *MRS Internet Journal of Nitride Semiconductor Research*, **2004**, 9, e1.

17. Skuridina, D., Dinh, D.V., Pristovsek, M., Lacroix, B., Chauvat, M.P., et al., "Surface and crystal structure of nitridated sapphire substrates and their effect on polar InN layers." *Applied Surface Science*, **2014**, 307, 461-467.

18. French, T.M. and Somorjai, G.A., "Composition and surface structure of the (0001) face of α-alumina by low-energy electron diffraction." *The Journal of Physical Chemistry*, **1970**, 74, 2489-2495.

19. Soares, E.A., Van Hove, M.A., Walters, C.F. and McCarty, K.F., "Structure of the alpha-Al2O3(0001) surface from low-energy electron diffraction: Al termination and evidence for anomalously large thermal vibrations." *Physical Review B*, **2002**, 65, 195405.

20. Agnarsson, B., Gothelid, M., Olafsson, S., Gislason, H.P. and Karlsson, U.O., "Influence of initial surface reconstruction on nitridation of Al_2O_3 (0001) using low pressure ammonia." *Journal of Applied Physics*, **2007**, 101, 013519-7.

21. Ito, T., Ohtsuka, K., Kuwahara, K., Sumiya, M., Takano, Y., et al., "Effect of AlN buffer layer deposition conditions on the properties of GaN layer." *Journal of Crystal Growth*, **1999**, 205, 20-24.

22. Lee, K., Kim, J., Eom, D., Jeon, M., Heo, C., et al., "Polarity of Aluminum Nitride Layers Grown by High-Temperature Metal Organic Chemical Vapor Deposition." *Journal of Nanoscience and Nanotechnology*, **2016**, 16, 11807-11810.

23. Sumiya, M., Tanaka, M., Ohtsuka, K., Fuke, S., Ohnishi, T., et al., "Analysis of the polar direction of GaN film growth by coaxial impact collision ion scattering spectroscopy." *Applied Physics Letters*, **1999**, 75, 674-676.

24. Sumiya, M. and Fuke, S., "Polar surface structure of wurtzite GaN epitaxial film grown by MOCVD." *Oyo Buturi*, **2001**, 70, 178-182.

25. Liu, F., Collazo, R., Mita, S., Sitar, Z., Duscher, G., et al., "The mechanism for polarity inversion of GaN via a thin AlN layer: Direct experimental Evidence." *Applied Physics Letters*, **2007**, 91, 203115.

26. Wu, Y., Hanlon, A., Kaeding, J.F., Sharma, R., Fini, P.T., et al., "Effect of nitridation on polarity, microstructure, and morphology of AlN films." *Applied Physics Letters*, **2004**, 84, 912-914.

27. Rouviere, J.L., Arlery, M., Niebuhr, R., Bachem, K.H. and Briot, O., "Correlation between surface morphologies and crystallographic structures of GaN layers grown by MOCVD on sapphire." *MRS Internet Journal of Nitride Semiconductor Research*, **1996**, 1, e33.

28. Rouviere, J.-L., Bougerol, C., Amstatt, B., Bellet-Almaric, E. and Daudin, B., "Measuring local lattice polarity in AlN and GaN by high resolution Z-contrast imaging:

The case of (0001) and $(1\bar{1}00)$ GaN quantum dots." *Applied Physics Letters*, **2008**, 92, 201904.

29. Koukitu, A., Mayumi, M. and Kumagai, Y., "Surface polarity dependence of decomposition and growth of GaN studied using in situ gravimetric monitoring." *Journal of Crystal Growth*, **2002**, 246, 230-236.

30. Koester, R., Hwang, J.S., Durand, C., Dang, D.L.S. and Eymery, J., "Self-assembled growth of catalyst-free GaN wires by metal–organic vapour phase epitaxy." *Nanotechnology*, **2010**, 21, 015602.

31. Kitamura, S., Hiramatsu, K. and Sawaki, N., "Fabrication of GaN Hexagonal Pyramids on Dot-Patterned GaN/Sapphire Substrates via Selective Metalorganic Vapor Phase Epitaxy." *Japanese Journal of Applied Physics*, **1995**, 34, L1184.

32. Hiramatsu, K., Kitamura, S. and Sawaki, N., "Facets Formation Mechanism of GaN Hexagonal Pyramids on Dot-Patterns via Selective MOVPE." *MRS Proceedings*, **1995**, 395, 267.

33. Kapolnek, D., Underwood, R.D., Keller, B.P., Keller, S., Denbaars, S.P., et al., "Selective area epitaxy of GaN for electron field emission devices." *Journal of Crystal Growth*, **1997**, 170, 340-343.

34. Nam, O.-H., Bremser, M.D., Ward, B.L., Nemanich, R.J. and Davis, R.F., "Growth of GaN and Al0.2Ga0.8N on Patterened Substrates via Organometallic Vapor Phase Epitaxy." *Japanese Journal of Applied Physics*, **1997**, 36, L532.

35. Li, S.F., Fuendling, S., Wang, X., Merzsch, S., Al-Suleiman, M.A.M., et al., "Polarity and Its Influence on Growth Mechanism during MOVPE Growth of GaN Sub-micrometer Rods." *Crystal Growth & Design*, **2011**, 11, 1573-1577.

36. Bergbauer, W., Strassburg, M., Ch, K., Linder, N., Roder, C., et al., "Continuous-flux MOVPE growth of position-controlled N-face GaN nanorods and embedded InGaN quantum wells." *Nanotechnology*, **2010**, 21, 305201.

37. Chen, X.J., Perillat-Merceroz, G., Sam-Giao, D., Durand, C. and Eymery, J., "Homoepitaxial growth of catalyst-free GaN wires on N-polar substrates." *Applied Physics Letters*, **2010**, 97, 151909.

38. Bergbauer, W., Strassburg, M., Kölper, C., Linder, N., Roder, C., et al., "N-face GaN nanorods: Continuous-flux MOVPE growth and morphological properties." *Journal of Crystal Growth*, **2011**, 315, 164-167.

39. Wang, X., Li, S., Fündling, S., Wei, J., Erenburg, M., et al., "Polarity Control in 3D GaN Structures Grown by Selective Area MOVPE." *Crystal Growth & Design*, **2012**, 12, 2552-2556.

40. Li, S., Wang, X., Fündling, S., Erenburg, M., Ledig, J., et al., "Nitrogen-polar core-shell GaN light-emitting diodes grown by selective area metalorganic vapor phase epitaxy." *Applied Physics Letters*, **2012**, 101, 032103.

41. Hersee, S.D., Sun, X. and Wang, X., "The Controlled Growth of GaN Nanowires." *Nano Letters*, **2006**, 6, 1808-1811.

42. Choi, K., Arita, M. and Arakawa, Y., "Selective-area growth of thin GaN nanowires by MOCVD." *Journal of Crystal Growth*, **2012**, 357, 58-61.

43. Yoshiji, H., Minoru, K. and Hiroshi, Y., "Low-Temperature Growth of GaAs and AlAs-GaAs Quantum-Well Layers by Modified Molecular Beam Epitaxy." *Japanese Journal of Applied Physics*, **1986**, 25, L868.

44. Foxon, C.T., Novikov, S.V., Hall, J.L., Campion, R.P., Cherns, D., et al., "A complementary geometric model for the growth of GaN nanocolumns prepared by plasma-assisted molecular beam epitaxy." *Journal of Crystal Growth*, **2009**, 311, 3423-3427.

45. Lin, Y.-T., Yeh, T.-W. and Dapkus, P.D., "Mechanism of selective area growth of GaN nanorods by pulsed mode metalorganic chemical vapor deposition." *Nanotechnology*, **2012**, 23, 465601.

46. Jung, B.O., Bae, S.-Y., Kato, Y., Imura, M., Lee, D.-S., et al., "Morphology development of GaN nanowires using a pulsed-mode MOCVD growth technique." *CrystEngComm*, **2014**, 16, 2273-2282.

47. Bae, S.-Y., Jung, B.O., Lekhal, K., Kim, S.Y., Lee, J.Y., et al., "Highly elongated vertical GaN nanorod arrays on Si substrates with an AlN seed layer by pulsed-mode metal-organic vapor deposition." *CrystEngComm*, **2016**, 18, 1505-1514.

48. Lin, Y.-T., Yeh, T.-W., Nakajima, Y. and Dapkus, P.D., "Catalyst-Free GaN Nanorods Synthesized by Selective Area Growth." *Advanced Functional Materials*, **2014**, 24, 3162-3171.

49. Coulon, P.M., Alloing, B., Brändli, V., Lefebvre, D., Chenot, S., et al., "Selective area growth of Ga-polar GaN nanowire arrays by continuous-flow MOVPE: A systematic study on the effect of growth conditions on the array properties." *physica status solidi (b)*, **2015**, 252, 1096-1103.

50. Wang, X., Li, S., Mohajerani, M.S., Ledig, J., Wehmann, H.-H., et al., "Continuous-Flow MOVPE of Ga-Polar GaN Column Arrays and Core–Shell LED Structures." *Crystal Growth & Design*, **2013**, 13, 3475-3480.

51. Hersee, S.D., Rishinaramangalam, A.K., Fairchild, M.N., Zhang, L. and Varangis, P., "Threading defect elimination in GaN nanowires." *Journal of Materials Research*, **2011**, 26, 2293-2298.

52. Coulon, P.-M., Alloing, B., Brändli, V., Vennéguès, P., Leroux, M., et al., "Dislocation filtering and polarity in the selective area growth of GaN nanowires by continuous-flow metal organic vapor phase epitaxy." *Applied Physics Express*, **2016**, 9, 015502.

53. Kato, Y., Kitamura, S., Hiramatsu, K. and Sawaki, N., "Selective growth of wurtzite GaN and AlxGa1−xN on GaN/sapphire substrates by metalorganic vapor phase epitaxy." *Journal of Crystal Growth*, **1994**, 144, 133-140.

54. Kato, T., Honda, Y., Kawaguchi, Y., Yamaguchi, M. and Sawaki, N., "Selective Growth of GaN/AlGaN Microstructures by Metalorganic Vapor Phase Epitaxy." *Japanese Journal of Applied Physics*, **2001**, 40, 1896-1898.

55. Boughaleb, S., Martin, B., Matei, C., Templier, R., Borowik, Ł., et al., "Selective area growth of AlGaN nanopyramids by conventional and pulsed MOVPE." *Nanotechnology*, **2021**, 32, 195203.

56. Jindal, V., Grandusky, J.R., Tripathi, N., Shahedipour-Sandvik, F., LeBoeuf, S., et al., "Selective area heteroepitaxy of nano-AlGaN ultraviolet excitation sources for biofluorescence application." *Journal of Materials Research*, **2007**, 22, 838-844.

57. Jindal, V., Grandusky, J., Jamil, M., Tripathi, N., Thiel, B., et al., "Effect of interfacial strain on the formation of AlGaN nanostructures by selective area heteroepitaxy." *Physica E: Low-dimensional Systems and Nanostructures*, **2008**, 40, 478-483.

58. Akasaka, T., Kobayashi, Y., Ando, S., Kobayashi, N. and Kumagai, M., "Selective MOVPE of GaN and $Al_xGa_{1-x}N$ with smooth vertical facets." *Journal of Crystal Growth*, **1998**, 189-190, 72-77.

59. Kozawa, T., Ohwaki, T., Taga, Y. and Sawaki, N., "Field emission study of gated GaN and $Al_{0.1}Ga_{0.9}N$/GaN pyramidal field emitter arrays." *Applied Physics Letters*, **1999**, 75, 3330-3332.

60. Jie, C., Pu-Man, H., Xiao-Biao, H., Zheng-Zhou, P., Chang-Ming, Z., et al., "Influence of adatom migration on wrinkling morphologies of AlGaN/GaN micro-pyramids grown by selective MOVPE." *Chinese Physics B*, **2017**, 26, 068101.

61. Mohd Sharizal Alias, M.T., Jorge A. Holguín-Lerma, Edgars Stegenburgs, Abdullah A. Alatawi, Islam Ashry, Ram Chandra Subedi, Davide Priante, Mohammad Khaled Shakfa, Tien Khee Ng, Boon S. Ooi, "Review of nanophotonics approaches using nanostructures and nanofabrication for III-nitrides ultraviolet-photonic devices." *Journal of Nanophotonics*, **2018**, 12, 043508.

62. Guttmann, M., Mehnke, F., Belde, B., Wolf, F., Reich, C., et al., "Optical light polarization and light extraction efficiency of AlGaN-based LEDs emitting between 264 and 220 nm." *Japanese Journal of Applied Physics*, **2019**, 58, SCCB20.

63. Nam, K.B., Nakarmi, M.L., Li, J., Lin, J.Y. and Jiang, H.X., "Mg acceptor level in AlN probed by deep ultraviolet photoluminescence." *Applied Physics Letters*, **2003**, 83, 878-880.

64. Taniyasu, Y., Kasu, M. and Makimoto, T., "An aluminium nitride light-emitting diode with a wavelength of 210 nanometres." *Nature*, **2006**, 441, 325-328.

65. Pampili, P. and Parbrook, P.J., "Doping of III-nitride materials." *Materials Science in Semiconductor Processing*, **2017**, 62, 180-191.

66. Jeon, S.-R., Ren, Z., Cui, G., Su, J., Gherasimova, M., et al., "Investigation of Mg doping in high-Al content p-type $Al_xGa_{1-x}N$ ($0.3<x<0.5$)." *Applied Physics Letters*, **2005**, 86, 082107.

67. Zhao, S., Connie, A.T., Dastjerdi, M.H.T., Kong, X.H., Wang, Q., et al., "Aluminum nitride nanowire light emitting diodes: Breaking the fundamental bottleneck of deep ultraviolet light sources." *Scientific Reports*, **2015**, 5, 8332.

68. Connie, A.T., Zhao, S., Sadaf, S.M., Shih, I., Mi, Z., et al., "Optical and electrical properties of Mg-doped AlN nanowires grown by molecular beam epitaxy." *Applied Physics Letters*, **2015**, 106, 213105.

69. Tran, N.H., Le, B.H., Zhao, S. and Mi, Z., "On the mechanism of highly efficient p-type conduction of Mg-doped ultra-wide-bandgap AlN nanostructures." *Applied Physics Letters*, **2017**, 110, 032102.

70. Hsu, T.-C., Teng, Y.-T., Yeh, Y.-W., Fan, X., Chu, K.-H., et al., "Perspectives on UVC LED: Its Progress and Application." *Photonics*, **2021**, 8, 196.

71. Ban, K., Yamamoto, J.-i., Takeda, K., Ide, K., Iwaya, M., et al., "Internal Quantum Efficiency of Whole-Composition-Range AlGaN Multiquantum Wells." *Applied Physics Express*, **2011**, 4, 052101.

72. Iwaya, M., Tanaka, S., Omori, T., Yamada, K., Hasegawa, R., et al., "Recent development of UV-B laser diodes." *Japanese Journal of Applied Physics*, **2022**, 61, 040501.

73. Mondal, R.K., Adhikari, S., Chatterjee, V. and Pal, S., "Recent advances and challenges in AlGaN-based ultra-violet light emitting diode technologies." *Materials Research Bulletin*, **2021**, 140, 111258.

74. Li, H., Zhang, H., Song, J., Li, P., Nakamura, S., et al., "Toward heteroepitaxially grown semipolar GaN laser diodes under electrically injected continuous-wave mode: From materials to lasers." *Applied Physics Reviews*, **2020**, 7, 041318.

75. Song, J. and Han, J., "High Quality, Mass-Producible Semipolar GaN and InGaN Light-Emitting Diodes Grown on Sapphire." *physica status solidi (b)*, **2020**, 257, 1900565.

76. Chen, H., Zhang, X., Chen, S., Fan, A., Li, C., et al., "Properties of Si-doped a-plane AlGaN layers." *Materials Science in Semiconductor Processing*, **2020**, 119, 105270.

77. Zhao, J., Pan, J., Liu, B., Tao, T., Chen, D., et al., "Improved Optical Properties of Nonpolar AlGaN-Based Multiple Quantum Wells Emitting at 280 nm." *IEEE Photonics Journal*, **2021**, 13, 1-7.

78. Zhao, J., Zhang, X., He, J., Chen, S., Wu, Z., et al., "High Internal Quantum Efficiency of Nonpolar a-Plane AlGaN-Based Multiple Quantum Wells Grown on r-Plane Sapphire Substrate." *ACS Photonics*, **2018**, 5, 1903-1906.

79. Kim, J., Choi, U., Pyeon, J., So, B. and Nam, O., "Deep-Ultraviolet AlGaN/AlN Core-Shell Multiple Quantum Wells on AlN Nanorods via Lithography-Free Method." *Scientific Reports*, **2018**, 8, 935.

80. Zollner, C.J., DenBaars, S.P., Speck, J.S. and Nakamura, S., "Germicidal ultraviolet LEDs: a review of applications and semiconductor technologies." *Semiconductor Science and Technology*, **2021**, 36, 123001.

81. J. Lynn Davis, K.R., Roger Pope, Clint Clayton, Andrew Dart, Michelle McCombs, and Wallace, A., "Initial Benchmarks of UV LEDs and Comparison with White LEDs". **2021**, U.S. Department of Energy's Office of Energy Efficiency and Renewable Energy (EERE) under the National Energy Technology Laboratory (NETL).

82. Ryu, H.-Y., Choi, I.-G., Choi, H.-S. and Shim, J.-I., "Investigation of Light Extraction Efficiency in AlGaN Deep-Ultraviolet Light-Emitting Diodes." *Applied Physics Express*, **2013**, 6, 062101.

83. Neuschl, B., Helbing, J., Knab, M., Lauer, H., Madel, M., et al., "Composition dependent valence band order in c-oriented wurtzite AlGaN layers." *Journal of Applied Physics*, **2014**, 116, 113506.

84. Murotani, H., Yamada, Y., Miyake, H. and Hiramatsu, K., "Silicon concentration dependence of optical polarization in AlGaN epitaxial layers." *Applied Physics Letters*, **2011**, 98, 021910.

85. Feneberg, M., Winkler, M., Klamser, J., Stellmach, J., Frentrup, M., et al., "Anisotropic optical properties of semipolar AlGaN layers grown on m-plane sapphire." *Applied Physics Letters*, **2015**, 106, 182102.

86. Kurai, S., Shimomura, K., Murotani, H., Yamada, Y., Miyake, H., et al., "Correlation between in-plane strain and optical polarization of Si-doped AlGaN epitaxial layers as a function of Al content and Si concentration." *Journal of Applied Physics*, **2012**, 112, 033512.

87. Zhang, L., Guo, Y., Yan, J., Wu, Q., Lu, Y., et al., "Deep ultraviolet light-emitting diodes based on a well-ordered AlGaN nanorod array." *Photonics Research*, **2019**, 7, B66-B72.

88. Tian, P., Shan, X., Zhu, S., Xie, E., McKendry, J.J.D., et al., "AlGaN Ultraviolet Micro-LEDs." *IEEE Journal of Quantum Electronics*, **2022**, 58, 1-14.

89. Li, X., Zhu, Y., Cai, W., Borysiak, M., Han, B., et al., "Transfer of Large-Area Graphene Films for High-Performance Transparent Conductive Electrodes." *Nano Letters*, **2009**, 9, 4359-4363.

90. Feng, S., Dong, B., Lu, Y., Yin, L., Wei, B., et al., "Graphene/p-AlGaN/p-GaN electron tunnelling light emitting diodes with high external quantum efficiency." *Nano Energy*, **2019**, 60, 836-840.

91. Parimoo, H., Zhang, Q., Vafadar, M., Sivasundarampillai, J. and Zhao, S., "AlGaN nanowire deep ultraviolet light emitting diodes with graphene electrode." *Applied Physics Letters*, **2022**, 120, 171108.

92. Guthy, C., Nam, C.-Y. and Fischer, J.E., "Unusually low thermal conductivity of gallium nitride nanowires." *Journal of Applied Physics*, **2008**, 103, 064319.

93. Zou, J., "Lattice thermal conductivity of freestanding gallium nitride nanowires." *Journal of Applied Physics*, **2010**, 108, 034324.

94. Beechem, T.E., McDonald, A.E., Fuller, E.J., Talin, A.A., Rost, C.M., et al., "Size dictated thermal conductivity of GaN." *Journal of Applied Physics*, **2016**, 120, 095104.

Chapter 3. Experimental Methods

3.1. Introduction

This chapter describes the procedures used in preparing samples for selective area growth (SAG) of GaN nanowires and the principles of equipment used in the sample preparation, epitaxial growth, and characterisation.

3.2. Substrate preparation for selective area growth

Research on GaN growth is still largely carried out using *c*-plane sapphire substrates due to the cost and paucity of native GaN substrates. We started the substrate preparation for SAG of GaN nanowires by first growing a layer of GaN layer on 2-inch *c*-plane sapphire substrates. All of our nanowire growths discussed in this thesis have been carried out on such GaN/sapphire substrates.

Step 1: GaN on sapphire substrates

GaN growth is carried out in an Aixtron 3×2 close-coupled showerhead (CCS) metal organic chemical vapour deposition (MOCVD) system. Sapphire substrates are baked at a temperature of 1090 °C in hydrogen ambient. Nitridation of the sapphire substrates are carried out at a temperature of 585 °C by flowing 4000 sccm of NH_3. Growth of low-temperature GaN nucleation layer immediately followed the nitridation step by introducing 9 sccm (47 μmol min^{-1}) of trimethylgallium (TMGa). After a growth duration of 110 sec for the nucleation layer, TMGa flow is switched off and the reactor temperature is ramped up to 1098 °C. High-temperature GaN growth is initiated by flowing 26 sccm (137 μmol min^{-1}) of TMGa maintaining a V/III ratio of 1300. Unintentionally doped GaN layer is grown to a thickness of 3.5 μm, followed by 1.5 μm-thick Si-doped n-type GaN. In this thesis, such epitaxial GaN on sapphire substrate will be referred to as GaN pseudo-substrate.

Step 2: Deposition of SiO_x mask

An SiO_x layer of ~15 nm thickness is deposited on the GaN pseudo-substrate at a temperature of 300 °C using Picosun SUNALE plasma-assisted atomic layer deposition (ALD) system. The notation *x* is used here considering that precisely controlling the stoichiometry of thin-film in ALD is challenging [1]. The thickness of SiO_x layer is evaluated using a J. A. Wollam spectroscopic ellipsometer.

Step 3: Electron beam lithography and pattern transfer

A 100 nm-thick electron beam resist (mr-PosEBR) is spin coated at 3000 rpm for 1 min on top of the SiO_x layer. The electron-beam resist is then baked on a hotplate at 150 °C for 1 min and allowed to cool down to room temperature. Due to the electrically insulating nature of the underlying sapphire substrate, a water-based anti-charging agent (DisCharge, Dischem Inc.) is spin-coated at 1000 rpm for 1 min to prevent charge accumulation during electron beam lithography.

Hexagonally arranged holes with nominal diameters of 50, 100, 200, and 400 nm are defined by exposing the resist to electron beam in a Raith 150 electron beam lithography system. After the electron beam lithography, the anti-charging agent is removed by rinsing the wafer in deionised water. The exposed patterns are then developed by dipping the wafer in n-amyl acetate for 30 sec.

An Oxford Plasmalab reactive-ion etching system is used to transfer the developed patterns on to the SiO_x mask by etching the ~15 nm-thick SiO_x layer in a CHF_3-based chemistry. The remaining electron beam resist is removed by ultrasonication in acetone for 10 minutes followed by cleaning in isopropyl alcohol and deionised water. Subsequently, the wafer is exposed to oxygen plasma for 5 minutes in order to ensure complete removal of any residual organic contaminants.

The patterned 2-inch wafer is diced into 10×10 mm^2 pieces using a dicing machine (DAD321, Disco). These individual pieces are cleaned again by ultrasonication in acetone, isopropyl alcohol, deionised water for 5 minutes each and blown dry with N_2 before loading into the MOCVD chamber for growth.

The process steps of substrate preparation for selective area growth along with process parameters are listed in Table 3.1

Table 3.1 Details of substrate preparation for selective area growth of GaN and AlGaN nanowires.

Process step	Process parameters	Equipment
GaN growth	3.5 μm-thick undoped GaN, followed by 1.5 μm-thick n-type GaN on sapphire substrates	MOCVD
SiO_x deposition	15 nm at 300 °C	ALD
Electron beam resist coating	mr-PosEBR0.1, 3000 rpm, 1 min	Spin coater
Anti-charging agent	DisChargeH_2O, 1000 rpm, 1 min	Spin coater
EBL exposure	HT 20 kV, aperture 10 μm, write-field 100 μm, dose 100 – 120 μCcm^{-2}	EBL
Anti-charging agent removal	Rinse with deionized water	Wet bench
Resist development	30 sec in n-amyl acetate	Wet bench
Pattern transfer	2 min 30 sec in CHF_3 plasma, 20 mTorr, 100 W RF power	RIE
Resist removal	Ultrasonication in acetone	Ultrasonicator
Residual organic removal	O_2 plasma 5 min, 300 sccm, 0.2 mbar, 100 W	Barrel etcher
Wafer dicing	Blade rotation 30,000 rpm, feed-speed 0.8 mm sec^{-1}	Dicing machine
Selective area growth	Details in Chapters 4, 5, and 6.	MOCVD

3.3. Metal organic chemical vapour deposition

Metal-organic chemical vapour deposition (MOCVD) system is a state-of-the-art tool for epitaxial growth. The use of MOCVD for the growth of semiconductor materials started in the late 1960's and early 70's [2-4]. Ever since the seminal work of Amano *et al.* who achieved featureless GaN layer grown on sapphire substrate with an AlN buffer layer using MOCVD [5], MOCVD is widely used and still remains the *de facto* technique for growth of III-nitride semiconductors. Reviews on the growth of GaN, AlGaN, and AlN epitaxial films using MOCVD can be found in [6-9].

MOCVD is specialised sub-class of the widely used chemical vapour deposition (CVD) technique in which material deposition is achieved by chemical reaction of gaseous precursors over a heated substrate. In MOCVD, metal organic precursors such as trimethylaluminium

(TMAl), trimethylgallium (TMGa) and trimethylindium (TMIn) are supplied to the heated reactor using H_2 or N_2 carrier gas and used as precursors for Al, Ga, and In, respectively. Gaseous hydrides of N (ammonia), P (phosphine), and As (arsine) are used as sources of group V. An Aixtron 3×2" CCS MOCVD is used for the deposition of GaN on sapphire and subsequent growth of GaN and AlGaN nanowires. Figure 3.1 shows a schematic view of CCS MOCVD reactor. In order to avoid unwanted pre-reactions in the gas-phase, the metal organic sources and hydrides are supplied to reactor through two separate lines and injected into reactor separately from top and bottom plenums of the showerhead. The wafers are placed on a SiC-coated graphite susceptor. The susceptor is heated by three-zone resistive tungsten coils. Temperature of the substrate is monitored with a thermocouple, as well as emissivity corrected pyrometer through the optical probe.

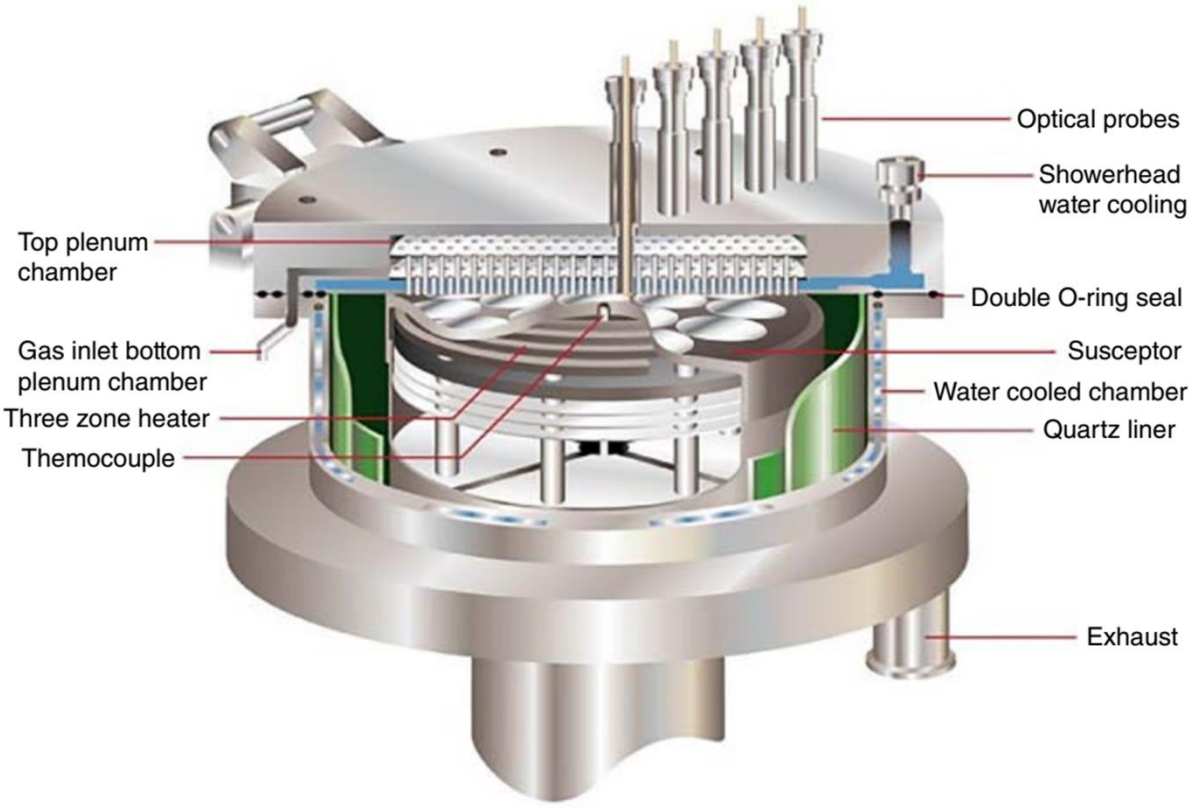

Figure 3.1 Schematic of close-coupled showerhead MOCVD reactor [10].

MOCVD is a complex process involving fluid dynamics, reaction chemistry and thermodynamics. The major process steps that occur in a MOCVD is shown schematically in Figure 3-2 and can be summarised as follows:

(I) Transport of group III and V reagents to the reactor using a carrier gas.

(II) Pyrolysis and reactions in the gas phase.

(III) Mass transport of the precursors towards the substrate.

(IV) Adsorption and diffusion of adatoms on the wafer surface.

(V) Surface reactions and adatom incorporation resulting in crystal growth.

(VI) Desorption of species.

(VII) Removal of gaseous by-products through the exhaust.

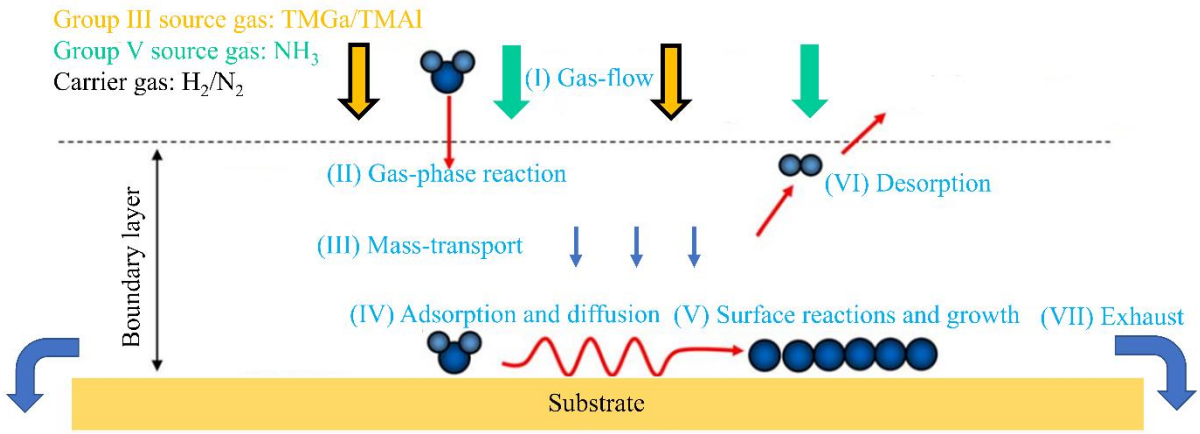

Figure 3.2 Schematic of physical and chemical processes inside the MOCVD. Adapted from [7].

3.4. Atomic layer deposition

Atomic layer deposition (ALD) is a technique of thin film deposition with a capability to control thickness at the atomic level (fraction of a monolayer) and coat complex shapes with a conformality unmatched by any other deposition technique. ALD shares some similarity with MOCVD in which both are chemical vapour deposition techniques. ALD also uses metal organic sources such as TMAl and deposition is controlled by physicochemical process [11].

ALD is carried out in four essential steps: *(i)* precursor exposure for a self-terminating reaction, *(ii)* purging or evacuation of the unreacted precursor and gaseous by-products, *(iii)* reactant species exposure, such as oxygen plasma, and *(iv)* purging of the reactant and by-products [11, 12]. The first two steps are referred to as precursor half-cycle and the latter two steps as reactant half-cycle. A Picosun-SUNALE™ plasma-enhanced ALD system is used for deposition of 15 nm-thick SiO_x layer to serve as the mask for selective area growth. Bis(diethylamino)silane (BDEAS) is used as the Si precursor, and oxygen plasma is used as the reactant to form SiO_x. Figure 3.3 shows a schematic of the SiO_x deposition in ALD using BDEAS and oxygen plasma.

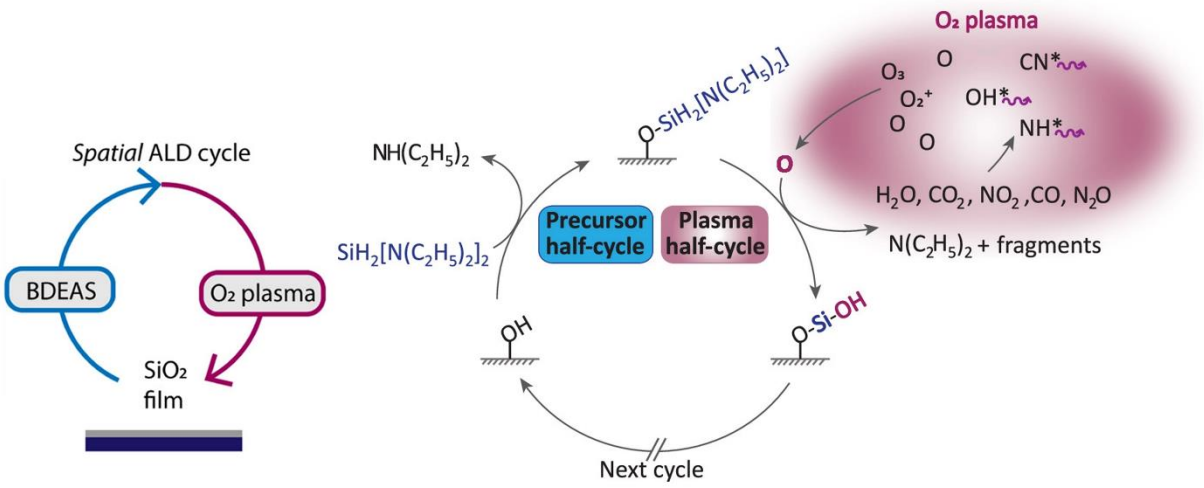

Figure 3.3 Schematic representation of SiO_x deposition in ALD using BDEAS and oxygen plasma. Adapted from [13].

3.5. Electron beam lithography

Electron beam lithography (EBL) is a technique that exposes electron-sensitive resist with a fine electron beam (e-beam) and can create extremely small patterns of nanometer dimension. Owing to its fine resolution and versatility in creating regular as well as arbitrary patterns, EBL has been extensively employed in nanofabrication [14].

Pattern generation using electron beam started by modification of existing scanning electron microscope in the late 1960s [16]. The basic working principle of EBL is generation of pattern by exposing an electron-beam sensitive resist to a focused electron beam, which changes the solubility of the resist based on the energy deposited by the electron beam [15]. In this thesis, a Raith150 EBL operated at 20 kV is used to write circular holes of diameters 50 – 400 nm. A schematic of an EBL system is shown in Figure 3.4. EBL system consists of an electron gun in a high vacuum chamber, and a column where the electron beam is accelerated by an electrostatic field of 10 – 100 kV and finally directed to the sample. A high-speed beam blanker capable of operating in MHz frequency controls beam on/off during the electron beam scan to selectively expose and create patterns. Before exposing the sample, the electron beam is shaped by using apertures and modulated by electromagnetic lenses and deflection coils. The deflection and scanning coils are used to direct the electron beam at specified area on the sample for writing the desired patterns by scanning the beam without moving the substrate. Such area that can be patterned by scanning without having to move the stage is referred to as “write field”.

and a write field of 100 × 100 μm^2 has been used for patterning all of the structures discussed in this thesis.

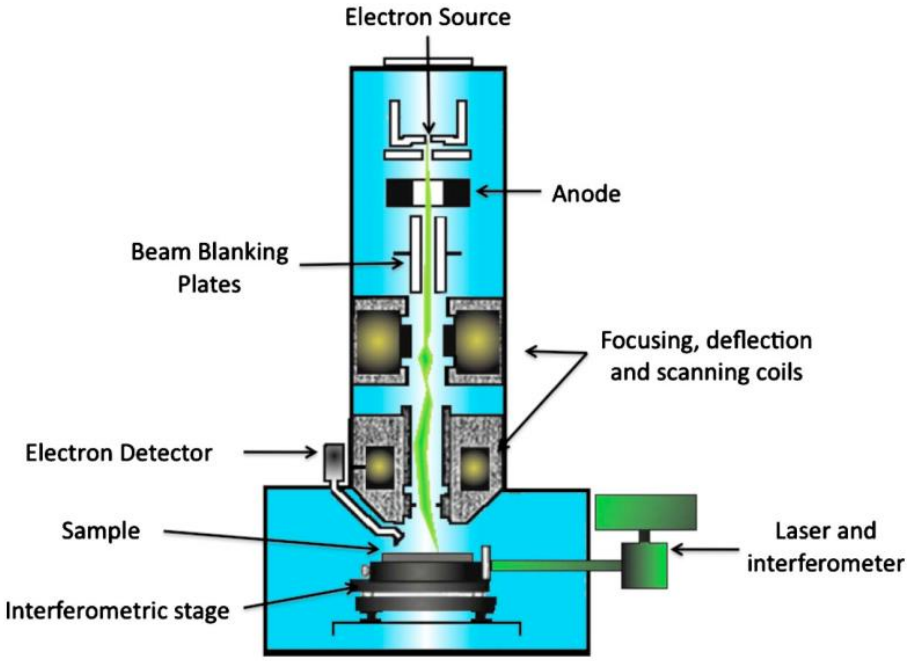

Figure 3.4 Schematic of an EBL system [15].

3.6. Reactive ion etching

Reactive ion etching (RIE) is used to transfer the patterns generated by EBL and subsequent development of electron beam resist to the underlying SiO_x layer. RIE is a plasma-based etching technique extensively used in micro- and nano-fabrication. RIE is capable of producing higher accuracy than the HF solution-based wet etching of SiO_x owing to the highly anisotropic etching characteristic in the vertical direction.

A schematic of an RIE system is shown as Figure 3.5. RIE system consists of a pair of electrodes in the form of parallel plates inside a vacuum chamber. Sample to be etched is mounted on the bottom plate (cathode) which isolated from rest of the system, while the top plate (anode) and the vacuum chamber is grounded. Process specific gases are supplied to the vacuum chamber through mass flow controllers and pressure inside the vacuum chamber (10 – 100 mTorr) is maintained by using a combination of pressure control valve and downstream vacuum pumps. After maintaining the necessary pressure, radio frequency (RF) power is applied to the cathode, which ionises the gases between the two plates and generates a plasma consisting of electrons, ions and energetic radicals. The more mobile electrons in the plasma oscillates between the two plates and keeps ionising the gas molecules by stripping electrons,

while the heavier ions move relatively little. During this process, electrons hitting the grounded anode and the vacuum chamber exits the system continuously, while electrons on the cathode gets accumulated due to its isolation. The negative charge on the cathode develops a negative voltage of the order of 100 V, referred to as DC bias. The positively charged ions accelerate towards cathode due to the potential difference and collide with the sample. The ions react with the material to be etched forming volatile products which are easily evacuated from the chamber.

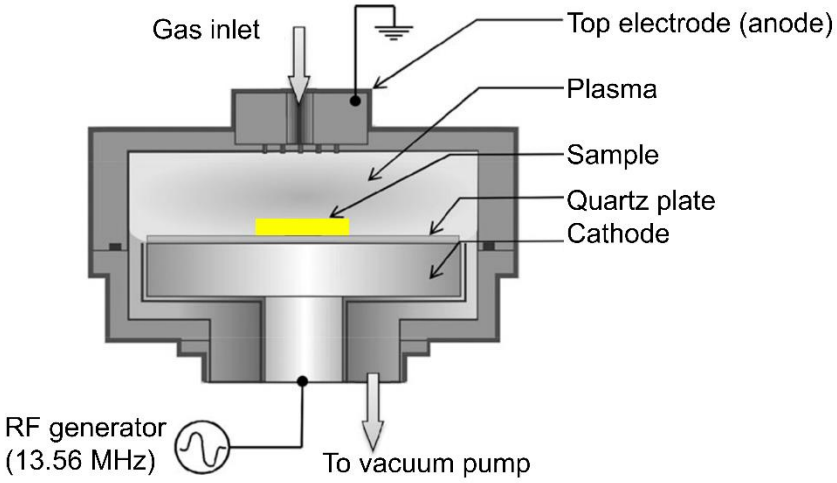

Figure 3.5 Schematic of an RIE system. Adapted from [17].

An Oxford Plasmalab 80Plus RIE system has been used to etch SiO_x in CHF_3 chemistry. The following process parameter has been maintained in all of the experiments: a CHF_3 flow rate of 25 sccm, a chamber pressure of 30 mTorr, and RF power of 100 W. The etch rate of SiO_x with the above conditions is ~15 nm/min.

3.7. Electron microscopy

In this section, electron microscopy techniques used for sample characterisation by scanning electron microscope (SEM), transmission electron microscope (TEM) and related characterisation techniques of cathodoluminescence (CL) and energy dispersive x-ray spectroscopy (EDS) will be discussed.

3.7.1. Scanning electron microscopy (SEM)

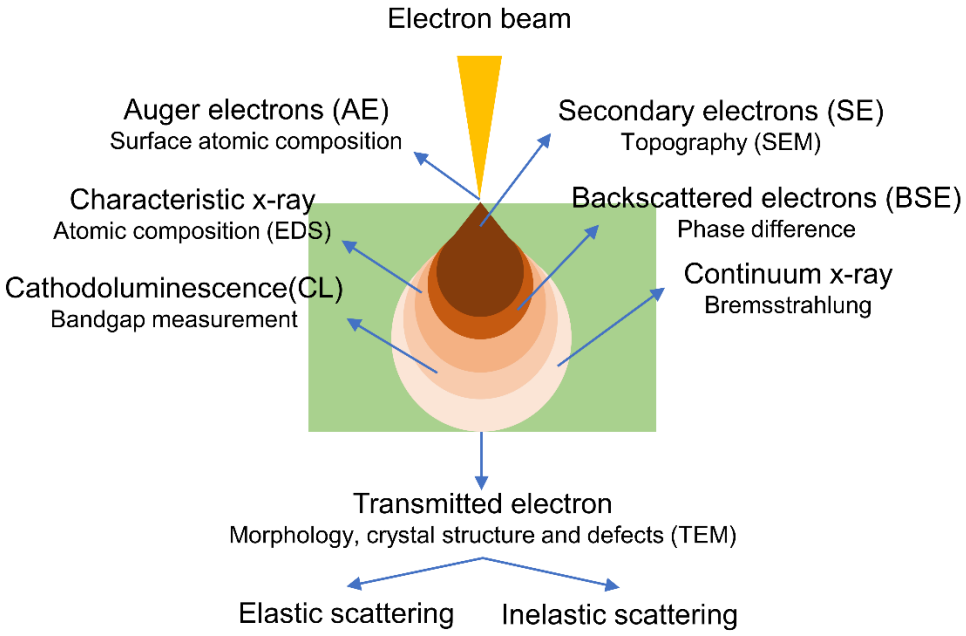

Figure 3.6 Schematic illustration of the different signals generated upon interaction of electron beam with a sample.

Scanning electron microscopy is a powerful technique for observing submicron structures or details, which are otherwise invisible or unresolvable in an optical microscope. SEM has very high resolution of about 10 nm compared to optical microscopy due to the very short de Broglie wavelength of electrons. The de Broglie wavelength of an electron accelerated at 1 kV is 1.227 nm, whereas optical microscopy uses the visible wavelength of 400-700 nm and the resolution in optical microscope is limited to about 200 nm at best. Therefore, SEM is a suitable tool for morphology characterisation of the selective area grown GaN and AlGaN nanostructures discussed in this thesis.

The basic components in an SEM are *(i)* an electron gun to generate electron beam, *(ii)* condenser and objective electromagnetic lenses to shape and focus the electron beam, *(iii)* scanning coils to deflect and scan the electron beam and *(iv)* detectors. All of these components and the specimen to be analysed are housed in vacuum. The working of an SEM involves scanning a focussed electron beam over the specimen. The interaction of electron beam with the specimen generates various signals such as secondary electrons (SE), backscattered electrons (BSE) and x-rays. Figure 3.6 shows the different signals generated when an incident electron beam interacts with the specimen.

In the imaging mode of SEM, SEs are generally used. SEs are generated when the weakly bound electrons from conduction or valence bands are ejected by inelastic scattering of the incident electron beam. Although the incident electron beam can penetrate much deeper into the samples, the generated SEs have low kinetic energy of 2 – 50 eV, therefore, only SEs close to the surface are able to escape and contribute to imaging. The SEs are detected using an Everhart-Thornley detector, which consists of a scintillator enclosed in a Faraday cage. A positive voltage of the order of 100 V is applied to the Faraday cage to attract the SEs emitted from the sample, then the SEs are accelerated further with a higher positive voltage applied to the scintillator. Modern day SEMs are additionally equipped with another SE detector called the in-lens, through-the-lens, or immersion-lens detector. This type of detector is arranged in rotational symmetry around the optic axis of the electron beam and has higher efficiency in SE collection than the Everhart-Thornley detector. As SEs emitted from or near the surface are only detected, SEM imaging with SEs correspond to the surface of the sample. Additionally, the yield of SE also depends on the surface topography, edges and angled surfaces emit more SE than a flat surface and appear brighter, and hence aids in morphology characterisation. An FEI Verios 460 SEM has been used for morphology characterisation discussed throughout this thesis.

3.7.2. Cathodoluminescence

Cathodoluminescence (CL) is the emission of light as a result of electron-matter interaction as shown in Figure 3.6. CL is a powerful non-destructive characterisation technique often used to characterise the optical and electronic properties of semiconductors [18]. When an electron beam with sufficient energy hits a semiconductor material, electrons in the valence band are excited to the conduction band. The excited electron then returns from conduction band to the valence band and the energy lost by the electron is emitted as light in the direct bandgap materials. The wavelength of emitted light (of energy of the photon) provides information on bandgap of the material. CL has been used to determine the AlGaN alloy composition based on their bandgap. The excited electron may also get trapped at an intrinsic structural defect or at extrinsic level introduced by dopants during its transition to the valence band, resulting in emission of light at different wavelengths, and such information are useful in determining defect levels and their types. Thus, CL can provide key information on band structure and impurity levels of semiconductors.

CL systems are generally integrated in an SEM as shown in Figure 3.7. An aluminium parabolic mirror is inserted between the SEM pole piece and sample as shown in Figure 3.7 (a). The parabolic mirror is used to collect and direct the light from the sample to the photomultiplier tube or Si-CCD for detection as shown in Figure 3.7 (b). The parabolic mirror also has a small hole on top to allow passage of electron beam from the pole piece to the sample and secondary electrons (SE) from the sample to the SE detector. High energetic electron beam (1 - 20 keV) and high spatial resolution of the electron beam (~10 nm) make CL a very useful technique for studying wide bandgap AlGaN nanostructures. Additionally, CL can also be used for depth-resolved studies of the sample by changing acceleration voltage of the electron beam [19].

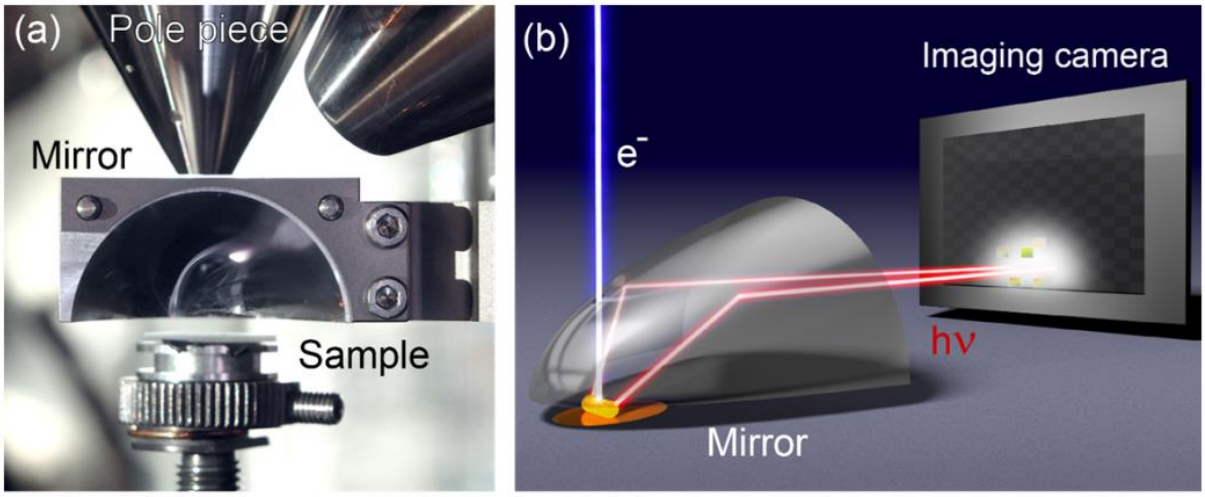

Figure 3.7 (a) Image of sample and the light collection system for CL in an SEM. (b) Schematic representation of light collection using a parabolic mirror [20].

In this thesis, a Gatan MonoCL4 integrated to an FEI Verios 460 SEM is used for obtaining CL panchromatic and hyperspectral images. CL panchromatic image is acquired using a photomultiplier tube and contains integrated intensity of light over the entire wavelength range (200 - 1000 nm) and provides information on the luminescence characteristics of the whole sample. CL hyperspectral imaging is carried out using a Si CCD detector. In hyperspectral imaging, electron beam is scanned pixel by pixel over a defined region and luminescence spectrum is recorded for every pixel, creating an information-rich map of the sample. Using CL hyperspectral mapping, regions of nanowire-core and quantum wells has been distinguished based on the different emission wavelengths.

3.7.3. Transmission electron microscopy

Transmission electron microscopy (TEM) is an extremely useful technique for analysis of crystalline structure and their defects in the field of materials science. TEM can provide atomic

scale resolution as the electrons are accelerated with 100 to 1000 of kV resulting in electron's de Broglie wavelength of a few picometers. Unlike in the SEM, electrons transmitted through the sample (shown above in Figure 3.6) are used for TEM analysis, thus requiring preparation of electron transparent samples, commonly referred to as lamella, with typical thickness of ≤ 100 nm.

The main components in a TEM are: the electron gun, condenser lenses, sample holder, objective lens, projection lens, camera and sample holder as shown schematically in Figure 3.8. Two condenser lenses are located below the electron gun to control spot size and intensity. Most TEMs are equipped with a twin objective lens, one above the sample to gain extra control on the beam, and one below the sample to provide magnification of about 50 times. The image formed by the objective lens consists of a diffraction pattern at the back focal plane and image of the crystal at the image plane. In the case of selected area electron diffraction (SAED) a diffraction lens (also called intermediate lens) is used to select the diffraction pattern by focussing on the back focal plane. The other intermediate and projection lenses are used for magnification and projection of the final image on to a screen.

In TEM, the sample is kept near the top of the column and the transmitted electrons are imaged further down the column after magnification and projection. Thus, the electrons travel a distance of about 1 to 2 meters and this requires a high vacuum column to provide sufficient mean-free-path to electrons. The transmitted electrons in TEM carry a wealth of information, and there are two types of transmitted electrons: *(i)* elastically and *(ii)* inelastically scattered electrons.

The large difference in the mass of electron (from the electron beam) and nucleus (from atoms in the sample) hardly results in energy or momentum transfer to the nucleus and such event is called elastic scattering. Majority of electrons from the primary beam pass through the sample with elastic scattering and such electrons are useful for high-resolution TEM (HRTEM) imaging. Inelastic scattering occurs for electron-electron interactions where the energy of primary electron is transferred to electrons of atomic shell in the sample. The inelastically scattered electrons with reduced kinetic energy interact differently with the lenses and are not focused in the same way as the elastically scattered electrons. Inelastic scattering is important for electron energy loss spectroscopy (EELS) and energy dispersive x-ray analysis (EDS).

The wave nature of electrons, passing through an array of atoms behaving like a grating, generates diffraction pattern in TEM. Thus, the diffraction pattern depends on the orientation

of the crystal plane and crystal lattice. In this thesis, as well as in general TEM operation, such diffraction patterns are used to align the sample orientation to a specific zone axis. All of the HRTEM images acquired and reported in this thesis used $< 11\bar{2}0 >$ zone axis, unless specified otherwise. HRTEM image is a phase contrast image formed by interference of the transmitted electrons and diffracted electrons. HRTEM images can be acquired at very high magnifications resolving atomic positions in a crystal.

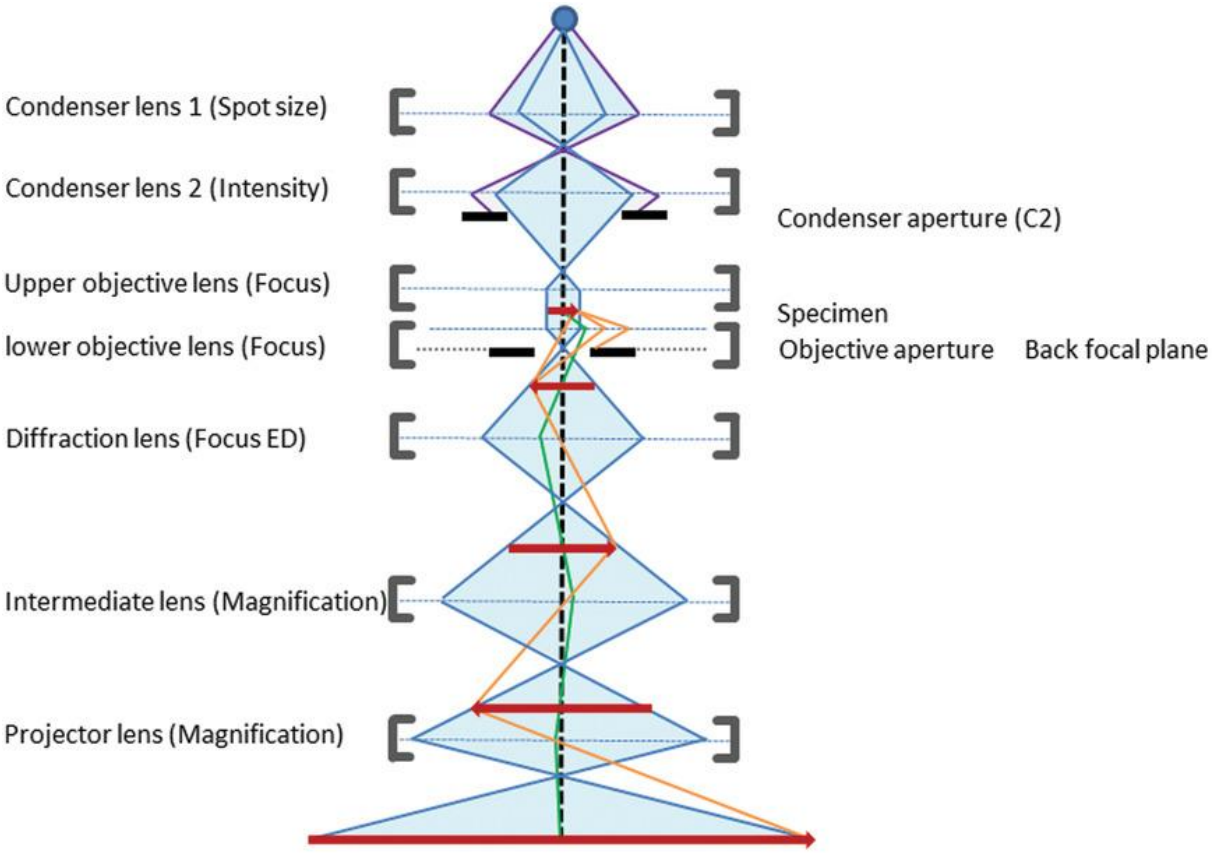

Figure 3.8 Schematic diagram of a transmission electron microscope [21].

TEM can also be operated in a manner that the electron beam is focused to a fine spot and this finely focussed beam is raster-scanned on the specimen. This mode of operation is called scanning transmission electron microscopy (STEM). A bright field (BF) detector or a high-angle annular dark field (HAADF) detector is used in STEM. BF detector collects the directly transmitted electrons, whereas, HAADF detector detects the highly scattered electrons, whose scattering depends on the atomic number of the elements in the specimen. Hence, HAADF-STEM is very useful in distinguishing regions of different atomic compositions such as GaN nanowire core and AlGaN shell.

A JEOL 2100F TEM operating at 200 kV is used for structural characterisation in this thesis.

3.7.4. Energy dispersive x-ray spectroscopy

Energy dispersive x-ray spectroscopy (EDS) is a technique to analyse the chemical composition. In this thesis, an Oxford X-Max EDS detector in an FEI Verios 460 SEM is used to determine the Al composition in GaN/AlGaN core-shell nanowires, and a JEOL EDS detector in a JEOL F2100 TEM is used to analyse the $Al_xGa_{1-x}N/Al_yGa_{1-y}N$ multiple quantum wells. The spatial resolution of EDS in TEM is higher compared to the EDS in SEM and hence makes it suitable for analysis of elemental distribution in quantum structures.

X-rays are generated during the interaction of incident electron beam with atoms in the specimen as shown in Figure 3.6. Energetic incident electron can knock out electron from an inner-shell of an atom in the specimen creating a vacancy of electron. The vacancy is filled by an electron from the outer shell and emits quanta of x-ray corresponding to the energy difference between the outer and inner shell. Such x-ray with a discrete energy is unique to each element and its shells, and are called the characteristic x-ray. The processes of electron removal from an inner shell by impinging electron and subsequent filling up of the vacancy resulting in generation of characteristic x-ray is shown schematically in Figure 3.9.

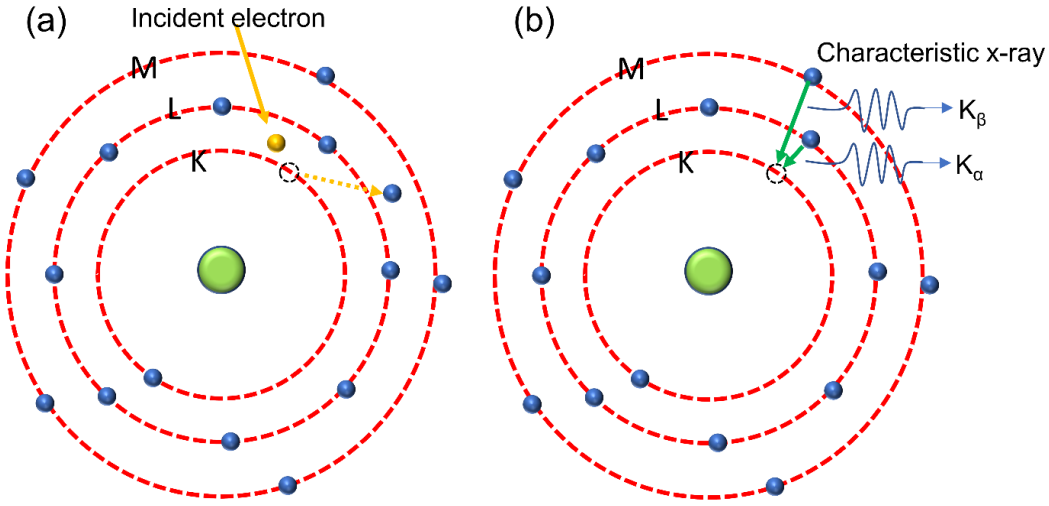

Figure 3.9 Schematic process in EDS. (a) removal of electron from K-shell by an incident electron and (b) filling up of electron in inner shell with an electron from outer shell.

3.8. Summary

The procedures for sample preparation and basic principles of experimental techniques related to this thesis are described in this chapter. In Section 3.2, the detailed procedures for preparing patterned substrates for SAG are discussed. Section 3.3 and 3.4 describes the deposition techniques of MOCVD and ALD, respectively. The operational principle of electron beam lithography is discussed in Section 3.5, followed by reactive ion etching in Section 3.6. Electron microscopy and the related characterisation methods of EDS and CL are discussed in Section 3.7.

References

1. Ma, H.-P., Yang, J.-H., Yang, J.-G., Zhu, L.-Y., Huang, W., et al., "Systematic Study of the SiO_x Film with Different Stoichiometry by Plasma-Enhanced Atomic Layer Deposition and Its Application in SiO_x/SiO_2 Super-Lattice." *Nanomaterials*, **2019**, 9, 55.

2. Manasevit, H.M. and Simpson, W.I., "The Use of Metal-Organics in the Preparation of Semiconductor Materials: I. Epitaxial Gallium-V Compounds." *Journal of the Electrochemical Society*, **1969**, 116, 1725-1732.

3. Manasevit, H.M., Erdmann, F.M. and Simpson, W.I., "The Use of Metalorganics in the Preparation of Semiconductor Materials: IV. The Nitrides of Aluminum and Gallium." *Journal of the Electrochemical Society*, **1971**, 118, 1864-1868.

4. Duffy, M., Wang, C., O'clock, G., McFarlane, S. and Zanzucchi, P., "Epitaxial growth and piezoelectric properties of AlN, GaN, and GaAs on sapphire or spinel." *Journal of Electronic Materials*, **1973**, 2, 359-372.

5. Amano, H., Sawaki, N., Akasaki, I. and Toyoda, Y., "Metalorganic vapor phase epitaxial growth of a high quality GaN film using an AlN buffer layer." *Applied Physics Letters*, **1986**, 48, 353-355.

6. Watson, I.M., "Metal organic vapour phase epitaxy of AlN, GaN, InN and their alloys: A key chemical technology for advanced device applications." *Coordination Chemistry Reviews*, **2013**, 257, 2120-2141.

7. Tang, L., Tang, B., Zhang, H. and Yuan, Y., "Review—Review of Research on AlGaN MOCVD Growth." *ECS Journal of Solid-State Science and Technology*, **2020**, 9, 024009.

8. Hagedorn, S., Walde, S., Knauer, A., Susilo, N., Pacak, D., et al., "Status and Prospects of AlN Templates on Sapphire for Ultraviolet Light-Emitting Diodes." *physica status solidi (a)*, **2020**, 217, 1901022.

9. Nagasawa, Y. and Hirano, A., "A Review of AlGaN-Based Deep-Ultraviolet Light-Emitting Diodes on Sapphire." *Applied Sciences*, **2018**, 8, 1264.

10. Pierre, G., "Metal organic vapour phase epitaxy of GaN and lateral overgrowth." *Reports on Progress in Physics*, **2004**, 67, 667.

11. Puurunen, R.L., "Surface chemistry of atomic layer deposition: A case study for the trimethylaluminum/water process." *Journal of Applied Physics*, **2005**, 97, 121301.

12. Kim, H., Lee, H.-B.-R. and Maeng, W.J., "Applications of atomic layer deposition to nanofabrication and emerging nanodevices." *Thin Solid Films*, **2009**, 517, 2563-2580.

13. Mione, M.A., Vandalon, V., Mameli, A., Kessels, W.M.M. and Roozeboom, F., "Atmospheric-Pressure Plasma-Enhanced Spatial ALD of SiO_2 Studied by Gas-Phase Infrared and Optical Emission Spectroscopy." *The Journal of Physical Chemistry C*, **2021**, 125, 24945-24957.

14. Chen, Y., "Nanofabrication by electron beam lithography and its applications: A review." *Microelectronic Engineering*, **2015**, 135, 57-72.

15. Altissimo, M., "E-beam lithography for micro-/nanofabrication." *Biomicrofluidics*, **2010**, 4, 026503.

16. Chang, T.H.P. and Nixon, W.C., "Electron beam formation of 800 Å wide aluminium lines." *Journal of Scientific Instruments*, **1967**, 44, 231.

17. Galvin, E., Morshed, M.M., Cummins, C., Daniels, S., Lally, C., et al., "Surface Modification of Absorbable Magnesium Stents by Reactive Ion Etching." *Plasma Chemistry and Plasma Processing*, **2013**, 33, 1137-1152.

18. Yacobi, B.G. and Holt, D.B., "Cathodoluminescence scanning electron microscopy of semiconductors." *Journal of Applied Physics*, **1986**, 59, R1-R24.

19. Götze, J., "Potential of cathodoluminescence (CL) microscopy and spectroscopy for the analysis of minerals and materials." *Analytical and Bioanalytical Chemistry*, **2002**, 374, 703-708.

20. Coenen, T. and Haegel, N.M., "Cathodoluminescence for the 21st century: Learning more from light." *Applied Physics Reviews*, **2017**, 4, 031103.

21. Franken, L.E., Grünewald, K., Boekema, E.J. and Stuart, M.C.A., "A Technical Introduction to Transmission Electron Microscopy for Soft-Matter: Imaging, Possibilities, Choices, and Technical Developments." *Small*, **2020**, 16, 1906198.

Chapter 4. Selective Area Growth and Characterisation of GaN Nanowires

4.1. Introduction

The history of semiconductors is broadly classified in to three generations. The first-generation semiconductors of Ge and Si led to the rapid growth of microelectronics. The second-generation semiconductors comprising of III-Vs such as GaAs and InP have enabled infrared opto-electronics. Recent wide bandgap semiconductors such as GaN, SiC, and ZnO comprises the third-generation semiconductors with important implications in high-power electronics and lighting. Each generation is marked by a revolutionary growth in technological advent closely tied to our lives. The developments in Si, III-Vs, and GaN has led to computers, high-speed optical communications and high-efficiency lighting industry, respectively.

Amongst the third-generation semiconductors, GaN has unmatched advantages due to its direct bandgap, high breakdown field, excellent thermal and chemical stability, ability to make both *p*-type and *n*-type, and most importantly GaN can be alloyed with In or Al to tune the bandgap. The rise in popularity of GaN may be traced back to the mid-1990s when efficient blue and green light-emitting diodes (LEDs) were successfully demonstrated [1-3]. Currently, there are a lot of interests in nanostructures, especially nanowires, to explore and unleash the potential for high-efficiency devices. Owing to a high surface-to-volume ratio at nanoscale, nanowires are a promising candidate for the next generation LEDs [4], lasers [5], solar cells [6], transistors [7], photodetectors [8], electronic sensors [9] and biosensors [10].

The breakthrough in GaN came about with the successful growth of high-quality epitaxial layers, synonymously, successful growth of GaN nanowires holds the key to their future. Growth of GaN nanowires, arranged in an orderly pattern, is generally carried out *via* selective area growth (SAG) using metal organic chemical vapour deposition (MOCVD) [11] or molecular beam epitaxy (MBE) [12]. SAG provides the advantage of catalyst-free, well-aligned and uniform nanowires with controllability of site and dimensions. Unlike the conventional

semiconductors (Si, Ge or III-V's), GaN epitaxial layers grown on foreign substrates are associated with high threading dislocation density (10^8 cm^{-2}) and SAG provides a path to alleviate this issue. Selective area-grown GaN nanowires are dislocation-free and additionally provides a large non-polar surface area, which are advantageous for achieving high-efficiency devices.

As reviewed earlier in Chapter 2, GaN crystallises in a wurtzite structure and this gives rise to crystal polarity making atomic arrangements in +*c* (0001) and -*c* $(000\bar{1})$ planes different, and hence different growth characteristics. Growth of $(000\bar{1})$oriented N-polar GaN nanowires is relatively easy, however, such nanowires contain dislocations and inversion domain boundaries. On the other hand, growth of (0001) oriented Ga-polar GaN nanowires is challenging due to a strong tendency to form pyramids. Successful SAG of Ga-polar GaN nanowires using MOCVD was reported for the first time by Hersee *et al*. in 2006 using a pulsed-flow scheme of precursors [11]. However, it adds more parameters and complexity, utilises precursors inefficiently and results in slow growth rate.

It was not until 2012 that continuous-flow scheme for SAG of GaN nanowires in MOCVD was reported [13]. Since then, the unanimous conclusion to achieve GaN nanowires by continuous-flow growth is to use a low V/III ratio and low precursor flows [13, 14]. Although, this conclusion gives a fair idea however, the term "low" is vague and begs the question, what actual value demarcates low or high V/III ratio. This may be answered based on the ratio of desorption rates of nitrogen, k_N, and gallium, k_{Ga}, at a certain growth temperature, *T*, given by $k_N/k_{Ga} = 1.9205\times10^{16}\times\exp(-39563/T(K))$ [15]. It should be noted that, the k_N/k_{Ga} ratio has been deduced from planar epitaxial growth of GaN, and further, experimental evidence from GaN nanowire growth suggests a lower V/III ratio than their planar counterparts. Thus, it may be established that the ideal k_N/k_{Ga} ratio would set the upper limit of V/III ratio for nanowire growth. For instance, in the planar epitaxial growth of GaN, the ideal V/III ratio is 172 at a growth temperature of 950 °C. Therefore, at 950 °C, V/III ratios below 172 may be considered low, and if GaN nanowires are to be grown at this temperature, a V/III ratio lower than 172 should be used.

The necessity for a lower V/III ratio in the growth of GaN nanowires compared to the planar films is due to the requirement of a Ga-rich growth condition. First principles calculation for GaN growth in MOCVD revealed that Ga adatom terminated or Ga bilayer surfaces are stable under Ga-rich conditions (low V/III), whereas, N-H bonds are favoured under nitrogen-

rich conditions (high V/III) [16]. The major issue in growth of Ga-polar nanowires has been the passivation of inclined $\{10\bar{1}1\}$ *r*-planes by the formation of N-H bonds under high V/III ratio. The inclined $\{10\bar{1}1\}$ *r*-planes of Ga-polar GaN are N-terminated and easily passivated by hydrogen through the formation of N-H bonds under high V/III ratio due to the extremely high affinity of hydrogen for N-terminated surface [17, 18]. The very high stability of such hydrogen terminated surface leads to slow growth rate of $\{10\bar{1}1\}$ planes and results in pyramidal structure for SAG Ga-polar GaN with high V/III ratio. Thus, it is necessary to carry out SAG of Ga-polar GaN nanowires under Ga-rich conditions by using a low V/III ratio, and hence V/III ratio as a parameter has gained a lot of attention.

As pointed out earlier a V/III ratio less than 172 may be considered low. Ga-polar GaN nanowire growth with V/III ratios from less than 10 to above 100 have been reported in the selective area growth [19-26]. Müller *et al*. [27] obtained nanowires for a V/III ratio of 100, however, Wang *et al*. [22] and Li *et al*. [28] obtained pyramidal GaN for the same V/III ratio of 100. So, what is the range of V/III ratio and what other parameters are important for the SAG of Ga-polar GaN nanowires still lacks a clear answer. To answer these questions and provide an insight into the role of growth parameters, a systematic investigation on SAG of Ga-polar GaN nanowires in MOCVD is carried out. From a large set of GaN nanowire growth experiments, it is concluded that all of the MOCVD growth parameters, apart from temperature, can be unified into one single parameter as *partial pressure* to explain the mechanism and morphology of Ga-polar GaN nanowires. A quantitative determination of different growth parameters in terms of partial pressures allow the estimation of the range of V/III ratio for which GaN nanowires can be obtained. Further, our analysis through partial pressure also highlights that, although V/III ratio is an important parameter, it is not a sufficient parameter for achieving GaN nanowire growth.

4.2. Experimental methods

Selective area growths of GaN nanowires is carried out in a 3 × 2" close-coupled showerhead MOCVD reactor (Aixtron). A GaN grown on *c*-plane sapphire is used as the substrate for SAG. A 15 nm-thick SiO_x layer is deposited on top of the 4 µm-thick GaN using an atomic layer deposition system (Picosun SUNALE^{TM}). Circular holes with diameters of 50, 100, 200, 400, and 600 nm arranged in a hexagonal pattern with pitches of 500 nm to 2 µm are defined using electron beam lithography (Raith 150). The developed patterns after electron beam lithography is transferred by reactive ion etching of the SiO_x layer using CHF_3 chemistry.

The patterned wafer is subsequently cleaned with acetone, isopropyl alcohol and deionised water. After the cleaning, the patterned wafer is treated with oxygen plasma to remove any residual organic contaminants. The patterned 2-inch wafer is then diced into 1 × 1 cm^2 pieces using a dicing machine (Disco DAD321) and cleaned again with acetone, isopropyl alcohol and deionised water before loading into the MOCVD growth chamber.

Triethylgallium (TEGa) and NH_3 are used as the sources of Ga and N, respectively. SAG of GaN nanowires is carried out, unless specified otherwise, at a reactor pressure of 100 mbar, growth duration of 15 minutes and a growth temperature of 955 °C using a mixed carrier gas composed of 6 standard litre per minute (slm) of N_2 and 4 slm of H_2, making up a total gas flow rate of 10 slm. The temperatures reported here are the in-situ emissivity corrected temperature measured using a Laytec EpiTT system. The nanowire morphology is analysed using an FEI Verios 460 scanning electron microscope (SEM). Transmission electron microscopy (TEM) study is carried out using a JEOL 2100 FEG TEM operating at 200 kV. Room temperature cathodoluminescence (CL) is carried out using a Gatan MonoCL 4 system. Partial pressures, P_X, of the constituent gases TEGa, NH_3 and H_2 are calculated as follows:

$$P_X = \frac{F_X}{F_{Total}} P_{Reactor} \tag{4.1}$$

where, x is either TEGa, NH_3, or H_2, F_X is the volumetric flow rate of x in sccm, F_{Total} is the total gas flow rate through the reactor in sccm, and $P_{Reactor}$ is pressure of the reactor in mbar.

4.3. Effect of TEGa partial pressure

The effect of TEGa partial pressure, P_{TEGa}, on the growth characteristics of Ga-polar GaN nanowires is investigated by changing the TEGa flow rates while maintaining the other parameters fixed. TEGa flow rates of 15, 30 and 45 sccm are used in this set of experiments which correspond to P_{TEGa} of 0.15, 0.30 and 0.45 mbar as the reactor pressure and total flow rates are maintained 100 mbar and 10 slm, respectively. The growth duration is maintained 15 minutes for the growth with TEGa flow rates of 30 and 45 sccm, whereas, the growth duration is increased to 20 minutes in the case of 15 sccm to compensate for the low TEGa flow rate. In these set of experiments, NH_3 flow rate is fixed at 10 sccm, which results in V/III ratios of 87, 44 and 29, respectively.

SEM images for these three growth conditions are shown arranged vertically in Figure 4.1. At the lowest P_{TEGa} of 0.15 mbar, the 50 nm holes are empty and nanowire growth is not

observed due to insufficient Ga supply. This suggests that a minimum amount of P_{TEGa} is required to overcome GaN decomposition to sustain nanowire growth. It should be noted that GaN growth is a dynamic process in which growth and decomposition are in constant competition. At a P_{TEGa} of 0.30 mbar, growth of uniform GaN nanowires occur but a few holes are left empty. At a higher P_{TEGa} of 0.45 mbar, homogenous growth of nanowires occurs from all of the holes. However, increasing the P_{TEGa} to 0.45 mbar (V/III = 29) results in significant increase of the nanowire diameter (111±8 nm) compared to the nanowire grown with lower P_{TEGa} of 0.30 mbar (78±4 nm).

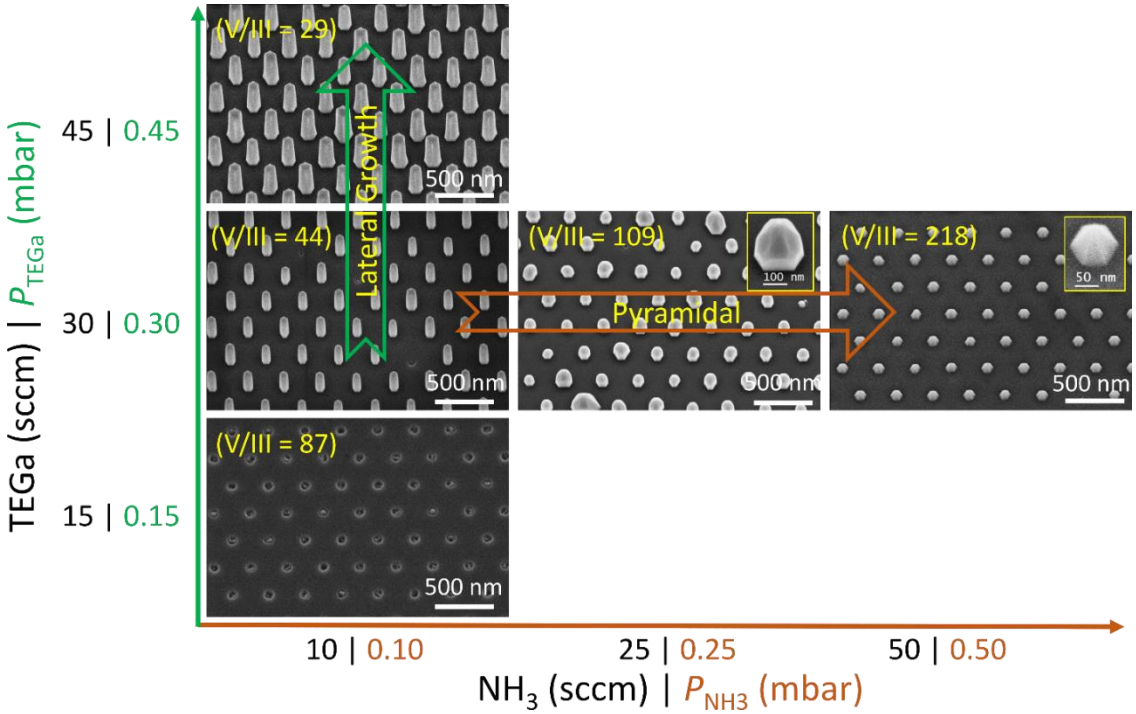

Figure 4.1 Effect of P_{TEGa} and P_{NH3} on the morphology of GaN nanowires grown on 50 nm diameter holes. Vertical and horizontal arrangements represent the change in P_{TEGa} and P_{NH3}, respectively [30].

Higher V/III ratio is known to promote lateral growth in the conventional planar epitaxy of GaN, however, the present result indicates an opposite trend. Therefore, the lateral growth cannot be simply explained by V/III ratio, but it emphasises that P_{TEGa} as an individual parameter has important role in determining the nanowire morphology. In essence, increasing P_{TEGa}, leads to increased nanowire growth rate in both height and diameter, however, the predominant increase in diameter needs to be kept in check for nanowires. The enhanced lateral growth of the nanowires with increased P_{TEGa} is attributed to the formation of Ga-Ga dimer

terminated surface on $\{10\bar{1}0\}$ sidewalls under Ga-rich growth conditions which facilitate lateral growth [29].

4.4. Effect of NH_3 partial pressure

Earlier discussion on the topic of V/III ratio have highlighted that contradictory results of nanowires as well as pyramidal structures have been reported at the same V/III ratio. Therefore, the morphology of GaN nanostructures with respect to NH_3 partial pressure, P_{NH3}, is investigated while keeping the same P_{TEGa}. NH_3 flow rates of 10, 25 and 50 sccm are used while P_{TEGa}, reactor pressure and total flow rate are maintained at 0.30 mbar, 100 mbar, and 10 slm, respectively. Under these conditions of SAG, P_{NH3} corresponds to 0.10, 0.25 and 0.50 mbar with V/III ratios of 44, 109 and 218, respectively.

SEM images of the GaN nanostructures from this study are shown in Figure 4.1 arranged horizontally. It is evident that nanowire morphology is obtained only for the lowest P_{NH3} of 0.10 mbar used in this investigation. At increased P_{NH3} of 0.25 mbar, the height of the nanostructures decreases and morphology becomes hexagonal prisms. The term prism is used for nanostructures with a very short vertical sidewall whereas, structures without the vertical sidewall is referred to as pyramid. At this P_{NH3} of 0.25 mbar, the V/III ratio is 109, and the observation of prismatic structure under this condition suggests that the P_{NH3} (and V/III ratio) is relatively high and unfavourable for achieving GaN nanowires. At further increased P_{NH3} of 0.50 mbar (V/III ratio of 219), pure pyramidal structures defined by $\{10\bar{1}1\}$ inclined facets are obtained without any vertical growth.

The formation of pyramidal GaN at high P_{NH3} is due to the passivation of N-terminated dangling bonds on the inclined $\{10\bar{1}1\}$ facets by formation of N-H bonds. Ambacher *et al.* carried out growth of GaN by replacing H_2 carrier gas with deuterium and concluded that no noticeable deuterium incorporation was detected [31]. Therefore, hydrogen generated from the pyrolysis of NH_3 is responsible for formation of N-H bond. The passivated $\{10\bar{1}1\}$ planes grows slowly compared to *c*-plane and results in pyramidal GaN with increased P_{NH3}. According to Wulff's theory [32], it may be understood that the faster growing planes grows to extinction and the slow-growing planes determines the crystal morphology at the end of growth. The effect of P_{NH3} on GaN nanostructure growth resulting in either nanowires or pyramidal structures may be summarised as follows:

- At low P_{NH3}, formation of N-H bonds with hydrogen from NH_3 pyrolysis is reduced and the growth rate of $\{10\bar{1}1\}$ exceeds that of *c*-plane resulting in nanowire growth.

- At higher P_{NH3}, the $\{10\bar{1}1\}$ inclined planes are passivated owing to the presence of a large amount of hydrogen in the growth chamber, hence, the resulting crystal structure is determined by the slowest growing $\{10\bar{1}1\}$ planes and takes the shape of pyramids.

Therefore, Ga-polar GaN nanowires are obtained at low P_{NH3}, whereas, pyramidal structures are obtained in the case of high P_{NH3} as indicated by a horizontal arrow in Figure 4.1.

4.5. Effect of carrier gas composition

Pure nitrogen [19], pure hydrogen [22], and a mixture of the nitrogen and hydrogen [13, 26] has been reported as carrier gas for the SAG of GaN nanowires. Majority of the reports have suggested that addition of H_2 in the carrier gas as a necessary condition for obtaining vertical GaN structure [28, 33, 34]. Whenever a mixture has been used, it needs further elucidation. The carrier gas composition is changed by partially substituting nitrogen with hydrogen and the resulting nanostructure morphology is examined. P_{TEGa}, P_{NH3}, reactor pressure and total carrier gas flow rate are maintained 0.30 mbar, 0.10 mbar, 100 mbar and 10 slm, respectively.

GaN nanostructure morphology obtained with different P_{H2} in the range of 0 to 45 mbar is shown in Figure 4.2. Pyramidal nanostructures, mostly triangular as well as some hexagonal pyramids, are obtained in pure N_2 carrier gas. Pyramidal GaN structures have also been obtained by Bergbauer *et al.* [33] and Wang *et al.* [22] in the SAG of N-polar and Ga-polar GaN using pure N_2 carrier gas. Such nanopyramids may find application in planar UV LED structures for improving light extraction efficiency. However, in the present context, conditions of GaN nanowire growth is the primary focus and the role of H_2 in the carrier gas is discussed. The necessity for addition of H_2 in the carrier gas during SAG of GaN has been highlighted by Li *et al.* [28]. The inclined {10-11} *r*-planes with a higher dangling-bond density of 16.1 nm^{-1} are preferentially etched by H_2 from the carrier gas. This etching by H_2 leaves the nanostructure with vertical $\{10\bar{1}0\}$ *m*-plane sidewalls with a lower dangling-bond density of 12.1 nm^{-1}. The exposed $\{10\bar{1}0\}$ *m*-plane vertical sidewalls are necessary to maintain nanowire morphology during the SAG of GaN.

Introducing H_2 in the carrier gas with a P_{H2} of 10 mbar is achieved by substituting 1 slm of N_2 by H_2 in the carrier gas while the total flow rate is maintained at 10 slm. Under this condition, nanostructure morphology started transformation from pyramids to nanowires. Smaller nanostructures grown on 50 nm diameter holes shows a faster transformation towards nanowire morphology, whereas, larger nanostructures grown on larger holes exhibits a slower transformation to nanowires due to insufficient etching for these larger nanostructures.

Nanowire yield, aspect ratio and homogeneity are improved on increasing P_{H2} up to 40 mbar, however, the nanowire volume decreases with P_{H2} due to increased etching. At the highest P_{H2} of 45 mbar, used in this series of experiments, the aspect ratio of the nanowires decreases in larger diameter holes of 100 and 200 nm, while, most of the nanowires in 50 nm-diameter holes have been completely etched and only a few nanowires are left due to considerably higher etching by H_2. Therefore, appropriate P_{H2} is critical for transforming pyramidal structures and maintaining nanowire morphology without etching excessively.

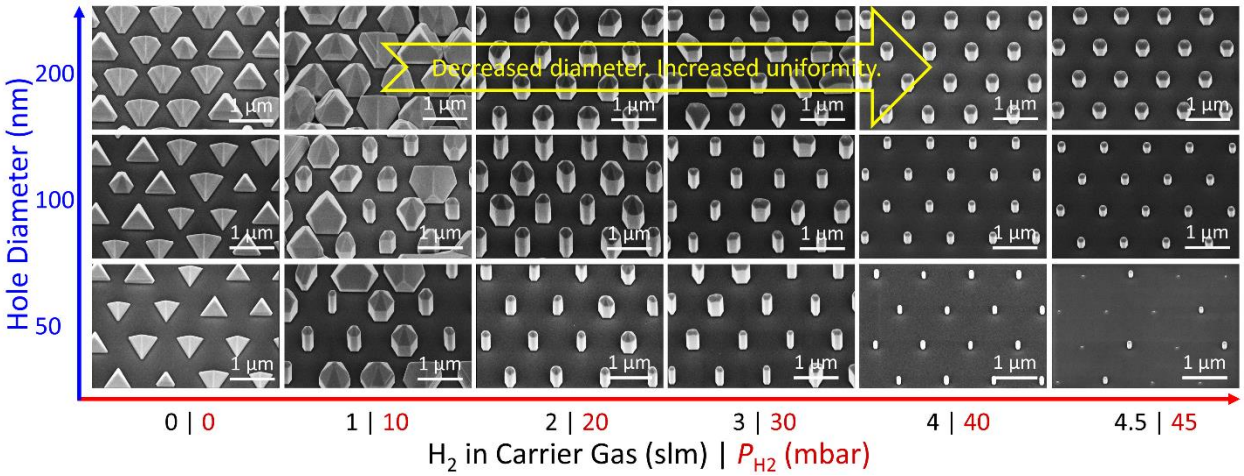

Figure 4.2 Effect of carrier gas composition on the morphology of nanowires for hydrogen partial pressures, P_{H2}, of 0, 10, 20, 30, 40 and 45 mbar. The first column with P_{H2} = 0 indicates growth in pure N_2 carrier gas [30].

4.6. Effect of total gas flow rate

Until now, the effect on GaN nanostructure morphology with partial pressures of TEGa, NH_3 and H_2 has been investigated and discussed. As eq. 4.1 indicates, these partial pressures can be modulated by changing the individual volumetric flow rates. Further, it may also be understood from eq. 4.1 that, changing the total flow rate can also modify the partial pressure. In fact, when the flow rates of TEGa, NH_3 and H_2 are fixed, changing the total flow rate through

the reactor modifies partial pressures of TEGa, NH_3 and H_2 simultaneously. The effect of total gas flow rate during the SAG of GaN nanostructure is investigated using flow rates of 6, 10 and 14 slm. The flow rates for TEGa and NH_3 are fixed at 30 and 10 sccm, respectively. H_2 in the carrier gas is maintained at 40% of the total gas flow rate to ensure a P_{H2} of 40 mbar in this set of experiments to avoid different GaN etching characteristics with variation of P_{H2} as discussed earlier.

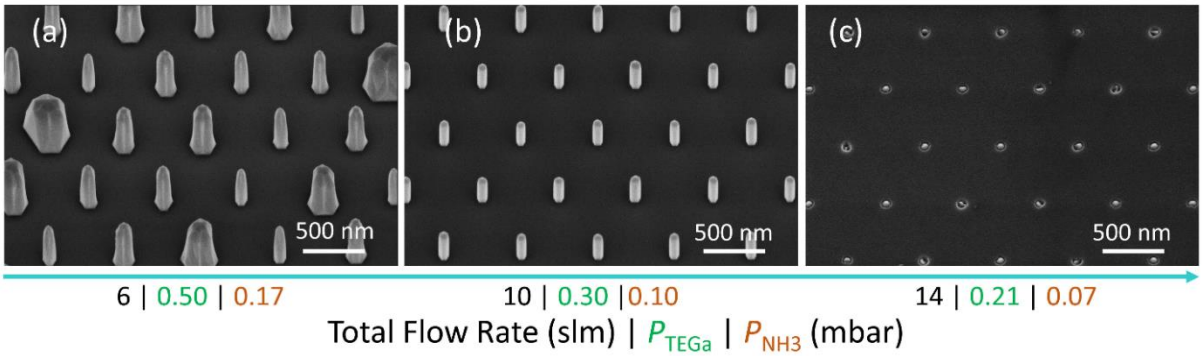

Figure 4.3 GaN nanostructures for total gas flow rates of (a) 6, (b) 10 and (c) 14 slm [30].

Figure 4.3(a – c) shows the morphology of the GaN nanostructures obtained with different total gas flow rates of 6 to 14 slm. Total gas flow rate, F_{Total}, is the denominator in eq 4.1 and implies that a lower F_{total} increases the partial pressure. As the flow rates of TEGa and NH_3 are fixed at 30 and 10 sccm, their respective partial pressures are 0.50 and 0.17 mbar at a total gas flow rate of 6 slm. Preceding discussions have highlighted that increasing P_{TEGa} increases nanowire height and diameter, while passivation of the inclined $\{10\bar{1}1\}$ *r*-planes increases with P_{NH3}. Therefore, nanowires with increased height and diameter with a pyramidal top are obtained for an F_{total} of 6 slm as shown in Figure 4.3(a). At an F_{total} of 10 slm, P_{TEGa} is reduced from 0.50 to 0.30 mbar and P_{NH3} is reduced from 0.17 to 0.10 mbar, compared to the condition with F_{total} of 6 slm. Uniform nanowires with improved aspect ratio are obtained at F_{total} of 10 slm as shown in Figure 4.3(b). Increasing F_{total} to 14 slm results in further dilution of TEGa and NH_3 thereby reducing P_{TEGa} and P_{NH3} to 0.21 and 0.07 mbar, respectively. Figure 4.3(c) shows that majority of the holes are just filled with GaN nucleation seeds, however, no growth is observed due to low P_{TEGa}.

4.7. Effect of pressure

The effect of partial pressures on the moephology of GaN nanostructures with respect to P_{TEGa}, P_{NH3}, P_{H2} and F_{total} have been discussed. The remaining parameter in eq. 4.1 that can

modulate partial pressure is the reactor pressure, $P_{reactor}$. Similar to the case of F_{total}, $P_{reactor}$ can modify the partial pressures of TEGa, NH_3 and H_2 simultaneously. Different $P_{reactor}$ of 50, 100, 200 and 300 mbar have been used to investigate the morphology of the nanostructures. Flow rates of TEGa, NH_3, H_2 and F_{total} are fixed at 30, 10, 4000, and 10,000 sccm, respectively.

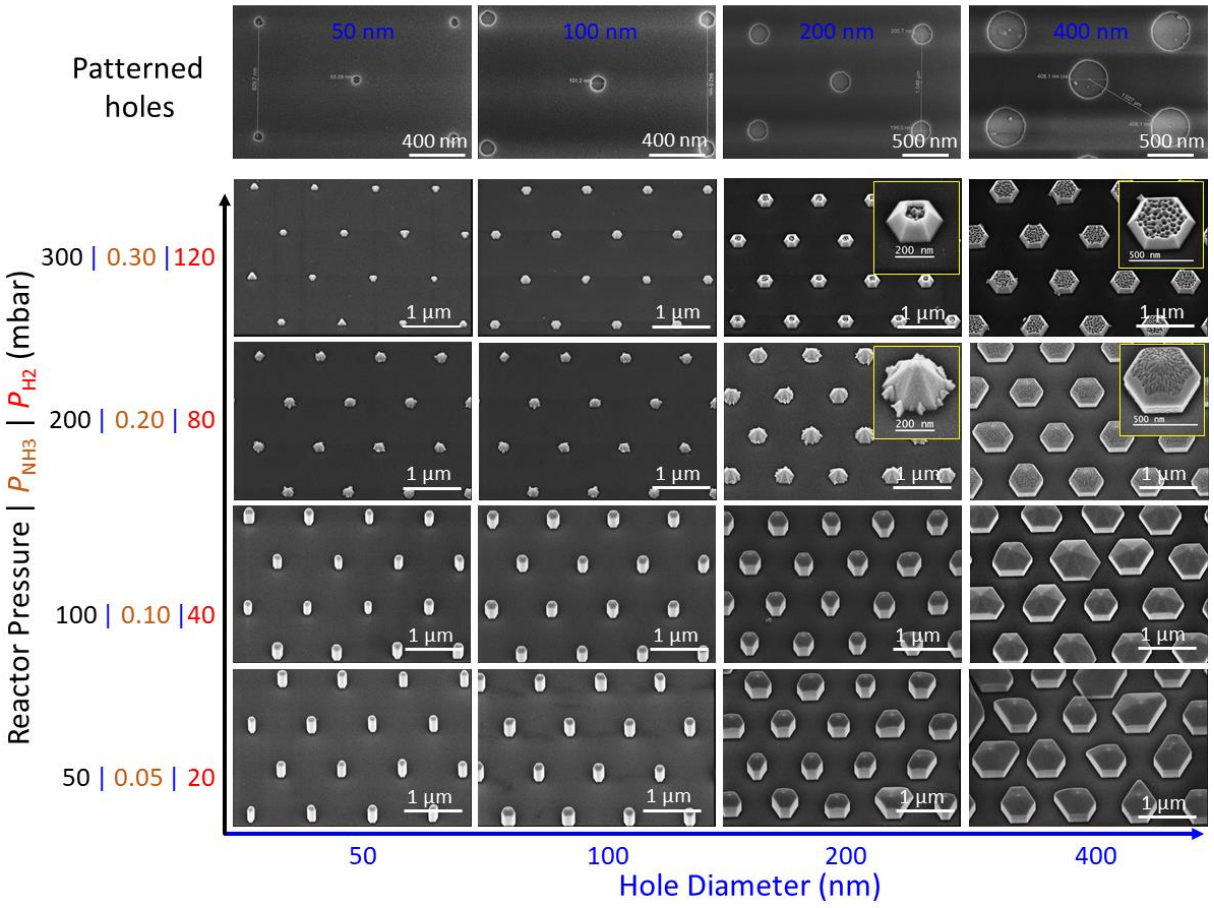

Figure 4.4 Morphology of GaN nanostructures obtained at $P_{reactor}$ of 50, 100, 200, and 300 mbar for various hole diameters of 50 – 400 nm. The top row in this figure shows the SEM image of the patterned holes used for the SAG of GaN nanostructures.

The top row in Figure 4.4 shows the patterned holes with diameters of 50 – 400 nm, used for the SAG of GaN nanostructures. GaN nanostructures obtained at various $P_{reactor}$ on holes of different diameters are also shown in Figure 4.4. From the observed morphology of the GaN nanostructures, the effect of $P_{reactor}$ can be summarised as follows:

$P_{reactor}$ of 50 – 100 mbar: At $P_{reactor}$ of 50 and 100 mbar, nanowires grow in 50 and 100 nm diameter holes, while, the nanostructures exhibit reduced aspect ratio in larger holes with diameters of 200 and 400 nm. Nonetheless, all the nanostructures possess vertical sidewalls

composed of $\{10\bar{1}0\}$ *m*-planes. Another noteworthy fact is that, at the $P_{reactor}$ of 50 mbar, P_{NH3} is a mere 0.05 mbar and such low P_{NH3} can support GaN nanowire growth.

$P_{reactor}$ of 200 mbar: SAG of GaN nanowire at $P_{reactor}$ of 200 mbar exhibits pyramidal structures for hole diameters of 50 to 200 nm. The observation of pyramidal structures in this case may seem to be due to increased P_{NH3}. However, the P_{NH3} is only 0.20 mbar in this case as noted in Figure 4.4, and earlier discussion on the effect of P_{NH3} suggested that either nanowire or prismatic structures with vertical sidewalls should be obtained for P_{NH3} up to 0.25 mbar, and not pyramids. A closer look at the nanostructures on 400 nm diameter holes actually proves that vertical sidewalls are present as expected in accordance with the criteria of P_{NH3}.

Under this growth condition, on the other hand, P_{H2} has reached 80 mbar. The effect of P_{H2} discussed earlier elaborated that majority of the GaN nanostructures on 50 nm diameter holes have been etched at a P_{H2} of 45 mbar. Thus, the P_{H2} of 80 mbar in this growth condition is excessively high to obtain GaN nanowires. Therefore, the observation of pyramidal structure at a P_{reator} of 200 mbar is not due to increased P_{NH3}, but due to the increased P_{H2} and its associated etching of GaN.

$P_{reactor}$ of 300 mbar: Further increasing the $P_{reactor}$ to 300 mbar results in P_{NH3} of 0.30 mbar and P_{H2} of 120 mbar. The GaN nanostructures in this case are either pyramidal, as observed for 50 and 100 nm holes, or displays presence of only inclined sidewalls and without any vertical sidewalls, as observed for 200 and 400 nm holes. At P_{NH3} of 0.30 mbar in this growth condition, which is higher than 0.25 mbar where prismatic structures are obtained, significant passivation of the inclined $\{10\bar{1}1\}$ *r*-planes occurs, and results in the formation of inclined sidewalls only. Further, the top surface of the nanostructures on 200 and 400 nm holes exhibits clear sign of enhanced etching due to the excessively high P_{H2} of 120 mbar. Therefore, low $P_{reactor}$ of 50 to 100 mbar is conducive for selective area growth of GaN nanowires.

4.8. Analysis of TEGa, NH_3 and H_2 partial pressures

GaN nanostructure morphology obtained from investigation on partial pressures of TEGa, NH_3 and H_2 are consolidated into three categories as (*i*) no-growth, (*ii*) nanowire growth, and (*iii*) pyramidal structure formation, as listed in Table 4.1.

The conditions resulting in *no-growth* are listed in Table 4.1 as rows I and II. Under these conditions, nucleation of GaN is observed within the patterned holes, however, no vertical or

pyramidal growth occurs. The amount of nucleation inside the patterned holes increases from 17 to 77% with increasing P_{TEGa} from 0.15 to 0.21 mbar. Considering that P_{NH3} of 0.10 and 0.07 mbar and P_{H2} of 40 mbar in these two cases satisfy the criteria for achieving GaN nanowire morphology, the *no-growth* regime is therefore due to insufficient P_{TEGa}. These growth conditions thus underline the fact that a minimum P_{TEGa} (> 0.21 mbar) needs to be maintained during SAG of GaN.

Table 4.1 Summary of GaN nanostructure morphology with respect to partial pressures.

Row	Vol. Flow, F_X (sccm)		Partial Pressure, P_X (mbar)			V/III	Morphology (Comment)	Section
	TEGa	NH_3	TEGa	NH_3	H_2			
I	15	10	0.15	0.10	40	87	No Growth (Low P_{TEGa})	Effect of TEGa (15 sccm)
II	30	10	0.21	0.07	40	44	No Growth (Low P_{TEGa})	Effect of Total Gas Flow (14 slm)
III	30	10	0.15	0.05	20	44	Nanowire	Effect of Pressure (50 mbar)
IV	30	10	0.30	0.10	40	44	Nanowire	Effect of Pressure (100 mbar)
V	45	10	0.45	0.10	40	29	Nanowire	Effect of TEGa (45 sccm)
VI	30	10	0.50	0.17	40	44	Nanowire	Effect of Total Gas Flow (6 slm)
VII	30	10	0.60	0.20	80	44	Pyramid (High P_{H2})	Effect of Pressure (200 mbar)
VIII	30	25	0.30	0.25	40	109	Pyramid (High P_{NH3})	Effect of NH_3 Flow (25 sccm)
IX	30	10	0.90	0.30	120	44	Pyramid (High P_{NH3})	Effect of Pressure (300 mbar)
X	30	50	0.30	0.50	40	218	Pyramid (High P_{NH3})	Effect of NH_3 Flow (50 sccm)

The conditions satisfying *nanowire* growth have P_{TEGa} ranging from 0.15 to 0.50 mbar and P_{NH3} from 0.05 to 0.17 as listed in rows III to VI. Using eq. 4.1 and considering a $P_{reactor}$ of 100 mbar, and F_{Total} of 10 slm, P_{TEGa} and P_{NH3} may be interpreted into volumetric flow rates. P_{TEGa} of 0.15 to 0.50 mbar correspond to TEGa flow rates of 15 to 50 sccm, and P_{NH3} of 0.05 to 0.17 corresponds to NH_3 flow rates of 5 to 17 sccm. Based on the flow rates of NH_3 and TEGa, the range of V/III ratio for GaN nanowire growth is determined to be from 13 to 74.

Prismatic or *pyramidal* structures are obtained when P_{NH3} is increased beyond 0.20 mbar. At higher P_{NH3}, an increase in passivation of N-terminated $\{10\bar{1}1\}$ inclined planes occur due to

the increased hydrogen available from pyrolysis of NH_3. This passivation leads to slower growth rate of the inclined $\{10\bar{1}1\}$ planes and hence results in pyramidal structures.

Table 4.1 also reveals some more significant aspects in the SAG of GaN nanostructures. First, all three categories of no-growth, nanowire, and pyramidal growth occurs for a V/III ratio of 44. Therefore, a low V/III ratio is a necessary but not sufficient criteria to achieve GaN nanowires. Second, growth conditions in rows I and III uses the same P_{TEGa} of 0.15 mbar and row I has no-growth while row III exhibits nanowire growth. This discrepancy is a consequence of the different GaN decomposition rate associated with different P_{H2} in these two growths (40 and 20 mbar). Therefore, partial pressures of TEGa, NH_3 and H_2 play a crucial role in the SAG of GaN nanostructures.

Verification of analysis and summary

From the investigation of partial pressures, the range of P_{TEGa} for nanowire growth is determined as 0.30 to 0.50 mbar, and that of P_{NH3} as 0.05 to 0.17 mbar. In order to verify and ascertain the analysis of GaN nanowire growth through partial pressures, two more growth experiments are carried out with P_{NH3} of 0.06 and 0.16 mbar, while P_{TEGa} and P_{H2} are maintained at 0.40 and 40 mbar, respectively. The growth duration, $P_{Reactor}$, and F_{Total} are fixed at 15 minutes, 100 mbar and 10 slm in both experiments.

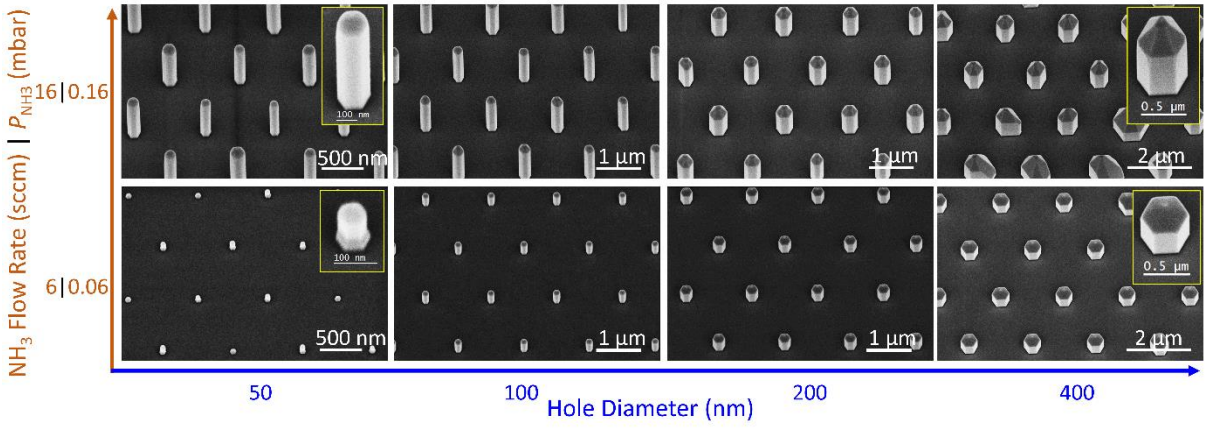

Figure 4.5 Morphology GaN nanowires for NH_3 flow rates of 6 and 16 sccm, corresponding to P_{NH3} of 0.06 and 0.16 mbar, respectively.

Figure 4.5 shows the SEM images of nanowires obtained with P_{NH3} of 0.06 and 0.16 mbar. Nanowire growth is observed for both lower and upper limit of P_{NH3} and therefore confirms the validity of interpreting GaN nanowire growth using partial pressures. It is noteworthy that the

limit of NH_3 flow rates from 6 to 16 sccm, which is necessary for achieving GaN nanowire morphology is a very small parameter window. This is in contrast to the requirement of NH_3 flow rates of several 1000s during the growth of planar GaN. For instance, NH_3 flow rate of 5000 sccm is used during the planar GaN growth in the same MOCVD reactor while preparing the GaN pseudo-substrate.

Shorter nanowires are obtained for low P_{NH3} of 0.06 mbar and longer nanowires are obtained at higher P_{NH3} of 0.16 mbar while P_{TEGa}, P_{H2} and growth duration are the same. This implies that grow rate of GaN nanowires is limited by P_{NH3}. In other words, this proves that Ga-rich conditions, which were mentioned in the introduction, are required for GaN nanowire growth. Further, the inclination angle of semipolar planes on top of the GaN nanostructures are different for P_{NH3} of 0.06 and 0.16 mbar as can be seen from the inset of 400 nm features in Figure 4.5. This implies that the availability of hydrogen from NH_3 pyrolysis controls the creation of a specific semipolar plane.

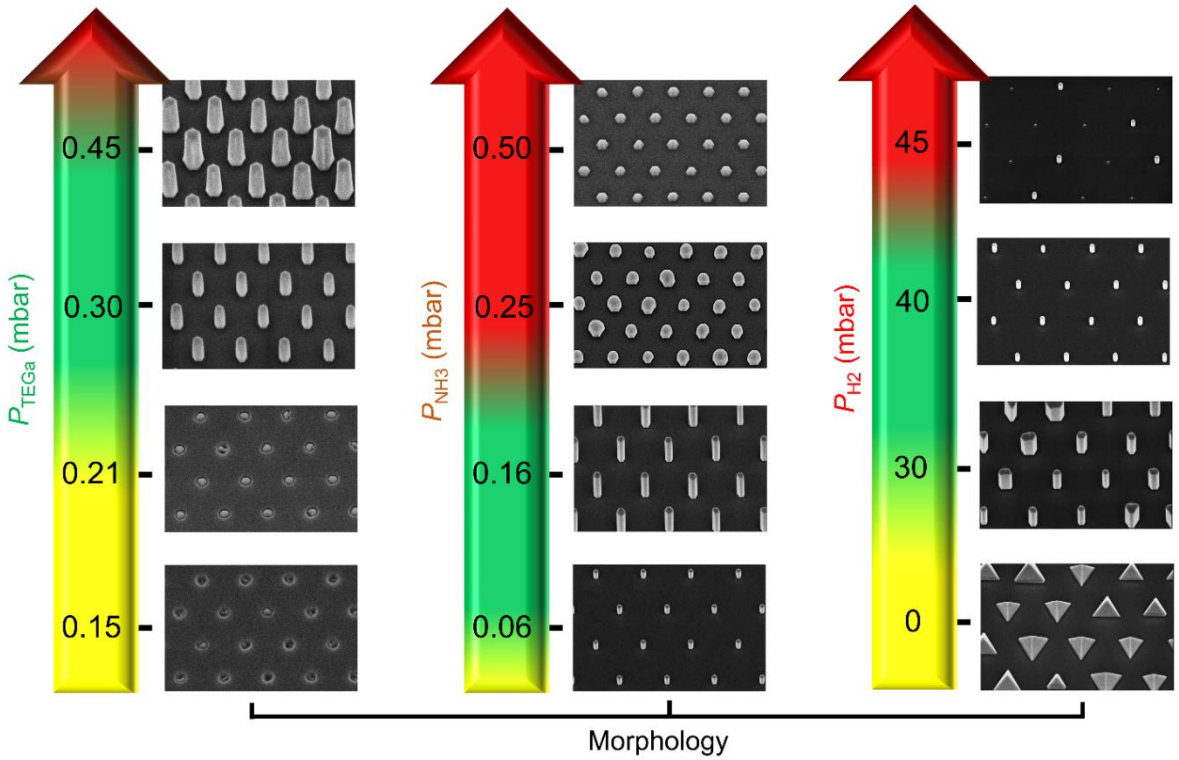

Figure 4.6 GaN nanostructure morphology with respect to P_{TEGa}, P_{NH3}, and P_{H2}, highlighting the insufficient (yellow), optimal (green) and excessive (red) values of P_{TEGa}, P_{NH3} and P_{H2}.

Different sets of SAG experiments have been conducted to identify the growth parameters of Ga-polar GaN nanowires with MOCVD. A close relationship has been established between

GaN nanostructure morphology with partial pressures of TEGa, NH_3 and H_2 and is shown in Figure 4.6. A general trend of *insufficient*, *optimal*, and *excessive* value is observed with each of P_{TEGa}, P_{NH3} and P_{H2} and is identified by *yellow*, *green*, and *red* regions on the vertical axis, respectively.

Therefore, the role of P_{TEGa}, P_{NH3}, and P_{H2} in the SAG of GaN nanowires can be summarised as follows:

***P_{TEGa}*:** GaN nanowire growth does not occur for $P_{TEGa} \leq 0.21$ mbar due to inadequate Ga precursor. Growth of uniform GaN nanowires is observed under the condition $0.30 \leq P_{TEGa} \leq 0.45$ mbar. It is anticipated that increasing P_{TEGa} above 0.50 mbar will result in significant increase of nanowire diameter and risk coalescence between the nanowires.

***P_{NH3}*:** GaN nanowire growth is hindered at a low P_{NH3} of 0.06 mbar and any lower P_{NH3} value may be insufficient for GaN nanowire growth. The condition for obtaining uniform GaN nanowires is about $0.05 \leq P_{NH3} \leq 0.17$ mbar. Higher P_{NH3} values above 20 mbar leads to prismatic or pyramidal structures.

***P_{H2}*:** At $P_{H2} = 0$, pure pyramidal structures are obtained due to lack of GaN etching and gradually increasing transformation towards uniform nanowire occurs for $P_{H2} \leq 40$ mbar. However, excessive etching of GaN nanostructure occurs at $P_{H2} \geq 45$ mbar and results in decreased height, leading up to missing nanowires due to complete etching.

4.9. Effect of growth temperature

4.9.1. Single-temperature growth

In addition to the partial pressures discussed in the preceding sections, growth temperature plays a crucial role in SAG of GaN nanowires. GaN nanowires grown at higher temperature have been reported to show enhanced vertical growth, reduced lateral growth and improved uniformity, however, growth at elevated temperature above the optimal temperature resulted in roughened $\{10\bar{1}0\}$ *m*-plane sidewalls [26]. Within the permissible temperature window for GaN nanowire growth, higher temperature is reported to aid in flattening of the nanowire tip by increasing the growth rate anisotropy of (0001) *c*-plane with respect to inclined $\{10\bar{1}1\}$ *r*-planes [19]. The effect of growth temperature on GaN nanowire morphology is investigated by carrying out SAG at growth temperatures of 933, 955 and 986 °C.

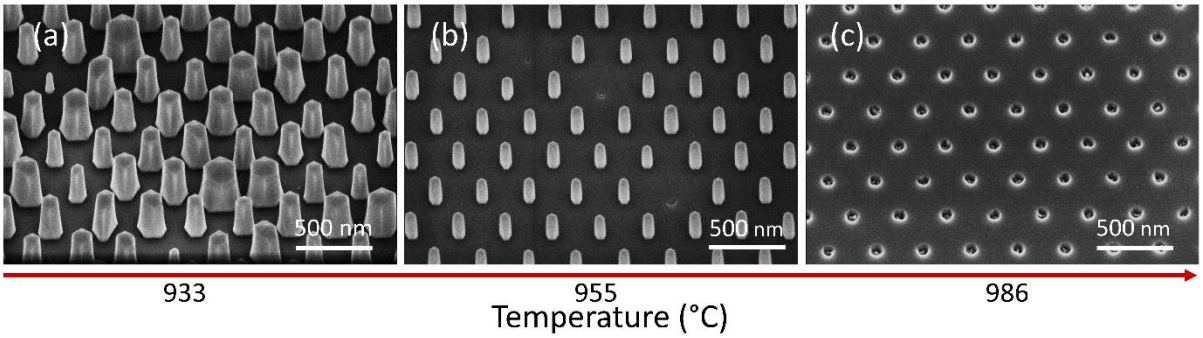

Figure 4.7 Morphology of GaN nanostructures at the growth temperature of (a) 933, (b) 955, and (c) 986 °C [30].

Figure 4.7 shows the GaN nanostructures obtained using single-temperature growth at 933, 955 and 986 °C. At a growth temperature of 933 °C, nanowire growth occurs from all of the holes, however, the diameter is non-uniform at this low growth temperature as shown in Figure 4.7(a). Several coalesced islands are also frequently observed in the case of low growth temperature. SAG at a growth temperature to 955 °C results in increased aspect ratio of GaN nanowires and significantly improved uniformity across the array, however, nanowire growth is absent from a few holes as shown in Figure 4.7(b). At a growth temperature of 986 °C, nanowire growth is not observed anymore due to excessive thermal decomposition as shown in Figure 4.7(c). It is inferred from these results that uniform GaN nanowire growth may be achieved by employing a two-temperature growth. A low-temperature growth (≈ 933 °C) at initial stage to achieve uniform nucleation from all the holes, followed by a high-temperature growth (≈ 955 °C) to achieve uniform nanowires. The two-temperature growth method is discussed in the following section.

4.9.2. Two-temperature growth

In the two-temperature SAG of GaN, a low-temperature growth is carried out for 90 seconds to fill up all of the holes, which is then followed by a temperature ramp of ~10 – 15 °C in 60 seconds while the growth continues. Three growth experiments are carried at $_{940}$949, $_{945}$957 and $_{949}$965 °C. The subscripts represent the temperature for the initial growth step.

Figure 4.8 shows SEM images of GaN nanostructures for two-temperature SAG. For each hole diameter, nanowires with poor uniformity across the array occurs at lower growth temperatures for large diameter holes. On the other hand, decomposition rate of GaN nanowires

is enhanced above the optimal growth temperature and results in prismatic or pyramidal nanostructures.

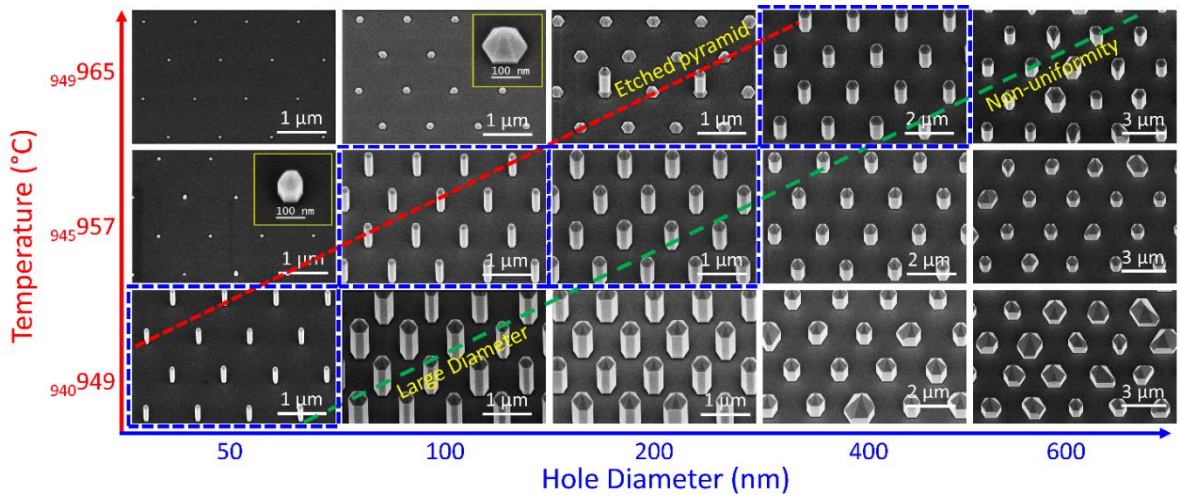

Figure 4.8 Morphology of Ga-polar GaN nanostructures from two-temperature growth for different hole diameters. Optimal nanowire morphologies are highlighted with blue rectangles, while red and green dashed lines serve as a guide to the eye for optimal growth window.

Figure 4.8 also reveals the requirement of a systematic increase in growth temperature with hole diameter. The optimal growth temperatures for GaN nanowires on 50, 100, 200 and 400 nm holes are determined to be about 949, 955, 957, and 965 °C, respectively. Higher growth temperatures required for achieving uniform nanowires on larger hole diameters is due to the fact that uniformity of GaN nanowire is primarily controlled by GaN decomposition. Earlier discussion on the effect of P_{H2} has elaborated the necessity of GaN decomposition with increased P_{H2} to achieve uniform GaN nanowires across the array. It should be noted that GaN decomposition increases with temperature and P_{H2} [35], and moreover, GaN nanowire decomposition strongly depends on temperature [36]. Therefore, growth temperature plays an important role in determining the uniformity of GaN nanowires.

Table 4.2 Diameter and height of GaN nanowires with their corresponding standard deviations.

Hole Diameter		50 nm		100 nm		200 nm		400 nm	
Nanowire Dimensions (nm)		Diameter	Height	Diameter	Height	Diameter	Height	Diameter	Height
Growth Temp. (°C)	965							506.4±10.5	1096.8±25.6
	957			164.3±5.2	719.1±19.7	287.1±7.1	734.7±10.1	545.6±12.2	809.4±23.1
	949	104.0±4.7	512.0±16.5	333.2±41.7	1054.4±19.1	407.1±36.1	896.8±20.3	773.7±165.5	707.8±69.7

From the nanowires obtained with two-temperature SAG experiments, the nanowire dimensions along with their corresponding standard deviations have been determined using the image analysis software ImageJ [37] and are listed in Table 4.2. The deviations of the nanowire dimensions are determined from the 16 nanowires in each set of growth (Figure 4.8). For each set of growth condition, height and diameter of every individual nanowire are measured and then the standard deviation is calculated based on the measured values of heights and diameters of the 16 nanowires.

Increase in growth temperature significantly improves the uniformity of nanowire diameter across the array as can be inferred from marked reductions in standard deviations of the diamters. For instance, in the case of 100 nm patterned holes, the standard deviation of the diameter decreased from 41.7 nm to a mere 5.2 nm on increasing the growth temperature from 949 °C to 957 °C. From these experiments, it is evident that different hole diameters, and consequently different nanowire diameters, require different growth temperatures. Therefore, a specific growth temperature needs to be set for a specific hole diameter. The relationship between the hole diameter, d (nm), and the required growth temperature, T (°C), to achieve uniform array of GaN nanowires has been determined as:

$$T = 0.04d + 948.7 \tag{4.2}$$

Eq. (4.2) signifies that the growth temperature required for SAG of GaN nanowires increase linearly from smaller to larger hole diameters. Substituting the hole diameters of 50 and 200

nm in Eq (4.2) yields the required growth temperatures of 951 °C for 50 nm holes and 965 °C for 200 nm holes. Therefore, Eq (4.2) provides a pre-emptive knowledge for the required growth temperature to be set for the specific hole diameters on the substrate.

4.10. Annealing of GaN nanowires

Ga-polar GaN nanowire normally exhibits a pyramidal or truncated pyramidal top, whereas N-polar GaN nanowire has a flat top. The pyramidal top of Ga-polar GaN pose a hurdle for incorporating vertical heterostructures such as axial quantum wells. The pyramidal top of Ga-polar GaN nanowires can be reshaped to flat top by annealing theme in N_2+NH_3 ambient as shown in Figure 4.9. The annealing experiment is carried out at a temperature of 980 °C for 10 minutes using 2000 sccm of NH_3 and 8000 sccm of N_2. Yoshida *et al.* have reported that addition of NH_3 in an otherwise N_2 ambient enhances decomposition of (0001) +*c* - plane while decomposition of $(000\bar{1})$ -*c*-plane and $\{10\bar{1}0\}$ *m*-planes are suppressed [38]. Therefore, GaN nanowires with flat top morphology, suitable for axial heterostructures, can be obtained by an annealing step in N_2+NH_3 environment after growth.

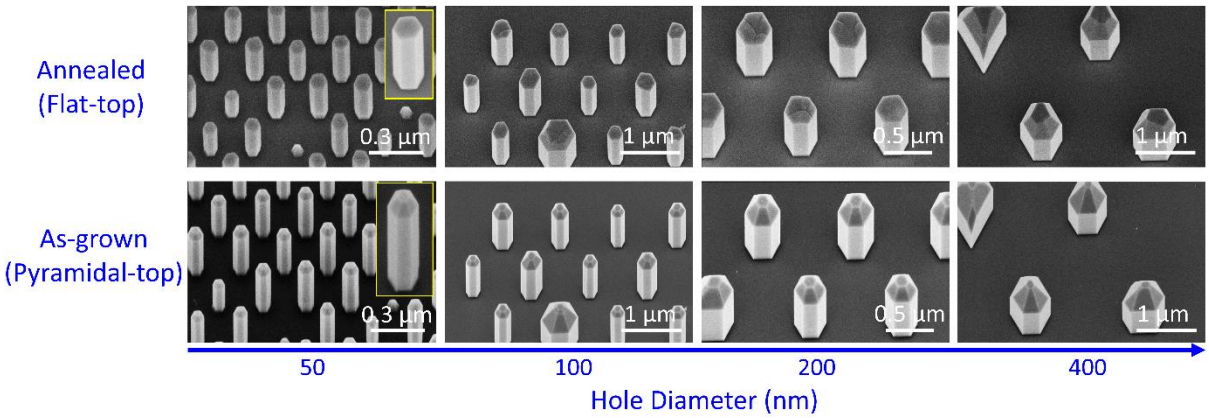

Figure 4.9 As-grown Ga-polar GaN nanowires with truncated pyramidal top (bottom row), and reshaped GaN nanowire with flat top upon annealing in N_2+NH_3 (top row).

4.11. Sub-100 nm diameter GaN nanowires and characterisation with TEM

Using the criteria of partial pressures and growth temperature set out above for SAG of GaN nanowires, sub-100 nm GaN nanowires have been grown as shown in Figure 4.10 (a). Measurement from 26 such nanowires showed that height and diameter are 962.5±39.3 nm and 86.1±10.1 nm, respectively. A low-resolution TEM image consisting of an array of such nanowires is shown in Figure 4.10 (b). Weak-beam dark-field (WBDF) TEM images of two

such nanowires are shown as Figure 4.10 (c) and (d). WBDF images are taken close to the $[11\bar{2}0]$ zone axis with g = (0002). Figure 4.10 (c) illustrates the case of dislocation filtering in which threading dislocation present in the GaN pseudo-substrate is masked-off in SAG and nanowire growth occurs from dislocation-free areas. From the array, a nanowire is found to grow exactly above a threading dislocation as shown in Figure 4.10 (d). Interestingly, the threading dislocation does not propagate through the nanowire, confirming the dislocation-free nature of selective area grown GaN nanowires even though they are grown on GaN pseudo-substrate with threading dislocations of the order of 10^8-10^9 cm^{-2}.

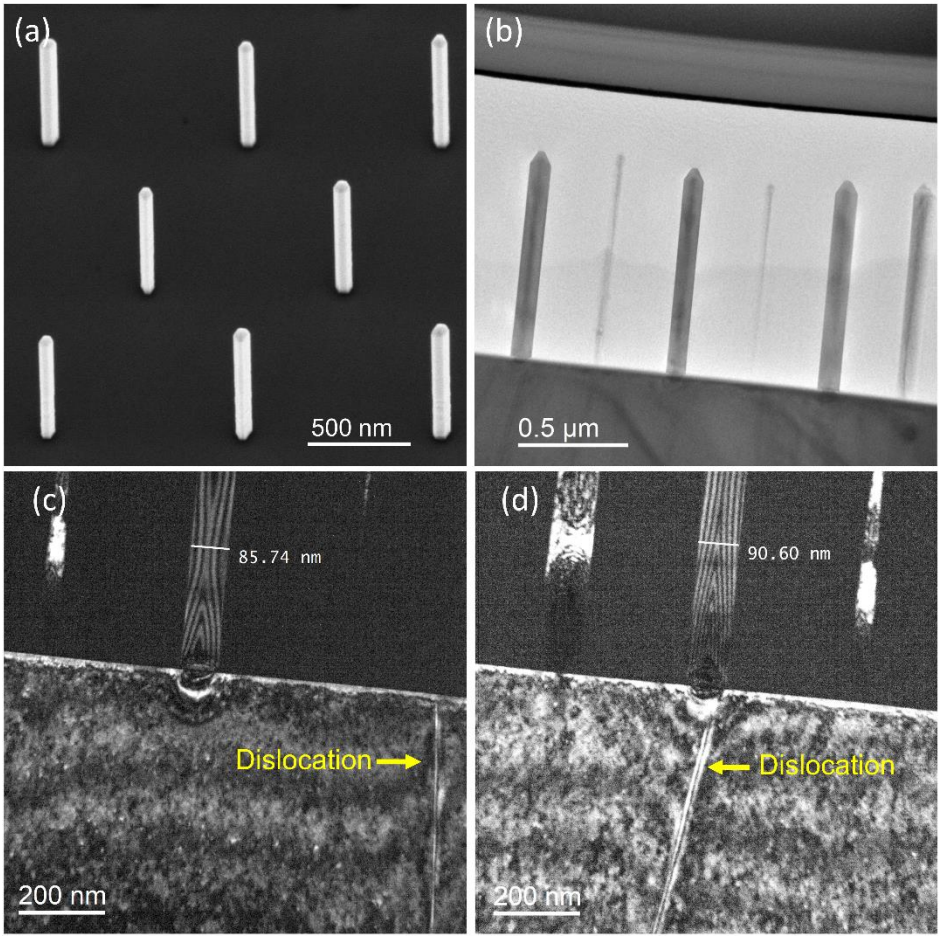

Figure 4.10 (a) SEM image of sub-100 nm GaN nanowires, (b) low-resolution TEM image of GaN nanowire array. (c, d) weak beam dark-field images of a GaN nanowire grown away from and above a threading dislocation.

4.12. Silicon doping of GaN nanowires and cathodoluminescence characterisation

Si is a well-known n-type dopant for GaN and SiH_4 is used as the precursor of Si. Addition of SiH_4 during GaN nanowire growth is known to enhance the vertical growth rate of the

nanowires [22, 39-41]. Si doping of GaN nanowires is reported to result in the formation of a SiN layer preferentially on the *m*-plane sidewalls, which aids in vertical growth by promoting Ga adatom diffusion to the top (0001) plane as well as by inhibiting further growth of *m*-plane [23, 40]. On a different note, the enhancement in vertical growth of GaN nanowire with Si doping has been suggested to be due to an enhanced reaction on the top *c*-plane of the nanowires [42].

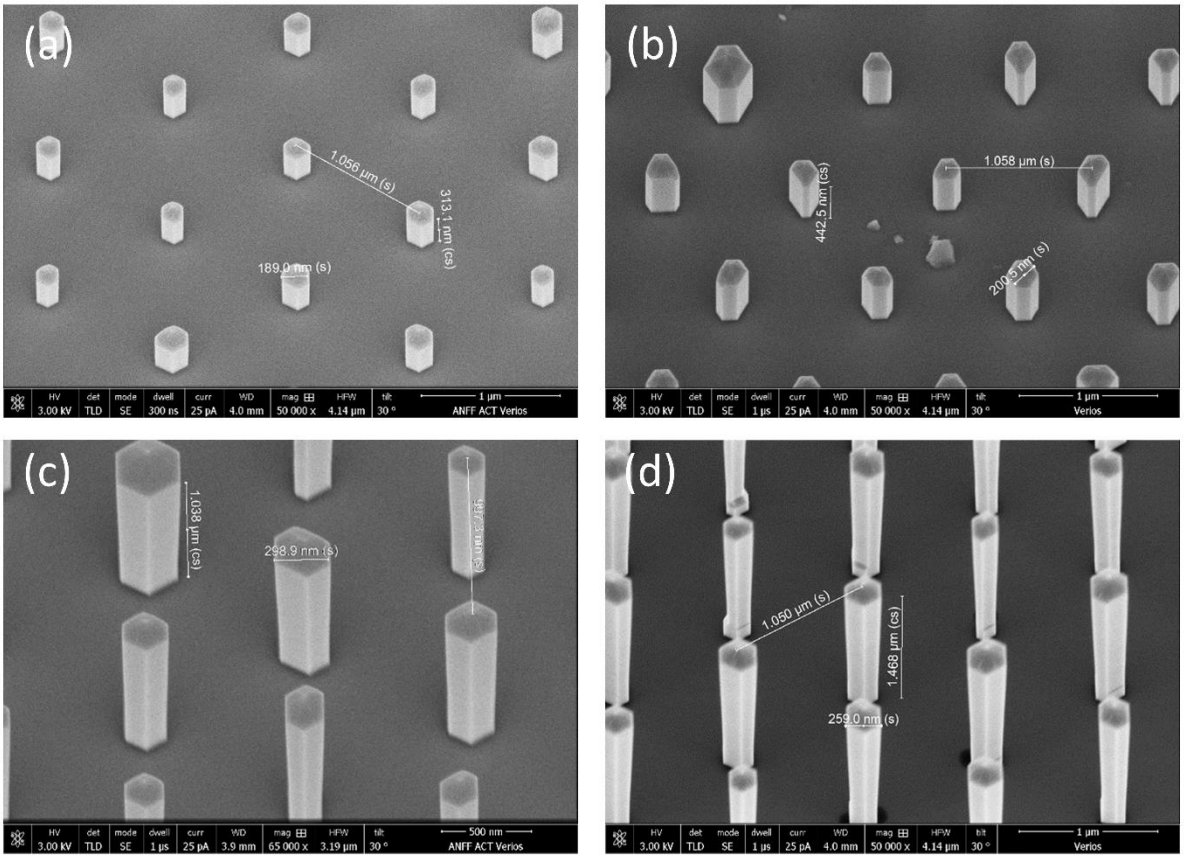

Figure 4.11 Morphology GaN nanowires grown with various SiH_4 flows rates of (a) 0, (b) 25, (c) 50 and (d) 75 sccm, corresponding to 0, 50, 100 and 150 nmol/min, respectively.

Table 4.3 GaN nanowire growth rate with SiH_4.

SiH_4 (sccm)	Height (nm)	Vert. Growth Rate (nm/min)	Remark on growth enhancement
0	312	15.6	Insignificant
25	442	22.1	
50	1038	51.9	Significant
75	1468	73.4	

Si doping experiments are carried out with four different SiH_4 flow rates of of 0, 25, 50 and 75 sccm corresponding to 0, 50, 100 and 150 nmol/min, respectively. The growth is divided into two steps: the first 200 seconds of growth is carried out without SiH_4 flow at ~940 °C and then the following 1000 seconds of growth with SiH_4 flow at ~955 °C.

Figure 4.11 shows the morphology of GaN nanowires for various SiH_4 flow rates. The observation of GaN nanowires may be classified into two regimes as- insignificant and significant vertical growth rate enhancement. When the SiH_4 flow is 50 nmol/min or below, the enhancement on the vertical growth rate of GaN nanowire is insignificant and the height is similar to that of the undoped one as shown in Figure 4.11 (a) and (b). However, marked changes in the vertical growth rates are observed on increasing the SiH_4 flow rate to 100 and 150 nmol/min and the nanowires achieved heights of 1.038 and 1.468 μm, respectively, for the similar growth conditions with vertical growth rates exceeding 50 nm/min as listed in Table 4.3.

Another growth experiment involving Si doping of GaN nanowires is carried out. The first 10 minutes of growth without SiH_4 flow is followed by 10 minutes of growth with a SiH_4 flow rate of 150 nmol min^{-1}. Figure 4.12(a) shows the SEM image of a GaN nanowire transferred to a Si substrate from this growth experiment. Panchromatic cathodoluminescence (CL) image of this nanowire is shown as Figure 4.12(b). The panchromatic image shows two regions of distinct brightness. The short bright region at the bottom corresponds to GaN nanowire growth without Si doping, while the remaining longer portion of the nanowire with darker contrast corresponds to the growth with Si doping. As discussed earlier, the growth rate of nanowire is

significantly enhanced with Si doping, however, such highly doped region exhibits lower CL intensity.

The adverse effect of heavy Si doping is reported to show up as decrease in PL intensity due to increased non-radiative recombination centres, broadening of the FWHM and a blue shift of the near-band-edge (NBE) due to band-filling effect [42]. Therefore, despite the enhancement in vertical growth rate, Si doping leads to lower CL intensity.

Figure 4.12(c) shows the CL spectrum of the GaN nanowire. A peak emission wavelength of 366 nm, corresponding to 3.4 eV of GaN bandgap is observed. Notably, the higher intensity of emission for NBE compared to the yellow luminescence centred around 550 nm confirms the overall good quality of the GaN nanowire.

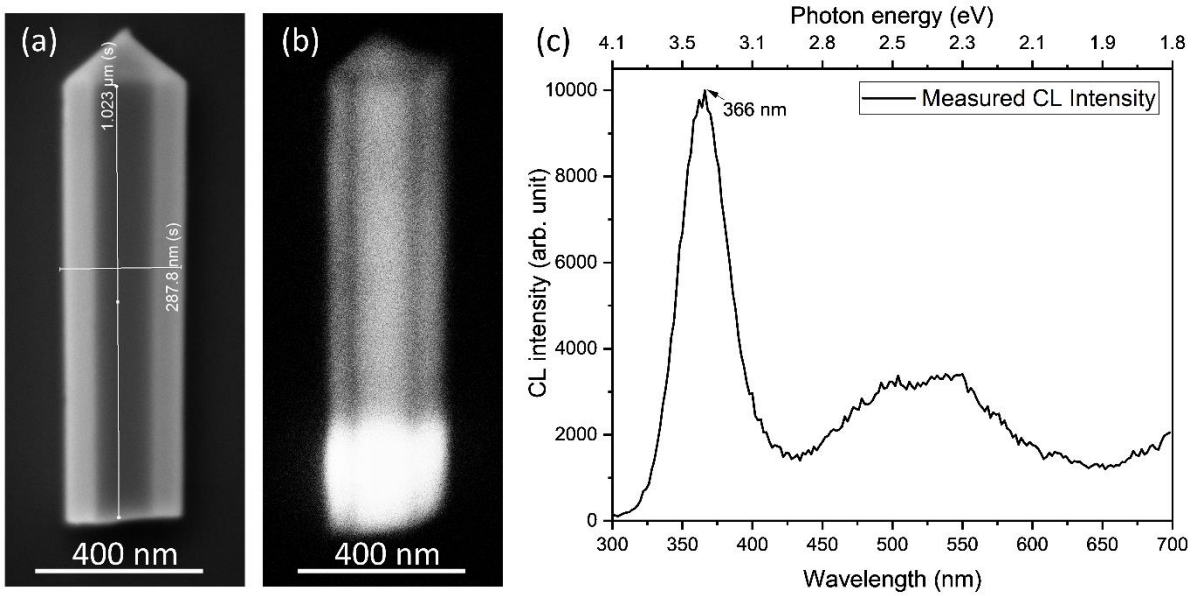

Figure 4.12 (a) SEM image of a GaN nanowire grown with Si doping. (b) Panchromatic CL image of the same nanowire showing the undoped and Si-doped regions. (c) CL spectrum obtained from the Ga-polar GaN nanowire.

4.13. Summary

SAG of Ga-polar GaN nanowires has been carried out using MOCVD. Analysis of GaN nanostructure morphology has been carried out through partial pressures of TEGa, NH_3 and H_2. The effect of P_{TEGa}, P_{NH3}, and P_{H2} on the GaN nanostructure morphology has been investigated by changing each partial pressure individually by modulating the individual flow rate, as well as by changing them simultaneously through changing the total flow rate and reactor pressure.

Increasing P_{TEGa} results in increased height and diameter of nanowires, thus P_{TEGa} has an additive effect in the SAG of GaN nanowires. The optimal range of P_{TEGa} has been determined as 0.30 to 0.50 mbar.

P_{NH3}, on the other hand, has a very narrow range of 0.05 to 0.17 mbar for GaN nanowire growth, and within this limit, nanowire height increases with P_{NH3} and can be considered as additive. However, increasing P_{NH3} above 0.20 mbar leads to increased formation of N-H bonds due to increased availability of hydrogen from NH_3 dissociation and significantly passivates the $\{10\bar{1}1\}$ inclined planes, ultimately resulting in pyramidal structures without any vertical sidewalls. Therefore, P_{NH3} has as an additive effect as well as subtractive effect with respect to GaN nanowire growth.

Hydrogen in the carrier gas is necessary for GaN nanowire growth. Without H_2 in the carrier gas, only pyramidal structures bound by inclined $\{10\bar{1}1\}$ facets are obtained. H_2 aids in preferential etching of $\{10\bar{1}1\}$ inclined planes due to the highest density of dangling bonds on these planes compared to top (0001) *c*-plane and vertical $\{10\bar{1}0\}$ sidewall facets. The optimal value of P_{H2} for GaN nanowire growth is determined as 40 mbar.

Growth temperature plays a pivotal role in obtaining nanowires with uniform diameter across the array. A two-temperature growth method is found to be suitable for GaN nanowire growth with lower growth temperature for nanowires with smaller diameters and higher temperature for larger diameters. In addition to growth, high temperature (980 °C) annealing of GaN nanowires in N_2+NH_3 environment inside the MOCVD can reshape the truncated pyramidal structure at the top of GaN nanowires to a flat top, suitable to incorporation of axial heterostructures.

Transmission electron microscopy studies have confirmed the elimination of threading dislocations in selective area-grown GaN nanowires. The absence of threading dislocations in GaN nanowires make them a potential candidate for high-efficiency devices. Si doping experiments have confirmed the enhancement in vertical growth rate of GaN nanowires. However, Si doping reduces the emission intensity of GaN nanowires in CL. Good quality GaN nanowire growth has been confirmed by higher intensity of NBE emission compared the yellow luminescence.

Overall, a remarkable relationship has been established between the observed morphology and partial pressures of TEGa, NH_3 and H_2 during the SAG of GaN nanowires at a particular

growth temperature. Therefore, all of the selective area growth parameters for GaN nanowires in MOCVD can be reduced to just two parameters (*i*) partial pressures and (*ii*) growth temperature. Based on the range of TEGa and NH_3 partials pressures, the optimal range of V/III ratio for GaN nanowire growth has been determined as 13 to 73. However, it should be noted that V/III ratio is not a sufficient criterion to determine GaN nanowire growth, but partial pressures and temperature are the key parameters that determine GaN nanostructure morphology. Hence, this study has uncovered ways to obtain specific GaN nanostructures, more specifically, Ga-polar GaN nanowires, based on partial pressures and growth temperature.

References

1. Nakamura, S., Mukai, T. and Senoh, M., "High-brightness InGaN/AlGaN double-heterostructure blue-green-light-emitting diodes." *Journal of Applied Physics*, **1994**, 76, 8189-8191.

2. Nakamura, S., Senoh, M., Iwasa, N. and Nagahama, S.-i., "High-Brightness InGaN Blue, Green and Yellow Light-Emitting Diodes with Quantum Well Structures." *Japanese Journal of Applied Physics*, **1995**, 34, L797.

3. Nakamura, S., Senoh, M., Iwasa, N., Nagahama, S.-i., Yamada, T., et al., "Superbright Green InGaN Single-Quantum-Well-Structure Light-Emitting Diodes." *Japanese Journal of Applied Physics*, **1995**, 34, L1332.

4. Yan, R., Gargas, D. and Yang, P., "Nanowire photonics." *Nature Photonics*, **2009**, 3, 569-576.

5. Eaton, S.W., Fu, A., Wong, A.B., Ning, C.-Z. and Yang, P., "Semiconductor nanowire lasers." *Nature Reviews Materials*, **2016**, 1, 16028.

6. Haverkort, J.E.M., Garnett, E.C. and Bakkers, E.P.A.M., "Fundamentals of the nanowire solar cell: Optimization of the open circuit voltage." *Applied Physics Reviews*, **2018**, 5, 031106.

7. Jia, C., Lin, Z., Huang, Y. and Duan, X., "Nanowire Electronics: From Nanoscale to Macroscale." *Chemical Reviews*, **2019**, 119, 9074-9135.

8. Chen, H., Liu, K., Hu, L., Al-Ghamdi, A.A. and Fang, X., "New concept ultraviolet photodetectors." *Materials Today*, **2015**, 18, 493-502.

9. Dasgupta, N.P., Sun, J., Liu, C., Brittman, S., Andrews, S.C., et al., "25th Anniversary Article: Semiconductor Nanowires – Synthesis, Characterization, and Applications." *Advanced Materials*, **2014**, 26, 2137-2184.

10. Zhang, A. and Lieber, C.M., "Nano-Bioelectronics." *Chemical Reviews*, **2016**, 116, 215-257.

11. Hersee, S.D., Sun, X. and Wang, X., "The Controlled Growth of GaN Nanowires." *Nano Letters*, **2006**, 6, 1808-1811.

12. Sekiguchi, H., Kishino, K. and Kikuchi, A., "Ti-mask Selective-Area Growth of GaN by RF-Plasma-Assisted Molecular-Beam Epitaxy for Fabricating Regularly Arranged InGaN/GaN Nanocolumns." *Applied Physics Express*, **2008**, 1, 124002.

13. Choi, K., Arita, M. and Arakawa, Y., "Selective-area growth of thin GaN nanowires by MOCVD." *Journal of Crystal Growth*, **2012**, 357, 58-61.

14. Alloing, B. and Zúñiga-Pérez, J., "Metalorganic chemical vapor deposition of GaN nanowires: From catalyst-assisted to catalyst-free growth, and from self-assembled to selective-area growth." *Materials Science in Semiconductor Processing*, **2016**, 55, 51-58.

15. Koleske, D.D., Wickenden, A.E., Henry, R.L., DeSisto, W.J. and Gorman, R.J., "Growth model for GaN with comparison to structural, optical, and electrical properties." *Journal of Applied Physics*, **1998**, 84, 1998-2010.

16. Van de Walle, C.G. and Neugebauer, J., "Structure and energetics of nitride surfaces under MOCVD growth conditions." *Journal of Crystal Growth*, **2003**, 248, 8-13.

17. Northrup, J.E. and Neugebauer, J., "Strong affinity of hydrogen for the GaN $(000\bar{1})$ surface: Implications for molecular beam epitaxy and metalorganic chemical vapor deposition." *Applied Physics Letters*, **2004**, 85, 3429-3431.

18. Feenstra, R.M., Dong, Y., Lee, C.D. and Northrup, J.E., "Recent developments in surface studies of GaN and AlN." *Journal of Vacuum Science & Technology B*, **2005**, 23, 1174-1180.

19. Lin, Y.-T., Yeh, T.-W., Nakajima, Y. and Dapkus, P.D., "Catalyst-Free GaN Nanorods Synthesized by Selective Area Growth." *Advanced Functional Materials*, **2014**, 24, 3162-3171.

20. Colvin, J., Ciechonski, R., Lenrick, F., Hultin, O., Khalilian, M., et al., "Surface and dislocation investigation of planar GaN formed by crystal reformation of nanowire arrays." *Physical Review Materials*, **2019**, 3, 093604.

21. Chen, X.J., Gayral, B., Sam-Giao, D., Bougerol, C., Durand, C., et al., "Catalyst-free growth of high-optical quality GaN nanowires by metal-organic vapor phase epitaxy." *Applied Physics Letters*, **2011**, 99, 251910-3.

22. Wang, X., Li, S., Mohajerani, M.S., Ledig, J., Wehmann, H.-H., et al., "Continuous-Flow MOVPE of Ga-Polar GaN Column Arrays and Core–Shell LED Structures." *Crystal Growth & Design*, **2013**, 13, 3475-3480.

23. Hartmann, J., Wang, X., Schuhmann, H., Dziony, W., Caccamo, L., et al., "Growth mechanisms of GaN microrods for 3D core–shell LEDs: The influence of silane flow." *physica status solidi (a)*, **2015**, 212, 2830-2836.

24. Mohajerani, M.S., Khachadorian, S., Schimpke, T., Nenstiel, C., Hartmann, J., et al., "Evaluation of local free carrier concentrations in individual heavily-doped GaN:Si micro-rods by micro-Raman spectroscopy." *Applied Physics Letters*, **2016**, 108, 091112.

25. Schimpke, T., Mandl, M., Stoll, I., Pohl-Klein, B., Bichler, D., et al., "Phosphor-converted white light from blue-emitting InGaN microrod LEDs." *physica status solidi (a)*, **2016**, 213, 1577-1584.

26. Coulon, P.M., Alloing, B., Brändli, V., Lefebvre, D., Chenot, S., et al., "Selective area growth of Ga-polar GaN nanowire arrays by continuous-flow MOVPE: A systematic study on the effect of growth conditions on the array properties." *physica status solidi (b)*, **2015**, 252, 1096-1103.

27. Müller, M., Veit, P., Krause, F.F., Schimpke, T., Metzner, S., et al., "Nanoscopic Insights into InGaN/GaN Core–Shell Nanorods: Structure, Composition, and Luminescence." *Nano Letters*, **2016**, 16, 5340-5346.

28. Li, S.F., Fuendling, S., Wang, X., Merzsch, S., Al-Suleiman, M.A.M., et al., "Polarity and Its Influence on Growth Mechanism during MOVPE Growth of GaN Sub-micrometer Rods." *Crystal Growth & Design*, **2011**, 11, 1573-1577.

29. Northrup, J.E. and Neugebauer, J., "Theory of GaN $(10\bar{1}0)$ and $(11\bar{2}0)$ surfaces." *Physical Review B*, **1996**, 53, R10477-R10480.

30. Adhikari, S., Lysevych, M., Jagadish, C. and Tan, H.H., "Selective Area Growth of GaN Nanowire: Partial Pressures and Temperature as the Key Growth Parameters." *Crystal Growth & Design*, **2022**, 22, 5345-5353.

31. Ambacher, O., Angerer, H., Dimitrov, R., Rieger, W., Stutzmann, M., et al., "Hydrogen in Gallium Nitride Grown by MOCVD." *physica status solidi (a)*, **1997**, 159, 105-119.

32. Wulff, G., "XXV. Zur Frage der Geschwindigkeit des Wachsthums und der Auflösung der Krystallflächen." *Zeitschrift fur Kristallographie - Crystalline Materials*, **1901**, 34, 449.

33. Bergbauer, W., Strassburg, M., Ch, K., Linder, N., Roder, C., et al., "Continuous-flux MOVPE growth of position-controlled N-face GaN nanorods and embedded InGaN quantum wells." *Nanotechnology*, **2010**, 21, 305201.

34. Bergbauer, W., Strassburg, M., Kölper, C., Linder, N., Roder, C., et al., "N-face GaN nanorods: Continuous-flux MOVPE growth and morphological properties." *Journal of Crystal Growth*, **2011**, 315, 164-167.

35. Koukitu, A., Mayumi, M. and Kumagai, Y., "Surface polarity dependence of decomposition and growth of GaN studied using in situ gravimetric monitoring." *Journal of Crystal Growth*, **2002**, 246, 230-236.

36. Zettler, J.K., Corfdir, P., Hauswald, C., Luna, E., Jahn, U., et al., "Observation of Dielectrically Confined Excitons in Ultrathin GaN Nanowires up to Room Temperature." *Nano Letters*, **2016**, 16, 973-980.

37. Schneider, C.A., Rasband, W.S. and Eliceiri, K.W., "NIH Image to ImageJ: 25 years of image analysis." *Nature Methods*, **2012**, 9, 671-675.

38. Yoshida, K., Yamanobe, S., Konishi, K., Takashima, S., Edo, M., et al., "Dependence of thermal stability of GaN on substrate orientation and off-cut." *Japanese Journal of Applied Physics*, **2019**, 58, SCCD17.

39. Haffouz, S., Beaumont, B. and Gibart, P., "Effect of Magnesium and Silicon on the lateral overgrowth of GaN patterned substrates by Metal Organic Vapor Phase Epitaxy." *MRS Internet Journal of Nitride Semiconductor Research*, **1998**, 3, e8.

40. Tessarek, C., Heilmann, M., Butzen, E., Haab, A., Hardtdegen, H., et al., "The Role of Si during the Growth of GaN Micro- and Nanorods." *Crystal Growth & Design*, **2014**, 14, 1486-1492.

41. Bae, S.-Y., Lekhal, K., Lee, H.-J., Min, J.-W., Lee, D.-S., et al., "Selective-area growth of doped GaN nanorods by pulsed-mode MOCVD: Effect of Si and Mg dopants." *physica status solidi (b)*, **2017**, 1600722.

42. Wang, X., Hartmann, J., Mandl, M., Mohajerani, M.S., Wehmann, H.-H., et al., "Growth kinetics and mass transport mechanisms of GaN columns by selective area metal organic vapor phase epitaxy." *Journal of Applied Physics*, **2014**, 115, 163104.

Chapter 5. Growth and Characterisation of GaN/AlGaN Core-Shell Nanowires

5.1. Introduction

The III-nitride alloy of AlGaN offers tunable direct bandgap from 3.4 eV of GaN to 6.2 eV of AlN, and hence, covers the ultraviolet (UV) wavelength range from 200 to 365 nm. Therefore, AlGaN alloys are the most suitable semiconductors for solid-state UV light source. Most of the research so far in the growth of AlGaN for UV light emission has been conducted on *c*-plane via planar epitaxial growth.

AlGaN layers grown on *c*-plane encounter crystal polarity due to lack of an inversion symmetry of the wurtzite crystal structure along the *c*-axis. As a consequence, strong electrostatic field as high as 1 $MVcm^{-1}$ is present along the *c*-axis due to spontaneous and piezoelectric polarisations [1]. The conduction and valence bands are tilted by this built-in electrostatic field, and creates triangular potential wells with spatially separated electron and hole wavefunctions. This phenomenon is called the quantum-confined Stark effect (QCSE)[2], and results in redshift of the emission wavelength with reduced internal quantum efficiency due to the decreased overlap of electron and hole wavefunctions. Further, the topmost valence band (VB) in AlGaN undergoes a crossover from heavy hole (HH) to crystal field split-off hole (CH) due to a negative crystal-field splitting energy of -219 meV in AlN compared to the positive value of +38 meV in GaN. The crossover depends on Al composition, strain and quantum size effect, and this leads to a wide range of estimated critical Al composition from 9 to 81% where VB crossover occurs [3, 4]. The most significant and adverse consequence of VB crossover to CH band is the switching from transverse electric (TE, $\boldsymbol{E}\perp c$) to predominantly transverse magnetic (TM, $\boldsymbol{E}\parallel c$) polarised light, resulting in poor light emission from planar *c*-plane surface [5].

The aforementioned issues of QCSE and switching of the emitted light to TE polarisation in polar *c*-plane AlGaN can be alleviated by using nonpolar *m*-, or *a*-plane orientations. Polarisation switching does not occur for light emission from nonpolar planes as the electric field vector, ***E***, of the emitted light is always in the direction of *c*-axis (***E***||*c*) irrespective of alloy composition and hence, light can be extracted efficiently from nonpolar surfaces [6, 7]. Planar GaN and AlGaN multiple quantum wells (MQWs) on nonpolar *m*-plane have demonstrated QCSE-free emission with improved intensity compared to *c*-plane MQWs [8, 9]. Moreover, the light emission from nonpolar planes have a very high degree of polarisation due to the anisotropic in-plane stress whereas, light emission from *c*-plane with biaxial in-plane stress has low degree of polarisation. Light with high degree of polarisation is advantageous for increasing the efficiency of LEDs and lasers [10]. Taniyasu and Kaso have achieved a very high polarisation ratio of 0.9 in AlN-based p-n junction UV LEDs using nonpolar *a*-plane with an estimated enhancement of 25 times higher intensity in extracted light compared to that on the *c*-plane [11]. Despite the advantages of nonpolar planes, growth of planar nonpolar AlGaN on foreign substrates suffers from low crystal quality and high density of stacking faults (SFs) of the order of 10^5 cm^{-1}[12]. The high density of SFs in nonpolar epitaxial layer deteriorates the device performance [13]. Nonpolar bulk substrates, on the other hand, have limited size and high cost, thus limiting the research in universities as well as industries [14].

Nanowires in the form of GaN/AlGaN core-shell structure can potentially tap the advantage of nonpolar AlGaN and at the same time resolve the existing issues related to SFs and costly nonpolar substrate. Selective area-grown GaN nanowires, discussed in Chapter 4, are a suitable template for subsequent growth of nonpolar AlGaN. First, the GaN nanowires are free of threading dislocations. Second, they provide large area of nonpolar *m*-plane sidewalls, suitable for epitaxial growth of nonpolar AlGaN in a core-shell geometry. Third, GaN nanowires are grown on conventional *c*-plane GaN pseudo-substrate (GaN on 2-inch *c*-plane sapphire substrate) via selective area growth, therefore, overcomes the issue of limited size and high cost of bulk nonpolar substrates. Fourth, nanowire core-shell heterostructures can tolerate elastic strain relaxation better than planar heterostructures, and hence, thicker shells as well as higher Al composition AlGaN can be grown without formation of surface cracks [15-17]. Fifth, simulations and top-down fabricated regularly arranged nanowires have shown higher light extraction efficiency than the conventional planar structure in AlGaN-based UV LEDs [18-21].

In this chapter, a systematic study is carried out on the growth of AlGaN shells on GaN nanowire template using MOCVD in order to develop GaN/AlGaN core-shell nanowires.

Surface morphology of nonpolar *m*-plane AlGaN shell, AlGaN alloy composition, optical properties, nature of point defect and microstructural defects in GaN/AlGaN core-shell nanowires are investigated for gas-phase Al compositions from 15 to 60%. Consequently, growth of nonpolar *m*-plane $Al_xGa_{1-x}N/Al_yGa_{1-y}N$ MQW nanowires are explored for ultraviolet light emission.

5.2. Experimental Methods

A GaN pseudo-substrate consisting of 4 µm-thick GaN on 2-inch *c*-plane sapphire substrate is used for selective area growth (SAG) of GaN nanowires and subsequent growth of AlGaN shells. The GaN pseudo-substrate as well as GaN nanowires and GaN/AlGaN core-shell nanowires are grown using an Aixtron 3×2" close-coupled showerhead MOCVD system.

Substrate preparation for the SAG starts with depositing a 15 nm-thick SiO_x layer on GaN pseudo-substrate using an atomic layer deposition system (Picosun SUNALE). A 100 nm-thick electron beam resist (mr-PosEBR, micro resist technology GmbH) is then deposited on top of the SiO_x layer by spin coating (3000 rpm, 1 min). Further, a water-based anti-charging agent (DisCharge, DisChem Inc. USA) for electron beam lithography (EBL) is then spin-coated (1000 rpm, 1 min) on top of the electron beam resist to minimise charging of the electrically insulating sapphire substrate during EBL. Circular holes of 100 nm diameter, arranged in a hexagonal array, are patterned using an EBL system (Raith 150). After exposure in EBL, the anti-charging agent is rinsed with deionised water followed by blow-drying with a nitrogen gun. The exposed patterns on electron beam resist are developed using n-amyl acetate (30 sec) and rinsed with isopropyl alcohol. The developed pattern is then transferred to the SiO_x layer by etching the layer using CHF_3 chemistry in a reactive-ion etching system (Oxford Plasmalab 80Plus). The remaining electron beam resist on the substrate is cleaned by ultrasonication for 5 minutes each successively in acetone, isopropyl alcohol and deionised water. An oxygen plasma treatment for 5 minutes is carried out to ensure removal of any residual organic contaminants on the substrate. The patterned 2-inch wafer is then diced into 10×10 mm^2 pieces using a dicing machine (Disco DAD321, Japan). A final cleaning of the 10×10 mm^2 wafer pieces is carried out using acetone, isopropyl alcohol and deionised water before loading into the MOCVD for SAG.

SAG of GaN nanowires is carried out using triethylgallium (TEGa) and ammonia as precursors for a growth duration of 25 minutes in a mixed carrier gas of N_2+H_2. The flow rates of TEGa, NH_3 and total gas flow are maintained 45, 14 and 10,000 sccm, respectively.

Additional details on the growth of GaN nanowires have been presented in Chapter 4. Growth of GaN nanowires is immediately followed by AlGaN shell growth by introducing trimethylaluminium (TMAl) and reducing the TEGa flow rate. A constant trimethylindium flow of 5 µmol/min is also added in this step and continues throughout the entire AlGaN shell growth to promote adatom mobility. After a minute of AlGaN deposition, the carrier gas is switched to pure N_2 and the growth temperature is ramped down from 955 to 925 °C in 2 minutes to promote lateral growth. Unlike the N_2+H_2 mixed carrier gas used during GaN nanowire growth, AlGaN growth is carried out using pure N_2 carrier gas, unless specified otherwise.

The morphology of the GaN/AlGaN core-shell nanowires is analysed using a scanning electron microscope (SEM, FEI Verios 460). Energy dispersive x-ray spectroscopy (EDS, Oxford) and room temperature cathodoluminescence (CL, Gatan MonoCL4 Elite) measurements are also carried out in the same SEM. Electron transparent lamella of the nanowires for transmission electron microscopy studies are prepared using a focused ion beam system (FIB, Zeiss Crossbeam 550). Microstructural characterisation of the nanowires is carried out in a transmission electron microscope (TEM, JEOL 2100F FEGTEM) operating at an accelerating voltage of 200 kV.

GaN/AlGaN core-shell nanowires with different alloy compositions are prepared and studied. Table 5.1 list the details of the samples, Al composition in the gas phase, volumetric and molar flow rates of precursors and V/III ratio. The V/III ratio is maintained at about 35.5 during all of the growth experiments.

Table 5.1 Sample identification, gas-phase Al composition, volumetric and corresponding molar flow rates of TMAl, TEGa and NH_3 flow rates, and V/III ratio used for AlGaN shell growth.

Sample	Al	TMAl		TEGa		TMAl+TEGa	NH_3	V/III
	(%)	(sccm)	(µmol/min)	(sccm)	(µmol/min)	(µmol/min)	(sccm)	
Al-15	15.0	3	2.64	44	14.99	17.63	14	35.4
Al-20	20.1	4	3.52	41	13.97	17.49	14	35.7
Al-30	30.1	6	5.28	36	12.26	17.55	14	35.6
Al-40	40.0	8	7.04	31	10.56	17.60	14	35.5
Al-50	49.8	10	8.80	26	8.86	17.66	14	35.4
Al-60	60.8	12	10.56	20	6.81	17.38	14	35.9

5.3. Effect of carrier gas on the surface morphology of AlGaN

Initial experiments on the growth of AlGaN shell using a mixed carrier gas of $6N_2$+$4H_2$, the same gas composition used during the growth of GaN nanowires, resulted in rough sidewalls due to striations as shown in Figure 5.1(a). The striations or undulations are elongated in $[11\bar{2}0]$ direction while closely spaced in [0001] direction. Such striated surface formed by elongated pyramidal hillocks are commonly observed in the planar homoepitaxial growth of nonpolar *m*-plane GaN [22-26]. Similar slate-like undulations perpendicular to [0001] has also been reported in homoepitaxial growth of AlN on *m*-plane AlN substrate [27]. The origin of elongated pyramidal hillocks leading to striations on the surface has been suggested to be due to the manifestation of spiral growth around screw dislocations [24], while theoretical calculations by Lymperakis *et al.* and Jindal *et al.* have suggested them to be due to the anisotropy in adatom diffusion barriers along [0001] and $[11\bar{2}0]$ directions [28, 29].

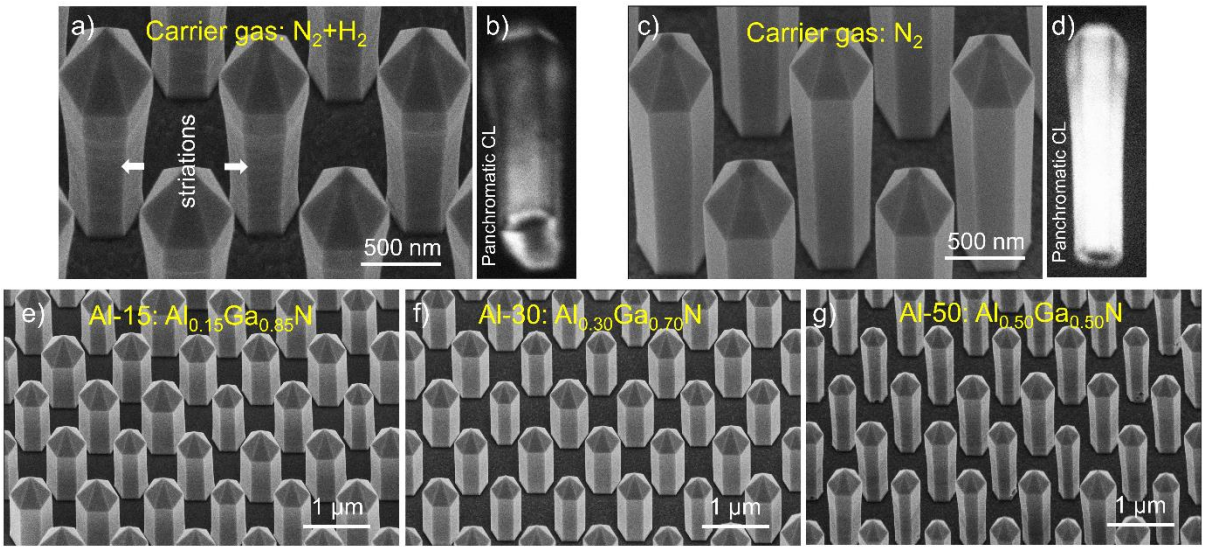

Figure 5.1 SEM images of GaN/AlGaN core-shell nanowires. (a, b) AlGaN shell grown using $6N_2$+$4H_2$ carrier gas and corresponding panchromatic cathodoluminescence image of a single nanowire, (c, d) AlGaN shell grown using pure N_2 carrier gas and panchromatic cathodoluminescence image of a single nanowire, (e, f, and g) SEM images of GaN/AlGaN core-shell nanowire samples Al-15, Al-30, and Al-50, respectively, grown in pure N_2 carrier gas.

For the conventional planar growth, striations on the surface of nonpolar *m*-plane GaN have been successfully reduced by using miscut substrates [30-32], and in the case of *m*-plane AlN using a very high growth temperature (>1350 °C) [27, 33]. However, the challenge in GaN/AlGaN core-shell nanowire heteroepitaxy on *m*-plane sidewalls is that a preferential

miscut cannot be defined for the nanowire sidewalls while the high temperature growth suggested in the case of AlN risks thermal decomposition of the GaN nanowires. Nonetheless, for practical applications of GaN/AlGaN core-shell nanowires, smooth sidewall surface is a key requirement to obtain sharp interfaces in radial multiple quantum well heterostructures.

GaN/AlGaN core-shell nanowires with smooth sidewalls are achieved by using pure N_2 carrier gas during the AlGaN growth as shown in Figure 5.1(c). The improvement in surface morphology of AlGaN by using N_2 carrier gas during the growth can be attributed to the reduced disparity in diffusion lengths of Al and Ga adatoms. The difference in adatom mobilities pose a significant problem in the growth of semiconductor alloys as it could lead to step-bunching and surface faceting along with non-uniform alloy composition [34]. The diffusion lengths of Al and Ga adatoms have been reported to be about 31 - 44 nm and 300 – 800 nm, respectively [35, 36]. This disparity in the diffusion lengths between Al and Ga adatoms can be minimised either by increasing mobility of Al adatoms or by decreasing mobility of Ga adatoms. Monte Carlo simulation has shown that Al adatom has a higher mobility in N_2 carrier gas compared to H_2 carrier gas [37]. Meanwhile, the diffusion length of Ga is reported to reduce by about 4 times in N_2 carrier gas compared to H_2 [38]. Therefore, the disparity in diffusion lengths of Al and Ga adatoms are minimised in pure N_2 carrier gas and results in GaN/AlGaN core-shell nanowires with smooth sidewall surface free of striations.

In addition to the smooth surface of AlGaN shell grown using pure N_2 carrier gas, panchromatic cathodoluminescence image also exhibits a brighter luminescence compared to the AlGaN shell grown using H_2+N_2 mixed carrier gas as can be seen from Figure 5.1(b) and (d). Near-band-edge (NBE) luminescence is observed only in the case of AlGaN shell grown using pure N_2 carrier gas and is attributed to the better crystalline quality and reduced impurity incorporation for AlGaN grown in N_2 carrier gas. Superior crystalline and optical properties have been reported in the planar epitaxial growth of GaN/$Al_{0.17}Ga_{0.83}N$ MQW [39] and AlN [40] using N_2 carrier gas. More recently, Barry *et al.* achieved atomically-flat planar homoepitaxial *m*-plane GaN with reduced incorporation of C, O, and Si in N_2 carrier gas, whereas, heavily undulated surface resulted with H_2 carrier gas [41]. Henceforth, growth of AlGaN shells for the remaining discussion are conducted in pure N_2 carrier gas.

GaN/AlGaN core-shell nanowires with different alloy compositions are grown using the conditions listed in Table 5.1. SEM images of core-shell nanowires grown with gas-phase Al compositions [TMAl/(TMAl+TEGa)] of 15, 30, and 50% are shown as Figure 5.1 (e, g, and g),

respectively. Statistical analysis of the diameters and heights for these GaN/AlGaN core-shell nanowires are carried out using the image analysis software ImageJ [42]. The core-shell nanowire diameters are determined to be 563±55, 504±37, and 433±37 nm for the samples Al-15, Al-30, and Al-50, respectively, with corresponding heights of 1263±37, 1210±27, and 1659±21 nm. Hence, uniform array of GaN/AlGaN core-shell nanowires with different Al compositions can be grown reproducibly on GaN nanowires using MOCVD.

5.4. Study of AlGaN alloy composition: SEM-EDS

The alloy composition of AlGaN shells are studied using an SEM (FEI Verios 460) equipped with and energy dispersive x-ray spectrometer (EDS). In the form of nanowires, SEM-EDS analysis of the GaN/AlGaN core-shell nanowires are prone to underestimate the Al composition of the AlGaN shell due to the underlying GaN core. During the SEM-EDS analysis, the electron beam penetrates into the GaN core and the excited x-ray from the GaN core is added to the signal, which results in the underestimation of Al composition. In order to avoid the underestimation of Al composition, thin lamella of GaN/AlGaN core-shell nanowires are prepared using focussed ion beam (FIB). Considering the tedious nature of lamella preparation and the possibility to estimate the Al composition by interpolation, four different samples of GaN/AlGaN core-shell nanowires viz. Al-15, Al-30, Al-50, and Al-60 are considered.

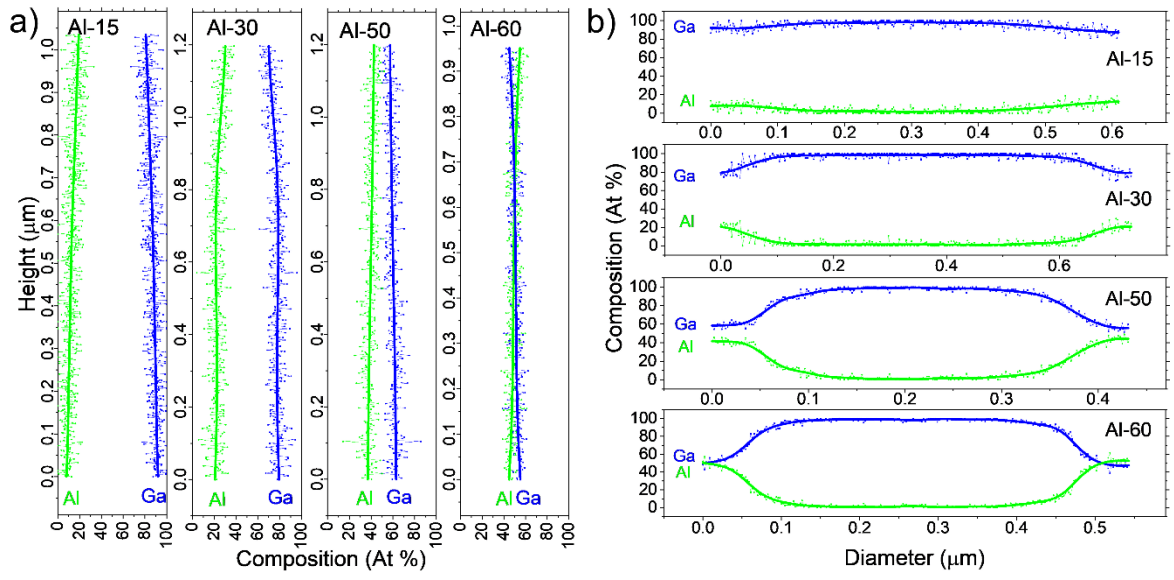

Figure 5.2 Alloy composition of GaN/AlGaN core-shell nanowires from EDS linescans along the (a) length and (b) diameter. Respective sample IDs are indicated.

Figure 5.2(a) reveals that Al composition of the AlGaN shell decreases slightly from top to bottom. The gradual variation of Al composition along the height is due to the higher sticking

coefficient of Al compared to Ga and the vapour-phase diffusion mode of flux supply for the growth. The higher sticking coefficient of Al leads to preferential Al incorporation near the top region of already grown GaN nanowire core and in this process, Al in the vapour-phase is slowly depleted towards the bottom of nanowire and results in gradual variation of Al incorporation from top to bottom of the the nanowire. Figure 5.2(b) shows Al composition across the diameter of GaN/AlGaN core-shell lamella and confirms the controlled incorporation of different Al compositions in AlGaN shells around the GaN nanowire core.

Table 5.2 Sample IDs, gas-phase Al composition and solid-phase Al compositions determined by SEM-EDS and SEM-CL.

Sample	Al composition (%)		
	Gas phase	SEM-EDS	SEM-CL
Al-15	15.0	11.7±2.2	10.3
Al-20	20.1	*	15.0
Al-30	30.1	23.1±2.5	22.0
Al-40	40.0	*	30.5
Al-50	49.8	39.8±1.8	40.2
Al-60	60.8	50.5±2.3	#

Al compositions determined from different GaN/AlGaN core-shell nanowires using SEM-EDS are listed in Table 5.2. It is evident that the solid-phase Al composition, determined from SEM-EDS, is lower than the gas-phase Al composition. In general, the alloy composition of AlGaN grown by MOCVD is known to deviate from the gas-phase composition due to a complex interdependence on growth temperature, reactor pressure, gas-phase TMAl/III ratio, and V/III ratio used during the growth [43-46]. The potential causes for the lower Al incorporation in the solid-phase compared to the gas-phase composition will be discussed later in the section 5.6.

5.5. Study of AlGaN alloy composition: SEM-CL

In addition to the EDS analysis, cathodoluminescence (CL) is also used to determine the alloy composition of AlGaN shells. Emission spectra from room-temperature CL measurements on GaN/AlGaN core-shell nanowire samples of Al-15, Al-20, Al-30, Al-40, and Al-50 are shown in Figure 5.3(a). A systematic increase in near-band-edge (NBE) emission from 3.58 eV

* Lamellas have not been prepared for SEM-EDS.
# NBE emission has not been observed in SEM-CL.

for sample Al-10 to 4.14 eV for sample Al-50 is observed. The dashed line in Figure 5.3(a) indicates the NBE emission from the GaN nanowire core.

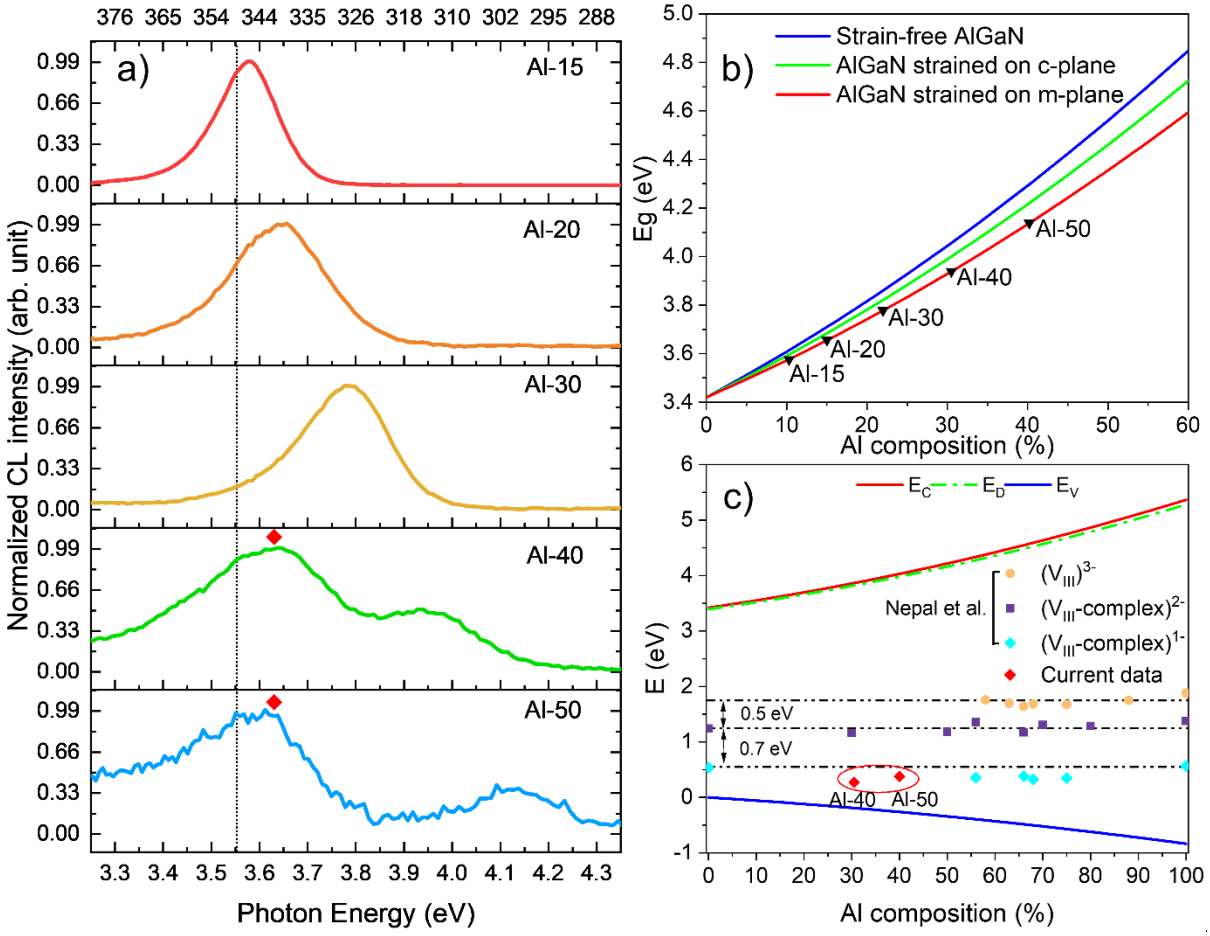

Figure 5.3 (a) CL spectra of the GaN/AlGaN nanowire samples with different Al-compositions as indicated. (b) Calculated bandgap energy for strain-free AlGaN (blue line), AlGaN strained on *c*-plane GaN (green line) and AlGaN strained on *m*-plane GaN (red line). The black triangular data points are the NBE emission energies of GaN/AlGaN nanowires obtained through CL, as shown in (a). (c) Deep acceptor levels in AlGaN classified as $(V_{III})^{3-}$, $(V_{III}$ complex$)^{2-}$, and $(V_{III}$ complex$)^{1-}$ with data from Nepal et al. [50], and the current data from samples Al-40 and Al-50, with solid phase Al compositions of ~30 and 40%, respectively, are shown as red diamonds.

The alloy compositions of AlGaN shells may be determined from the NBE emissions using the Vegard's law, which is an interpolation of the bandgap energies between GaN and AlN. However, it should be noted that, AlGaN shells on GaN nanowire cores are subjected to tensile strain due to the smaller lattice parameters of AlN compared to those of GaN. The resulting strain due to the lattice mismatch further modifies the emission wavelength determined through

Vegard's law. Therefore, the strain-modified NBE emission of AlGaN on *m*-plane GaN is calculated as discussed in the following paragraphs, using the lattice parameters, bandgap energies, elastic constants, and deformation potentials of GaN and AlN [47-49], whose values are listed in Chapter 2.

The lattice parameters, *a* and *c*, elastic constants, *C*, and deformation potentials, *D*, for the ternary AlGaN alloys are calculated using the values of AlN and GaN by linear interpolation as follows:

$$a_{\mathrm{AlGaN}} = a_{\mathrm{AlN}} \times x + a_{\mathrm{GaN}} \times (1 - x)$$

$$c_{\mathrm{AlGaN}} = c_{\mathrm{AlN}} \times x + c_{\mathrm{GaN}} \times (1 - x)$$

$$C_{\mathrm{AlGaN}} = C_{\mathrm{AlN}} \times x + C_{\mathrm{GaN}} \times (1 - x)$$

$$D_{\mathrm{AlGaN}} = D_{\mathrm{AlN}} \times x + D_{\mathrm{GaN}} \times (1 - x) \tag{5.1}$$

For the strain-free AlGaN alloys, bandgap energies are calculated simply by using the Vegard's law using a bowing parameter, $b = 1$ [51] as follows:

$$E_{\mathrm{g\,AlGaN}} = E_{\mathrm{g\,AlN}} \times x + E_{\mathrm{g\,GaN}} \times (1 - x) + b \times x(1 - x) \tag{5.2}$$

For the more general heteroepitaxial growth of AlGaN on *c*-plane GaN, AlGaN experiences a biaxial tensile strain due to larger lattice constant *c* of the underlying GaN. The biaxial strain under this condition is:

$$\varepsilon_{xx} = \varepsilon_{yy} = (a_{\mathrm{GaN}} - a_{\mathrm{AlGaN}})/a_{\mathrm{AlGaN}} \tag{5.3}$$

As a consequence of this in-plane biaxial tensile strain, a corresponding out-plane compressive strain is induced in the [0001] direction as:

$$\varepsilon_{zz} = -\frac{2C_{13}}{C_{33}}\varepsilon_{xx} \tag{5.4}$$

According to Yan *et al.* [49], the bandgap energy of strained AlGaN on *c*-plane GaN can then be calculated using the strain component as follows:

$$E_{\mathrm{g\,AlGaN}} = E_{\mathrm{g\,AlGaN}}(0) + (a_{cz} - D_1)\varepsilon_{zz} + (a_{ct} - D_2)\varepsilon_{\perp} - (D_3\varepsilon_{zz} + D_4\varepsilon_{\perp}) \tag{5.5}$$

where, $E_{\mathrm{g\,AlGaN}}(0)$ is the bandgap energy of strain-free AlGaN obtained using Eq. (5.2), $\varepsilon_{\perp} = (\varepsilon_{xx} + \varepsilon_{yy})$, and $(a_{cz}\text{-}D_1)$, $(a_{ct}\text{-}D_2)$, D_3, D_4 are the deformation potentials obtained using Eq. (5.1).

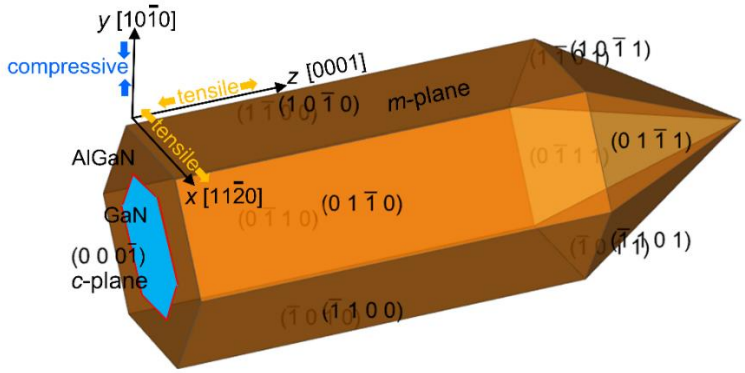

Figure 5.4 Schematic representation of GaN/AlGaN core-shell nanowire showing the anisotropic in-plane strains due to mismatch in both *c* and *a* lattice constant.

For the case of AlGaN grown on nonpolar $(10\bar{1}0)$ *m*-plane GaN nanowire sidewalls, there exists different in-plane tensile strains due to different lattice mismatch in *a* and *c*. The notations for strain along $[11\bar{2}0]$ is ε_{xx} and along [0001] is ε_{zz}, respectively. Figure 5.4 illustrates these in-plane strains along the respective axes. The anisotropic in-plane strains, ε_{xx}, and, ε_{zz}, in this case are determined independently using Eq. (5.3) in the respective directions. The in-plane tensile strains ε_{xx} and ε_{zz} collectively induce a compressive strain, ε_{yy}, on AlGaN along the $[10\bar{1}0]$ direction. This out-of-plane compressive strain, ε_{yy}, may be calculated using elastic constants as follows:

$$\varepsilon_{yy} = -\frac{C_{11}}{C_{33}}\varepsilon_{xx} - \frac{C_{12}}{C_{33}}\varepsilon_{zz} \tag{5.6}$$

The bandgap energy of strained AlGaN on *m*-plane GaN may then be calculated, according to Yan *et al.* [49], as follows:

$$E_{\mathrm{g\,AlGaN}}(1) = E_{\mathrm{g\,A/B}}(0) + (D_2 + D_4)\varepsilon_{xx} + D_5\varepsilon_{xx}$$

$$E_{\mathrm{g\,AlGaN}}(2) = E_{\mathrm{g\,A/B}}(0) + (D_2 + D_4)\varepsilon_{xx} - D_5\varepsilon_{xx}$$

$$E_{\mathrm{g\,AlGaN}}(3) = E_{\mathrm{g\,C}}(0) + D_2\varepsilon_{xx} \tag{5.7}$$

Using Eq. (5.2), (5.5) and (5.7), the bandgap energies for strain-free AlGaN, AlGaN strained on *c*-plane GaN, and AlGaN strained on *m*-plane GaN are calculated and plotted in Figure 5.3 (b).

The solid-phase Al composition of AlGaN shells are determined to be 10.3, 15.0, 22.0, 30.5 and 40.2% for the samples Al-15, Al-20, Al-30, Al-40, and Al-50, respectively, by fitting

the experimentally determined NBE emission energies (Figure 5.3 (a)) on the calculated bandgap energy of strained AlGaN on *m*-plane GaN (red line in Figure 5.3 (b)). NBE emission has not been observed for the sample Al-60, possibly due to the poor crystalline quality as a result of the large lattice mismatch between the GaN core and AlGaN shell, therefore, Al composition cannot be estimated using SEM-CL for this sample. Nevertheless, the Al compositions determined from NBE emissions, as discussed here, agree well with the compositions determined by SEM-EDS and are listed in Table 5.2.

5.5.1. Defect-related luminescence from AlGaN

Figure 5.3 (a) shows the CL spectra of GaN/AlGaN core-shell nanowires. The sample IDs are labelled against each spectrum. The vertical dashed line indicates the photon energy of GaN NBE emission. A subtle influence on the spectra due to emission from the GaN core may also be observed in Figure 5.3 (a). More importantly, it is evident from Figure 5.3 (a) that all of the spectra shown here exhibit emission peaks at higher photon energies compared to that of GaN, as expected for AlGaN with wider bandgap. Therefore, the well-defined peaks in the samples Al-15, Al-20, and Al-30 are assigned as NBE emission from the AlGaN shells.

Further, the defect levels in semiconductor lies in the subgap, and hence, if the defects are optically active, they emit at lower photon energies compared to the NBE emission due to the recombination of electrons from the conduction band with the acceptor energy levels of the defects, which are located above the valence band edge. Therefore, the observation of only one emission peak in the samples Al-15, Al-20, and Al-30, which are commensurate with the determined Al-compositions, and exhibiting emission at higher photon energies compared to that of GaN corroborates the fact that these are NBE emissions from AlGaN and not due to defects.

However, the CL spectrum of samples Al-40 and Al-50 display two luminescence peaks. In these two samples, the respective peaks centred at higher photon energies of 3.94 eV in Al-40 and 4.14 eV in Al-50 concur with the determined alloy compositions of ~30% and ~40%, respectively, hence, these peaks are assigned as NBE emissions. The additional broad luminescence peak in these two samples are centred at lower photon energy of about 3.64 eV as indicated by red diamonds in Figure 5.3 (a). Similar defect luminescence peaks have also been reported for Al compositions ≥ 25% by Hoshi *et al*. from their planar epitaxial growth of AlGaN on bulk *m*-plane GaN substrate [52]. The authors suggested the origin of these defects to be due to the defect complex of cation vacancy with oxygen or the DX centre. The term “DX”

centre was coined originally to represent the trap state of a defect complex involving a donor level, 'D', complexed with an unknown defect level 'X'. Although the term "DX" has remained till date due to historical reasons, it is now known that DX centres are formed by a known donor impurity which transitions into a deep acceptor level due to the displacement of the donor impurity from its normal lattice site.

In AlGaN, oxygen behaves as a donor impurity for low Al compositions, however, it transitions from donor to deep acceptor level at higher Al compositions. The threshold Al composition of AlGaN at which the onset of DX behaviour occurs is 30% [53-57]. Therefore, the observation of defect luminescence peaks only in the samples Al-40 and Al-50 with the determined Al compositions of 30 and 40%, respectively, suggests that point defect complex associated with oxygen-related deep acceptor level is responsible for the defect luminescence.

In order to to further understand the nature of this defect-related luminescence, we calculated the acceptor energy levels, E_A, for the samples Al-40 and Al-50 according to Nepal *et al.* [50], as follows:

$$E_A = E_g(x) - E_{impurity} - E_D + E_V \tag{5.8}$$

Here, $E_g(x)$ is the bandgap of $Al_xGa_{1-x}N$, $E_{impurity}$ is the photon energy of the defect-related emission peak measured from CL spectra, E_D and E_V are the energy levels of shallow donor and valence band, respectively. Using Eq (5.8) and the measured $E_{impurity}$ value of 3.64 eV (peaks indicated by red diamonds in Figure 5.3 (a)), the acceptor energy levels, E_A, are determined to be 0.182 and 0.341 eV, which are located 372 and 603 meV above the valence band edges in samples Al-40 and Al-50, respectively, with corresponding solid-phase Al compositions of ~ 30 and 40%. The calculated acceptor energy levels are plotted as red diamonds in Figure 5.3 (c).

The energy levels of point-defects such as due to oxygen and hydrogen in semiconductors are universally pinned below the vacuum level at fixed energy levels of -5.0 and -4.5 eV, respectively, for oxygen and hydrogen, irrespective of the semiconductor material [58, 59]. Therefore, these defects show universal alignment in all of the semiconductor materials. Similarly, the energy levels of $(V_{III})^{3-}$, $(V_{III}\text{-complex})^{2-}$ and $(V_{III}\text{-complex})^{1-}$ point-defects are aligned within the bandgap throughout the alloy composition of AlGaN as shown by the dashed horizontal lines in Figure 5.3 (c). Using Eq. (5.8), the acceptor energy levels in the samples Al-40 and Al-50 are determined to be 0.182 and 0.341 eV, respectively, and are plotted as red diamonds in Figure 5.3 (c). It is evident from figure 5.3 (c) that, the location of these impurity

levels (red diamonds) align with the horizontal dashed line representing the $(V_{III}\text{-complex})^{1-}$ point-defect.

Whether carbon or oxygen is responsible for this $(V_{III}\text{-complex})^{1-}$ can be distinguished from the fact that the defect energy levels are aligned throughout GaN to AlN as shown in Figure 5.3 (c). Therefore, we can deduce the nature of this $(V_{III}\text{-complex})^{1-}$ point-defect as either due to carbon or oxygen by referring to the well-known defect energy levels of carbon and oxygen in GaN and AlN. Carbon-related defects show luminescence bands centred at 2.15 and 3.9 eV in GaN and AlN respectively [60, 61]. On the other hand, oxygen-related defect luminescence in GaN and AlN are centred at 2.8 and 4.7 eV, respectively [62, 63]. The currently observed defects with acceptor energy levels of 0.182 eV (sample Al-40) and 0.341 eV (sample Al-50) are aligned with the $(V_{III}\text{-complex})^{1-}$ point-defects that exhibits defect-related emissions at 2.8 eV in GaN and 4.7 eV in AlN, which are associated with oxygen. Therefore, the $(V_{III}\text{-complex})^{1-}$ is deduced to be due to oxygen and can be assigned as $(V_{III}\text{-}2O_N)^{1-}$ defect-complex formed by the combination of a metal vacancy with a pair of substitutional oxygen at the N site. In summary, the major point defect in GaN/AlGaN core-shell nanowires are due to oxygen. Oxygen behave as donor impurity for Al composition < 30%, however, at higher Al compositions, oxygen transitions from donor to deep acceptor level, wherein, the oxygen-related point defect exists as $(V_{III}\text{-}2O_N)^{1-}$.

5.6. Discussion on reduced Al incorporation

Solid-phase Al composition of the AlGaN shells have been determined by using SEM-EDS and SEM-CL. The Al composition determined from these two different measurements agree well, yet concomitantly indicates that the solid-phase Al fraction incorporated is lower than the gas-phase Al composition. The expected Al composition based on the input gas-phase ratio as well as the experimentally determined Al composition from SEM-EDS and SEM-CL measurements are plotted in Figure 5.5. The possible factors leading to reduced Al incorporation are discussed in the following paragraphs.

Growth of AlGaN on non-planar geometry and epitaxial lateral overgrowth experiments have consistently reported lower Al incorporation on the sidewall facets [64-67]. Ishibashi *et al.* pointed out that the reduced Al incorporation in non-planar structures are due to (*i*)different growth rates in vertical and lateral directions, (*ii*) modification of vapour-phase Al and Ga adatom diffusion by the non-planar structures, and (*iii*) the difference in surface diffusion on top and sidewall facets [68]. Planar AlGaN growth on co-loaded horizontal substrates of

different crystal orientations, on the other hand, have concluded that Al incorporation is comparable for polar (0001) plane, semipolar $(10\bar{1}3)$ and $(11\bar{2}2)$ planes, as well as nonpolar $(10\bar{1}0)$ and $(11\bar{2}0)$ planes [69]. These two distinct results imply that Al-incorporation is reduced on non-planar facets and therefore, geometrical factor is a primary cause of low Al incorporation during the growth of GaN/AlGaN core-shell nanowires.

Given that similar GaN nanowire array geometry is used for the growth of AlGaN shell, it is anticipated that the reduced Al incorporation caused by the non-planar geometry will remain constant. Therefore, we draw a hypothetical dashed-line parallel to the experimentally determined Al composition in Figure 5.5 and identify the gap between this hypothetical line and the experimentally determined Al composition as "geometric loss".

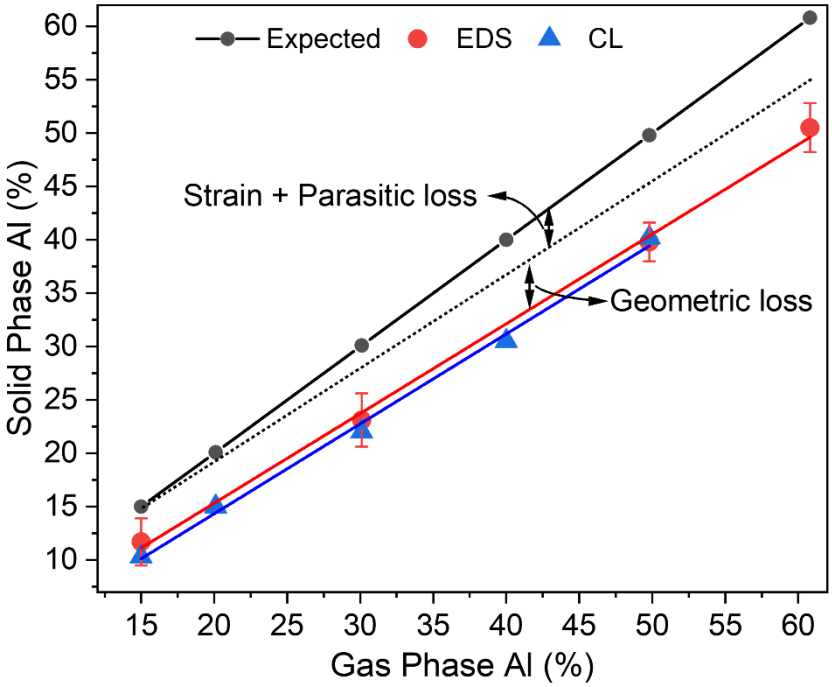

Figure 5.5 Reduced Al incorporation in AlGaN shell due to geometric loss and strain + parasitic loss.

Additionally, AlGaN shells grown on nonpolar *m*-plane sidewalls of GaN nanowires experience an anisotropic tensile strain as shown in Figure 5.4, and tensile strain is known to decrease Al incorporation [70]. Besides, the residual strain also determines the uniformity of Al composition away from the heterointerface [71]. In addition to strain, the gas phase parasitic reaction increases with TMAl flow rate, resulting in lower Al incorporation efficiency at higher TMAl flow rates [72]. Thus, increased strain in the heterostructure with higher Al content and gas-phase parasitic reaction with higher TMAl flow rate result in a non-monotonic reduction of

Al incorporation. Figure 5.5 shows a further deviation in Al incorporation with reference to the hypothetical line due to increased strain and parasitic reaction. The gap between the hypothetical line and expected Al composition is identified as "strain + parasitic loss". Therefore, the reduced Al incorporation in AlGaN shells are attributed to (*i*) geometric loss, and (*ii*) strain + parasitic loss.

5.7. Transmission electron microscopy (TEM) studies of AlGaN shells

Heteroepitaxial growth of AlGaN on GaN is frequently associated with dense misfit dislocations and crack formation in order to partially relieve the tensile strain caused by lattice mismatch [73]. Dislocations of pure edge type, pure screw type, as well as mixed type (edge + screw) dislocations are the major defects observed in the growth of *c*-plane oriented III-nitrides. However, basal-plane stacking faults (BSFs) and partial dislocations (PDs) have been identified as the predominant defects in nonpolar *m*- and *a*-plane oriented growths [74]. Although threading dislocations due to edge, screw, and mixed dislocations have been eliminated by using selective area-grown GaN nanowires, a large number of BSFs and associated PDs are known to exist in the heteroepitaxy of nonpolar III-nitrides [75-77]. BSFs and PDs in crystals can be discerned by analyzing the high-resolution transmission electron microscopy (HRTEM) images through their Bragg filtered images.

Figure 5.6(a) shows an HRTEM image of AlGaN shell (sample Al-15) grown on nonpolar *m*-plane sidewall of the GaN nanowire. All of the HRTEM images discussed in this study are captured along the $[11\bar{2}0]$ zone axis and the crystallographic orientation is indicated in Figure 5.6(a). Diffraction pattern obtained by fast Fourier transform of the HRTEM image is shown as Figure 5.6(b). The (0002) and $(1\bar{1}00)$ diffraction spots, red and green circles, respectively, in Figure 5.6(b) are used for dislocation analysis and generation of strain maps.

Figure 5.6(c), and (d) shows Bragg filtered images of the HRTEM image, generated using (0002) and $(1\bar{1}00)$ diffraction spots, respectively. Analysis of these images reveal the presence of three types of PDs, viz. Frank-Shockley, Shockley, and Frank PDs. Frank-Shockley PDs have a Burgers vector, $\boldsymbol{b}$ = 1/6<20$\bar{2}$3> which is composed of 1/2<0001> with an associated 1/3<1$\bar{1}$00> slip, therefore, this type of PD is identified by analysis of Bragg filtered images with $\boldsymbol{g}$(0002) as well as $\boldsymbol{g}(1\bar{1}00)$. Shockley and Frank PDs, on the other hand, have only Burgers vector of $\boldsymbol{b}$ = 1/3<1$\bar{1}$00> and $\boldsymbol{b}$ = 1/2<0001>, hence each is visible only in $\boldsymbol{g}(1\bar{1}00)$ and $\boldsymbol{g}$(0001), respectively. Frank-Shockley, Shockley, and Frank PDs are indicated with red,

yellow and blue arrows, respectively, in Figure 5.6 (b) and (c). Hence, the dominant type of defects in *m*-plane AlGaN shell are PDs.

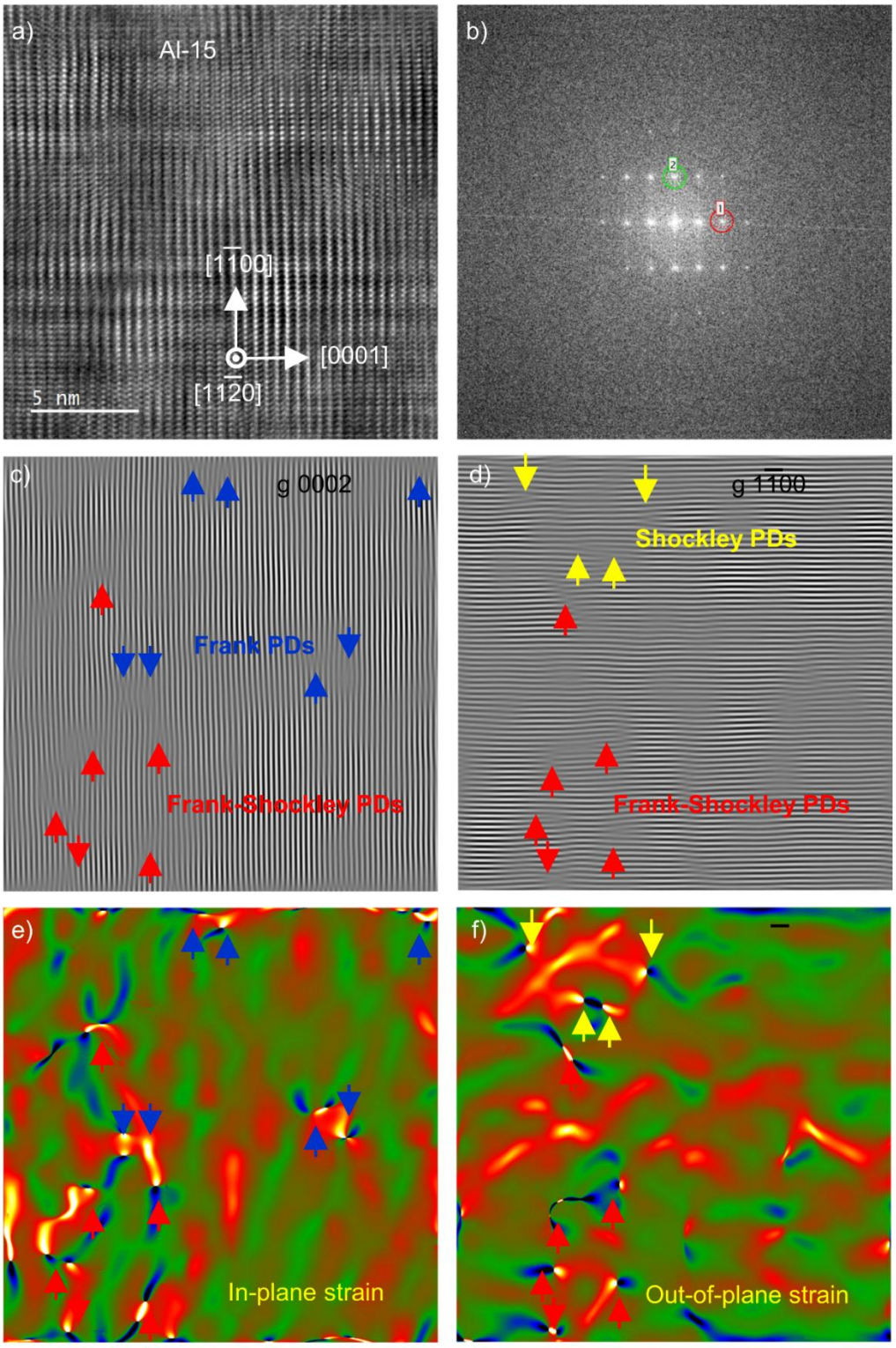

Figure 5.6 Transmission electron microscopy and related images of sample Al-15. The *c*-axis is oriented horizontally in these images. (a) HRTEM image of AlGaN shell. (b) Fast Fourier transform image highlighting diffraction spots (0002), (1$\bar{1}$00). (c, d) Bragg filtered images of

(a) using the diffraction spots (0002) and $(1\bar{1}00)$, respectively. (e, f) In-plane and out-of-plane strain maps of AlGaN shell in (a).

Geometric phase analysis (GPA) is a useful method to analyse strain from HRTEM images [78]. In-plane and out-of-plane strain maps from the HRTEM image, shown as Figure 5.6(e) and (f), respectively, are generated using the GPA plugin [79] in DigitalMicrograph software [80]. Local strain components determined from GPA can be used as a visual aid to locate the dislocation cores from strain maps. A sudden change in strain from being compressive to tensile or vice-versa at the dislocation core results in a high contrast node (yellow for tensile strain and blue for compressive strain) as can be seen in Figure 5.6(e) and (f). Dislocation cores located by strain maps correspond to those identified by Bragg filtered images, and hence, the formation of PDs for AlGaN shell with different Al compositions may be visualised using strain maps from GPA.

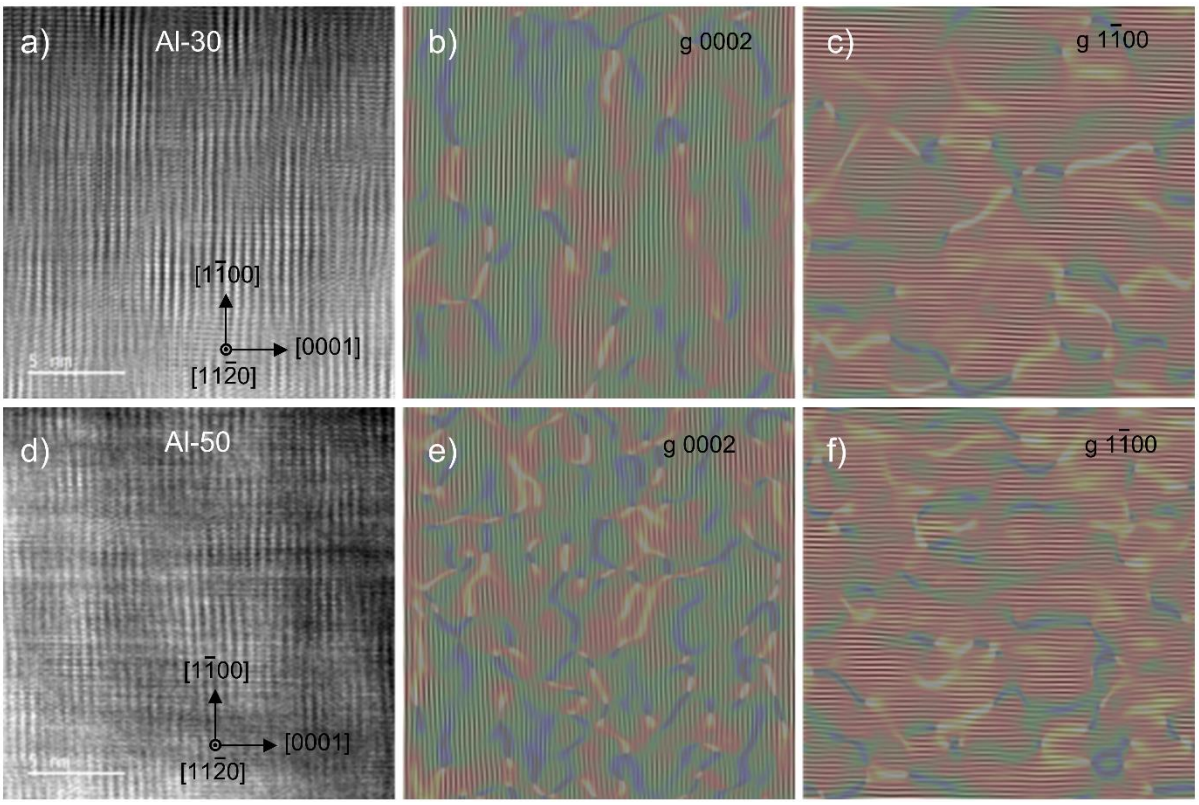

Figure 5.7 (a, d) HRTEM images of AlGaN shell in samples Al-30 and Al-50. (b, e) In-plane strain maps overlaid on $\boldsymbol{g}(0002)$ Bragg filtered images for samples Al-30 and Al50, respectively. (c, f) Out-of-plane strain maps overlaid on $\boldsymbol{g}(1\bar{1}00)$ Bragg filtered images for samples Al-30 and Al-50, respectively.

Figure 5.7 shows the HRTEM images of samples Al-30 and Al-50 along with their corresponding Bragg filtered images superimposed on strain maps. In-plane (Figure 5.7(b), (e)) and out-of-plane (Figure 5.7(c), (f)) strain maps overlaid on Bragg filtered images clearly show an increase in formation of PDs with increasing Al composition. The increase in formation of PDs with Al composition is to counteract the increased tensile strain experienced by *m*-plane AlGaN shell. Therefore, PDs are the predominant microstructural defect in AlGaN shells and the formation of PDs increase with Al composition.

5.8. $Al_xGa_{1-x}N/Al_yGa_{1-y}N$ multiple quantum wells

Following the successful growth of GaN/AlGaN core-shell nanowires, we explored the growth of $Al_xGa_{1-x}N/Al_yGa_{1-y}N$ multiple quantum wells (MQWs) on the GaN nanowire arrays. The gas phase Al compositions for quantum wells and barriers are fixed at 17.3 and 46.3%. Figure 5.8(a) shows a high-angle annular dark-field (HAADF) – scanning tunneling electron microscope (STEM) image, also referred to as Z-contrast image, of the MQWs incorporated on nonpolar *m*-plane sidewalls of GaN nanowire. GaN nanowire core in the middle appears bright owing to the higher atomic number (Z) of Ga while the AlGaN barriers appear darker due to effective lower atomic number of AlGaN. Furthermore, the *m*-plane AlGaN sidewalls have a smooth surface that is free of cracks and macro-steps. On the other hand, a rough surface is observed on the SiO_x mask due to parasitic polycrystalline AlGaN deposition.

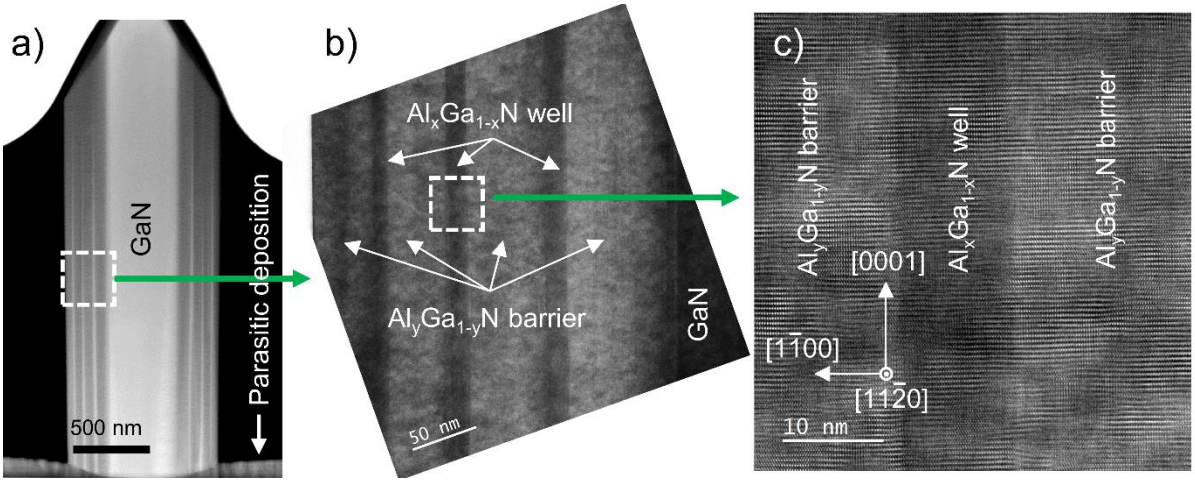

Figure 5.8 (a) HAADF-STEM image of $Al_xGa_{1-x}N/Al_yGa_{1-y}N$ MQWs on the sidewalls of GaN nanowire. (b) Low-magnification TEM image of the MQW region. (c) HRTEM image of an $Al_xGa_{1-x}N/Al_yGa_{1-y}N$ quantum well.

A low-magnification TEM image of the MQW region corresponding to the white dashed square region in Figure 5.8(a) is shown as Figure 5.8(b) with the $Al_xGa_{1-x}N$ wells and Al_yGa_{1-}

$_y$N barriers identified. An HRTEM image of the MQW region indicated with a white dashed square in Figure 5.8(b) is shown as Figure 5.8(c). The HRTEM image reveals a sharp interface between the quantum well and barrier. Overall, TEM study of the AlGaN MQWs shows successful incorporation of three MQWs on the *m*-plane sidewalls. The MQWs run along the length of nanowire and has sharp interface between well and barrier regions.

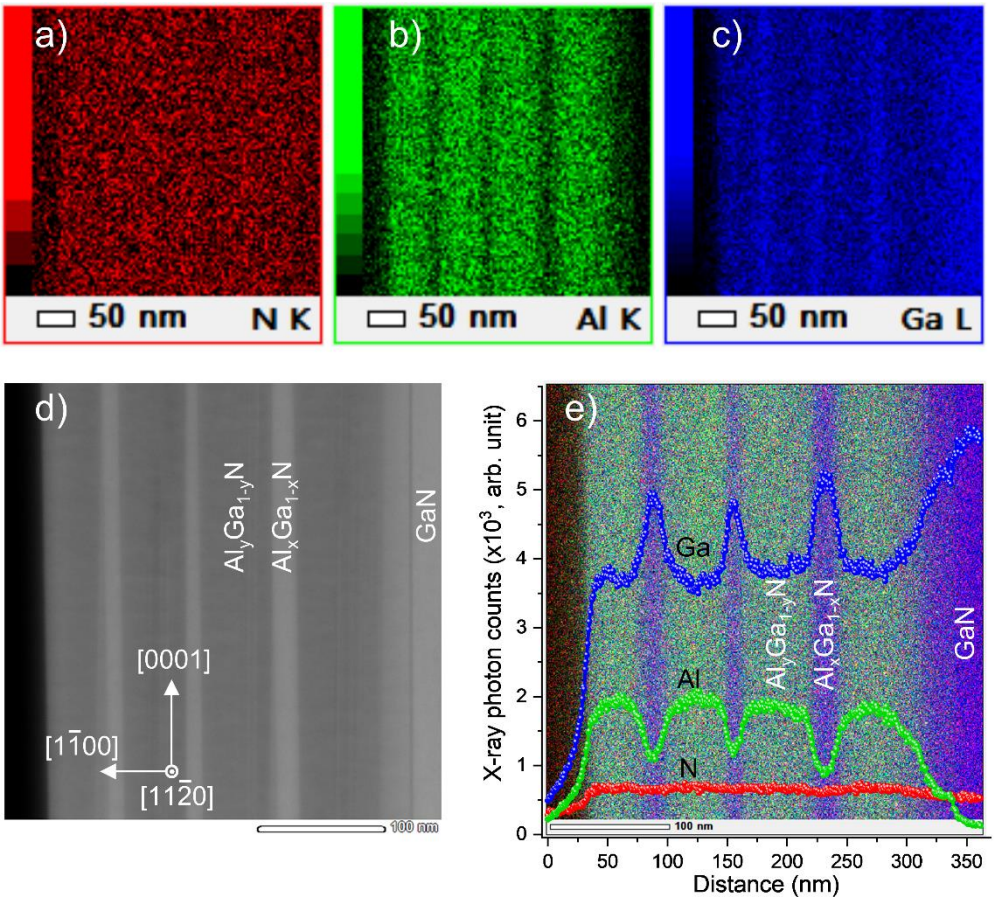

Figure 5.9 (a, b, and c) EDS elemental maps of nitrogen, aluminium and gallium, respectively. (d) HAADF-STEM image of $Al_xGa_{1-x}N/Al_yGa_{1-y}N$ MQWs on the sidewall of GaN nanowire. (e) Superimposed image of the elemental map with x-ray photon counts of the $Al_xGa_{1-x}N/Al_yGa_{1-y}N$ MQWs.

EDS mapping of the $Al_xGa_{1-x}N/Al_yGa_{1-y}N$ MQW region is carried out in TEM. Figure 5.9(a) – (c) shows the elemental map of nitrogen (red), aluminium (green), and gallium (blue), respectively. Uniform distribution of nitrogen throughout the region (Figure 5.9(a)), as well as composition modulations of Al and Ga (Figure 5.9(b) and (c)) at quantum wells and barrier regions are evident. Figure 5.9(d) shows HAADF-STEM image of the region used for elemental mapping, a region similar to the one shown in Figure 5.8(b). Figure 5.9(e) depicts a composite

elemental mapping image of nitrogen (red), aluminium (green) and gallium (red) overlaid with x-ray photon counts of each element. The plot clearly confirms the composition modulations of Al and Ga at the quantum wells and barrier regions. Hence, TEM studies demonstrated that the growth of smooth nonpolar *m*-plane $Al_xGa_{1-x}N/Al_yGa_{1-y}N$ MQWs on GaN nanowire sidewalls is feasible and could be a suitable candidate for nanostructured ultraviolet light sources and detectors.

Finally, in order to analyse the optical characteristics of $Al_xGa_{1-x}N/Al_yGa_{1-y}N$ MQWs, one such nanowire is partially milled using a focused ion beam to expose part of the GaN nanowire core as shown in Figure 5.10(a). CL mapping is carried out on this nanowire at room temperature using electron beam conditions of 5 kV and 13 nA, mapping pixel size of 30 nm and exposure duration of 200 ms at each pixel. Distinct emissions from the GaN nanowire core and the MQW regions are observed and are shown as Figure 5.10(b) and (c), respectively. Emission from the GaN nanowire core is centred around a peak wavelength of 348 nm (3.56 eV), while the emission from MQW, with a much higher intensity, is centred around a peak wavelength of 332 nm as shown in Figure 5.10(d). Hence, in addition to growth and analysis of GaN/AlGaN core-shell, the possibility for incorporation of $Al_xGa_{1-x}N/Al_yGa_{1-y}N$ MQWs for UV emission is demonstrated.

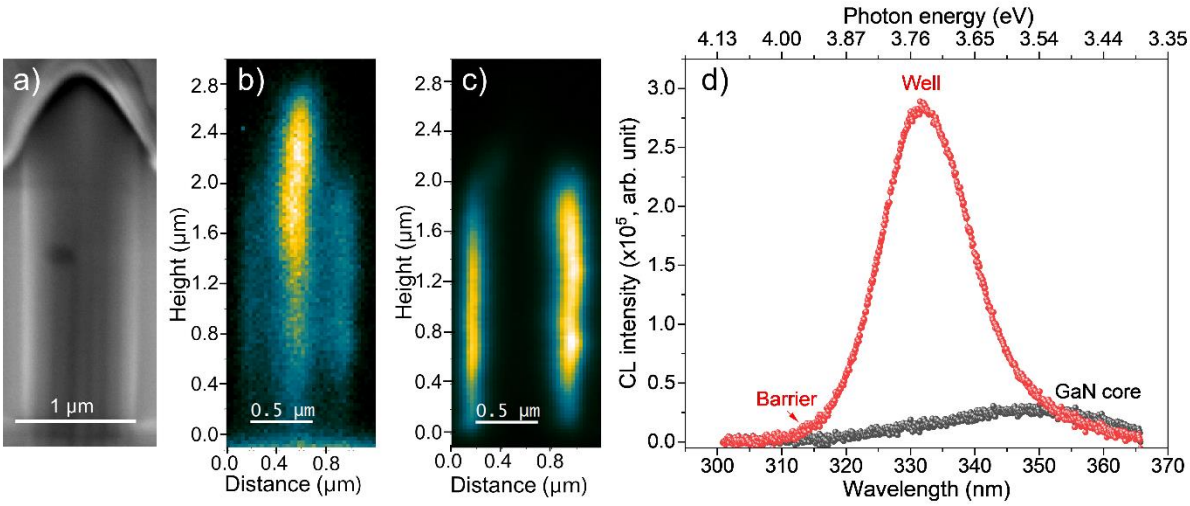

Figure 5.10 (a) SEM image of a partially milled $Al_xGa_{1-x}N/Al_yGa_{1-y}N$ MQW on GaN nanowire. (b) CL mapping showing the 348 nm emission from partially exposed GaN nanowire core. (c) CL mapping showing the 332 nm emission from MQWs on nonpolar *m*-plane sidewalls. (d) CL spectra of the GaN nanowire core and the MQW.

5.9. Summary

Growth of GaN/AlGaN core-shell nanowire array using MOCVD has been presented. Striations, commonly observed on the surface of nonpolar III-nitrides are present when the growth is conducted with H_2 as the carrier gas. The issue of rough surface on *m*-plane AlGaN due to striations has been resolved by growing the AlGaN shells in pure N_2 carrier gas. The achievement of smooth surface on *m*-plane AlGaN sidewalls using N_2 carrier gas is attributed to reduced disparity of Al and Ga adatom diffusion lengths. Alloy compositions of AlGaN shells determined through EDS and CL correlated well, albeit indicating a reduced Al incorporation in the solid phase compared to the gas phase input ratio. The reduced Al-incorporation is primarily attributed to the vertical orientation of the growth surface, while, strain and gas phase parasitic reaction of TMAl also reduces the Al incorporation efficiency. Higher Al content (≥30%) *m*-plane AlGaN shells showed defect-related luminescence and such defects have been identified as $(V_{III}\text{-}2O_N)^{1-}$ complexes. Microstructural characterisation through TEM studies of *m*-plane AlGaN shells revealed that the dominant type of defects are partial dislocations and the formation of partial dislocations increased with Al-content in AlGaN shell to counteract the increased tensile strain. In addition to the growth of GaN/AlGaN core-shell nanowires, incorporation of $Al_xGa_{1-x}N/Al_yGa_{1-y}N$ MQWs has been explored. TEM studies confirmed the successful incorporation of AlGaN MQWs with controlled modulation of Al and Ga compositions with sharp interface between quantum well and barrier. UV emission at a peak wavelength of 332 nm from the AlGaN MQW region inside the nonpolar *m*-plane shell has been demonstrated.

References

1. Grandjean, N., Massies, J. and Leroux, M., "Self-limitation of AlGaN/GaN quantum well energy by built-in polarization field." *Applied Physics Letters*, **1999**, 74, 2361-2363.

2. Miller, D.A.B., Chemla, D.S., Damen, T.C., Gossard, A.C., Wiegmann, W., et al., "Band-Edge Electroabsorption in Quantum Well Structures: The Quantum-Confined Stark Effect." *Physical Review Letters*, **1984**, 53, 2173-2176.

3. Neuschl, B., Helbing, J., Knab, M., Lauer, H., Madel, M., et al., "Composition dependent valence band order in c-oriented wurtzite AlGaN layers." *Journal of Applied Physics*, **2014**, 116, 113506.

4. Murotani, H., Yamada, Y., Miyake, H. and Hiramatsu, K., "Silicon concentration dependence of optical polarization in AlGaN epitaxial layers." *Applied Physics Letters*, **2011**, 98, 021910.

5. Bryan, Z., Bryan, I., Mita, S., Tweedie, J., Sitar, Z., et al., "Strain dependence on polarization properties of AlGaN and AlGaN-based ultraviolet lasers grown on AlN substrates." *Applied Physics Letters*, **2015**, 106, 232101.

6. Atsushi Yamaguchi, A., "Valence band engineering for remarkable enhancement of surface emission in AlGaN deep-ultraviolet light emitting diodes." *physica status solidi c*, **2008**, 5, 2364-2366.

7. Yamaguchi, A.A., "Theoretical investigation of optical polarization properties in Al-rich AlGaN quantum wells with various substrate orientations." *Applied Physics Letters*, **2010**, 96, 151911.

8. Waltereit, P., Brandt, O., Trampert, A., Grahn, H.T., Menniger, J., et al., "Nitride semiconductors free of electrostatic fields for efficient white light-emitting diodes." *Nature*, **2000**, 406, 865-868.

9. Banal, R.G., Taniyasu, Y. and Yamamoto, H., "Deep-ultraviolet light emission properties of nonpolar M-plane AlGaN quantum wells." *Applied Physics Letters*, **2014**, 105, 053104.

10. Matioli, E., Brinkley, S., Kelchner, K.M., Hu, Y.-L., Nakamura, S., et al., "High-brightness polarized light-emitting diodes." *Light: Science & Applications*, **2012**, 1, e22.

11. Taniyasu, Y. and Kasu, M., "Surface 210 nm light emission from an AlN p–n junction light-emitting diode enhanced by A-plane growth orientation." *Applied Physics Letters*, **2010**, 96, 221110.

12. Chen, H., Zhang, X., Chen, S., Fan, A., Li, C., et al., "Properties of Si-doped a-plane AlGaN layers." *Materials Science in Semiconductor Processing*, **2020**, 119, 105270.

13. Song, J. and Han, J., "High Quality, Mass-Producible Semipolar GaN and InGaN Light-Emitting Diodes Grown on Sapphire." *physica status solidi (b)*, **2020**, 257, 1900565.

14. Zhao, Y., Fu, H., Wang, G.T. and Nakamura, S., "Toward ultimate efficiency: progress and prospects on planar and 3D nanostructured nonpolar and semipolar InGaN light-emitting diodes." *Advances in Optics and Photonics*, **2018**, 10, 246-308.

15. Glas, F., "Chapter Two - Strain in Nanowires and Nanowire Heterostructures", in *Semiconductors and Semimetals*, A.F.I. Morral, S.A. Dayeh, and C. Jagadish, Editors. **2015**, Elsevier. p. 79-123.

16. Raychaudhuri, S. and Yu, E.T., "Critical dimensions in coherently strained coaxial nanowire heterostructures." *Journal of Applied Physics*, **2006**, 99, 114308.

17. Nazarenko, M.V., Sibirev, N.V., Wei Ng, K., Ren, F., Son Ko, W., et al., "Elastic energy relaxation and critical thickness for plastic deformation in the core-shell InGaAs/GaAs nanopillars." *Journal of Applied Physics*, **2013**, 113, 104311.

18. Dai, J., Liu, B., Zhuang, Z., He, G., Zhi, T., et al., "Fabrication of AlGaN nanorods with different Al compositions for emission enhancement in UV range." *Nanotechnology*, **2017**, 28, 385205.

19. Zhang, L., Guo, Y., Yan, J., Wu, Q., Lu, Y., et al., "Deep ultraviolet light-emitting diodes based on a well-ordered AlGaN nanorod array." *Photonics Research*, **2019**, 7, B66-B72.

20. Liu, X., Mashooq, K., Szkopek, T. and Mi, Z., "Improving the Efficiency of Transverse Magnetic Polarized Emission from AlGaN Based LEDs by Using Nanowire Photonic Crystal." *IEEE Photonics Journal*, **2018**, 10, 1-11.

21. Djavid, M. and Mi, Z., "Enhancing the light extraction efficiency of AlGaN deep ultraviolet light emitting diodes by using nanowire structures." *Applied Physics Letters*, **2016**, 108, 051102.

22. Yamada, H., Iso, K., Saito, M., Fujito, K., DenBaars, S.P., et al., "Impact of Substrate Miscut on the Characteristic of m-plane InGaN/GaN Light Emitting Diodes." *Japanese Journal of Applied Physics*, **2007**, 46, L1117-L1119.

23. Wernicke, T., Ploch, S., Hoffmann, V., Knauer, A., Weyers, M., et al., "Surface morphology of homoepitaxial GaN grown on non- and semipolar GaN substrates." *physica status solidi (b)*, **2011**, 248, 574-577.

24. Farrell, R.M., Haeger, D.A., Chen, X., Gallinat, C.S., Davis, R.W., et al., "Origin of pyramidal hillocks on GaN thin films grown on free-standing m-plane GaN substrates." *Applied Physics Letters*, **2010**, 96, 231907.

25. Yamada, H., Chonan, H., Takahashi, T. and Shimizu, M., "Impact of substrate off-angle on the m-plane GaN Schottky diodes." *Japanese Journal of Applied Physics*, **2018**, 57, 04FG01.

26. Tanaka, A., Barry, O., Nagamatsu, K., Matsushita, J., Deki, M., et al., "Facet dependence of leakage current and carrier concentration in m-plane GaN Schottky barrier diode fabricated with MOVPE." *physica status solidi (a)*, **2017**, 214, 1600829.

27. Bobea Graziano, M., Bryan, I., Bryan, Z., Kirste, R., Tweedie, J., et al., "Structural characteristics of m-plane AlN substrates and homoepitaxial films." *Journal of Crystal Growth*, **2019**, 507, 389-394.

28. Lymperakis, L. and Neugebauer, J., "Large anisotropic adatom kinetics on nonpolar GaN surfaces: Consequences for surface morphologies and nanowire growth." *Physical Review B*, **2009**, 79, 241308.

29. Jindal, V. and Shahedipour-Sandvik, F., "Density functional theoretical study of surface structure and adatom kinetics for wurtzite AlN." *Journal of Applied Physics*, **2009**, 105, 084902.

30. Hirai, A., Jia, Z., Schmidt, M.C., Farrell, R.M., DenBaars, S.P., et al., "Formation and reduction of pyramidal hillocks on m-plane {$1\bar{1}00$} GaN." *Applied Physics Letters*, **2007**, 91, 191906.

31. Farrell, R.M., Haeger, D.A., Fujito, K., DenBaars, S.P., Nakamura, S., et al., "Morphological evolution of InGaN/GaN light-emitting diodes grown on free-standing m-plane GaN substrates." *Journal of Applied Physics*, **2013**, 113, 063504.

32. Tanaka, A., Ando, Y., Nagamatsu, K., Deki, M., Cheong, H., et al., "m-Plane GaN Schottky Barrier Diodes Fabricated with MOVPE Layer on Several Off-Angle m-Plane GaN Substrates." *physica status solidi (a)*, **2018**, 215, 1700645.

33. Bryan, I., Bryan, Z., Bobea, M., Hussey, L., Kirste, R., et al., "Homoepitaxial AlN thin films deposited on m-plane ($1\bar{1}00$) AlN substrates by metalorganic chemical vapor deposition." *Journal of Applied Physics*, **2014**, 116, 133517.

34. Venezuela, P. and Tersoff, J., "Alloy decomposition during growth due to mobility differences." *Physical Review B*, **1998**, 58, 10871-10874.

35. Banal, R.G., Funato, M. and Kawakami, Y., "Surface diffusion during metalorganic vapor phase epitaxy of AlN." *physica status solidi (c)*, **2009**, 6, 599-602.

36. Narita, T., Honda, Y., Yamaguchi, M. and Sawaki, N., "The surface diffusion of Ga on an AlGaN/GaN stripe structure in the selective MOVPE." *physica status solidi (b)*, **2006**, 243, 1665-1668.

37. Kangawa, Y., Akiyama, T., Ito, T., Shiraishi, K. and Nakayama, T., "Surface Stability and Growth Kinetics of Compound Semiconductors: An Ab Initio-Based Approach." *Materials*, **2013**, 6, 3309.

38. Rozhavskaya, M.M., Lundin, W.V., Troshkov, S.I., Tsatsulnikov, A.F. and Dubrovskii, V.G., "Determination of the diffusion lengths of Ga adatoms using GaN stripe profiling." *physica status solidi (a)*, **2015**, 212, 851-854.

39. Yamaguchi, S., Kariya, M., Kosaki, M., Yukawa, Y., Nitta, S., et al., "Control of strain in GaN by a combination of H2 and N2 carrier gases." *Journal of Applied Physics*, **2001**, 89, 7820-7824.

40. Kakanakova-Georgieva, A., Gueorguiev, G.K., Stafström, S., Hultman, L. and Janzén, E., "AlGaInN metal-organic-chemical-vapor-deposition gas-phase chemistry in hydrogen and nitrogen diluents: First-principles calculations." *Chemical Physics Letters*, **2006**, 431, 346-351.

41. Barry, O.I., Lekhal, K., Bae, S.-Y., Lee, H.-J., Pristovsek, M., et al., "Reduction of Residual Impurities in Homoepitaxial m-Plane GaN by Using N2 Carrier Gas in Metalorganic Vapor Phase Epitaxy." *physica status solidi (RRL) – Rapid Research Letters*, **2018**, 12, 1800124.

42. Schneider, C.A., Rasband, W.S. and Eliceiri, K.W., "NIH Image to ImageJ: 25 years of image analysis." *Nature Methods*, **2012**, 9, 671-675.

43. Tang, L., Tang, B., Zhang, H. and Yuan, Y., "Review—Review of Research on AlGaN MOCVD Growth." *ECS Journal of Solid-State Science and Technology*, **2020**, 9, 024009.

44. Lundin, W.V., Nikolaev, A.E., Rozhavskaya, M.M., Zavarin, E.E., Sakharov, A.V., et al., "Fast AlGaN growth in a whole composition range in planetary reactor." *Journal of Crystal Growth*, **2013**, 370, 7-11.

45. Dinh, D.V., Alam, S.N. and Parbrook, P.J., "Effect of V/III ratio on the growth of (112¯2) AlGaN by metalorganic vapour phase epitaxy." *Journal of Crystal Growth*, **2016**, 435, 12-18.

46. Huang, G.S., Yao, H.H., Kuo, H.C. and Wang, S.C., "Effect of growth conditions on the Al composition and quality of AlGaN film." *Materials Science and Engineering: B*, **2007**, 136, 29-32.

47. Vurgaftman, I. and Meyer, J.R., "Band parameters for nitrogen-containing semiconductors." *Journal of Applied Physics*, **2003**, 94, 3675-3696.

48. Wright, A.F., "Elastic properties of zinc-blende and wurtzite AlN, GaN, and InN." *Journal of Applied Physics*, **1997**, 82, 2833-2839.

49. Yan, Q., Rinke, P., Janotti, A., Scheffler, M. and Van de Walle, C.G., "Effects of strain on the band structure of group-III nitrides." *Physical Review B*, **2014**, 90, 125118.

50. Nepal, N., Nakarmi, M.L., Lin, J.Y. and Jiang, H.X., "Photoluminescence studies of impurity transitions in AlGaN alloys." *Applied Physics Letters*, **2006**, 89, 092107.

51. Yun, F., Reshchikov, M.A., He, L., King, T., Morkoc, H., et al., "Energy band bowing parameter in AlxGa1-xN alloys." *Journal of Applied Physics*, **2002**, 92, 4837-4839.

52. Hoshi, T., Hazu, K., Ohshita, K., Kagaya, M., Onuma, T., et al., "Impacts of anisotropic lattice relaxation on crystal mosaicity and luminescence spectra of m-plane $Al_xGa_{1-x}N$ films grown on m-plane freestanding GaN substrates by NH_3 source molecular beam epitaxy." *Applied Physics Letters*, **2009**, 94, 071910.

53. Van de Walle, C.G., " DX-center formation in wurtzite and zinc-blende $Al_xGa_{1-x}N$." *Physical Review B*, **1998**, 57, R2033-R2036.

54. Mattila, T., Nieminen R.M., "Ab initio study of oxygen point defects in GaAs, GaN, and AlN." *Physical Review B*, **1996**, 54**,** 16676-16682.

55. McCluskey, M. D., Johnson, N.M., Van de Walle, C.G., Bour, D.P., Kneissl, M., et al. "Evidence for oxygen DX centers in AlGaN." *MRS Online Proceedings Library*, **1998**, 512**,** 531-536.

56. McCluskey, M. D., Johnson, N.M., Van de Walle, C.G., Bour, D.P., Kneissl, M., et al. "Metastability of oxygen donors in AlGaN." *Physical Review Letters*, **1998**, 80, 4008-4011.

57. McCluskey, M. D., Van de Walle, C.G., Johnson, N.M., Bour, D.P., and Kneissl, M., "DX centers in AlGaN." *International Journal of Modern Physics B*, **1999**, 13, 1363-1378.

58. Van de Walle, C.G., Neugebauer, J., "Universal alignment of hydrogen levels in semiconductors, insulators and solutions." *Nature*, **2003**, 423, 626-628.

59. Chakrapani, V., "Universal alignment of surface and bulk oxygen levels in semiconductors." *Applied Physics Letters*, **2021**, 119, 021601.

60. Reshchikov, M.A., Morkoc, H., "Luminescence properties of defects in GaN." *Journal of Applied Physics*, **2005**, 97, 061301.

61. Alden, D., Harris, J.S., Bryan, Z., Baker, J.N., Reddy, P., et al. "Point-defect nature of the ultraviolet absorption band in AlN." *Physical Review Applied*, **2018**, 9, 054036.

62. Yang, H.C., Lin, T.Y. and Chen, Y.F., "Nature of the 2.8-eV photoluminescence band in Si-doped GaN." *Physical Review B*, **2000**, 62, 12593-12596.

63. Wang, W.-Y., Jin, P., Liu, G.-P., Li, W., Liu, B., et al., "Effect of high-temperature annealing on AlN thin film grown by metalorganic chemical vapor deposition." *Chinese Physics B*, **2014**, 23, 087810.

64. Mehnke, F., Fischer, A.M., Xu, Z., Bouchard, H., Detchprohm, T., et al., "Realizing crack-free high-aluminum-mole-fraction AlGaN on patterned GaN beyond the critical layer thickness." *Journal of Applied Physics*, **2022**, 131, 073103.

65. Kueller, V., Knauer, A., Brunner, F., Zeimer, U., Rodriguez, H., et al., "Growth of AlGaN and AlN on patterned AlN/sapphire templates." *Journal of Crystal Growth*, **2011**, 315, 200-203.

66. Follstaedt, D.M., Allerman, A.A., Lee, S.R., Michael, J.R., Bogart, K.H.A., et al., "Dislocation reduction in AlGaN grown on patterned GaN." *Journal of Crystal Growth*, **2008**, 310, 766-776.

67. Bell, A., Liu, R., Parasuraman, U.K., Ponce, F.A., Kamiyama, S., et al., "Spatial variation of luminescence from AlGaN grown by facet controlled epitaxial lateral overgrowth." *Applied Physics Letters*, **2004**, 85, 3417-3419.

68. Ishibashi, A., Murotani, H., Yokogawa, T. and Yamada, Y., "Spatial Inhomogeneity of Aluminum Content in Air-Bridged Lateral Epitaxially Grown AlGaN Ternary Alloy Films Probed by Cross-Sectional Scanning Near-Field Optical Microscopy." *Japanese Journal of Applied Physics*, **2012**, 51, 035604.

69. Dinh, D.V., Hu, N., Honda, Y., Amano, H. and Pristovsek, M., "Aluminium incorporation in polar, semi- and non-polar AlGaN layers: a comparative study of x-ray diffraction and optical properties." *Scientific Reports*, **2019**, 9, 15802.

70. Jindal, V., Grandusky, J., Jamil, M., Tripathi, N., Thiel, B., et al., "Effect of interfacial strain on the formation of AlGaN nanostructures by selective area heteroepitaxy." *Physica E: Low-dimensional Systems and Nanostructures*, **2008**, 40, 478-483.

71. He, C., Qin, Z., Xu, F., Zhang, L., Wang, J., et al., "Mechanism of stress-driven composition evolution during hetero-epitaxy in a ternary AlGaN system." *Scientific Reports*, **2016**, 6, 25124.

72. Coltrin, M.E., Randall Creighton, J. and Mitchell, C.C., "Modeling the parasitic chemical reactions of AlGaN organometallic vapor-phase epitaxy." *Journal of Crystal Growth*, **2006**, 287, 566-571.

73. Floro, J.A., Follstaedt, D.M., Provencio, P., Hearne, S.J. and Lee, S.R., "Misfit dislocation formation in the AlGaN/GaN heterointerface." *Journal of Applied Physics*, **2004**, 96, 7087-7094.

74. Liliental-Weber, Z., Jasiński, J. and Zakharov, D., "GaN grown in polar and non-polar directions." *Opto-Electronics Review*, **2004**, 12, 339-346.

75. Philippe, V., Zahia, B. and Tobias, G., "Microstructural Characterization of Semipolar GaN Templates and Epitaxial-Lateral-Overgrown Films Deposited on M -Plane Sapphire by Metalorganic Vapor Phase Epitaxy." *Japanese Journal of Applied Physics*, **2007**, 46, 4089.

76. Craven, M.D., Lim, S.H., Wu, F., Speck, J.S. and DenBaars, S.P., "Structural characterization of nonpolar (11$\bar{2}$0) a-plane GaN thin films grown on (1$\bar{1}$02) r-plane sapphire." *Applied Physics Letters*, **2002**, 81, 469-471.

77. Zakharov, D.N., Liliental-Weber, Z., Wagner, B., Reitmeier, Z.J., Preble, E.A., et al., "Structural TEM study of nonpolar a-plane gallium nitride grown on (11$\bar{2}$0) 4H-SiC by organometallic vapor phase epitaxy." *Physical Review B*, **2005**, 71, 235334.

78. Hÿtch, M.J., Snoeck, E. and Kilaas, R., "Quantitative measurement of displacement and strain fields from HREM micrographs." *Ultramicroscopy*, **1998**, 74, 131-146.

79. Du, H. "Geometrical phase analysis software." **2018** [Accessed on: 16/11/2021]; Available from: https://er-c.org/index.php/software/stem-data-analysis/gpa/.

80. "DigitalMicrograph Software." [Accessed on: 11/10/2021]; Available from: https://www.gatan.com/products/tem-analysis/gatan-microscopy-suite-software.

Chapter 6. Growth and Characterisation of $Al_xGa_{1-x}N/Al_yGa_{1-y}N$ Multiple Quantum Wells

6.1. Introduction

AlGaN alloys offer tunable direct bandgap from 3.4 to 6.2 eV with corresponding emission wavelength range from 200 to 365 nm. This unique property is unmatched by any other semiconductor material and hence, $Al_xGa_{1-x}N/Al_yGa_{1-y}N$ multiple quantum wells (MQWs) undoubtedly form the backbone for solid-state ultraviolet (UV) light sources. The major issue with AlGaN-based UV light emitting diodes (LEDs) is their poor external quantum efficiency (EQE). EQE of UV-LEDs for emission wavelengths shorter than 365 nm has stagnated to a value less than 10% [1]. With efforts on improving the light extraction efficiency (LEE) from planar AlGaN MQW, the highest EQE of 20.3% has been reported in 2017 for UV LED with a peak emission wavelength of 275 nm and this record still holds today [2]. To put this in the context of LEDs, this EQE is still modest compared to the 84.3% EQE achieved on InGaN/GaN blue LEDs [3]. Apart from low LEE, low EQE is also a direct consequence of low internal quantum efficiency (IQE), which in turn depends on orientation of the quantum wells (polar or nonpolar) and dislocation density. Thus, choosing the right MQW orientation, reducing the dislocation density and improving LEE are all important to achieve efficient UV emission.

Polar *c*-plane MQWs of wurtzite III-nitride semiconductor encounters an inherent internal electric field due to spontaneous and piezoelectric polarisations. This built-in electric field gives rise to spatially separated electron and hole wavefunctions that results in weak intensity and redshift of emission wavelength, referred to as quantum-confined Stark effect (QCSE) [4, 5]. Experimentally, a much longer exciton decay time of ≥ 6 ns has been observed on polar *c*-plane GaN/AlGaN MQWs, compared to 450 ps on nonpolar *m*-plane [6]. Such long radiative recombination lifetime for MQWs in polar *c*-plane implies a low IQE for LEDs.

Further, the redshift of emission wavelength due to QCSE on polar *c*-plane MQWs seldom goes to the extent of "below the bandgap emission", and puts a severe limit on QW-width. Therefore, the advantage of relatively thicker quantum wells, which provide a larger recombination volume and hence higher light output cannot be implemented in *c*-plane MQWs. The QW width for GaN/AlGaN MQWs on polar *c*-plane is limited to less than 3 nm to observe emission above the GaN bandgap [7-9]. Kajitani *et al.* reported that $Al_{0.15}Ga_{0.85}N$ MQWs on polar *c*-plane showed the highest photoluminescence (PL) intensity at QW-widths of 1.5 and 2 nm for barrier Al compositions of 30 and 40%, respectively, while PL intensity decreased with increasing QW width in both cases [10]. Further, GaN/AlGaN MQWs on polar *c*-plane cease to show PL when the well width exceeded 5 nm [11]. Nonpolar *m*-plane sidewalls available on GaN nanowires provide a path to study and alleviate these issues arising out of QCSE for efficient UV emission.

Unlike the efficient GaN/InGaN-based blue LEDs, IQE for AlGaN MQWs is much more sensitive to the dislocation density of underlying the AlGaN layer. Excitation density-dependent PL measurement revealed a drastic drop in IQE of AlGaN MQWs from 64% to a mere 4% for a change in dislocation density from $2x10^8$ to $6x10^9$ cm^{-2} [12]. This critical issue of low IQE in planar AlGaN due to threading dislocations may be resolved by using dislocation-free Al(Ga)N nanowires. Dislocation-free Ga-polar GaN nanowires can be achieved by selective area growth (SAG) on GaN pseudo-substrates using metal organic chemical vapour deposition (MOCVD) as discussed in Chapter 4 and reported by others [13-16]. Hence, using dislocation-free selective area grown GaN nanowires as template for subsequent growth of AlGaN has the potential to resolve low IQE.

Using nanowire architecture also alleviates the long-standing issue of low conductivity in p-type Al(Ga)N planar layers leading to low injection efficiency. Enhanced Mg incorporation up to ~$1.5x10^{20}$ cm^{-3} by co-doping with indium [17], low activation energy of 23 meV for Mg-dopant [18], and high hole concentration of ~$6x10^{17}$ cm^{-3} have been reported in AlN nanowires [19]. Additionally, nanowires offer the potential for better light extraction efficiency compared to planar UV LEDs [20-22]. Nanowire array based AlGaN UV LED fabricated by top-down approach has demonstrated enhancement in light output power and EQE by 2.5 times compared to the planar LEDs, reaching an EQE of ~6% in the nanowire array UV LEDs [23].

In spite of the tremendous potential of AlGaN nanostructures to enhance the performance of UV LEDs, limited reports exist for AlGaN MQW growth on nanowires by MOCVD [24-27], possibly due to the difficulty in growth of AlGaN nanowires [28]. Further, the reports for

nanowire-based UV LED structures obtained by using MOCVD are either through Au-seeded vapour-liquid-solid (VLS) growth method [24], top-down etch and subsequent regrowth [25, 26], or through self-assembled N-polar GaN nanowires approach [27]. Therefore, a thorough investigation on bottom-up approach for regularly arranged AlGaN nanowires for UV emission is seriously lacking.

The key to realisation of efficient AlGaN nanowire-based UV LEDs lies in the successful growth of $Al_xGa_{1-x}N/Al_yGa_{1-y}N$ MQWs in the nanowires. As AlGaN MQW growth has been introduced towards the end of Chapter 5, this chapter focuses on the MQWs, and all of the nanowires discussed here consist of AlGaN MQWs. The growth of AlGaN immediately follows the SAG of GaN nanowire array in a single-run approach without having to remove and process the sample. GaN nanowire arrays are grown on n-type GaN pseudo-substrate (4 μm-thick GaN on sapphire), thus provides a dislocation-free nanowire array as well as paving the way for future electrically injected nanowire array UV-LEDs. The morphology of AlGaN nanostructures consisting of MQWs and their growth mechanism in MOCVD are analysed. Finally, tunable UV emission from nonpolar *m*-plane $Al_xGa_{1-x}N/Al_yGa_{1-y}N$ MQWs is demonstrated in the range of 318 - 343 nm.

6.2. Experimental methods

GaN pseudo-substrates

Growth of planar GaN layer is carried out on 2-inch *c*-plane sapphire substrates in an Aixtron 3×2-inch close-coupled showerhead MOCVD reactor. A 2.5 μm-thick undoped GaN layer followed by a 1.5 μm-thick Si-doped n-type GaN is deposited. Such substrates with a total GaN thickness of 4 μm on *c*-plane sapphire, referred to as GaN pseudo-substrates, are used for SAG of GaN nanowires after patterning.

Substrate preparation for SAG

A 15 nm-thick SiO_x layer is deposited on the GaN pseudo-substrates using an atomic layer deposition system (Picosun SUNALE™) to serve as the mask during SAG. A 100 nm-thick electron-beam resist (mr-PosEBR, micro resist technology GmbH) is spin-coated on top of the SiOx layer. Further, a water-based anti-charging agent (DisCharge, DisChem Inc. USA) for electron-beam lithography (EBL) is spin-coated on top of the electron-beam resist to avoid charging during electron beam exposure. Circular openings with diameters of 100, 200 and 400 nm, each with different pitch sizes of 1, 1.5, and 2 μm are defined using electron-beam

lithography (Raith 150). After the EBL exposure, the anti-charging agent is rinsed in deionised water and blown dry with a nitrogen gun. The electron-beam resist is then developed using n-amyl acetate for 30 seconds, followed by rinsing in isopropyl alcohol for 60 seconds. The patterns are then transferred by etching the SiO_x layer using a reactive-ion etching system with CHF_3 chemistry. The remaining electron-beam resist after the pattern transfer is removed using acetone in an ultrasonic bath and subsequently cleaned with isopropyl alcohol and deionised water. Further, an oxygen plasma treatment is carried out using a barrel etcher (PVA Tepla 400) to remove any residual organic contaminants. The patterned 2-inch wafer is then diced into 1×1 cm^2 pieces for SAG using a wafer dicing machine (DAD321, Disco Japan). Subsequently, the patterned wafer pieces are cleaned by ultrasonication in acetone, isopropyl alcohol and deionised water before loading into the MOCVD.

Growth of AlGaN MQW on GaN nanowires

Initially, SAG of GaN nanowires is carried out on the patterned substrates using triethylgallium (13.6 μmol/min) and NH_3 (535 μmol/min) at a growth temperature of 950 °C in a mixed carrier gas composed of $4H_2 + 6N_2$. A buffer $Al_yGa_{1-y}N$ shell of approximately 80 nm thick is grown immediately after the GaN nanowire growth by introducing trimethylaluminium (8.8 μmol/min) and reducing the triethylgallium flow (10.2 μmol/min) while maintaining the same NH_3 flow (535 μmol/min). Subsequently, five pairs of $Al_xGa_{1-x}N/Al_yGa_{1-y}N$ MQWs are grown on this buffer AlGaN shell. After the growth of last barrier, a 45 nm-thick Mg-doped AlGaN shell with a graded Al composition is grown. The growth of AlGaN is carried out in pure N_2 carrier gas and at a reduced temperature of 930 °C with a small additional injection of trimethylindium (5.0 μmol/min). Trimethylindium is used as a surfactant to promote adatom mobilities of Al and Ga during the growth of AlGaN in N_2 carrier gas. Growth temperature in excess of 900 °C, low flow-rate of trimethylindium and absence of any characteristic peak in cathodoluminescence at wavelength longer than 365 nm rules out any In incorporation.

Lamella preparation for TEM studies

Electron-transparent lamellae used for structural characterisation by transmission electron microscopy (TEM) are prepared using a Zeiss Crossbeam 550 focused ion beam (FIB) system. Before loading into the FIB, the substrate with selective area-grown nanowires is spin-coated with ma-P 1210 photoresist (micro resist technology GmbH) to fill-up the gaps between nanowires to avoid Pt deposition in the gaps. Subsequently, a 15 nm-thick Au layer is deposited to mitigate charging in the FIB due to the insulating sapphire substrate. In the FIB, a 1 μm-thick

Pt strip is deposited over a few rows of nanowires to avoid Ga ion beam damage. A lamella containing the nanowires is cut out of the substrate. A standard lift-out procedure is used to pick up the lamella which is then glued to a half Cu grid. The lamella on half Cu grid is milled to a final thickness of ~100 nm for TEM observations.

Characterisation methods

Morphology of the AlGaN nanowires are analysed using an FEI Verios 460 scanning electron microscope (SEM). Cathodoluminescence (CL) is carried out at room temperature using a Gatan MonoCL4 inside the same SEM on single nanowires transferred to Si substrates. High-resolution transmission electron microscopy (HRTEM) and high-angle annular dark field scanning transmission electron microscopy (HAADF-STEM) are carried out in a JEOL 2100F FEGTEM.

6.3. Morphology and growth mechanism of AlGaN MQW on GaN nanowires

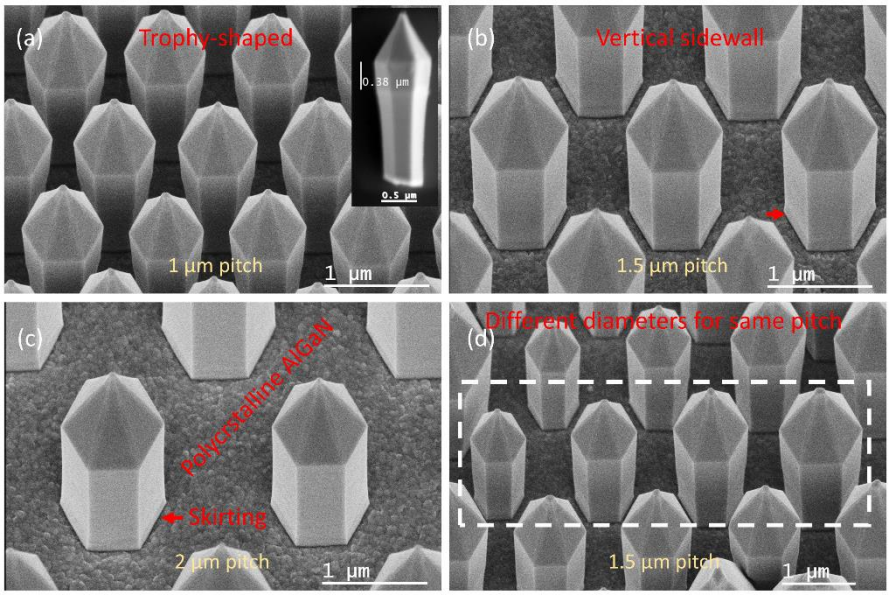

Figure 6.1 Scanning electron micrographs for arrays of GaN nanowires with $Al_xGa_{1-x}N/Al_yGa_{1-y}N$ MQWs for a pitch of (a) 1, (b) 1.5 and (c) 2 µm, and (d) varied mask opening diameters ranging from 100 to 400 nm in increments of 100 nm for a fixed pitch of 1.5 µm. The inset in (a) shows the side view of an individual nanowire with $Al_xGa_{1-x}N/Al_yGa_{1-y}N$ MQWs transferred to a Si substrate.

Figure 6.1 shows the SEM images of nanowires with $Al_xGa_{1-x}N/Al_yGa_{1-y}N$ MQWs incorporated on the sidewalls of GaN nanowires. Figure 6.1(a) – (c) shows the nanowire array with a pitch size of 1, 1.5 and 2 µm, respectively. The diameter of the circular openings for SAG of GaN nanowires in this case is 200 nm. The morphology adopts a characteristic shape with an enlarged diameter at the top and tapering down towards the bottom, resembling that of a "trophy" when the pitch is small (1 µm) as shown in Fig. 1(a) and the inset therein. Nanowire array with uniform shape and straight sidewalls are obtained for pitch ≥ 1.5 µm as evident from Figure 6.1(b) and (c). The development of "skirting" at the base of nanostructures, indicated by red arrows in Figure 6.1(b) and (c) is another interesting characteristic. Additionally, parasitic deposition of polycrystalline AlGaN on the masked area due to the low mobility and high sticking coefficient of Al adatoms is clearly visible on samples with larger pitch [29, 30].

The observed morphologies of trophy-shaped, uniform sidewall, and skirting in the GaN/AlGaN nanostructure will be discussed within the context of source-supply mechanisms of SAG in MOCVD. The major flux supply paths for SAG in MOCVD may be classified into two as:

(i) vapour phase diffusion (VPD), and

(ii) surface diffusion on the mask (SDM).

VPD induced SAG has a direct diameter-height relationship, i.e. nanowire with larger diameter grows taller. On the other hand, SDM dominant SAG has the characteristics of inverse diameter-height relationship. In order to verify the predominant flux supply mechanism, we have incorporated mask opening diameters of 100, 200, 300 and 400 nm in an array with a fixed pitch of 1.5 µm. The resulting morphology of $Al_xGa_{1-x}N/Al_yGa_{1-y}N$ structure on this array is shown in Figure 6.1(d). The observation of taller structures for larger diameters, as can be seen highlighted by a white dashed rectangle, implies that the growth of $Al_xGa_{1-x}N/Al_yGa_{1-y}N$ on GaN nanowires is predominantly driven by VPD mechanism. The reason for VPD being the predominant source-supply mechanism in SAG of AlGaN is due to the small diffusion length of Al adatom. Diffusion length of Al adatom on (0001) AlN surface at a growth temperature of 1200 °C has been reported to be 44 nm in migration enhanced epitaxy, and is further reduced to 31 nm in simultaneous source supply growth [31]. Such low diffusion lengths cannot support the vertical growth via SDM and results in predominantly VPD growth.

The schematic illustrations of VPD and SDM are shown in Figure 6.2. The predominant flux supply mechanism of VPD, identified in the case of AlGaN growth can be further classified

into two diffusion components due to the concentration gradients in vertical and lateral directions as:

(i) vertical vapour diffusion, and

(ii) lateral vapour diffusion.

In VPD driven SAG, the top facet receives flux from direct impingement through vertical vapour diffusion and the sidewalls receive flux from lateral vapour diffusion as shown in Figure 6.2(a) for nanowire array with a large pitch. Figure 6.2(b) illustrates the case of VPD for AlGaN growth on GaN nanowires with a small pitch.

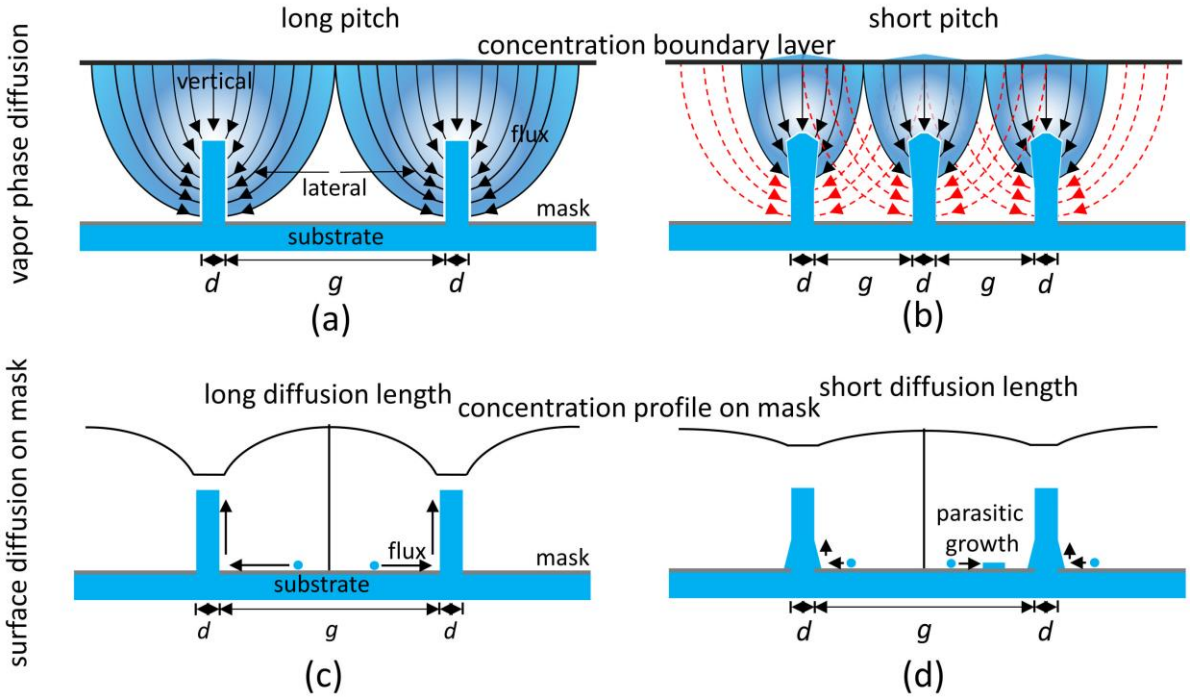

Figure 6.2 Schematic illustration of flux supply during SAG in MOCVD. Vapour phase diffusion (VPD) modes for (a) large and (b) small pitch size of the nanowire array. Surface diffusion on the mask (SDM) for (c) long and (d) short diffusion lengths of adatoms.

i. Uniform nanowires:

$Al_xGa_{1-x}N/Al_yGa_{1-y}N$ structures with uniform sidewalls are observed for pitch ≥ 1.5 µm as already shown in Figure 6.1(b) and (c). This observation suggests that each nanowire in the array receives sufficient lateral vapour diffusion flux without competition from neighbouring nanowires. This condition of SAG through mass transport by VPD is schematically illustrated

as Figure 6.2(a), where the pitch is sufficiently large and the whole length of nanowire receives uniform flux from lateral vapour diffusion, resulting in nanowire with uniform sidewalls.

Lateral vapour diffusion length, $\lambda_{lateral}$, of Al in VPD may now be determined from this condition with the premise that, a pitch of 1.5 µm is adequate to provide uniform flux throughout an array of nanowires with a height of 1.8 µm. However, it is important to note that, due to substantial lateral growth, the diameter, *d*, of GaN/AlGaN nanowire is significantly increased. Hence, it is more meaningful to define $\lambda_{lateral}$ with the gap, *g*, between the nanowires (*g* = pitch – diameter) such that $\lambda_{lateral} = g/2$. Using the pitch and measured diameter of nanowire, 1500 nm and 900 nm, respectively, we obtain $\lambda_{lateral}$ = 300 nm. Hence, for 1.8 µm-long GaN/AlGaN nanowires, a minimum gap of 600 nm needs to be maintained between the adjacent nanowires for uniform lateral flux to achieve straight sidewalls.

ii. Trophy-shaped nanowires:

Trophy-shaped AlGaN nanowires have been obtained when the pitch is reduced to 1 µm as shown in Figure 6.1(a). With a diameter of ~750 nm at the top and a pitch of 1 µm, the gap, *g,* between neighbouring AlGaN nanowires in this case is 250 nm, which is well below the necessary gap of 600 nm. As a consequence of close proximity, adjacent nanowires compete for flux and results in reduced flux for each nanowire at the top (vertical vapour diffusion) as well as on the sidewalls (lateral vapour diffusion) as schematically shown in Figure 6.2(b). The reduced flux due to proximity of nanowires is indicated by red dashed lines in the Figure 6.2(b), and notably becomes increasingly depleted towards the bottom of the nanowire. As a result, for reduced pitch (gap ≤ 600 nm), SAG of AlGaN on GaN nanowires encounters a shadowing effect. The contribution in AlGaN growth by non-shadowed flux, represented by black arrows in Figure 6.2(b), creates a distinctive hexagonal section with larger diameter near the top of nanowire. On the other hand, lateral growth towards the bottom of nanowire is increasingly impeded due to shadowing effect and results in the trophy-shaped nanowire morphology.

iii. Skirting and parasitic growth:

Figure 6.2(c) and (d) schematically illustrates the cases of SDM driven SAG for large and small diffusion lengths of adatoms, respectively. Figure 6.2(d) illustrates the case of standard SAG with flux supply through SDM where the diffusion lengths on the mask as well as on the nanowire sidewalls are large. Such a case results in growth of long nanowires with uniform diameters. A smaller diameter nanowire possessing a smaller cross section grows faster compared to a larger diameter nanowire. This is referred to as the inverse diameter-height

relationship and observed in SAG of GaN. Figure 6.2(d) illustrates the SAG mechanism for adatom with small diffusion lengths, applicable to the growth of AlGaN on GaN nanowires. In this case, only adatoms very close to the bottom of nanowire can contribute to the growth due to their small diffusion length. The limited mobility of adatoms on the mask and more importantly on the sidewalls results in "skirting" at the bottom of nanowire. The adatoms beyond the diffusion length will either re-evaporate or cause parasitic growth. High reactivity and high sticking coefficient of Al adatoms result in parasitic polycrystalline AlGaN deposition on the masked region during SAG [32, 33].

6.4. Growth rate and surface energy ratios of AlGaN facets

Figure 6.3(a) shows a high angle annular dark field – scanning transmission electron microscopy (HAADF-STEM) image of the top section of AlGaN MQWs grown on GaN nanowire. A measured angle of about 62° for the inclined sidewall facet with respect to (0001) confirms the inclined planes as semipolar $\{10\bar{1}1\}$ planes. The thicknesses of AlGaN along the vertical direction due to growth on (0001) plane, along the lateral direction due to growth on $\{10\bar{1}0\}$ planes and on the top inclined $\{10\bar{1}1\}$ planes are determined as 132, 77 and 20 nm, respectively, for a growth duration of 30 minutes. Ratios of growth rate, which facilitate better interpretability than the individual growth rates, are calculated with respect to (0001) and listed in Table 6.1. A growth rate ratio of 0.58 is obtained for AlGaN on $\{10\bar{1}0\}$ planes which agrees remarkably well with the surface energy ratio of 0.59 or 0.60 reported for GaN [34, 35]. This ratio implies a lateral to vertical growth rate of 58% in AlGaN. Lateral to vertical growth rates of about 25 to 35% has been reported for SAG of AlN in MBE [36, 37]. The higher value of lateral to vertical growth rate observed in MOCVD is a result of vapour-phase diffusion (VPD) dominated growth of AlGaN. The lateral growth of 58% for AlGaN in MOCVD signify two important points. First, achieving AlGaN nanowires with high aspect ratio will be more difficult in MOCVD than MBE. Second, growth of an AlGaN shell on existing nanowires will be more efficient in MOCVD than MBE. We take advantage of this efficient lateral growth in MOCVD to incorporate nonpolar *m*-plane AlGaN MQWs for UV emission.

Table 6.1 Experimentally determined growth rate ratios for AlGaN on $\{10\bar{1}0\}$ and $\{10\bar{1}1\}$ planes with respect to (0001) plane and the surface energy ratios of GaN deduced from surface energies reported in literature [34, 35].

Crystal plane		AlGaN: growth rate ratio with respect to (0001)	GaN: surface energy ratio with respect to (0001) [34, 35]
Name	Index		
c	(0001)	1	1
m	$\{10\bar{1}0\}$	0.58	0.59, 0.60
s	$\{10\bar{1}1\}$	0.15	1.19
-c	$(000\bar{1})$	-	1.19

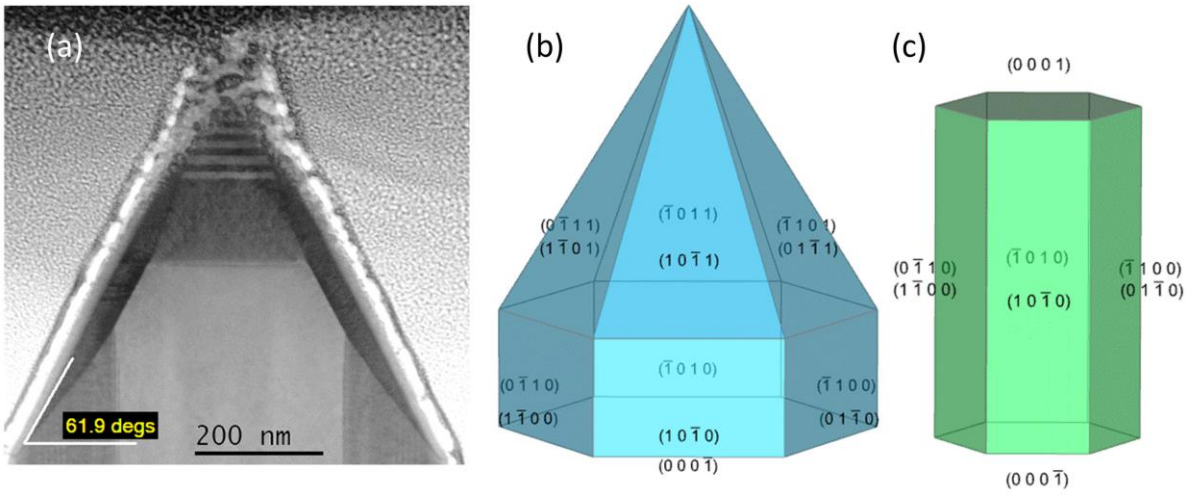

Figure 6.3 (a) HAADF-STEM image of the top section of AlGaN on GaN nanowire. Crystal morphology of (b) AlGaN generated from growth rate ratios, and (c) GaN generated from surface energy ratios.

On the $\{10\bar{1}0\}$ inclined semipolar planes, a growth rate ratio of only 0.15 is determined with respect to the (0001) *c*-plane. This value is critically very low compared to the surface energy ratio of 1.19 in the case of GaN for the same set of planes. The implication of this slow growth rate on the semipolar planes of AlGaN with respect to the *c*-plane will be discussed in the context of equilibrium crystal shapes. The theory of equilibrium crystal shapes developed by Wulff [38] and later advanced by Herring [39] provides that the kinetic crystal shape may be obtained from growth rate ratios with the premise that these ratios are equivalent to the

surface energy ratios. Using the determined growth rate ratios, crystal morphology of AlGaN is generated with the software WinXMorph [40, 41] and is shown as Figure 6.3(b). Similarly, the crystal morphology of GaN is shown as Figure 6.3(c), generated using surface energy ratios [34, 35].

The stark difference between crystal morphologies of AlGaN and GaN, shown in Figure 6.3(b) and (c), implies that growth of metal-polar AlGaN nanowires will terminate the top surface with a pyramidal shape, as deduced from kinetics, whereas, growth of Ga-polar GaN nanowires is possible according to energetics. During AlGaN growth, the faster-growing (0001) *c*-plane grows to extinction due to the very slow growth rate of inclined $\{10\bar{1}0\}$ facets and results in pyramidal shape. Such pyramidal structures have been frequently observed in the SAG of AlGaN [28, 42, 43], limiting the achievement of AlGaN nanowires. Apart from this strong tendency to form a pyramidal shape, small diffusion length of Al adatoms also limits vertical growth. We therefore, attribute the very slow growth rate of $\{10\bar{1}1\}$ planes and small diffusion length of Al adatoms as the major hindrances in achieving AlGaN nanowires by SAG in MOCVD. Additionally, we also highlight here that the difficulty in AlGaN nanowire growth can be circumvented by employing selective area grown GaN nanowires for UV emission by incorporating nonpolar AlGaN MQWs as the shell.

6.5. Microstructural analysis of $Al_xGa_{1-x}N/Al_yGa_{1-y}N$ MQWs

Figure 6.4(a) shows a HAADF-STEM image of a trophy-shaped nanowire obtained from the array of 1 μm pitch. From the HAADF-STEM image, the GaN nanowire core, AlGaN buffer, five radial $Al_xGa_{1-x}N/Al_yGa_{1-y}N$ MQWs on *m*-plane, and the outermost AlGaN shell can be seen clearly owing to the Z-contrast. Higher Al-containing regions show a darker contrast due to the effective lower atomic number compared to GaN nanowire core or Ga-rich quantum wells. Variation in thickness of the quantum wells and barriers along the length of the nanowire as a result of shadowing effect is also evident here. Thin quantum wells on *m*-plane sidewalls are present near the top of nanowire but gradually increases towards the bottom of the distinctive hexagonal section before undergoing a gradual decrease towards the bottom of nanowire. Figure 6.4(b) shows the HAADF-STEM image of an $Al_xGa_{1-x}N/Al_yGa_{1-y}N$ MQWs on GaN nanowire with a pitch of 2 μm. This nanowire possesses straight sidewalls and MQWs with better uniformity along the whole length. Figure 6.4(c) shows HRTEM image of the MQW region from trophy-shaped nanowire, viewed along $[11\bar{2}0]$ zone axis. The corresponding area of HRTEM is indicated with a dashed rectangle in Figure 6.4(a). We have not observed any

threading dislocations in the GaN nanowire core nor in the AlGaN region, attesting to the benefit of using dislocation-free GaN nanowires for the growth of $Al_xGa_{1-x}N/Al_yGa_{1-y}N$ MQWs. Measurement of quantum well thickness at different locations along the length in trophy-shaped structure showed a variation from ~1 - 5 nm.

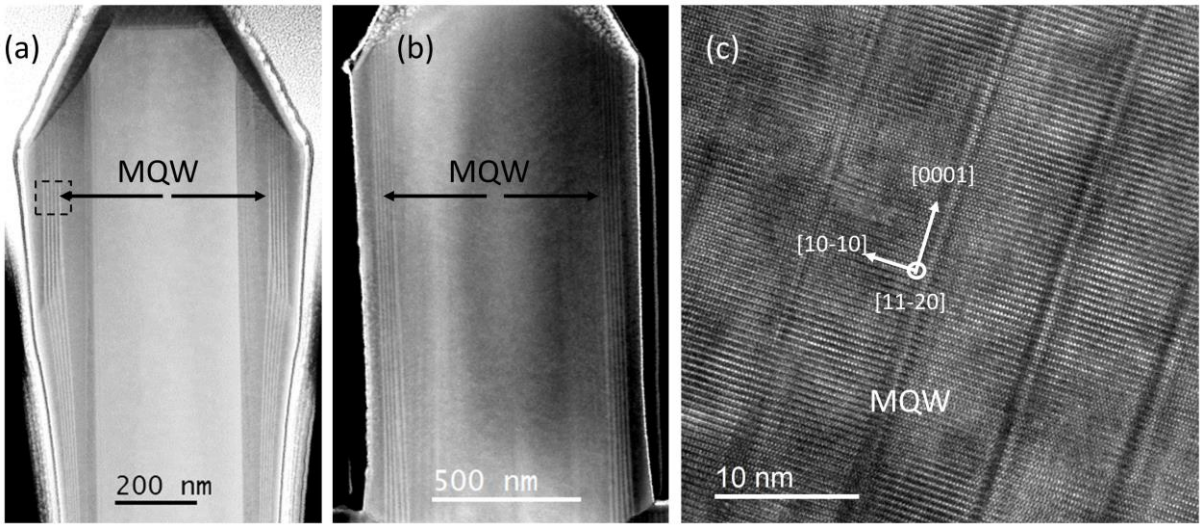

Figure 6.4 HAADF-STEM images of $Al_xGa_{1-x}N/Al_yGa_{1-y}N$ MQW for (a) trophy-shaped, and (b) uniform sidewall nanowire. (c) HRTEM image of the MQW region in the trophy-shaped nanowire viewed along $[11\bar{2}0]$ zone axis (the corresponding region is marked by a dashed rectangle in (a)).

Spontaneous superlattice in AlGaN

The buffer AlGaN shell grown on GaN nanowires shows spontaneous superlattice formation on both *m*- and *c*-planes. Although spontaneous superlattice formation has been observed and discussed in planar growths of InGaN [44, 45], AlGaN [46-48], AlInN [49], and AlInGaN [50], few reports exist for nanowires [51, 52]. Figure 6.5(a) shows a low-resolution TEM image of quantum well-like spontaneous superlattice formed on *m*-plane AlGaN near the GaN/AlGaN interface. Inset of Figure 6.5(a) shows a HAADF-STEM image of the spontaneous superlattice and reveals that the pseudo-periodic stripes on *m*-plane AlGaN are composed of Ga-rich (bright) and Ga-poor (dark) regions.

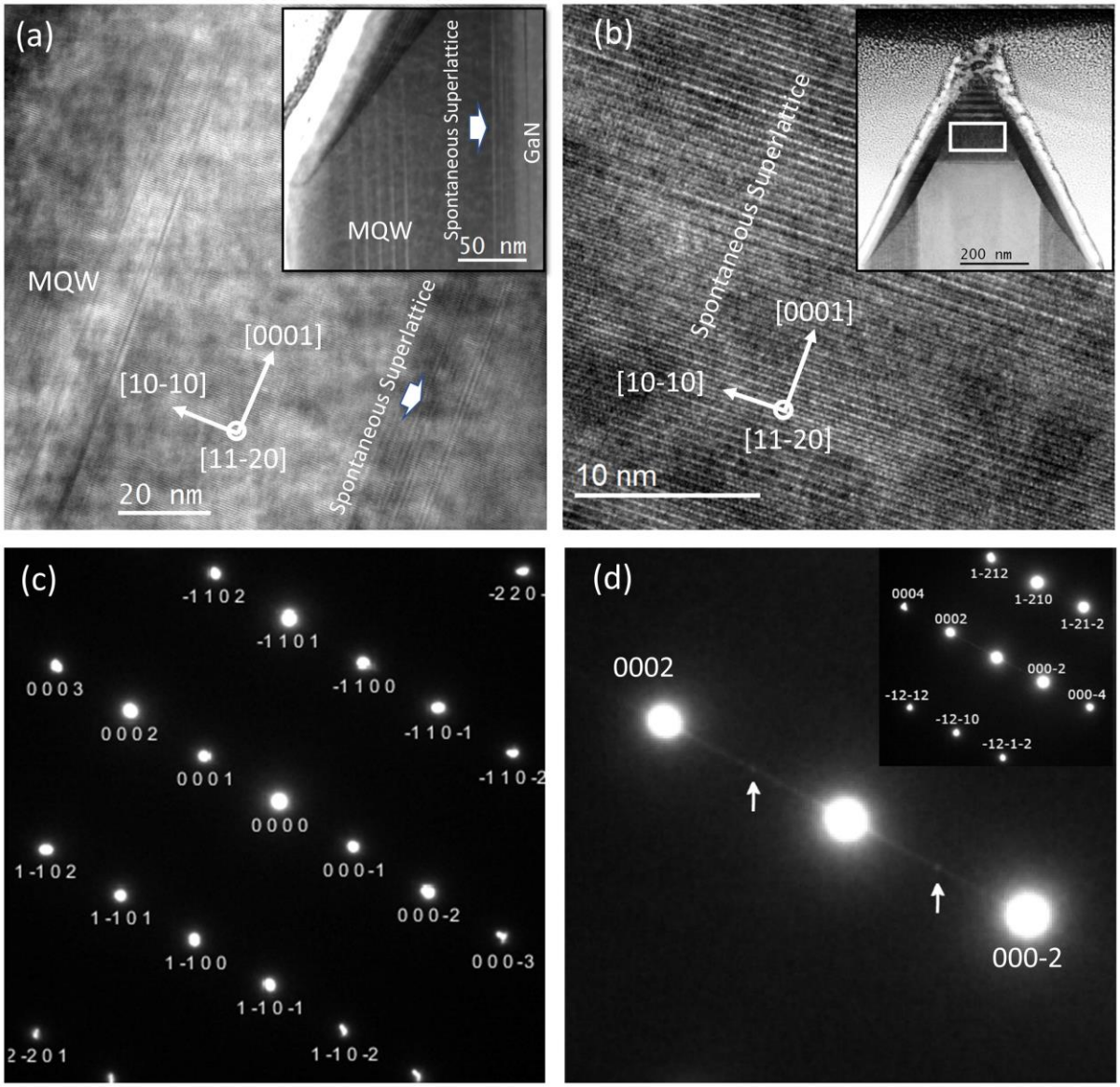

Figure 6.5 (a) TEM image of spontaneous superlattice formed on $(10\bar{1}0)$ *m*-plane. The inset shows the corresponding HAADF-STEM image. (b) HR-TEM image of spontaneous superlattice on (0001) *c*-plane, with the corresponding area shown with a white rectangle in the inset. Selected area electron diffraction (SAED) patterns of the spontaneous superlattice formed on *c*-plane along the (c) $[11\bar{2}0]$ and (d) $[10\bar{1}0]$ zone axes. Arrows in (d) show the presence of forbidden (0001) spots and inset shows the original SAED pattern.

On the other hand, spontaneous superlattice on the *c*-plane is visibly different from that of quantum well-like spontaneous superlattice of *m*-plane as revealed by the HRTEM image as shown in Figure 6.5(b). It occurs at a much finer scale on *c*-plane and is akin to chemical ordering of few monolayers [53-55]. White rectangular region in the inset of Figure 6.5(b)

indicates the region of the HRTEM image. In order to investigate the spontaneous superlattice formation on *c*-plane, SAED patterns are recorded along the $[11\bar{2}0]$ and $[10\bar{1}0]$ zone axes and shown in Figure 6.5(c) and (d), respectively. The zone axes of SAED patterns are confirmed and the diffraction spots are indexed using the software CrystTBox [56]. SAED pattern recorded along the $[11\bar{2}0]$ zone axis shows the single crystallinity with wurtzite symmetry but does not provide any information on the spontaneous superlattice. However, SAED pattern recorded along the $[10\bar{1}0]$ zone axis shows the presence of a faint streak line on the {0002} spots, suggesting the possibility of multiple orderings present on the *c*-plane of AlGaN. Further, the notable presence of a faint but distinct spot at the middle of direct beam and {0002} spots, as indicated by arrows in Figure 6.5(d), confirms the occurrence of GaN/AlN ordering. Figure 6.5(d) is a magnified (cropped) image of the original SAED pattern shown by the inset.

The self-organiSed phenomenon of spontaneous superlattice formation observed here in the heteroepitaxy of AlGaN on GaN nanowires is considered to be driven by the need to minimise strain energy. The different nature of spontaneous superlattices formed on *m*-plane and *c*-plane are attributed to the different nature of strain on these two planes. On *c*-plane, the growing AlGaN layer experiences an isotropic biaxial tensile strain due to mismatch of lattice parameter *a* alone, whereas, the epitaxial layer on *m*-plane is subjected to anisotropic tensile strain due to mismatch in both *c* and *a* lattice parameters, thus giving rise to two different nature of spontaneous superlattices.

6.6. Cathodoluminescence study of AlGaN MQW

Cathodoluminescence (CL) measurements on AlGaN MQWs are carried out at room temperature in an FEI Verios 460 SEM equipped with a Gatan MonoCL4.

6.6.1. Variation of MQW growth duration

This section discusses three trophy-shaped samples of $Al_xGa_{1-x}N/Al_yGa_{1-y}N$ MQWs grown on GaN nanowire templates (1 μm pitch), with different MQW growth durations of 180, 120 and 60 seconds (hereinafter referred to as N180, N120 and N60, respectively). SEM images of these samples and their corresponding panchromatic CL images are shown in Figure 6.6. Bright emissions from *m*-plane sidewalls are observed from the panchromatic CL images. However, the pyramidal section at the top, composed of $\{10\bar{1}1\}$ semipolar planes are dark, despite a weak emission from MQWs on (0001) plane. The weak emission from MQWs on *c*-plane in our samples is a result of thicker quantum well due to faster growth rate on *c*-plane.

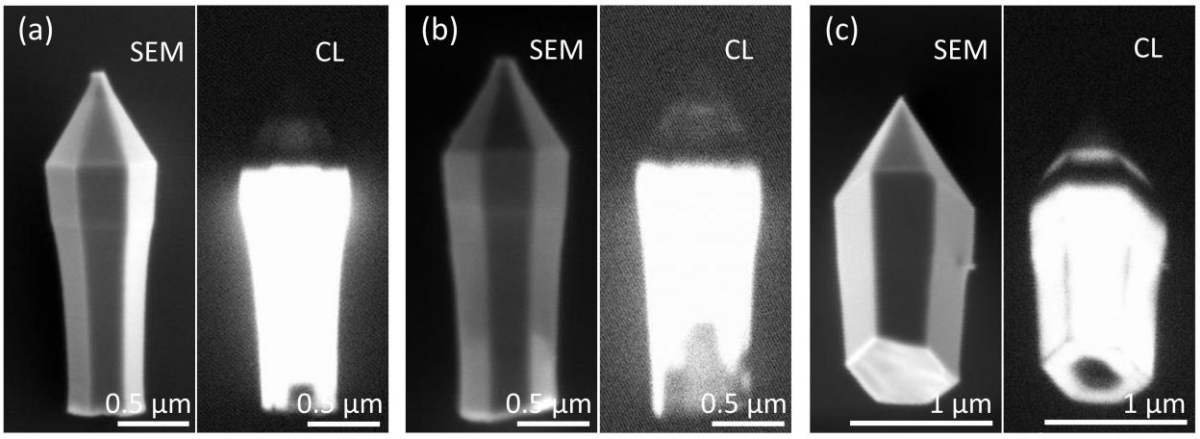

Figure 6.6 SEM and the corresponding panchromatic CL images of $Al_xGa_{1-x}N/Al_yGa_{1-y}N$ MQWs grown on GaN nanowires (a) N180, (b) N120 and (c) N60.

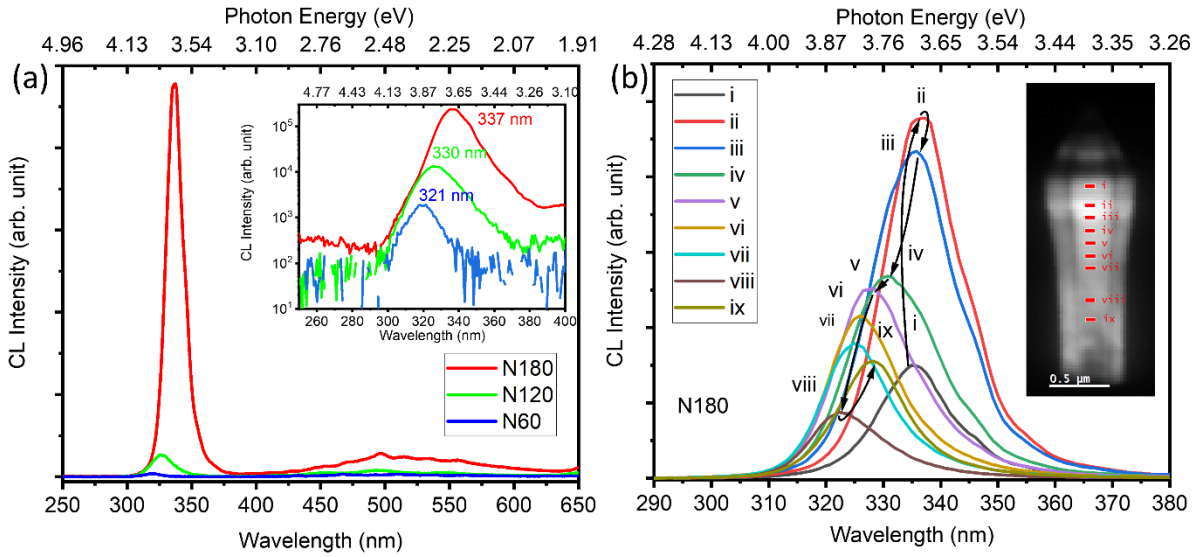

Figure 6.7 (a) CL spectra of $Al_xGa_{1-x}N/Al_yGa_{1-y}N$ MQW samples N180, N120 and N60. Inset shows a semi-logarithmic plot of the spectra with peak emission wavelengths identified. (b) CL spectra at different points along the length of trophy-shaped structure for sample N180.

UV emission spectra of these three samples measured using CL at room temperature are shown in Figure 6.7(a). Blueshift in emission wavelength, associated with a decrease in CL intensity is evident as the quantum well growth duration is reduced from 180 to 120, and then to 60 seconds. Figure 6.7(a) also reveals that the intensity ratio of emission from MQW to that of yellow luminescence, I_{MQW}/I_{YL}, is significantly high in sample N180, suggestive of good

optical quality. The I_{MQW}/I_{YL} ratio is reduced with decreasing quantum well width as evident in sample N120 and the ratio becomes smallest in the case of sample N60. The inset of Figure 6.7(a) shows a semi-logarithmic plot of UV emission for samples N180, N120 and N60. The peak wavelengths of emission from these samples are determined to be 337, 330 and 321 nm, respectively, exhibiting a blueshift associated with increased quantum confinement due to decreasing QW width.

Increase in photoluminescence (PL) intensity with increasing QW width has been reported for nonpolar planar epitaxial samples of *m*-plane GaN/$Al_{0.2}Ga_{0.8}N$ MQWs [57], as well as *a*-plane GaN/$Al_{0.16}Ga_{0.84}N$ MQWs [11], exhibiting maximum intensity at well widths of 4.8 nm and 5.2 nm, respectively. Very thin QW, on the other hand, are reported to suffer from reduced recombination in the MQW region due to carrier leakage and extension of the electron and hole wavefunctions into the barrier region [58]. Increasing the QW width beyond 5 nm in *a*-plane GaN/$Al_{0.16}Ga_{0.84}N$ MQW, and above 6 nm in *a*-plane InGaN/GaN MQW have been reported to result in a decreased PL intensity due to increased exciton decay time with increasing QW width [59, 60]. Sample N180 with a maximum well width of ~5 nm, therefore shows the most intense emission and a systematic decrease in intensity is observed for decreasing growth duration of the MQWs as evident from CL of samples N120 and N60.

Variation in emission wavelength and intensity due to the non-uniformity of trophy-shaped structure is analysed by extracting the CL spectra at several points along the length of nanowire as shown in Figure 6.7(b) for sample N180. At the position marked as (i) in the inset of Figure 6.7(b), the peak wavelength of emission is centered at 335 nm, which then undergoes a redshift to 337 nm associated with an increase in CL intensity at position (ii) resulting from increase in quantum well width as seen earlier in Figure 6.4(a). Below this position and all the way to position (viii), the emission wavelength blueshifts to 322 nm, associated with a decrease in intensity as a result of decreasing quantum well width. Finally, towards the bottom of the nanowire at position (ix), the emission is slightly redshifted, associated with an increase in intensity as a result of slight increase in QW width near the bottom due to the “skirting” effect.

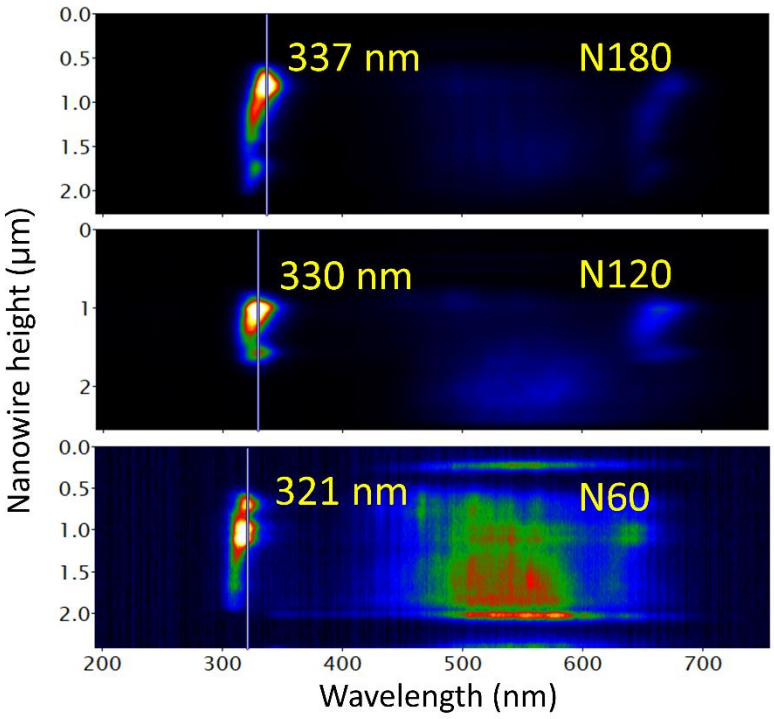

Figure 6.8 Intensity distribution of UV emission along the length of nanowire as a function of wavelength for samples N180, N120 and N60.

Spatial distribution of emission intensity along the length of nanowire as function of wavelength from CL mapping is shown in Figure 6.8. Peak emission wavelength of each sample is indicated by a line at the corresponding wavelength and highlights the blueshift in wavelength with reduced QW growth duration (QW width). The maximum dispersion in emission wavelength is limited to within 20 nm, despite a variation of quantum well width from ~1 to 5 nm due to shadowing effect during growth. Such a relatively small dispersion of emission wavelength for a considerable variation in quantum well width is a testament to the advantage of QCSE-free $Al_xGa_{1-x}N/Al_yGa_{1-y}N$ MQWs on nonpolar *m*-plane sidewalls.

6.6.2. Variation of MQW alloy composition

In this section, three different samples of $Al_xGa_{1-x}N/Al_{y0.46}Ga_{0.54}N$ MQWs are prepared by changing the Al composition of the MQWs: 0% (GaN QW), 17.3% (similar growth condition to sample N120) and 27%. These samples will be referred to as M0, M17 and M27 respectively. The gas phase alloy composition for barrier growth in all of these experiments is maintained the same at 46.3%, similar to the previous set of experiments.

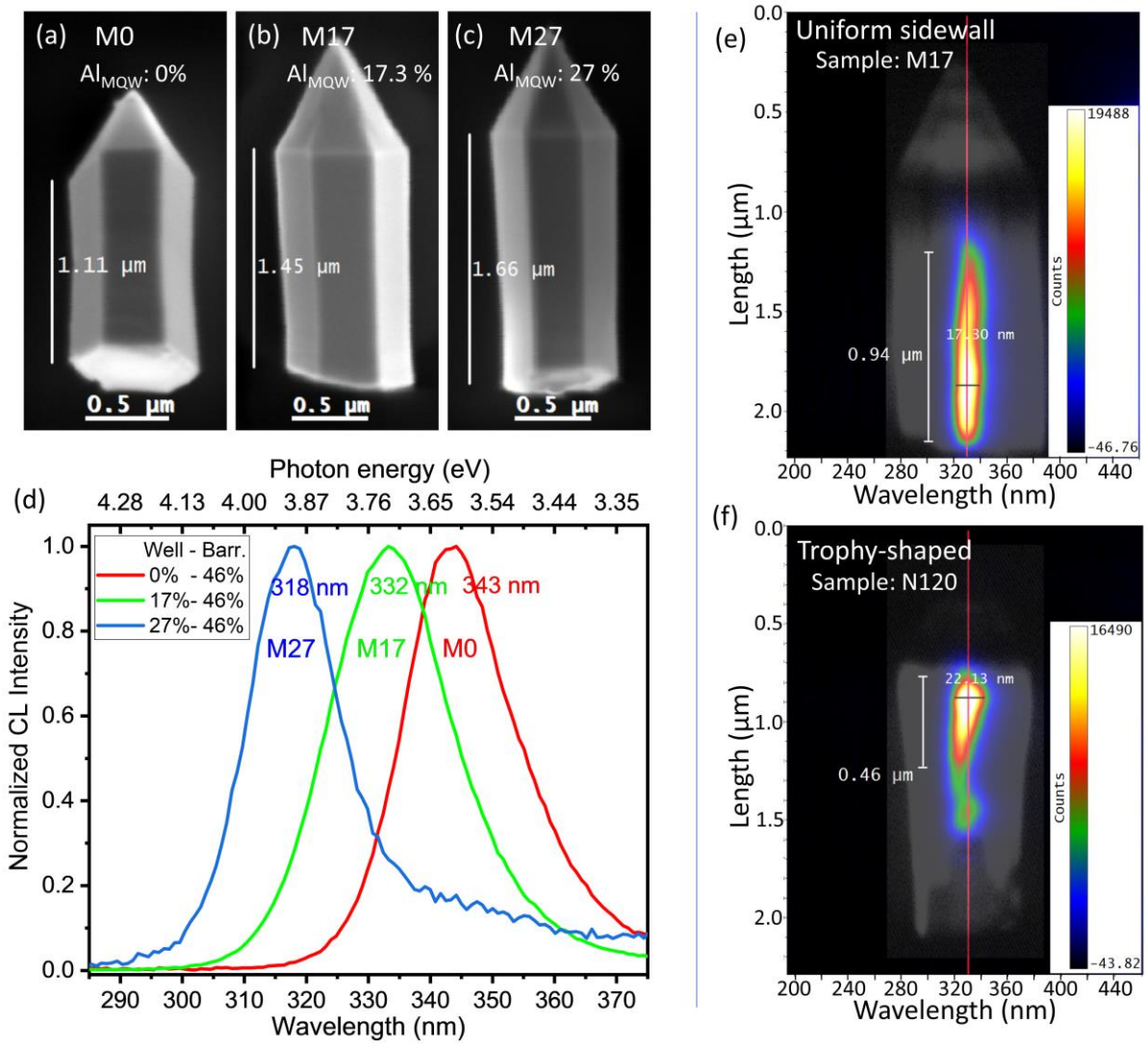

Figure 6.9 (a, b and c) SEM images of nanowires with uniform sidewalls for $Al_xGa_{1-x}N/Al_yGa_{1-y}N$ MQWs with x = 0 (M0), 0.17 (M17) and 0.27 (M27) respectively; y = 0.46 in all cases. (d) Normalised CL emission spectra of M0, M17 and M27. (e) and (f) CL emission intensity map for uniform sidewall sample (M17) and trophy-shaped (N120) nanowire with similar Al composition, respectively.

The nanowire morphologies and their corresponding CL spectra are shown in Figure 6.9. SEM images of the nanowires are shown as Figure 6.9(a – c) for samples M0, M17 and M27. These nanowires are from the arrays with 1.5 µm pitch, whereas, in the previous section of trophy-shaped nanowires, they are from the arrays with a pitch of 1 µm. Figure 6.9(d) shows the normalised CL intensity for samples M0, M17 and M27. Sample M0 shows a peak emission wavelength of 343 nm and the emission wavelength shows a blueshift with increasing Al content in the MQWs with samples M17 and M27 showing a peak emission wavelength of 332

and 318 nm, respectively. This demonstrates that, in addition to changing QW width (discussed in the previous section), the emission wavelength (bandgap) of nonpolar *m*-plane $Al_xGa_{1-x}N/Al_yGa_{1-y}N$ MQWs can also be controlled by changing their alloy composition.

Figure 6.9(e) and (f) show the emission intensity distribution from a linescan along the length of nanowire for samples M17 and N120, respectively. The emission intensity profile is overlaid on their respective panchromatic CL images to provide a visual aid. Both samples, grown with similar alloy composition and duration, have similar emission wavelength as indicated by vertical red lines at 330 nm. This confirms the reproducible growth of $Al_xGa_{1-x}N/Al_yGa_{1-y}N$ MQWs on GaN nanowire arrays using MOCVD. The sample with uniform sidewalls shows a narrower dispersion of emission wavelength (~17 nm) compared to the trophy-shaped sample (~22 nm), as measured and indicated by horizontal black lines. Further, the nanowire with uniform sidewalls also shows uniform emission over a longer length along the nanowire (~ 1 μm) compared to the trophy-shaped nanowire (0.5 μm). Thus, nonpolar $Al_xGa_{1-x}N/Al_yGa_{1-y}N$ MQWs grown on GaN nanowire arrays with a pitch of ≥ 1.5 μm provides uniform emission suitable for nanowire-based UV light source.

6.6.3. Uniform UV emission from nanowire arrays

Figure 6.10(a) shows a top-view SEM image of a nanowire array with $Al_xGa_{1-x}N/Al_yGa_{1-y}N$ MQWs over an area of 45×45 μm^2. The SEM image reveals the presence of only a few defects in the array as either missing or coalesced nanowires, in an otherwise largely uniform array. Figure 6.10(b) shows the corresponding panchromatic CL image obtained with an electron beam condition of 5 kV and 400 nA. The panchromatic CL image reveals bright emission from the sidewalls of $Al_xGa_{1-x}N/Al_yGa_{1-y}N$ MQWs array, while the substrate (outside the array) without nanowires appears dark. Thus, the prospect for efficient UV light source using nonpolar *m*-plane $Al_xGa_{1-x}N/Al_yGa_{1-y}N$ MQWs incorporated on GaN nanowire sidewalls is clearly demonstrated with the potential for large area UV LEDs as well as for the next generation micro-LEDs.

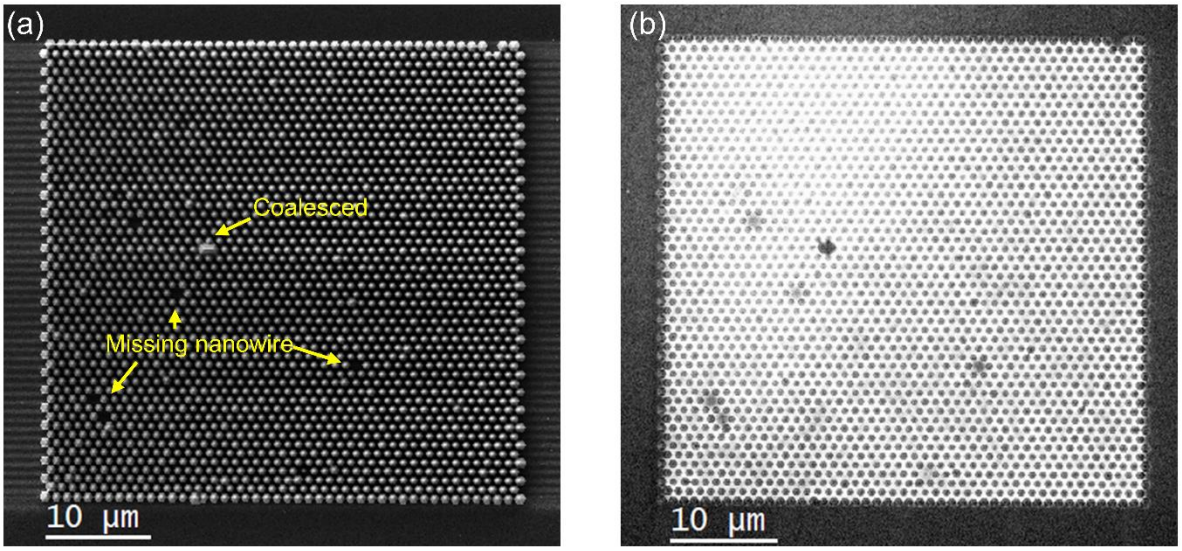

Figure 6.10 (a) Top-view SEM image of $Al_xGa_{1-x}N/Al_yGa_{1-y}N$ MQWs incorporated on GaN nanowire array. (b) Panchromatic CL image of the nanowire array.

6.7. Summary

In summary, a systematic investigation has been carried out on the growth of AlGaN MQWs on GaN nanowires for UV emission. Vapour phase diffusion (VPD) has been identified as the predominant flux supply mechanism in the selective area growth of AlGaN on GaN nanowires in MOCVD. Consequently, trophy-shaped nanowires are formed when the pitch is 1 µm (gap between adjacent nanowires ~250 nm) due to shadowing effect. Uniform nanowires with straight sidewalls are obtained when the gap between adjacent nanowires is ≥ 600 nm (or pitch ≥ 1.5 µm). The low diffusion length of Al adatoms on the nanowire sidewalls and mask results in skirting at the bottom of the nanowires and parasitic AlGaN deposition on the mask. Growth rates for AlGaN on nonpolar $\{10\bar{1}0\}$ and semipolar $\{10\bar{1}1\}$ planes, with respect to polar (0001) plane, have been determined to be 58% and 15%, respectively. These growth rates imply that AlGaN has a significant lateral growth in MOCVD which is beneficial for the growth of AlGaN shell. However, the slow growth rate of $\{10\bar{1}1\}$ semipolar planes leading to formation of pyramidal and the low diffusion length of Al adatoms on the sidewalls hampers the achievement of AlGaN nanowires in MOCVD. This difficulty in realisation of AlGaN nanowires can be circumvented by using GaN nanowires as the template for subsequent AlGaN shell. Simultaneous presence of spontaneous superlattices on *m*- and *c*-plane has been observed in AlGaN grown on GaN nanowires. Spontaneous superlattice on *m*-plane has a pseudo-periodic structure composed of Ga-rich and Ga-poor regions and appears like quantum wells, whereas, on *c*-plane SAED pattern confirms GaN/AlN ordering at the level of monolayers, due

to different manifestations of spontaneous superlattice to the different strain states on *m*- and c-planes. Reproducible growth and controlled tuning of the UV emission has been achieved in the wavelength range of 318 – 343 nm from $Al_xGa_{1-x}N/Al_yGa_{1-y}N$ MQWs grown on dislocation-free GaN nanowires by selective area growth in MOCVD. Finally, uniform growth and UV emission from AlGaN MQWs on GaN nanowire array over an area of 45×45 μm^2 has been demonstrated.

References

1. Kneissl, M., Seong, T.-Y., Han, J. and Amano, H., "The emergence and prospects of deep-ultraviolet light-emitting diode technologies." *Nature Photonics*, **2019**, 13, 233-244.

2. Takano, T., Mino, T., Sakai, J., Noguchi, N., Tsubaki, K., et al., "Deep-ultraviolet light-emitting diodes with external quantum efficiency higher than 20% at 275 nm achieved by improving light-extraction efficiency." *Applied Physics Express*, **2017**, 10, 031002.

3. Narukawa, Y., Ichikawa, M., Sanga, D., Sano, M. and Mukai, T., "White light emitting diodes with super-high luminous efficacy." *Journal of Physics D: Applied Physics*, **2010**, 43, 354002.

4. Miller, D.A.B., Chemla, D.S., Damen, T.C., Gossard, A.C., Wiegmann, W., et al., "Band-Edge Electroabsorption in Quantum Well Structures: The Quantum-Confined Stark Effect." *Physical Review Letters*, **1984**, 53, 2173-2176.

5. Takeuchi, T., Sota, S., Katsuragawa, M., Komori, M., Takeuchi, H., et al., "Quantum-Confined Stark Effect due to Piezoelectric Fields in GaInN Strained Quantum Wells." *Japanese Journal of Applied Physics*, **1997**, 36, L382.

6. Waltereit, P., Brandt, O., Trampert, A., Grahn, H.T., Menniger, J., et al., "Nitride semiconductors free of electrostatic fields for efficient white light-emitting diodes." *Nature*, **2000**, 406, 865-868.

7. Grandjean, N., Massies, J. and Leroux, M., "Self-limitation of AlGaN/GaN quantum well energy by built-in polarization field." *Applied Physics Letters*, **1999**, 74, 2361-2363.

8. Grandjean, N., Damilano, B., Dalmasso, S., Leroux, M., Laügt, M., et al., "Built-in electric-field effects in wurtzite AlGaN/GaN quantum wells." *Journal of Applied Physics*, **1999**, 86, 3714-3720.

9. Langer, R., Simon, J., Ortiz, V., Pelekanos, N.T., Barski, A., et al., "Giant electric fields in unstrained GaN single quantum wells." *Applied Physics Letters*, **1999**, 74, 3827-3829.

10. Kajitani, R., Kawasaki, K. and Takeuchi, M., "Barrier-height and well-width dependence of photoluminescence from AlGaN-based quantum well structures for deep-UV emitters." *Materials Science and Engineering: B*, **2007**, 139, 186-191.

11. Craven, M.D., Waltereit, P., Speck, J.S. and DenBaars, S.P., "Well-width dependence of photoluminescence emission from a-plane GaN/AlGaN multiple quantum wells." *Applied Physics Letters*, **2004**, 84, 496-498.

12. Ban, K., Yamamoto, J.-i., Takeda, K., Ide, K., Iwaya, M., et al., "Internal Quantum Efficiency of Whole-Composition-Range AlGaN Multiquantum Wells." *Applied Physics Express*, **2011**, 4, 052101.

13. Hersee, S.D., Sun, X. and Wang, X., "The Controlled Growth of GaN Nanowires." *Nano Letters*, **2006**, 6, 1808-1811.

14. Coulon, P.-M., Alloing, B., Brändli, V., Vennéguès, P., Leroux, M., et al., "Dislocation filtering and polarity in the selective area growth of GaN nanowires by continuous-flow metal organic vapor phase epitaxy." *Applied Physics Express*, **2016**, 9, 015502.

15. Colby, R., Liang, Z., Wildeson, I.H., Ewoldt, D.A., Sands, T.D., et al., "Dislocation Filtering in GaN Nanostructures." *Nano Letters*, **2010**, 10, 1568-1573.

16. Hersee, S.D., Rishinaramangalam, A.K., Fairchild, M.N., Zhang, L. and Varangis, P., "Threading defect elimination in GaN nanowires." *Journal of Materials Research*, **2011**, 26, 2293-2298.

17. Siladie, A.-M., Jacopin, G., Cros, A., Garro, N., Robin, E., et al., "Mg and In Codoped p-type AlN Nanowires for pn Junction Realization." *Nano Letters*, **2019**, 19, 8357-8364.

18. Connie, A.T., Zhao, S., Sadaf, S.M., Shih, I., Mi, Z., et al., "Optical and electrical properties of Mg-doped AlN nanowires grown by molecular beam epitaxy." *Applied Physics Letters*, **2015**, 106, 213105.

19. Tran, N.H., Le, B.H., Zhao, S. and Mi, Z., "On the mechanism of highly efficient p-type conduction of Mg-doped ultra-wide-bandgap AlN nanostructures." *Applied Physics Letters*, **2017**, 110, 032102.

20. Djavid, M. and Mi, Z., "Enhancing the light extraction efficiency of AlGaN deep ultraviolet light emitting diodes by using nanowire structures." *Applied Physics Letters*, **2016**, 108, 051102.

21. Ooi, Y.K., Liu, C. and Zhang, J., "Analysis of Polarization-Dependent Light Extraction and Effect of Passivation Layer for 230-nm AlGaN Nanowire Light-Emitting Diodes." *IEEE Photonics Journal*, **2017**, 9, 1-12.

22. Jain, B., Velpula, R.T., Tumuna, M., Bui, H.Q.T., Jude, J., et al., "Enhancing the light extraction efficiency of AlInN nanowire ultraviolet light-emitting diodes with photonic crystal structures." *Optics Express*, **2020**, 28, 22908-22918.

23. Zhang, L., Guo, Y., Yan, J., Wu, Q., Lu, Y., et al., "Deep ultraviolet light-emitting diodes based on a well-ordered AlGaN nanorod array." *Photonics Research*, **2019**, 7, B66-B72.

24. Ra, Y.-H., Kang, S. and Lee, C.-R., "Ultraviolet Light-Emitting Diode Using Nonpolar AlGaN Core–Shell Nanowire Heterostructures." *Advanced Optical Materials*, **2018**, 6, 1701391.

25. Kim, J., Choi, U., Pyeon, J., So, B. and Nam, O., "Deep-Ultraviolet AlGaN/AlN Core-Shell Multiple Quantum Wells on AlN Nanorods via Lithography-Free Method." *Scientific Reports*, **2018**, 8, 935.

26. Coulon, P.-M., Kusch, G., Martin, R.W. and Shields, P.A., "Deep UV Emission from Highly Ordered AlGaN/AlN Core–Shell Nanorods." *ACS Applied Materials & Interfaces*, **2018**, 10, 33441-33449.

27. Grenier, V., Finot, S., Jacopin, G., Bougerol, C., Robin, E., et al., "UV Emission from GaN Wires with m-Plane Core–Shell GaN/AlGaN Multiple Quantum Wells." *ACS Applied Materials & Interfaces*, **2020**, 12, 44007-44016.

28. Boughaleb, S., Martin, B., Matei, C., Templier, R., Borowik, Ł., et al., "Selective area growth of AlGaN nanopyramids by conventional and pulsed MOVPE." *Nanotechnology*, **2021**, 32, 195203.

29. Jindal, V., Grandusky, J.R., Tripathi, N., Shahedipour-Sandvik, F., LeBoeuf, S., et al., "Selective area heteroepitaxy of nano-AlGaN ultraviolet excitation sources for biofluorescence application." *Journal of Materials Research*, **2007**, 22, 838-844.

30. Fan, Z.Y., Rong, G., Newman, N. and Smith, D.J., "Defect annihilation in AlN thin films by ultrahigh temperature processing." *Applied Physics Letters*, **2000**, 76, 1839-1841.

31. Banal, R.G., Funato, M. and Kawakami, Y., "Surface diffusion during metalorganic vapor phase epitaxy of AlN." *physica status solidi (c)*, **2009**, 6, 599-602.

32. Iliopoulos, E., Ludwig, K.F., Moustakas, T.D., Komninou, P., Karakostas, T., et al., "Epitaxial growth and self-organized superlattice structures in AlGaN films grown by plasma assisted molecular beam epitaxy." *Materials Science and Engineering: B*, **2001**, 87, 227-236.

33. Iliopoulos, E. and Moustakas, T.D., "Growth kinetics of AlGaN films by plasma-assisted molecular-beam epitaxy." *Applied Physics Letters*, **2002**, 81, 295-297.

34. Li, H., Geelhaar, L., Riechert, H. and Draxl, C., "Computing Equilibrium Shapes of Wurtzite Crystals: The Example of GaN." *Physical Review Letters*, **2015**, 115, 085503.

35. Zhang, J., Zhang, Y., Tse, K., Deng, B., Xu, H., et al., "New approaches for calculating absolute surface energies of wurtzite (0001)/$(000\bar{1})$: A study of ZnO and GaN." *Journal of Applied Physics*, **2016**, 119, 205302.

36. Calarco, R., Meijers, R.J., Debnath, R.K., Stoica, T., Sutter, E., et al., "Nucleation and Growth of GaN Nanowires on Si (111) Performed by Molecular Beam Epitaxy." *Nano Letters*, **2007**, 7, 2248-2251.

37. Tchernycheva, M., Sartel, C., Cirlin, G., Travers, L., Patriarche, G., et al., "Growth of GaN free-standing nanowires by plasma-assisted molecular beam epitaxy: structural and optical characterization." *Nanotechnology*, **2007**, 18, 385306.

38. Wulff, G., "XXV. Zur Frage der Geschwindigkeit des Wachsthums und der Auflösung der Krystallflächen." *Zeitschrift fur Kristallographie - Crystalline Materials*, **1901**, 34, 449.

39. Herring, C., "Some Theorems on the Free Energies of Crystal Surfaces." *Physical Review*, **1951**, 82, 87-93.

40. Kaminsky, W., "WinXMorph: a computer program to draw crystal morphology, growth sectors and cross sections with export files in VRML V2.0 utf8-virtual reality format." *Journal of Applied Crystallography*, **2005**, 38, 566-567.

41. Kaminsky, W., "From CIF to virtual morphology using the WinXMorph program." *Journal of Applied Crystallography*, **2007**, 40, 382-385.

42. Kato, T., Honda, Y., Kawaguchi, Y., Yamaguchi, M. and Sawaki, N., "Selective Growth of GaN/AlGaN Microstructures by Metalorganic Vapor Phase Epitaxy." *Japanese Journal of Applied Physics*, **2001**, 40, 1896-1898.

43. Jindal, V., Grandusky, J., Jamil, M., Tripathi, N., Thiel, B., et al., "Effect of interfacial strain on the formation of AlGaN nanostructures by selective area heteroepitaxy." *Physica E: Low-dimensional Systems and Nanostructures*, **2008**, 40, 478-483.

44. Wu, Z.H., Kawai, Y., Fang, Y.Y., Chen, C.Q., Kondo, H., et al., "Spontaneous formation of highly regular superlattice structure in InGaN epilayers grown by molecular beam epitaxy." *Applied Physics Letters*, **2011**, 98, 141905.

45. Zheng, X.T., Wang, T., Wang, P., Sun, X.X., Wang, D., et al., "Full-composition-graded InxGa1−xN films grown by molecular beam epitaxy." *Applied Physics Letters*, **2020**, 117, 182101.

46. Strittmatter, A., Reissmann, L., Bimberg, D., Veit, P. and Krost, A., "Spontaneous Superlattice Formation in AlGaN Layers Grown by MOCVD on Si (111)-Substrates." *physica status solidi (b)*, **2002**, 234, 722-725.

47. Pakula, K., Bożek, R., Baranowski, J.M. and Jasinski, J., "Spontaneous superlattice formation in MOVPE growth of AlGaN." *physica status solidi (c)*, **2005**, 2, 1073-1076.

48. Wang, T., Liu, S., Zheng, X., Wang, P., Wang, D., et al., "Microstructure and dislocation evolution in composition gradient AlGaN grown by MOCVD." *Superlattices and Microstructures*, **2021**, 152, 106842.

49. Chichibu, S.F., Shima, K., Kojima, K. and Kangawa, Y., "Self-formed compositional superlattices triggered by cation orderings in m-plane $Al_{1-x}In_xN$ on GaN." *Scientific Reports*, **2020**, 10, 18570.

50. El-Masry, N.A., Behbehani, M.K., LeBoeuf, S.F., Aumer, M.E., Roberts, J.C., et al., "Self-assembled AlInGaN quaternary superlattice structures." *Applied Physics Letters*, **2001**, 79, 1616-1618.

51. Pierret, A., Bougerol, C., Hertog, M.d., Gayral, B., Kociak, M., et al., "Structural and optical properties of $Al_xGa_{1-x}N$ nanowires." *physica status solidi (RRL) – Rapid Research Letters*, **2013**, 7, 868-873.

52. Rigutti, L., Teubert, J., Jacopin, G., Fortuna, F., Tchernycheva, M., et al., "Origin of energy dispersion in $Al_xGa_{1-x}N$/GaN nanowire quantum discs with low Al content." *Physical Review B*, **2010**, 82, 235308.

53. Ruterana, P., De Saint Jores, G., Laügt, M., Omnes, F. and Bellet-Amalric, E., "Evidence for multiple chemical ordering in AlGaN grown by metalorganic chemical vapor deposition." *Applied Physics Letters*, **2001**, 78, 344-346.

54. Albrecht, M., Lymperakis, L., Neugebauer, J., Northrup, J.E., Kirste, L., et al., "Chemically ordered $Al_xGa_{1-x}N$ alloys: Spontaneous formation of natural quantum wells." *Physical Review B*, **2005**, 71, 035314.

55. Behbehani, M.K., Piner, E.L., Liu, S.X., El-Masry, N.A. and Bedair, S.M., "Phase separation and ordering coexisting in $In_xGa_{1-x}N$ grown by metal organic chemical vapor deposition." *Applied Physics Letters*, **1999**, 75, 2202-2204.

56. Klinger, M., "More features, more tools, more CrysTBox." *Journal of Applied Crystallography*, **2017**, 50, 1226-1234.

57. Vashaei, Z., Bayram, C., Lavenus, P. and Razeghi, M., "Photoluminescence characteristics of polar and nonpolar AlGaN/GaN superlattices." *Applied Physics Letters*, **2010**, 97, 121918.

58. Zeng, K.C., Li, J., Lin, J.Y. and Jiang, H.X., "Well-width dependence of the quantum efficiencies of $GaN/Al_xGa_{1-x}N$ multiple quantum wells." *Applied Physics Letters*, **2000**, 76, 3040-3042.

59. Garrett, G.A., Shen, H., Wraback, M., Imer, B., Haskell, B., et al., "Intensity dependent time-resolved photoluminescence studies of GaN/AlGaN multiple quantum wells of varying well width on laterally overgrown a-plane and planar c-plane GaN." *physica status solidi (a)*, **2005**, 202, 846-849.

60. Ko, T.S., Lu, T.C., Wang, T.C., Lo, M.H., Chen, J.R., et al., "Optical characteristics of a-plane InGaN⁄GaN multiple quantum wells with different well widths." *Applied Physics Letters*, **2007**, 90, 181122.

Chapter 7. Conclusions and Future Outlook

7.1 Conclusions

This thesis has developed an in-depth understanding of the selective area growth (SAG) of GaN nanowires using MOCVD. Heteroepitaxial growth of AlGaN alloys on GaN nanowires in a core-shell fashion has been investigated for different alloy compositions. These led to the development of $Al_xGa_{1-x}N/Al_yGa_{1-y}N$ multiple quantum wells (MQWs) growth for applications in ultraviolet (UV) emitters.

In Chapters 1 to 2, motivations for the research in AlGaN-based nanostructures are provided and the background on existing AlGaN-based UV LEDs. We also briefly introduce the experimental techniques used for the growth and characterisation of AlGaN nanostructures in Chapter 3.

Chapter 4 investigates selective area growth of GaN nanowires on *c*-plane GaN pseudo-substrate (GaN/*c*-sapphire) using metal organic chemical vapour deposition (MOCVD). Triethylgallium and NH_3 are used as source of Ga and N, respectively. A mixed carrier gas composed of N_2/H_2 is employed to carry the precursors into the reactor for GaN nanowire growth. A remarkable relationship has been established between the observed morphology and partial pressures of Triethylgallium, NH_3, and H_2 during the SAG of GaN nanowires at a particular growth temperature. Therefore, all of the selective are growth parameters for GaN nanowires in MOCVD can be reduced to just two parameters: (*i*) partial pressures and (*ii*) growth temperature. Based on the range of Triethylgallium and NH_3 partial pressures, the optimal range of V/III ratio for GaN nanowire growth has been determined as 13 to 73. However, it should be noted that V/III ratio is not a sufficient criterion to determine GaN nanowire growth, but partial pressures and temperature are the key parameters that determine

GaN nanostructure morphology. Hence, this study has uncovered ways to obtain specific GaN nanostructures, more specifically, Ga-polar GaN nanowires, based on the partial pressures and growth temperature.

In Chapter 5, the selective area-grown GaN nanowires are used as a growth template and GaN/AlGaN core-shell nanowires are grown using MOCVD. Initial growth experiment of AlGaN shell with a mixed carrier gas of N_2/H_2, employed in the GaN nanowire growth, resulted in striated surface of the AlGaN shell. A smooth surface of the AlGaN shell is a prerequisite to obtain sharp interface and avoid waviness in MQWs. Using pure N_2 as carrier gas, AlGaN shells with smooth surface and superior optical characteristics have been obtained. This achievement is attributed to minimisation of disparity in Al and Ga adatom mobilities and reduced incorporation of unintentional impurities using pure N_2 carrier gas. AlGaN shells with gas-phase Al compositions from 15 to 60% have been grown. Elemental analysis using EDS and alloy composition determined from emission spectra of GaN/AlGaN core-shell nanowires indicates a lower Al incorporation in the AlGaN shell compared to the gas-phase Al composition. The reduced Al incorporation is attributed to the geometry of nanowire, strain in AlGaN, and gas phase parasitic reaction of trimethylaluminium and NH_3. With the knowledge of GaN/AlGaN core-shell growth, $Al_xGa_{1-x}N/Al_yGa_{1-y}N$ MQWs growth is explored and UV emission at a wavelength of 332 nm from the MQW region on the nonpolar *m*-plane sidewalls has been demonstrated.

In Chapter 6, a systematic investigation on the growth and UV emission characteristics from $Al_xGa_{1-x}N/Al_yGa_{1-y}N$ MQWs is carried out. Microstructural and UV emission characteristics of AlGaN MQWs are studied with respect to pitch of the nanowire array. It has been determined that nanowires with uniform sidewalls are obtained when the gap between adjacent nanowires is $\geq$ 600 nm, whereas nanowires with an inverse tapered morphology, resembling a trophy, are obtained for smaller gaps. Such a dependence on nanowire morphology with pitch (or gap between the nanowires) is determined to be due to the growth of AlGaN predominantly controlled by vapour phase diffusion of the precursors and its associated shadowing effect. Nonuniformity in the sidewall thickness and hence, the well widths of MQWs for closely arranged AlGaN nanostructures with pitch $\leq$ 1 μm resulted in emission of different wavelengths along the length of the nanowire. Uniform emission along the length of the nanowire is achieved for nanowire array with pitch $\geq$ 1.5 μm. By changing the Al composition of MQWs from 0 to 27%, UV emission in the wavelength range of 318 – 343 nm has been achieved from nonpolar *m*-plane $Al_xGa_{1-x}N/Al_yGa_{1-y}N$ MQWs with uniform

emission from an array of 45×45 μm^2. This work demonstrated the possibility of GaN/AlGaN nanowires for UV emission and the thus, providing a significant step towards the future of efficient AlGaN nanowire UV LEDs.

7.2 Future outlook

Based on the knowledge and achievement from these studies, we propose three major directions for future work as follows:

1. Design and simulation of MQW structure and nanowire array for efficient UV emission.
2. Investigation of doping for efficient carrier injection.
3. Fabrication of electrically injected AlGaN nanowire UV LEDs.

As the growth of GaN nanowires, AlGaN shells, and AlGaN MQWs have been addressed in Chapters 4, 5, and 6 respectively, design and simulation of the MQW structure in terms of QW width and alloy composition with consideration of the GaN nanowire diameter will aid in achieving optimum internal quantum efficiency from the AlGaN MQWs. Further, design and simulation of the nanowire array using finite difference time domain methods (FDTD) will also be beneficial in optimising the light extraction efficiency to boost the overall external quantum efficiency.

For practical applications, electrically injected devices in the form of nanowire array UV LEDs will be required. To realise electrically driven efficient UV LEDs, optimisation of both n- and p-type dopants need to be carried out. In the planar epitaxial growth of III-nitrides, n-type doping using Si is relatively well established. However, Si doping in GaN nanowires often results in formation of a thin SiN_x layer around the nanowire sidewall and results in breakdown of epitaxial relationship or no growth. Hence, controlled doping of Si needs to be optimised. Further, p-type doping in III-nitrides usually carried out with Mg has remained a challenging issue, and exacerbated in the case of AlGaN due to high activation energy. Therefore, an insightful investigation on the limitations and achievable p-type doping in AlGaN nanowires is warranted to achieve efficient carrier injection.

Electrically injected efficient nanowire UV LED is the primary goal of solid-state UV light source. Yet, the nanowire morphology poses challenge for electrical contact fabrication, which needs to remain continuous on all of the nanowires and at the same time exhibit high transparency of UV light. Further, the conventional growth of GaN on insulating sapphire

substrate hinders electrical contact fabrication on bottom of the wafer, hence both p- and n-type electrical contacts need to be fabricated on top of the wafer. Specifically, the n-type contact needs to be fabricated via etching down to the n-type GaN layer followed by contact metal deposition using a lithography process to confine the metal deposition only in the exposed n-type regions.

Overall, the knowledge of GaN nanowire growth and the subsequently developed AlGaN shell and MQW growth emitting in UV wavelengths is expected to serve as key stepping stones toward electrically injected AlGaN nanowire UV LEDs of the future.